

On aspects of gravitational-wave detection: Detector characterisation, data analysis and source modelling for ground-based detectors

Von der Fakultät für Mathematik und Physik
der Gottfried Wilhelm Leibniz Universität Hannover
zur Erlangung des Grades

Doktor der Naturwissenschaften
- Dr. rer. nat. -

genehmigte Dissertation von

M. Sc. Ajith Parameswaran

geboren am 27 Mai 1980 in Chemmaniyode, Kerala, Indien.

Referent : Prof. B. F. Schutz
Koreferent : Prof. K. Danzmann
Tag der Promotion : 10 Dezember 2007

To Achan, Amma and Ammu.

“And how many hours a day did you do lessons?” said Alice, in a hurry to change the subject.

“Ten hours the first day”, said the Mock Turtle: “nine the next, and so on.”

“What a curious plan!” exclaimed Alice.

“That’s the reason they’re called lessons”, the Gryphon remarked: “because they lessen from day to day”.

– Lewis Carroll, in *Alice’s Adventures in Wonderland*.

Zusammenfassung

Die vorliegende Arbeit beschäftigt sich mit drei Aspekten der Suche nach Gravitationswellen (GW) mit erdgestützten Detektoren: Detektorcharakterisierung, Datenanalyse und Modellierung von Quellen. Der erste Teil behandelt die Detektorcharakterisierung und die Entwicklung von Vetostrategien für die Suche nach transienten unmodellierten GW-Ausbrüchen. Der zweite Teil enthält Methoden der Datenanalyse, die zur Suche nach GW-Ausbrüchen und verschmelzenden kompakten Doppelsternsystemen angewendet werden. Der dritte Teil befasst sich mit der Modellierung von GW, die von kompakten Binärsystemen erzeugt werden, mit post-Newtonschen (PN) Methoden.

Teil I. Kapitel 2 beschreibt die Charakterisierung der Qualität der Parameterabschätzung des *mHACR* Algorithmus für GW-Ausbrüche. In Kapitel 3 wird eine robuste Strategie zum Ausschluss bestimmter Klassen von Störimpulsen in interferometrischen GW-Detektoren vorgestellt. Dabei wurde die Kenntnis der Kopplung verschiedener Untersystemen des Detektors auf das Ausgangssignal des Interferometers genutzt. Diese Vetomethode wurde durch Einspeisung von Störimpulsen in das GEO 600 Interferometer demonstriert (Kapitel 4). Ein Beispiel der Anwendung dieser Vetomethode auf die von GEO 600 aufgenommenen Daten wird präsentiert. Kapitel 5 beschreibt eine weitere Vetomethode, basierend auf dem ‘*null stream*’, der aus den beiden Ausgangsquadraturen von GEO 600 konstruiert wird.

Teil II. Der ‘*null stream*’, der aus den Ausgängen mehrerer Detektoren konstruiert werden kann, kann als Veto zur Vermeidung falscher Alarme bei der Suche nach GW-Ausbrüchen verwendet werden. Die größte Fehlerquelle in der ‘*null stream*’ Analyse ist durch Kalibrationsfehler der aufgenommenen Daten gegeben. In Kapitel 6 wird die Einbindung eines ‘*null stream*’ Vetos in ein Netzwerk von zwei Detektoren, die sich am selben Ort befinden, vorgestellt. Dazu wird ein neues Verfahren zur Vermeidung des Einflusses von Kalibrationsfehlern vorgeschlagen. Ausserdem wird ein Beispiel der Anwendung auf die Daten des LIGO-Hanford Detektors vorgestellt. Kapitel 7 beschreibt die Konstruktion einer neuen ‘*template bank*’, die in der Lage ist, die ‘*inspiral*’ Phase, die Verschmelzungsphase und die Abklingphase verschmelzender, nicht rotierender schwarzer Löchern zu modellieren. Dadurch wird es möglich eine kohärente Suche bezüglich aller drei Phasen eines Binärsystems durchzuführen, die die Suchempfindlichkeit verbessern und die Ereignisrate der Interferometer steigern wird. Das Kapitel enthält ausserdem eine allgemeine Prozedur, um interpolierte ‘*template banks*’ zu erstellen. Dabei werden die Wellenformen von Doppelsternsystemen aus nicht-rotierenden schwarzen Löchern, wie sie mit Methoden der numerischen Relativität berechnet werden können, verwendet.

Teil III. In Kapitel 8 wird eine neue *vollständig adiabatische* Abschätzung für die Berechnung von GW von kompakten einspiralisierenden Binärsystemen unter Benutzung der PN Theorie vorgeschlagen. Sie enthält eine konsistente Behandlung der Beschleunigung des Binärsystems bis zur jeweiligen PN Ordnung, und ihre Ergebnisse liegen deutlich näher an der exakten Wellenform für den Fall eines Testteilchens, das sich in einer Umlaufbahn um ein Schwarzschild schwarzes Loch befindet.

Stichworte: Gravitationswellen, Detektorcharakterisierung, Datenanalyse, Quellenmodellierung.

Abstract

This thesis covers three topics related to the search for gravitational waves (GWs) using ground-based interferometric detectors — detector characterisation, data analysis and source modelling. The first part deals with detector characterisation and veto development for the search for transient, unmodelled GW bursts. The second part is related to data-analysis methods used in the search for GW bursts and coalescing compact binaries. The third part addresses some theoretical challenges related to the post-Newtonian (PN) modelling of GWs from inspiralling compact binaries.

Part I. Chapter 2 describes the studies carried out for characterising the parameter-estimation quality of the *mHACR* burst-detection algorithm. Chapter 3 presents a robust strategy to veto certain classes of instrumental glitches that appear at the output of interferometric GW detectors, making use of the knowledge of the coupling of different detector subsystems to the main detector output. This veto method is demonstrated by injecting instrumental glitches in the hardware of the GEO 600 detector (Chapter 4). An example application of the veto method to the data of GEO 600 is also presented. Another instrumental veto method making use of the *null stream* constructed from the two output quadratures of GEO 600 is described in Chapter 5.

Part II. The null stream constructed from multiple GW detectors can be used as a powerful veto against spurious instrumental triggers in the search for GW bursts. The biggest source of error in the null-stream analysis comes from the calibration errors in the data. Chapter 6 presents an implementation of the null-stream veto in a network of two co-located detectors, proposing a new formulation to overcome the effect of calibration errors. An example application to the data of the two LIGO-Hanford detectors is also presented. Chapter 7 constructs a new template bank which can model the inspiral, merger and ring down stages of the coalescence of non-spinning binary black holes. This will allow us to *coherently* search for all the three stages of the binary black hole coalescence, improving the sensitivity of the search and potentially bringing remarkable improvement in the event-rate for ground-based interferometers. This Chapter also prescribes a general procedure to construct interpolated template banks using non-spinning binary-black-hole waveforms produced by numerical relativity.

Part III. Chapter 8 proposes a new *complete adiabatic* approximation for the computation of gravitational waveforms from inspiralling compact binaries using PN theory. This approximation provides a consistent treatment of the acceleration of the binary up to the respective PN order. The new approximants are found to be much closer (than the *standard adiabatic* approximants) to the exact waveform in the case of a test particle orbiting a Schwarzschild black hole.

Key words: Gravitational waves, detector characterisation, data analysis, source modelling.

Contents

List of Figures	xv
List of Tables	xxiii
1. Gravitational-wave astronomy: Opening a new window onto the Universe	1
1.1. Introduction	1
1.2. Expected sources of gravitational waves	2
1.2.1. Coalescing compact binaries	3
1.2.2. Sources of gravitational-wave bursts	3
1.2.3. Sources of periodic gravitational waves	4
1.2.4. Stochastic gravitational-wave background	5
1.3. Gravitational-wave astronomy	5
1.3.1. Testing theories of gravity	6
1.3.2. Astrophysics using gravitational waves	6
1.3.3. Cosmology using gravitational waves	7
1.4. The search for gravitational waves	7
1.4.1. Detecting gravitational waves	8
1.4.2. Worldwide network of gravitational-wave detectors	8
1.4.3. Current observational results	9
1.4.4. Challenges in the search for gravitational waves	11
1.5. Overview and summary of this thesis	14
I. Detector characterisation and veto development for ground-based interferometers	19
2. Improving and characterising the hierarchical algorithm for curves and ridges	21
2.1. The burst detection algorithm mHACR	21
2.1.1. Detection algorithm	22
2.1.2. Parameter estimation	23
2.2. Quality of the parameter estimation	24
2.3. Application of mHACR in the detector characterisation of GEO 600	26
3. Physical instrumental vetoes for gravitational-wave burst triggers	29
3.1. The search for transient, unmodelled gravitational-wave bursts	29
3.2. Vetoes using known instrumental couplings	30
3.2.1. Noise transfer	30
3.2.2. A veto strategy using known instrumental couplings	31

3.2.3.	Test statistic: using null-stream	32
3.2.4.	Test statistic: using cross-correlation	33
3.2.5.	Implementation	34
3.3.	Software injections	35
3.3.1.	Causal injections	36
3.3.2.	Random injections	37
3.4.	An alternative method: ‘trigger mapping’	37
3.4.1.	Mapping the burst triggers	38
3.4.2.	Identifying consistent events	40
3.4.3.	Software injections	41
3.5.	Summary	42
4.	Physical instrumental vetoes: application to GEO 600 data	45
4.1.	The ‘real-life’ scenario	45
4.1.1.	Implementation	45
4.1.2.	Caveats	46
4.2.	Analysis on hardware-injected burst signals	47
4.2.1.	Injections mimicking instrumental bursts	47
4.2.2.	Injections mimicking gravitational-wave bursts	50
4.3.	An example application	51
4.4.	Summary and outlook	55
5.	A null-stream veto for GEO 600	59
5.1.	Introduction	59
5.2.	Signal injection and detection	61
5.3.	The amplitude consistency test	63
5.3.1.	Veto efficiency and false-veto probability studies	64
5.3.2.	Setting the consistency threshold	65
5.3.3.	Demonstrating veto safety: hardware injections	66
5.4.	Example application to GEO 600 data	67
5.5.	Summary	68
II.	Data analysis for coalescing compact binaries and unmodelled-burst sources	71
6.	Null-stream veto for two co-located detectors	73
6.1.	Introduction	73
6.2.	The null-stream veto	74
6.2.1.	Software injections	75
6.3.	Calibration uncertainties	76
6.3.1.	Dealing with calibration uncertainties	78
6.3.2.	Software injections with simulated calibration errors	79
6.4.	Example application to LIGO data	81
6.4.1.	Data conditioning	81
6.4.2.	Software injections	81

6.4.3.	Null-stream veto analysis on <i>Waveburst</i> triggers	83
6.5.	Summary	83
7.	A template bank for gravitational waveforms from coalescing binary black holes	85
7.1.	Introduction	85
7.1.1.	Summary and organisation of this chapter	87
7.2.	Numerical simulations and wave extraction	88
7.3.	Post-Newtonian waveforms and introduction to data-analysis concepts .	91
7.3.1.	Restricted post-Newtonian waveforms	91
7.3.2.	Introduction to matched filtering	92
7.3.3.	Template banks, effectualness and faithfulness	93
7.4.	A phenomenological template family for black-hole coalescence waveforms	95
7.4.1.	Strategy for constructing the phenomenological bank	95
7.4.2.	Constructing the ‘target signals’	97
7.4.3.	Parametrizing the hybrid waveforms	100
7.4.4.	Effectualness and faithfulness	105
7.4.5.	Verification of the results using more accurate hybrid waveforms	106
7.4.6.	The astrophysical range and comparison with other searches . .	110
7.5.	Summary and outlook	111
III.	Modelling of coalescing compact binaries	115
8.	New class of post-Newtonian approximants to the waveform templates of inspiralling compact binaries	117
8.1.	Introduction	117
8.1.1.	Standard approach to phasing formula	118
8.1.2.	Complete phasing of the adiabatic inspiral: an alternative	119
8.1.3.	What this study is about	121
8.1.4.	Effectualness and faithfulness	122
8.1.5.	Noise spectra of the interferometers	123
8.1.6.	Organization of this chapter	123
8.2.	Test mass waveforms in the adiabatic approximation	124
8.2.1.	The energy function	125
8.2.2.	The flux function	126
8.2.3.	Comparison of standard and complete adiabatic approximants .	127
8.3.	Comparable mass waveforms	140
8.3.1.	The energy function	141
8.3.2.	The flux function	142
8.3.3.	Comparable mass results in the adiabatic approximation	145
8.4.	Summary and conclusion	146
A.	Analytical calculation of the fitting factors	151
B.	Computing the horizon distance	153

B.1. Search using post-Newtonian templates	153
B.2. Search using ring down templates	154
B.3. Search using all the three stages of the binary black-hole coalescence . .	155
Bibliography	157

List of Figures

2.1.	Distribution of the errors in estimating the central time, central frequency and RSS amplitude of the injected sine-Gaussian waveforms. The errors in the frequency and amplitude estimation are normalised by the injected value of the parameters; i.e., $\hat{\Delta}f_0 = \Delta f_0 / f_{\text{cen}}$ and $\hat{\Delta}a = \Delta a / h_{\text{RSS}}$. Injections are done with Nine different values of h_{RSS} such that the SNR of the injections ranges from $\simeq 5$ to $\simeq 300$ (see Figure 2.2). Sample mean and standard deviation of each of the 9 populations are estimated separately. Each error is converted into a reduced normal variable by subtracting the corresponding sample mean and by normalising by the corresponding standard deviation. Also plotted are the probability densities of the standard normal distributions.	25
2.2.	Standard deviation of the distribution of the errors (fractional errors in the case of f_0 and a) in estimating the parameters of the injected sine-Gaussian waveforms, plotted as a function of the SNR of the triggers. Also shown are power-law fits to the data.	26
2.3.	Mean errors (fractional errors in the case of f_0 and a) in the parameter estimation, plotted as a function of the SNR of the triggers.	26
3.1.	Schematic diagram of the linear vector space in which the analysis methods are formulated.	32
3.2.	Transfer function from channel X to channel H used for the simulations.	35
3.3.	Amplitude spectral densities of \mathbf{x} , \mathbf{x}' , \mathbf{h} and $\tilde{\delta}$ in the presence of a sine-Gaussian injection. It can be seen that $\tilde{\delta}$ contains no trace of the injected signal. The injected sine-Gaussian has a central frequency of 1715 Hz and SNR of 140 in channel X	36
3.4.	[<i>Left</i>]: Fraction of causal injections vetoed by the null-stream method, plotted against the rejection probability corresponding to the chosen threshold. [<i>Right</i>]: Fraction of random injections vetoed by the cross-correlation method, plotted against the accidental veto probability corresponding to the chosen threshold. The dashed lines correspond to the case where the test statistics exactly fall in to the expected distributions.	38
3.5.	A schematic diagram of the parameter space of burst triggers. The cross represents a trigger in channel H and the circle represents a trigger in channel X , mapped to channel H . A distance vector \mathbf{w} is drawn from one point to another. The consistency volume chosen to veto the trigger is also shown.	39

3.6.	The RSS amplitude, E^a , of the burst events plotted against the central frequency, E^f . Shown in the figure are three population of events: events in channel X (\mathbf{E}_X); channel X events mapped to channel H (\mathbf{E}'_X); and events in channel H (\mathbf{E}_H).	41
3.7.	[<i>Left</i>]: Fraction of ‘causal’ injections vetoed, plotted against the rejection probability corresponding to the chosen threshold. [<i>Right</i>]: Fraction of ‘random’ injections vetoed, plotted against the rejection probability corresponding to the chosen threshold.	42
4.1.	Block diagram of the veto pipeline.	46
4.2.	Time shift analysis on instrumental-glitch-like hardware injections performed in the Φ_{MI} channel. The horizontal axis shows the time shift applied between x_i and h_i , and the vertical axis shows the excess-power ratio s . The (black) dots correspond to the coincident triggers in the time-shifted analysis and the (red) crosses correspond to the ones in the zero-lag analysis.	47
4.3.	Same as in Figure 4.2, except that the vertical axis shows the cross-correlation statistic z . The (black) dots correspond to the coincident triggers in the time-shifted analysis and the (blue) crosses correspond to the ones in the zero-lag analysis.	48
4.4.	Time shift analysis on the GW-like hardware injections. E_{ref} is used as the veto channel. The horizontal axis shows the time shift applied between x_i and h_i , and the vertical axis shows the excess-power ratio s . The (black) dots correspond to the coincident triggers in the time-shifted analysis and the (red) crosses correspond to the ones in the zero-lag analysis.	50
4.5.	Same as in Figure 4.4, except that the vertical axis shows the cross-correlation statistic z . The (black) dots correspond to the coincident triggers in the time-shifted analysis and the (blue) crosses correspond to the ones in the zero-lag analysis.	51
4.6.	Time-shifted analysis on 5 days of data from the Fifth science run of GEO 600 using E_{ref} as the veto channel. The horizontal axis shows the time shift applied between x_i and h_i , and the vertical axis shows the excess-power ratio s . The black dots correspond to the coincident triggers in the time-shifted analysis and the red crosses correspond to the ones in the zero-lag analysis.	52
4.7.	Same as in Figure 4.6, except that the vertical axis shows the cross-correlation statistic z . The black dots correspond to the coincident triggers in the time-shifted analysis and the blue crosses correspond to the ones in the zero-lag analysis.	53
4.8.	Histograms of the excess-power ratio s computed from the time-shifted analysis (left) and the zero-lag analysis (right).	54
4.9.	Histograms of the cross-correlation statistic z computed from the time-shifted analysis (left) and the zero-lag analysis (right).	54

4.10. A time-frequency plot of mHACR triggers from 5 days of GEO 600 data. The horizontal axis shows the time and the vertical axis shows the frequency of the the burst triggers in channel H , as estimated by mHACR. Only those triggers which are coincident with E_{ref} are plotted. The (green) circles correspond to coincident triggers which are vetoed using the null-stream method, and the (black) dots correspond to the ones which are vetoed using the cross-correlation method. Coincident triggers which are not vetoed by any of the methods are indicated by (red) crosses. The chosen veto thresholds correspond to one accidental veto per day.	55
4.11. Fraction of coincident triggers that are vetoed in the zero-lag plotted against the fraction of the coincident triggers that are vetoed in the time-shifted analysis. The solid curve corresponds to the analysis using null-stream and the dashed curve corresponds to the analysis using cross-correlation. The triangles, the squares, and the dots correspond to accidental veto rates of 1 per month, 1 per week, and 1 per day, respectively.	57
4.12. Excess-power ratio s (horizontal axis) computed from the coincident triggers plotted against the cross-correlation statistic z (vertical axis). The vertical (red) and horizontal (blue) lines correspond to the veto thresholds τ_s and λ on the two statistics, respectively.	57
5.1. Amplitude spectral densities of the $h(t)$ and $h_{\text{null}}(t)$ outputs of GEO 600. Calibration lines are marked for the two spectra, and the ratio of the calibration line amplitudes in $h(t)$ and $h_{\text{null}}(t)$ are indicated in the boxes.	60
5.2. Two example injected events into the data. The amplitude spectral density estimates are computed from 1 second of data with no averaging and using a Hann window. The parameters of the injected waveform are shown in the legend. The left plot shows an event with a high SNR; the right plot, one with a low SNR.	62
5.3. False alarm and efficiency plots for the time and frequency cuts (Δt and Δf) applied to events detected by mHACR. From these plots, a frequency window of 6 Hz and a time window of 40 ms was chosen for the null-stream experiments. Here ‘efficiency’ refers to the percentage of coincident events that are expected to pass the consistency test; ‘false-alarm’ refers to the percentage of non-coincident events which are falsely taken to be coincident when applying the consistency test.	63
5.4. The false-veto and efficiency curves for the null-stream veto. The efficiency curves are computed for different cases of signal injection—see text for details.	66
5.5. Time-frequency plot of mHACR triggers from hardware injections. The (red) crosses denote burst events in channel h and the (black) dots denote events in channel h_{null}	67

-
- 5.6. A time-frequency map of the events detected by mHACR in $h(t)$ and $h_{\text{null}}(t)$ for a 1 hour data stretch of GEO 600. Those events that were found to be time and frequency consistent between the two lists are marked with boxes; those that were subsequently vetoed are marked with triangles. 68
- 6.1. [*Left*]: Estimated false-veto fraction plotted against the predicted false-dismissal probability, assuming that the two detectors are perfectly calibrated. [*Right*]: Estimated false-veto fraction in the presence of $\pm 10\%$ calibration uncertainty, plotted against the combined SNR of the injections, for three different values of the predicted false-dismissal probability (γ). The three dashed lines show the predicted values of the false-dismissal probability in the absence of calibration uncertainties. 77
- 6.2. The excess-power statistic $\epsilon'(\xi)$ constructed from null stream $n'(t; \xi)$ plotted against the free parameter ξ , for three different values of δ . We assume that the maximum expected absolute value of δ is 0.1. $\epsilon'(-\delta/(1 + \delta))$ for each curve is marked with a square. It can be seen that the minimum value of $\epsilon'(\xi)$ is less than, or equal to $\epsilon'(-\delta/(1 + \delta))$ 78
- 6.3. [*Left*]: Estimated false-veto fraction plotted against the predicted false-dismissal probability. The relative calibration between $h_1(t)$ and $h_2(t)$ is assumed to be between $-0.1 \leq \delta \leq 0.1$. [*Right*]: Rejection power of the veto plotted against the predicted false-dismissal probability. Each curve in the plot corresponds to a particular range of SNR. 80
- 6.4. Cumulative distribution (left) and the probability density (right) of the test statistic ϵ calculated from H1-H2 playground data. Also shown are the cumulative distribution (left) and probability density (right) of the expected Gamma distribution. These correspond to injections performed with no calibration errors. 81
- 6.5. Left panel shows the fraction of vetoed sine-Gaussian injections plotted against the predicted false-veto probability. Right panel shows the same plot using band-limited white-noise burst injections. The injections are done simulating a relative calibration error $-0.1 \leq \delta \leq 0.1$ 82
- 6.6. Comparison of the null-stream veto analysis with the H1-H2 amplitude cut. The horizontal axis shows the false-dismissal probability of the null-stream in vetoing the coincident triggers, while the vertical axis shows the ratio of the h_{rss} of the coincident triggers in H1 and H2. The (red) dashed vertical line corresponds to a false-dismissal probability γ of 1%, and the triggers on the left of this line can be vetoed with $\gamma < 1\%$. The (green) horizontal lines correspond to the amplitude ratios ($h_{\text{rss}1}/h_{\text{rss}2}$) 0.5 and 2. Triggers with amplitude ratio less than 0.5 and greater than 2 are vetoed using the amplitude cut. 84

7.1.	Construction of the phenomenological template bank: (i) mapping physical signals (solid curve) into a sub-manifold (dashed curve, with example templates marked by dots) of a larger-dimensional template bank (curved surface), (ii) obtaining a lower-dimensional phenomenological bank with the same number of parameters as physical parameters, through interpolation (solid curve on the curved surface, with example templates marked by triangles), and (iii) Estimating the bias of the lower-dimensional interpolated bank by mapping physical signals into the bank (with images of example signals marked by dots).	94
7.2.	NR waveforms (thick/red), the ‘best-matched’ 3.5PN waveforms (dashed/black), and the hybrid waveforms (thin/green) from three binary systems. The top panel corresponds to $\eta = 0.25$ NR waveform produced by the AEI-CCT group. The second, third and fourth panels, respectively, correspond to $\eta = 0.25, 0.22$ and 0.19 NR waveforms from produced by the Jena group. In each case, the matching region is $-750 \leq t/M \leq -550$ and we plot the real part of the complex strain (the ‘+’ polarization).	98
7.3.	Fourier domain magnitude (left) and phase (right) of the (normalized) hybrid waveforms. For the phase the leading order linear in time part has already been subtracted. Symmetric mass-ratio η of each waveform is shown in the legends. These waveforms are constructed by matching 3.5PN waveforms with the long NR waveforms produced by the Jena group.	100
7.4.	Fitting factors of the hybrid waveforms with the phenomenological waveform family. Horizontal axis shows the symmetric mass ratio of the binary. Fitting factors are calculated assuming a white noise spectrum, and hence are independent of the mass of the binary.	101
7.5.	Hybrid waveforms (solid lines) in the frequency domain, and the ‘best-matched’ phenomenological waveforms (dashed lines). The left panel shows the Fourier domain magnitude, while the right panel shows the phase. For the phase the leading order linear in time part has already been subtracted. These waveforms correspond to a binary with $\eta = 0.25$, and are constructed from the ‘short’ NR waveforms produced by the Jena group (see Section 7.4.2). The ‘dip’ in the left panel at $Mf \simeq 2 \times 10^{-2}$ is due to the small eccentricity present in the first few cycles of the NR waveform.	102
7.6.	Best-matched amplitude parameters α_{\max} in terms of the physical parameters of the binary (assuming white noise spectrum). The horizontal axis shows the symmetric mass-ratio of the binary. Quadratic polynomial fits α_{int} to the data points are also shown.	104
7.7.	Best-matched phase parameters ψ_{\max} in terms of the physical parameters of the binary (assuming white noise spectrum). The horizontal axis shows the symmetric mass-ratio of the binary. Quadratic polynomial fits ψ_{int} to the data points are also shown.	105

7.8.	Fitting factor of the (two-dimensional) template family computed using three different noise spectra. The panel in the left correspond to the Initial LIGO noise PSD, the one in the middle to the Virgo noise PSD and the one in the right to the Advanced LIGO noise PSD. The horizontal axis reports the symmetric mass ratio η of the binary and the legends display the total mass M (in units of M_{\odot}).	107
7.9.	Same as in Figure 7.8, except that the plots show the faithfulness of the (two-dimensional) template family.	107
7.10.	Bias in the estimation of M . Horizontal axis reports the total mass M (in units of M_{\odot}) and vertical axis reports the symmetric mass ratio η of the binary. Colors in the plot corresponds to the percentage bias, $ \Delta M /M \times 100$. The left panel corresponds to the Initial LIGO noise PSD, the middle panel to the Virgo noise PSD and the right panel to the Advanced LIGO noise PSD.	108
7.11.	Same as in Figure 7.10, except that the plots show the percentage bias $ \Delta \eta /\eta \times 100$ in the estimation of η	108
7.12.	Same as in Figure 7.10, except that the plots show the percentage bias $ \Delta M_c /M_c \times 100$ in the estimation of $M_c = M\eta^{3/5}$	109
7.13.	Fitting factor of the (two-dimensional) template family with ‘more accurate’ hybrid waveforms (see Section 7.4.5). The overlaps are computed using three different noise spectra. The panel in the left correspond to the Initial LIGO PSD, the one in the middle to the Virgo noise PSD and the one in the right to the Advanced LIGO noise PSD. The horizontal axis represents the total mass M (in units of M_{\odot}) and the legends display the symmetric mass ratio η of the binary.	110
7.14.	Distance to optimally located and oriented equal-mass binaries which can produce an optimal SNR of 8 at the Initial LIGO (left plot), Virgo (middle plot) and Advanced LIGO (right plot) noise spectra. Horizontal axis reports the total mass of the binary (in units of M_{\odot}) and vertical axis reports the distance in Mpc. In each plot, the thin solid (blue) line corresponds to a search using standard PN templates truncated at ISCO, the dotted-dashed (black) line to a search using effective one body waveform templates truncated at the light ring, the the dashed (purple) line to a search using ring-down templates, and the thick solid (red) line to a search using the template family proposed in this chapter. The ring down horizon distance is computed assuming that $\epsilon = 0.7\%$ of the black hole mass is radiated in the ring down stage, while the Kerr parameter $a = 0.69$ is known from the numerical simulation. Since the value of ϵ has some amount of uncertainty in it, a shaded region is also included in the plot corresponding to $0.18\% \leq \epsilon \leq 2.7\%$	111
8.1.	Amplitude noise spectral densities of three ground-based interferometric detectors.	124

-
- 8.2. Various T-approximants of Newton-normalized (v -derivative of) energy function $E'_T(v)/E'_N(v)$ [left], and flux function $\mathcal{F}_T(v)/\mathcal{F}_N(v)$ [right] in the test mass limit along with the exact functions (denoted by X). 125
- 8.3. The difference, $\mathbb{F}_C - \mathbb{F}_S$, in the effectualness of complete adiabatic and standard adiabatic templates in the test mass limit. Overlaps are calculated assuming a flat spectrum for the detector noise (white noise). Plots on the left correspond to TaylorT1 approximants, while plots on the right correspond to TaylorF1 approximants. 127
- 8.4. The difference, $\mathbb{F}_C - \mathbb{F}_S$, in the faithfulness of complete adiabatic and standard adiabatic templates in the test mass limit. Overlaps are calculated assuming a flat spectrum for the detector noise (white noise). Plots on the left correspond to TaylorT1 approximants, while plots on the right correspond to TaylorF1 approximants. 130
- 8.5. The difference, $\mathbb{F}_C - \mathbb{F}_S$, in the effectualness between complete adiabatic and standard adiabatic templates in the test mass limit. The plots correspond to overlaps calculated using three different noise spectra — Initial LIGO (left), Virgo (middle), and Advanced LIGO (right). 131
- 8.6. The difference, $\mathbb{F}_C - \mathbb{F}_S$, in the faithfulness between complete adiabatic and standard adiabatic templates in the test mass limit. The plots correspond to overlaps calculated using three different noise spectra — Initial LIGO (left), Virgo (middle), and Advanced LIGO (right). 132
- 8.7. Top panel shows the approximants of $\hat{\mathcal{F}}(v)/\hat{E}'(v)$ plotted as a function of v . Dashed lines indicate standard approximants and solid lines indicate the corresponding complete approximants. Middle and bottom panels show the same approximants plotted as a function of the GW frequency $F = v^3/\pi m$ in the case of the $(1M_\odot, 10M_\odot)$ binary and the $(1M_\odot, 50M_\odot)$ binary, respectively. 135
- 8.8. Effectualness (left panels) and faithfulness (right panels) of various test mass TaylorT1 and TaylorF1 templates in detecting a signal from a $(1M_\odot, 10M_\odot)$, calculated for the initial LIGO noise PSD. The horizontal axis reports the order $[n]$ of the energy function, while the legends report the order n of the flux function. Each line shows how the overlaps are evolving as a function of the accuracy of the energy function. Standard adiabatic approximants $T(E_{[n]}, \mathcal{F}_n)$ are marked with thick dots. 137
- 8.9. Same as in Figure 8.8 except that the plot correspond to a $(1M_\odot, 50M_\odot)$ binary. 138
- 8.10. The fractional absolute difference $\delta\mathcal{N}_n$ between the number of cycles accumulated by various approximants and the exact waveform, plotted against the corresponding overlaps. Standard adiabatic approximants are marked with lighter markers and complete adiabatic approximants are marked with darker markers. Top panels show $\delta\mathcal{N}_n$ for the total number of cycles and bottom panels show $\delta\mathcal{N}_n$ for the number of useful cycles. The number of useful cycles are calculated for the initial LIGO noise PSD and the low frequency cut-off is chosen to be 40Hz. The plotted results are for a $(1M_\odot, 10M_\odot)$ binary. 141

-
- 8.11. Various T-approximants of Newton-normalized (v -derivative of) energy function $E'_T(v)/E'_N(v)$ (left) and flux function $\mathcal{F}_T(v)/\mathcal{F}_N(v)$ (right) in the comparable mass case, along with the corresponding fiducial ‘exact’ functions (denoted by X). 143
- 8.12. Effectualness of various TaylorT1 templates in the comparable mass case. The horizontal axis reports the PN order $[n]$ of the energy function, while the legends report the PN order n of the flux function. Each line shows how the overlaps are evolving as a function of the accuracy of the energy function. Standard adiabatic approximants are marked with thick dots. The top panes corresponds to the $(10M_\odot, 10M_\odot)$ binary and the bottom panel to the $(1.4M_\odot, 1.4M_\odot)$ binary. Overlaps are calculated for the initial LIGO (left plots), Advanced LIGO (middle plots) and Virgo (right plots) noise spectra. 144
- 8.13. Faithfulness of various TaylorT1 templates in the comparable mass case. The horizontal axis reports the PN order $[n]$ of the energy function, while the legends report the PN order n of the flux function. Each line shows how the overlaps are evolving as a function of the accuracy of the energy function. Standard adiabatic approximants are marked with thick dots. The top panes corresponds to the $(10M_\odot, 10M_\odot)$ binary and the bottom panel to the $(1.4M_\odot, 1.4M_\odot)$ binary. Overlaps are calculated for the initial LIGO (left plots), Advanced LIGO (middle plots) and Virgo (right plots) noise spectra. 145

List of Tables

2.1.	Input parameters required by mHACR and the values used for the analysis described in Section 2.2.	24
4.1.	Summary of the veto analysis on hardware injections mimicking instrumental bursts. τ_s and λ are the chosen veto thresholds on the excess-power ratio s and the cross-correlation statistic z , respectively. ξ is the fraction of <i>coincident</i> events that are vetoed in the time-shifted analysis. The fraction of coincident events vetoed in the zero-lag using the s statistic is denoted by χ_s , while the same using the z statistic is denoted by χ_z . The chosen thresholds correspond to an accidental veto rate of 1 per day.	49
4.2.	Summary of the veto analysis on 5 days of data from GEO 600. τ_s and λ are the chosen veto thresholds on the excess-power ratio s and the cross-correlation statistic z , respectively. ξ is the fraction of <i>coincident</i> events that are vetoed in the time-shifted analysis. The fraction of coincident events vetoed in the zero-lag using the s statistic is denoted by χ_s , while the same using the z statistic is denoted by χ_z . The chosen veto thresholds correspond to the accidental veto rates tabulated in the first column.	56
5.1.	The ranges of the waveform parameters used in the series of software injections.	61
7.1.	Polynomial coefficients of the best-matched amplitude parameters. The first column lists the amplitude parameters α_{int} . Eq.(7.41) shows how these parameters are related to the coefficients a_k, b_k, c_k	106
7.2.	Polynomial coefficients of the best-matched phase parameters. The first column lists the phase parameters ψ_{int} . Eq.(7.41) shows how these parameters are related to the coefficients x_k, y_k, z_k	109
8.1.	Effectualness of standard (S) and complete (C) adiabatic templates in the test mass limit. Overlaps are calculated assuming a flat spectrum for the detector noise (white noise).	128
8.2.	Faithfulness of standard (S) and complete (C) adiabatic templates in the test mass limit. Overlaps are calculated assuming a flat spectrum for the detector noise (white noise).	129
8.3.	Effectualness of standard (S) and complete (C) adiabatic approximants in the test mass limit. Percentage biases σ_m and σ_η in determining parameters m and η are given in brackets.	133

8.4. Faithfulness of standard (S) and complete (C) adiabatic templates in the test mass limit.	134
8.5. PN orders showing anomalous behavior in the context of different noise spectra. The best-sensitivity bandwidth of each detector is shown in brackets. Label A corresponds to the $(1M_{\odot}, 10M_{\odot})$ binary and label B to the $(1M_{\odot}, 50M_{\odot})$ binary.	136
8.6. Number of GW cycles accumulated by various standard (S) and complete (C) adiabatic approximants in the test mass limit. The number of useful cycles calculated for the initial LIGO noise PSD is also shown in brackets. The chosen low-frequency cut-off is 40Hz.	140
8.7. Effectualness of standard (S) and complete (C) adiabatic approximants in the comparable-mass case. Waveforms are generated using the TaylorT1 method. Percentage biases σ_m and σ_{η} in determining parameters m and η are given in brackets.	147
8.8. Faithfulness of the standard (S) and complete (C) adiabatic templates in the comparable-mass case. The waveforms are generated using the TaylorT1 method.	148

1. Gravitational-wave astronomy: Opening a new window onto the Universe

1.1. Introduction

¹ General relativity predicts the existence of gravitational waves. In general relativity, gravity is described as the curvature of spacetime, produced by the mass-energy, stress and momentum content of the spacetime. Compact concentrations of energy curve spacetime strongly, and changes in such a concentration can produce a dynamically changing spacetime curvature that propagates at the speed of light.

The generation of gravitational radiation is analogous to the generation of electromagnetic radiation by accelerated charges. While electromagnetic radiation, in its leading order, is produced by the time-varying dipole moment of the charge distribution, the leading-order gravitational radiation is produced by the time-varying quadrupole moment of the mass-energy distribution. But, while electromagnetic waves travel *through* spacetime, gravitational waves are freely propagating oscillations of the spacetime itself.

Unlike electromagnetic waves, the interaction of gravitational waves with matter is extremely weak. This is a great advantage for astronomy. This means that gravitational waves arrive at an observer nearly unaffected by any intervening matter they may have encountered since being generated. In that sense, gravitational waves carry ‘uncorrupted’ information about their sources. But the weak coupling also means that it is hard to detect them. The existence of gravitational waves is yet to be verified by a *direct* observation; though strong indirect evidence of the existence of gravitational waves is provided by the binary-pulsar observations.

The first evidence for the existence of gravitational waves is provided by the radio observations from the pulsar PSR 1913+16 [2]. The pulsar is in a binary orbit with an unseen neutron star. The orbital radius of the binary shrinks as the system loses energy due to gravitational-wave emission, which in turn, reduces the orbital period. The change in the orbital period of the pulsar was monitored for several years using radio observations, and was found to be extremely close to the prediction of general relativity [3]. Russell Hulse and Joseph Taylor were awarded the Nobel Prize in 1993 for their discovery of PSR 1913+16. A number of binary-pulsar observations later confirmed

¹The title of this chapter is inspired by that of the excellent review by Kip Thorne [1].

this first result [4]. With the discovery of the first double pulsar [5], much more accurate tests of general relativity and gravitational-wave emission can be performed [6].

An ongoing worldwide effort aims for the direct detection of gravitational waves. This will not only provide direct evidence for the existence of gravitational waves, but will also serve as a powerful probe of the Universe and of the nature of gravity. A number of laser-interferometric [7, 8, 9, 10] and resonant-bar [11, 12, 13, 14, 15] detectors are operational around the globe, forming a worldwide network of gravitational-wave detectors. While these ground-based detectors seek to detect gravitational waves in the frequency band $\sim 10 - 10^4$ Hz, the planned space-borne detector LISA [16] will operate in the frequency band $\sim 10^{-4} - 10^{-1}$ Hz. These detectors, collectively, cover an incredibly wide frequency band. These two frequency bands are dominated by different classes of gravitational-wave sources. Similarly, the experimental and theoretical challenges in the search for gravitational waves are also in general different in the two bands. This thesis deals with some issues related to the search for gravitational waves using ground-based laser-interferometric detectors. In particular, the focus of the thesis will be the search for gravitational waves from coalescing compact binaries and unmodelled burst sources (see Section 1.2).

The rest of this Introduction is organised as follows: Section 1.2 furnishes an overview of the possible sources of gravitational waves for ground-based detectors. Section 1.3 provides a brief introduction to gravitational-wave astronomy. Apart from the astrophysical and cosmological implications of gravitational-wave observations, some possible tests of the theories of gravity using gravitational-wave observations are discussed here. Section 1.4 reviews some aspects of the ongoing search for gravitational waves. After reviewing some basic ideas of gravitational-wave detection, this section overviews the present status of the global network of gravitational-wave detectors and summarises the current observational results. Some challenges in the search for gravitational waves are also briefly discussed here, introducing the topics covered in the rest of the thesis. Finally, Section 1.5 provides an overview and summary of this thesis.

1.2. Expected sources of gravitational waves

A worldwide network of gravitational-wave detectors consisting of ground-based interferometers and resonant-bars has started looking for signatures of gravitational waves produced by astrophysical and cosmological sources. This section summarises some of the most promising sources of gravitational waves for such *ground-based* detectors. Since this thesis mainly deals with various issues related to the search for gravitational waves from coalescing compact binaries and unmodelled burst sources, focus will be on these classes of astrophysical sources.

1.2.1. Coalescing compact binaries

The best understood (and perhaps, the most promising) astrophysical sources of gravitational waves for ground-based interferometers are coalescing compact binaries consisting of black holes and/or neutron stars. Black-hole/neutron-star binary systems result from the evolution of massive binary stars. Some binary star systems with components massive enough to produce neutron stars or black holes at the end of their thermonuclear evolution may remain bound after two supernova explosions [17]. The binary components start to spiral towards each other as they lose orbital energy and angular momentum through gravitational radiation.

The evolution of the compact binaries is conventionally split into three stages: *inspiral*, *merger* and *ring down*. In the inspiral stage, the two compact objects, driven by radiation reaction, move in quasi-circular orbits. Eccentricity, if present initially, is radiated away quickly. Eventually approaching the ultra-relativistic regime, the two bodies merge to each other forming a single excited Kerr black hole. In the ring down stage, the excited black hole loses its energy by gravitational-wave emission and settles into a Kerr black hole. In the case of neutron-star/neutron-star binaries, a hypermassive neutron star might form in the merger stage (depending on the total mass of the binary and the nuclear equation of state), which eventually will collapse to a black hole [18].

As the black holes/neutron stars spiral inward, their waves sweep upward in frequency and amplitude. The resultant waveform is called a ‘*chirp*’. The waveforms from the merger stage can be more complex, depending on the details of the merger, while the signal from the ring down stage can be decomposed as a superposition of exponentially damped modes.

What makes this class of sources extremely interesting is the fact that the expected waveforms can be accurately modelled, and easily parametrized by a few intrinsic parameters of the binary, like the component masses and spins (see Section 1.4.4 for a discussion). This allows the data analysts to use the matched filtering technique, which is the optimal strategy to detect well-modelled signals in Gaussian noise [19], for extracting the signal buried in the detector noise.

1.2.2. Sources of gravitational-wave bursts

There are other classes of gravitational-wave sources, like core-collapse of massive stars in supernovae, accretion induced collapse of white dwarfs, Gamma ray bursts etc., for which the physics is largely unknown, or too complex as yet to allow computation of detailed gravitational waveforms. These kind of sources are generally classified as ‘unmodelled burst sources’. The astrophysical scenarios and models discussed in this section are simplified versions of the current understanding on these sources, while the actual details can be quite complex.

Stars with masses below $8M_{\odot}$ end their lives ejecting their envelopes, leaving behind a white dwarf that gradually cools and fades away [20]. For white dwarfs in binaries, binary

accretion can reheat the dwarf. If this material burns non-degenerately, the white dwarf will gain mass. When the mass of the white dwarf exceeds the Chandrasekhar limit, it will collapse. This can end up in two possible scenarios: (i) the nuclear burning in the collapsing stellar core will increase the stellar pressure, producing Type Ia supernovae (ii) if the neutrino emission from electron capture damp this burning until the core has collapsed too deeply, the result of this collapse is the formation of a neutron star. During the collapse, emission of gravitational waves will occur if the infall of matter is aspherical. gravitational waves will also be produced if the collapsing star or neutron star remnant develops rotational or pulsational instabilities.

Isolated stars more massive than $\sim 8 - 10M_{\odot}$ are expected to undergo collapse at the end of their thermonuclear life cycles [20]. After the core bounces, most of the material is ejected producing a Type II/Ib/Ic supernova and, if the progenitor star has a mass $\lesssim 20M_{\odot}$, a neutron star is left behind. On the other hand, if the mass is $\gtrsim 20M_{\odot}$ fall-back accretion increases the mass of the formed protoneutron star, pushing it above the maximum mass limit, which results in the formation of a black hole [21]. Furthermore, if the progenitor star has a mass of roughly $M \gtrsim 45M_{\odot}$, no supernova explosion is launched and the star collapses directly to a black hole [22]. Gravitational waves are generated mainly at two stages: The initial signal is emitted due to the changing axisymmetric quadrupole moment during collapse. In the case of neutron-star formation, the gravitational collapse is stopped by the stiffening of the equation of state above nuclear densities, and the core bounces, driving an outwards moving shock. This excites many normal modes of the newly-formed protoneutron star, and produces the second part of the gravitational-wave signal, lasting hundreds of oscillation periods. On the other hand, if a black hole is directly formed, then black hole quasi-normal modes are excited, which will last only for a few cycles. A combination of neutron star and black hole oscillations will appear if the protoneutron star is not stable but collapses to a black hole.

The merger stage of the coalescence of compact binaries consisting of black holes and/or neutron stars are also sources of ‘burst’ gravitational waves. This is discussed in Section 1.2.1. The compact binary mergers can be accompanied by the release of a huge amount of electromagnetic energy (as gamma rays) in a burst and manifest themselves as *short-duration* gamma-ray bursts [17]. Another class of gamma-ray bursts, called *long-duration* gamma-ray bursts, are believed to be associated with the Type Ib/c supernovae produced by the core collapse of massive stars. In the former case, gravitational radiation would result from the inspiral, merger, and ring down phases of the coalescence (see Section 1.2.1), while in the latter case, gravitational waves would result from the collapse of a massive star’s core.

1.2.3. Sources of periodic gravitational waves

Rapidly rotating neutron stars are the most likely sources of continuous gravitational radiation in the frequency band of ground-based interferometers. These objects may generate gravitational waves through a variety of mechanisms, including non-axisymmetric

distortions of the solid part of the star, velocity perturbations in the star's fluid (r -modes), and free precession [23]. Regardless of the specific mechanism, the emitted signal is a quasi-periodic wave whose frequency changes slowly during the observation time due to energy loss through gravitational wave emission, and possibly other mechanisms. Non-axisymmetric distortions generate continuous gravitational waves with twice the rotation frequency. Additionally, if the symmetry axis of the neutron star does not coincide with its rotation axis, this 'wobble' will also produce gravitational waves with a frequency close to the rotation frequency. The r -modes (fluid oscillations dominated by the Coriolis restoring force) are also proposed as a source of gravitational waves from newborn neutron stars and from rapidly accreting neutron stars.

A particularly interesting class of continuous-wave sources are low-mass X-ray binaries. These are fast rotating neutron stars torqued by accreting material from a companion star. The quadrupole moment of the deformed crust is the source of the emitted gravitational radiation, which slows down the rotation. This is conjectured as the compensating mechanism against the 'spin up' by the accretion [24, 21].

1.2.4. Stochastic gravitational-wave background

Apart from the deterministic astrophysical sources discussed in the previous sections, a stochastic background of gravitational waves is also expected to be present. This background can be of either cosmological or astrophysical origin. The cosmological background can have its origin in primordial gravitational waves from the big bang, phase transitions in the early Universe, cosmic strings etc. [25, 26]. Alternatively, many deterministic signals from a number of astrophysical sources can add up to form a seemingly stochastic background. The astrophysical stochastic background can be produced by a collection of various sources such as rotating neutron stars [27], binary-neutron stars [28], supernovae [29] or low-mass X-ray binaries [30].

1.3. Gravitational-wave astronomy

Gravitational waves are emitted by coherent, bulk motions of huge amounts of mass-energy, not by individual atoms or electrons, as is normally the case for electromagnetic waves. Therefore the information carried by gravitational waves will be completely different from that carried by electromagnetic waves. Moreover, many of the expected gravitational-wave sources will not be seen electromagnetically at all. In this sense, gravitational-wave astronomy will open a new window to the universe providing unique information about various astrophysical and cosmological phenomena. Gravitational-wave observations will also provide accurate tests of theories of gravity. This section provides a brief overview of the theoretical/astrophysical/cosmological implications of gravitational-wave observations. As in the previous section, the focus will be on what can be learned from gravitational-wave observations from coalescing compact binaries and burst sources.

1.3.1. Testing theories of gravity

Gravitational-wave measurements will allow us to test a number of existing theories of gravity, including general relativity. For example, any metric theory of gravity, in general, permits six independent polarisation states for gravitational waves. In general relativity, only two polarisation states (expressed as ‘+’ and ‘×’ polarisations) are present, while scalar-tensor theories predict the existence of an additional ‘breathing mode’ also. A suitable number of gravitational-wave detectors can extract these polarisations and limit the number of modes present in a given gravitational-wave, thus constraining the validity of certain theories [31]. Additionally, gravitational-wave observations from coalescing compact binaries can put interesting bounds on the mass of graviton [31, 32]. Using advanced ground-based and space-based detectors, it will be possible to detect several quasi-normal modes from the ring down stage of the binary-black hole coalescence, and test the ‘no hair’ theorem, according to which all modes are only functions of the black hole’s mass and spin [33, 34, 35, 36, 37]. Tests of post-Newtonian gravity using gravitational-wave observations are also proposed by various authors [38, 39, 40, 41].

1.3.2. Astrophysics using gravitational waves

Apart from providing excellent tests of general relativity in the strongly-gravitating regions, gravitational-wave astronomy is expected to provide unique information about various astrophysical phenomena. For example, gravitational waves produced by a neutron star or a stellar-mass black hole spiraling into a supermassive black hole will provide a ‘map’ of the spacetime geometry around the larger object [37]. Indeed, the detection of gravitational waves from a black hole binary itself is an important astrophysical observation, as this will provide direct evidence for the existence of astrophysical black holes. Gravitational waves from the tidal disruption of a neutron star by a black hole in the final coalescence of a neutron-star/black-hole binary will carry detailed information of the nuclear equation of state [42]. Gravitational-wave observations from merging black hole binaries can bring very useful insights to the nonlinear dynamics of the spacetime curvature as the two black holes transform into a single Kerr black hole. Neutron-star binary merger is the currently favoured model for the progenitor of short gamma-ray bursts. Observation of an inspiral gravitational-wave signal in association with a short gamma-ray burst will confirm this model, while not observing the gravitational radiation can constrain such models. Also, it has been pointed out that gravitational-wave observations from relativistic binaries residing in globular clusters will bring useful information about the complex stellar dynamics in globular clusters [43].

Gravitational-wave bursts can also bring unique information about their sources. For example, gravitational waves associated with a gamma ray burst are expected to carry detailed information about its source, which cannot be probed via electromagnetic observations. Similarly, correlated neutrino and gravitational-wave observations from a core-collapse supernova could bring interesting insights into the newborn neutron star/black

hole in the core of the supernova [44]. In particular, gravitational waves from a pulsating neutron star formed by a core collapse will carry accurate information about the mass and radius of the star, thus enabling us to strongly constrain the supranuclear equation of state [45].

1.3.3. Cosmology using gravitational waves

Gravitational-wave observations will have tremendous impacts on our understanding of cosmology. Since many of the supermassive binary black hole mergers are likely to have electromagnetic counterparts, it is possible to constrain the values of cosmological parameters such as the Hubble constant, the deceleration parameter and the cosmological constant by combining the gravitational-wave and electromagnetic observations [46]. In particular, using the distance-redshift relation from many binary black hole ‘*standard sirens*’ (analogous to the electromagnetic ‘*standard candles*’), advanced detectors like LISA will be able to put interesting constraints on the equation of state of dark energy [47], thus shedding light on one of the outstanding issues of present-day cosmology. It has also been suggested that, by observing a number of compact binary inspiral signals, ground-based detectors can constrain the values of cosmological parameters without resorting to the presence of electromagnetic counterparts [48, 49].

The cosmological gravitational-wave background is expected to be produced by processes in the very early Universe. The observation of this stochastic background can provide a picture of the Universe very shortly ($\sim 10^{-21}$ s) after the big bang, while the cosmic-microwave background observation can only provide a picture of the Universe after $\sim 10^5$ years after the big bang [25]. Unfortunately, the expected strength of this background is too low for the current ground-based detectors (and the planned space-borne detector LISA) to detect. But these detectors can put interesting upper-limits on the strength of this background, thus test a number of current speculations about the very early Universe [25] (see Section 1.4.3 for a summary of current upper-limits). The proposed *big-bang observer* mission [50] will make a direct observation of this background possible.

1.4. The search for gravitational waves

A worldwide network of gravitational-wave detectors consisting of ground-based interferometers and resonant bars is currently operating with unprecedented sensitivity levels and bandwidths. Many of them have achieved their design sensitivity goals. A worldwide community is busy analysing the data gathered by these instruments, and the search for gravitational waves is going through an exciting period. This section presents some aspects of this exciting search for gravitational waves. We first review some basics of gravitational-wave detection. An overview of the present status of the detector network is given next, where we also summarise the current observational results from these detectors. The last part of the section presents an overview of the various challenges in

the search for gravitational waves from coalescing compact binaries and burst sources, some of which will be addressed in the rest of this thesis.

1.4.1. Detecting gravitational waves

In the case of weak gravitational fields, sufficiently far away from the source, the gravitational radiation can be described by the *linearised theory* of general relativity [51, 52]. In the linearised theory, the metric of the spacetime can be written as a linear perturbation of the background Minkowski metric. In a suitable gauge, the gravitational wave is completely described by only two (time-dependent) components describing the spacial part of the metric perturbation. These are the two independent polarisation states of gravitational waves, called $h_+(t)$ and $h_\times(t)$. See [52] for the formal derivation.

The effect of gravitational waves on a ring of free particles arranged in a plane perpendicular to the direction of travel of the wave is to deform them into ellipses. If the wave is travelling in the z direction, the $h_+(t)$ polarisation will ‘stretch’ the ring in the x direction and ‘squeeze’ it in the y direction in one half-cycle, and vice versa in the next half-cycle. The effect of $h_\times(t)$ is similar; but the deformation is along axes which are aligned 45° with the x and y axes. One way of detecting gravitational waves is by measuring the displacement of ‘freely falling’ test masses by using a Michelson interferometer. Interferometric gravitational-wave detectors measure tiny differential motions of the test masses (their end-mirrors, suspended as pendulums) placed long distance apart, as the spacetime metric gets perturbed when a gravitational wave impinge on the detector. See [53] for an introduction to interferometric gravitational-wave detectors.

The strength of gravitational waves produced by expected sources is extremely small. For example, the signals produced by a core-collapse supernova with a $25-M_\odot$ progenitor at a distance 10 kpc have amplitude $\sim 10^{-20}$ [54]. In order to detect these signals, km-scale interferometers should be able to measure displacements of $\sim 10^{-17}$ m.

1.4.2. Worldwide network of gravitational-wave detectors

A network of six interferometric detectors is operational around the globe. These are broadband detectors mostly sensitive in a frequency range of around 20 Hz — 3 kHz. These include three LIGO detectors [7] in Hanford and Livingston in USA, the Virgo detector [8] (operated by a French-Italian collaboration) in Pisa, Italy, the GEO 600 detector [9] (operated by a British-German collaboration) in Hannover, Germany and the TAMA 300 detector [10] in Tokyo, Japan. Two out of the three LIGO detectors are 4 km-long interferometers and the third detector in Hanford is a 2 km-long interferometer. The two LIGO interferometers in Hanford are co-located, but have different arm lengths. This means that the two detectors have identical responses to any gravitational wave impinging on them. This allows us to perform robust waveform consistency tests between these detectors (see Chapter 6).

LIGO, Virgo and TAMA 300 detectors are configured as *power-recycled* [55] Michelson interferometers with Fabry-Perot arm cavities. GEO 600 does not use Fabry-Perot arm cavities, but rather a combination of folded arms and dual-recycling (power recycling and *signal recycling* [56]). The 4 km LIGO interferometers are currently the most sensitive detectors in the network. The Virgo detector has 3 km arm length. Owing to the better seismic isolation system, Virgo is designed to have better low-frequency sensitivity than the LIGO detectors, and an overall sensitivity comparable to the LIGO detectors. Even though GEO 600 has an arm-length of only 600 m, the advanced technologies (such as signal recycling) employed in the detector help it to achieve a narrow-band sensitivity comparable to that of the km-scale instruments. TAMA 300 has an arm-length of 300 m and was the first large-scale interferometer to be operational.

Apart from these broadband interferometers, a number of resonant-bar detectors are also collecting data. These detectors are sensitive in a narrow-band of frequency (roughly in the 900 Hz — 920 Hz band). These include the ALLEGRO detector [13] in Louisiana, USA, the Nautilus detector [12] in Frascati, Italy, The Auriga detector [11] in Padova, Italy, the Explorer detector [14] in Geneva, Switzerland and the MiniGRAIL [15] in Leiden, Netherlands.

As part of the ‘fifth science run’, the LIGO detectors have successfully achieved their science goal of collecting one year worth of ‘science data’ (in three-detector coincidence) at design sensitivity [57]. The ‘first science run’ of the Virgo detector coincided with the last few months of the LIGO’s science run [58]. GEO 600 also participated in the fifth science run with improved sensitivity compared to the earlier science runs [59]. TAMA 300, which has participated in various earlier science runs, is currently undergoing a rapid commissioning process, and is expected to come on-line in near future with improved sensitivity and stationarity [60]. Apart from these interferometric detectors, many resonant bars are continuously taking data; see Refs. [61, 62, 63] for the current status of some of these detectors.

Currently the LIGO detectors getting upgraded to their enhanced stage, called Enhanced LIGO [64]. The Enhanced LIGO is expected to come on-line in 2009 with roughly a factor of two improvement in the sensitivity compared to that of the current LIGO detectors [65]. The second generation of interferometric detectors, such as Advanced LIGO [66], Advanced Virgo [67] and GEO-HF [68] are also expected to be operational in a few years with significantly improved sensitivity. A km-scale cryogenic interferometer, called LCGT [69], is also being built in Japan.

The LIGO Scientific Collaboration [70] is responsible for analysing the data from the LIGO and GEO 600 detectors, while the Virgo Collaboration [8] is responsible for the same from the Virgo detector. Starting from early 2007, the two collaborations have an agreement for data sharing and are working as a single joint collaboration. The LIGO Scientific Collaboration has performed joint searches with TAMA Collaboration [10], ALLEGRO Collaboration [13] and Auriga Collaboration [11] in the past science runs. These observational results will be summarised in the next section.

1.4.3. Current observational results

This section summarises the current observational results from the ground-based observatories, starting from the most recent results. *No detection of gravitational waves was made so far.* So the observational results mainly involve putting upper limits on the strength of possible gravitational-wave sources, and in some cases, constraining certain astrophysical and cosmological models.

Using data from LIGO’s third and fourth science runs, the LIGO Scientific Collaboration has searched for gravitational-wave signals from the inspiral phase of coalescing compact binaries [71]. The search considered primordial black hole binaries (with component masses in the range $0.35M_{\odot} < m_1, m_2 < 1.0M_{\odot}$), neutron-star binaries (in the range $1.0M_{\odot} < m_1, m_2 < 3.0M_{\odot}$) and stellar-mass black-hole binaries ($3.0M_{\odot} < m_1, m_2 < m_{\max}$ with the additional constraint $m_1 + m_2 < m_{\max}$, where $m_{\max} = 40.0M_{\odot}$ [80.0 M_{\odot}] in the third [fourth] science run). Assuming binary populations with Gaussian distributions around $0.75\text{--}0.75M_{\odot}$, $1.4\text{--}1.4M_{\odot}$, and $5.0\text{--}5.0M_{\odot}$, they derived 90%-confidence upper limit rates of $4.9 \text{ yr}^{-1} L_{10}^{-1}$ for primordial black hole binaries, $1.2 \text{ yr}^{-1} L_{10}^{-1}$ for binary neutron stars, and $0.5 \text{ yr}^{-1} L_{10}^{-1}$ for stellar-mass binary black holes, where L_{10} is 10^{10} times the blue light luminosity of the Sun.

The collaboration also reported results from an ‘all-sky’ search for gravitational-wave bursts using the data from the fourth science run of LIGO. Using archetypal burst waveforms and making simplifying assumptions on the emission pattern of sources (such as isotropic gravitational-wave emission), they came up with order-of-magnitude estimates of the ‘distance reach’ of the search [72]. By performing simulations and subsequent calculations using core-collapse supernova waveforms involving non-spinning $11\text{-}M_{\odot}$, $15\text{-}M_{\odot}$ and $25\text{-}M_{\odot}$ progenitors, they concluded that the search is sensitive to this class of sources up to distances of 0.2 kpc, 0.2 kpc and 8 kpc, respectively. Similarly, using non-spinning binary black hole merger waveforms with total mass $20 M_{\odot}$ and $100 M_{\odot}$, the search was estimated to be sensitive up to distances of 1.4 Mpc and 60 Mpc.

LIGO Scientific Collaboration also presented the results of a search for gravitational-wave bursts associated with 39 gamma-ray bursts detected by gamma-ray satellites during LIGO’s second, third and fourth science runs [73]. Simulating gravitational-wave bursts with sine-Gaussian waveforms, they have set upper limits on the gravitational-wave strain amplitude of such waveforms at the times of the gamma-ray bursts. They estimated that, in the most favourable cases, the search on the fourth science run was sensitive to a solar mass-equivalent of radiated gravitational-wave energy to distances of tens of Mpc. Although the upper limit obtained from these science runs is not astrophysically important, Advanced LIGO will be able to constrain the validity of certain models of long-duration gamma-ray bursts.

The collaboration also presented upper limits on the gravitational wave emission from 78 *known* radio pulsars based on data from the third and fourth science runs of LIGO and GEO 600 [74]. The search included pulsars from binary systems also. The tightest upper limit on the gravitational-wave strain is 2.6×10^{-25} for PSRJ1603-7202, and the

equatorial ellipticity of PSRJ2124-3358 is $< 10^{-6}$. These upper limits are becoming astrophysically important as the strain upper limit for the Crab pulsar is only 2.2 times greater than the fiducial spin-down limit.

Using the data from the fourth science run of LIGO, the collaboration also performed an ‘all-sky’ search for periodic gravitational waves in the range $50 \text{ Hz} \leq f \leq 1000 \text{ Hz}$, $-1 \times 10^{-8} \text{ Hz/s} \leq \dot{f} \leq 0$ (where f is the frequency and \dot{f} its time derivative) [75]. They reported upper limits on this radiation from isolated rotating neutron stars. The best population-based upper limit with 95% confidence on the gravitational-wave strain amplitude, found for simulated sources distributed isotropically across the sky and with isotropically distributed spin-axes, is 4.28×10^{-24} near $f = 140 \text{ Hz}$.

Using data from the LIGO’s fourth science run, the collaboration also placed a limit on the amplitude of an isotropic stochastic background of gravitational waves [76]. For a frequency-independent spectrum, they have computed an upper limit of $\Omega_{\text{GW}} < 6.5 \times 10^{-5}$ (see Ref. [76] for the exact definition of Ω_{GW}). This result is already exploring the parameter space of some models of the stochastic GW background, such as cosmic-string models and pre-big-bang models (see Ref. [76] and references therein). Results from the fifth science run and the future runs of Advanced LIGO are expected to surpass the bound set by the big-bang nucleosynthesis.

Another search using the same data set, targeted towards an anisotropic background of gravitational waves was also reported [77]. They produced upper-limit sky maps assuming two different power laws for the source strain power spectrum. For an f^{-3} power law, the upper limits on the source strain power spectrum vary between $1.2 \times 10^{-48} \text{ Hz}^{-1} (100 \text{ Hz}/f)^3$ and $1.2 \times 10^{-47} \text{ Hz}^{-1} (100 \text{ Hz}/f)^3$, depending on the position in the sky. For a frequency-independent power spectrum, the upper limits vary between $8.5 \times 10^{-49} \text{ Hz}^{-1}$ and $6.1 \times 10^{-48} \text{ Hz}^{-1}$.

Apart from the searches discussed above, a number of searches involving multiple detectors and multiple collaborations were also reported recently. LIGO Scientific Collaboration and TAMA Collaboration jointly published the results from searches for inspiralling neutron-star binaries [78] and gravitational-wave bursts [79] using the data from LIGO and TAMA 300. A joint search for gravitational-wave bursts using Auriga and LIGO detectors is reported in [80], while a search for stochastic background using LIGO and ALLEGRO detectors is reported in [81]. A joint search for gravitational-wave bursts using the data from the fourth science run of LIGO and GEO 600 was also performed [82]. Apart from this, a number of joint searches using the data from the fifth science run of LIGO and the first science run of Virgo is currently ongoing (see, for example, [83, 84, 85]).

1.4.4. Challenges in the search for gravitational waves

This section discusses some of the various challenges in the search for gravitational waves using ground-based interferometers. Unlike in the previous sections, the focus here will be entirely on the search for coalescing compact binaries and burst sources.

Interferometric gravitational-wave detectors aim to measure tiny differential motions of the test masses. Building instruments that are sensitive to displacements of sub-nuclear length scales itself is an enormous theoretical and experimental challenge, a discussion of which is beyond the scope of this thesis. For some excellent discussions, see Refs. [53, 86, 87]. Instead, what this thesis tries to address are some issues related to the detection of gravitational-wave signals in the data of these detectors. In general, any possible gravitational-wave signals produced by an astrophysical or cosmological source is deeply buried in the detector noise, and to extract these gravitational-wave signatures from the noise is a nontrivial challenge. This requires accurate models of the signal waveforms (if these are unavailable, we will have to rely on some generic properties of the signals; see below), sensitive and efficient data-analysis techniques and robust methods to reject noise artifacts which mimic gravitational-wave signals. This section introduces these three topics and reviews the current status of research in these directions.

Source modelling. As discussed in Section 1.2.1, the coalescence of compact binaries can be conveniently split into three stages: inspiral, merger and ring down. The inspiral part of the gravitational waveform is well described by the post-Newtonian approximation of general relativity. In this approximation, treating the sources as point particles and assuming slow motion, the Einstein equations are solved in the near zone (which contains the source) using an expansion in terms of the velocity (v/c) of the source. In the far zone, the vacuum equations are solved assuming weak gravitational fields, and these two solutions are matched in the intermediate region [88, 89, 90]. Presently, the post-Newtonian waveforms have been computed to a very high order (phase up to $(v/c)^7$ and amplitude up to $(v/c)^5$ beyond the leading order [91, 92]). But the post-Newtonian approximation becomes less accurate as the binary approaches the merger stage, where the full Einstein equations need to be solved numerically to extract gravitational waveforms. Recent progress in numerical relativity [93, 94, 95] has enabled us to compute accurate gravitational waveforms from the coalescence of black-hole/black-hole binaries. Gravitational waveforms from the final ring-down stage can also be computed by black-hole perturbation theory using a perturbation expansion about the background Kerr metric [96]. Section 8.1 provides some more details of the calculation of gravitational waveforms from inspiralling compact binaries using post-Newtonian theory, while Section 7.2 briefly discusses the calculation of binary-black-hole waveforms using numerical relativity.

Computation of accurate gravitational waveforms from binaries involving neutron stars is a harder challenge, as this requires the solution of the Einstein equations together with those of general-relativistic (magneto) hydrodynamics. There has been significant progress in the numerical modelling of the merger of neutron-star/neutron-star binaries with no magnetic fields [97, 98, 99, 100]. Some preliminary results from the simulations of neutron-star/black-hole binaries were also reported recently [101]. More progress is expected in the near future in the simulations of neutron-star binaries with magnetic fields and neutron-star/black-hole binaries [102].

Numerical modelling of the collapse of massive stars is also a highly nontrivial problem, because, in addition to a general-relativistic treatment of their gravity, an adequate treatment of the nuclear equation of state and the neutrino microphysics is crucial for accurate simulations. Although the core-collapse supernova problem remains unsolved in its full detail, recent simulations have given a lot of insights into the problem. There is an emerging consensus that the core-collapse supernova mechanism is essentially aspherical and that instabilities and the breaking of spherical symmetry are keys to the explosion [103]. Ref. [104] presented a new, acoustic mechanism for the explosion. Recent simulations also studied magnetohydrodynamic explosion mechanisms with improved accuracy [103]. Recently, full general-relativistic simulations of rotating stellar collapse have been performed with an approximate treatment of the microphysics [105, 106]. But gravitational waveforms computed from the current simulations are not yet robust enough to be used as waveform templates (see below).

Data analysis. Since the gravitational waveforms from coalescing compact binaries are well-modelled², the optimal detection strategy to extract these signals buried in the noise is the well-known matched filtering [19]. Matched filtering involves cross-correlating the detector data with the theoretically predicted waveforms, or templates. Different ways of constructing waveform templates for non-spinning binaries using post-Newtonian inputs are nicely summarised in Ref. [107]. These template waveforms are functions of the physical parameters of the binary (such as the component masses and spins). Since the parameters of the signal that is buried in the data are not known *a priori*, the data has to be filtered through a number of templates with different parameters. An elegant geometrical formalism for laying down the templates in the parameter space of the binary is presented in Ref. [108]. This formalism, extending the earlier work reported in Ref. [109, 110, 111], allows us to construct a ‘bank’ of templates discretely spaced in the parameter space in such a way that the loss of signal-to-noise ratio due to the *mismatch* between the signal and the template is restricted to an acceptable amount [108]. Apart from the ‘physical’ template banks that are constructed from well-motivated physical models, ‘phenomenological’ template banks can also be used in searches where there is uncertainty in the signal model [112], or when the parameter space of the binary is too large to be searched over [113]. See Section 7.3 for an introduction to the various aspects on the data analysis for coalescing compact binaries.

Unlike coalescing compact binaries, most of the expected sources of gravitational-wave bursts are poorly modelled. Thus, matched filtering may not be the best detection strategy in the search for these signals. Instead, a variety of different search algorithms making use of the generic properties of gravitational-wave bursts (such as their short-duration) are employed in the searches. Many of them look for short-lived ‘excess power’ in the data that is unlikely to be associated with the background noise [114, 115, 116, 117, 118, 119, 120]. Some algorithms, instead, cross-correlate the data with some archetypal ‘burst’ waveforms [121]. See

²In the case of binaries consisting of neutron stars, only the inspiral stage is well-modelled as yet.

Section 2.1 for a discussion on various burst-detection algorithms.

The existence of a global network of detectors with comparable sensitivities and bandwidths opens the possibility of performing *coherent searches* between multiple detectors. Coherent searches, apart from improving the sensitivity towards gravitational-wave signals, help to reject spurious signals of instrumental origin. A novel method for the coherent multi-detector search for well-modelled binary-inspiral signals is formulated in [122]. Coherent search strategies for unmodelled burst signals are discussed in [123] and [124], while the authors of [125, 126, 127] and [128] show how the coherent analysis can be used to reject spurious triggers in a search for gravitational-wave bursts (see also Chapter 6).

Searches for gravitational waves have to deal with large volumes of data (tens of terabytes associated with each science run). Many searches, such as the ones for unknown pulsars and spinning compact binaries, are heavily constrained by the availability of computational power. For computational efficiency, most of the search pipelines are designed employing hierarchical algorithms [129, 130]. The searches also benefit from distributed computing projects like ‘Einstein@Home’ [131].

Detector characterisation and veto development. Since current interferometric detectors are highly complex instruments, the detector data often contains a large number of noise transients. These noise artifacts can mimic the nature of certain signals that these algorithms seek to detect, thus producing false alarms. Therefore it is important to characterise the quality of the detector data and to develop robust strategies to reject these artifacts. Significant effort by various detector groups has been put into understanding and characterising the quality of the data. Some of the data-characterisation efforts by various detector groups in connection with the recent science runs are summarised in Ref. [132, 133, 134, 135]. Apart from this, various strategies to reject, or *veto*, spurious triggers are also formulated. Some of them are ‘signal-based vetoes’, making use of the known shape of the expected signals [136, 137]. Another class of ‘physical vetoes’ is based on general properties of gravitational waves and the knowledge of their coupling to different detector subsystems [138, 139, 140, 141]. Apart from these, different ‘statistical vetoes’ and ‘event-by-event vetoes’ are also employed in the searches [72, 142, 143, 144, 145]. See Section 3.1 for a detailed discussion.

1.5. Overview and summary of this thesis

The various topics discussed in this thesis are streamlined towards a single, larger aim: to identify with sufficient confidence a gravitational-wave signal buried in the noisy detector data. The thesis is organised as containing three parts. The first part deals with detector characterisation and veto development for ground-based detectors, giving particular focus to the GEO 600 detector. The second part is related to the data-analysis methods used in the search for unmodelled burst signals and coalescing compact binaries. Finally, the third part describes some interesting theoretical problems related

to the modelling of gravitational waves from the inspiral phase of the coalescing compact binaries using post-Newtonian approximation methods.

Part **I** of the thesis starts with Chapter **2**, presenting a discussion on the mHACR algorithm. This is a modified algorithm based on the *hierarchical algorithm for curves and ridges*, and is used to detect transient-burst events present in the gravitational-wave data. Simulations performed in order to characterise the quality of the algorithm in estimating the parameters of the detected burst events are presented in this chapter. Application of mHACR in the detector characterisation of GEO 600 is also briefly discussed.

Chapter **3** presents a robust strategy to veto certain classes of instrumental glitches that appear at the output of interferometric gravitational-wave detectors. This veto method is ‘physical’ in the sense that, in order to veto a burst trigger, we make use of our knowledge of the coupling of different detector subsystems to the main detector output. The main idea behind this method is that the noise in an instrumental channel X can be transferred to the detector output (channel H) using the transfer function from X to H , provided the noise coupling is linear and the transfer function is unique. If a non-stationarity in channel H is causally related to one in channel X , the two have to be consistent with the transfer function. Two methods for testing the consistency between the burst triggers in channel X and channel H are formulated. One method makes use of the *null stream* constructed from channel H and the ‘transferred’ channel X , and the second involves cross-correlating the two. This chapter also formulates a less-rigorous, but computationally inexpensive alternative to the above method. Here, the parameters of the triggers in channel X are compared to the parameters of the triggers in channel H to see whether a trigger in channel H can be ‘explained’ by a trigger in channel X and the measured transfer function.

In Chapter **4**, the physical instrumental-veto method constructed in Chapter **3** is demonstrated by injecting instrumental glitches in the hardware of the GEO 600 detector. The *veto safety* is demonstrated by performing gravitational-wave-like hardware injections. This chapter also shows an example application of this method using 5 days of data from GEO 600 taken as part of the fifth science run. The method is found to have high veto efficiency with a low accidental veto rate.

Another instrumental veto method making use of the null stream constructed from the two output quadratures of the GEO 600 detector is described in Chapter **5**. This method makes use of the fact that the two output quadratures of a dual-recycled interferometer, such as GEO 600, when calibrated to strain, will contain the same gravitational-wave signal but different noises. This allows us to construct a null stream from the two outputs, in which all the gravitational-wave information will be absent (to the level of the calibration accuracy). This chapter shows that the null stream can be used as a powerful veto against certain classes of transient events detected in the output data stream of GEO 600.

Making use of the redundant gravitational-wave information present, the time-series data from multiple gravitational-wave detectors can also be combined to form a null

stream. Similar to what described in Chapter 5, this null stream can be used to distinguish between actual gravitational-wave triggers and spurious instrumental triggers in a search for gravitational-wave bursts using a network of detectors. The biggest source of error in the null-stream analysis comes from the fact that the detector data are *not* perfectly calibrated. Chapter 6 presents an implementation of the null-stream veto in the simplest network of two co-located detectors. The detectors are assumed to have calibration uncertainties and correlated noise components. This chapter estimates the effect of calibration uncertainties in the null-stream veto analysis and proposes a new formulation to overcome this. This new formulation is demonstrated by doing software injections in Gaussian noise. An example application to the data of the two co-located LIGO detectors in Hanford is also presented. This chapter is included in the Part II (dealing with data-analysis methods) of the thesis because the null stream constructed from a network of detectors is also a powerful tool for coherent searches, enabling us to solve the so-called ‘inverse problem’ of gravitational-wave bursts [146].

Part II of the thesis continues with Chapter 7, proposing a new template bank which can model all the three different stages (inspiral, merger and ring down) of the coalescence of non-spinning binary black holes following quasi-circular inspiral. This template family is constructed making use of the recent results from numerical relativity and analytical approximation methods of general relativity, and will allow us to *coherently* search for all the three stages of the binary black hole coalescence. This two-dimensional template family is explicitly parametrized by the physical parameters of the binary. This chapter shows that the template family is not only *effectual* in detecting the signals from binary black hole coalescences, but also *faithful* in estimating the parameters of the binary. The sensitivity of the new search (in the context of different ground-based interferometers) is compared with other template-based searches which look for individual stages separately. The proposed search is found to be significantly more sensitive than other template-based searches over a substantial mass-range, potentially bringing about remarkable improvement in the event-rate of ground-based interferometers. This chapter also prescribes a general procedure to construct interpolated template banks using non-spinning binary-black-hole waveforms produced by numerical relativity.

Part III (source modelling) of the thesis contains Chapter 8 which revisits the *adiabatic approximation* used to compute the gravitational waveforms from the inspiral phase of the coalescing compact binaries. The *standard adiabatic* approximation to the phasing of gravitational waves uses the post-Newtonian (PN) expansions of the binding energy and gravitational wave flux both truncated at the *same relative* post-Newtonian order. From the viewpoint of the dynamics of the binary under conservative post-Newtonian forces and gravitational radiation damping, the standard approximation at leading order is equivalent to retaining the 0PN and 2.5PN terms in the acceleration and neglecting the intervening 1PN and 2PN terms. A complete mathematically consistent treatment of the acceleration at leading order should include all PN terms up to 2.5PN *without any gaps*. These define the *standard* and *complete non-adiabatic* approximants respectively. This chapter proposes a new and simple *complete adiabatic* approximant constructed from the energy and flux functions. At the leading order it uses the 2PN energy function rather than the 0PN one in the standard approximation so that in spirit it corresponds

to the dynamics where there are no missing post-Newtonian terms in the acceleration. This chapter compares the overlaps of the standard and complete adiabatic approximant templates with the exact waveform (in the adiabatic approximation) for a test-particle orbiting a Schwarzschild black hole. The complete adiabatic approximants lead to a remarkable improvement in the *effectualness* (i.e. larger overlaps with the exact signal) at lower PN ($< 3\text{PN}$) orders. However, standard adiabatic approximants of order $\geq 3\text{PN}$ are nearly as good as the complete adiabatic approximants for the construction of effectual templates. In general, *faithfulness* (i.e. smaller biases in the estimation of parameters) of complete approximants is also found to be better than that of standard approximants.

Part I.

Detector characterisation and veto
development for ground-based
interferometers

2. Improving and characterising the hierarchical algorithm for curves and ridges

2.1. The burst detection algorithm mHACR

As discussed in Chapter 1, among the most promising sources of gravitational waves (GWs) for the kilometer-scale interferometric detectors are the transient astrophysical phenomenon like core-collapse supernovae, binary black hole/neutron star mergers, accretion induced collapse of white dwarfs, Gamma ray bursts etc., for which the physics is largely unknown, or too complex to allow computation of detailed gravitational waveforms.

In general, any possible GW signal coming from an astrophysical or cosmological source is ‘buried’ in the detector noise, and to extract these GW signatures from the noise is a nontrivial data analysis problem. Indeed, if time evolution of the GW phase is accurately known, the optimal filter for searching for this signal buried in the noise is the well-known *matched filter*. But, since matched filtering relies on the prior knowledge of the signal, it may not be the best detection strategy in the search for unmodelled, short-lived GW bursts.

One class of search methods that is being employed in the burst data analysis is based on time-frequency decomposition of detector data. These algorithms construct time-frequency maps of the time-series data and look for ‘time-frequency regions’ containing excess power which are statistically unlikely to be associated with the background noise distribution [114, 115]. Some of these algorithms are based on clustering the ‘time-frequency pixels’ containing excess power, and applying another threshold on these clusters of pixels [116]. Time-frequency detection algorithms using basis functions other than the standard Fourier basis functions are also proposed [117, 121]. Another class of burst detection algorithms look for slopes or ridges in the time-series data, or in its time-frequency representation [118, 119, 120]. In general, these methods are claimed to be robust in detecting short-lived signals with minimum *a priori* information.

While the optimal filtering technique, along with accurate models of the waveforms, enables us to accurately estimate the physical parameters (such as masses and spins) of the GW source, the time-frequency methods, by construction, are unable to accomplish this. Instead, these algorithms try to parametrize the underlying gravitational waveforms using a set of quantities like the characteristic central frequency, duration,

bandwidth, etc. The detection algorithms implemented in the data analysis pipelines are usually referred to as *event trigger generators* (ETGs).

The *hierarchical algorithm for curves and ridges* (HACR) [147, 148] is a transient-detection algorithm based on time-frequency detection methods. This algorithm was first implemented as part of the *GEO++* software environment, and was subsequently modified over time to form the *modified HACR* (mHACR) algorithm. The mHACR algorithm provides improved estimation of the parameters associated with the burst triggers. This chapter describes the improved algorithm and the studies carried out in characterising the errors in the parameter estimation. The parameter estimation of the HACR algorithm and its characterisation are described in [147, 148].

Section 2.1.1 reviews the HACR detection algorithm. The improved parameter estimation is described in Section 2.1.2 while the software injections performed to characterise the quality of parameter estimation are discussed in Section 2.2. Applications of mHACR in the detector characterisation of GEO 600 are briefly discussed in Section 2.3.

2.1.1. Detection algorithm

The discretely-sampled time-series data h_j is divided into n short segments of length L and the discrete Fourier transform (DFT) of each segment is computed after multiplying the time-series data with a suitable window function w_j .

$$\tilde{h}_{kl} = \sum_{j=l(L-O)}^{l(L-O)+L-1} h_j w_j \exp(i2\pi jk/L), \quad k = 0..L/2, \quad l = 0..n-1. \quad (2.1)$$

The length, L , of the segment is chosen according to the time-scale of the burst signals that we are trying to detect (expected to range from a few milliseconds to a few tens of milliseconds). Typically, L is chosen to be 32 ms long, and a Hann window is used to avoid edge effects. Because of the window function, only the data at the centre of each segment make a significant contribution to the DFT. Therefore sufficient (typically $\geq 75\%$) overlap, O , is allowed between consecutive segments to make sure that each sample is ‘properly’ represented in the time-frequency map.

Often we are interested only in detecting non-stationarities appearing within some specific frequency band (say, where the detector is most sensitive). So, only frequency bins above a lower cutoff frequency, f_{low} , and below an upper cutoff frequency, f_{upp} , are retained in the constructed time-frequency map. These cutoff frequencies can be specified as input parameters to mHACR.

The time-frequency representation of the data that we use is called a *spectrogram*:

$$\rho_{kl} = 2A |\tilde{h}_{kl}|^2, \quad (2.2)$$

where $A = (f_s \sum_j w_j^2)^{-1}$ is a normalisation factor, chosen in such a way that ρ_{kl} has units of power spectral density, and f_s is the sampling frequency of the data. One can

associate a certain Fourier frequency, f_k , and time, t_l , with each time-frequency pixel, ρ_{kl} , such that

$$\begin{aligned} f_k &= kf_s/L, \\ t_l &= [l(L - O) + L/2] f_s^{-1}. \end{aligned} \quad (2.3)$$

These quantities will be used later while estimating the parameters of the burst triggers.

After constructing the time-frequency matrix, ρ , we want to identify time-frequency pixels, ρ_{kl} , which are statistically different from the background noise. We first estimate the mean, μ_k , and standard deviation, σ_k , of each row (frequency bin) of the matrix ρ . In each frequency bin, a fraction Ω of time-frequency pixels having the highest values of ρ_{kl} is excluded from this estimation. The *fraction of outliers*, Ω , is specified as an input parameter to mHACR, and, ideally, should be chosen in such a way that the non-Gaussian tails of the background noise distribution are excluded from the estimation of its mean and variance. The *significance*, s_{kl} , of each pixel, ρ_{kl} , is then calculated as

$$s_{kl} = \frac{\rho_{kl} - \mu_k}{\sigma_k}. \quad (2.4)$$

The following ‘colours’ are assigned to each time-frequency pixel, according to the following criteria:

$$\text{colour}(\rho_{kl}) = \begin{cases} \text{black,} & \text{if } s_{kl} \geq T_{\text{upp}} \\ \text{grey,} & \text{if } T_{\text{upp}} > s_{kl} \geq T_{\text{low}} \\ \text{white,} & \text{if } s_{kl} < T_{\text{low}}, \end{cases}$$

where T_{upp} and T_{low} are the upper and lower thresholds chosen for a particular analysis. Double threshold detection methods are more robust than single threshold methods, and are commonly used in satellite imaging, astronomy, particle physics etc. (See, for example, [149, 150]). The neighbouring black and grey pixels are clustered together, and, if a cluster contains at least two pixels, of which at least one is black, then it is identified as a burst *event*. Once the burst events are identified, mHACR proceeds to parametrise the events in terms of a few parameters. The parameter estimation is described below.

The input parameters required by mHACR and the values used for the analysis described in Section 2.2 are summarised in Table 2.1.

2.1.2. Parameter estimation

The *total power*, P_{tot} , associated with a burst event is the total signal power in all the (black and grey) pixels belonging to a burst event. It should be noted that, because of the overlaps between consecutive data segments, the time-frequency pixels are also overlapping in time. This redundancy in the power distribution among the pixels is taken into account when we estimate the total power by summing the signal power in pixels. The total power is estimated as

$$P_{\text{tot}} = \sum_{k,l} S_{kl} / r, \quad (2.5)$$

Parameter	Description	Value used
f_s	Sampling frequency of the data	16384 Hz
L	Number of samples in one segment	512
O	Number of overlapping samples	384
f_{low}	Low frequency cutoff	128 Hz
f_{high}	High frequency cutoff	3008 Hz
Ω	Fraction of outliers to be excluded in the parameter estimation of the noise	0.1
T_{low}	Lower threshold on pixel significance	5
T_{upp}	Upper threshold on pixel significance	20

Table 2.1.: Input parameters required by mHACR and the values used for the analysis described in Section 2.2.

where $r = L/(L - O)$ is the *redundancy factor* due to the overlapping segments, and the signal power is estimated by subtracting the mean noise power in each frequency bin from ρ_{kl} , i.e., $S_{kl} = \rho_{kl} - \mu_k$. Throughout this section, the indices range over all the black and grey pixels belonging to a particular event. mHACR also estimates the *peak power* of the burst event, as,

$$P_{\text{peak}} = \max(S_{kl}). \quad (2.6)$$

The estimation of the *central frequency*, f_0 , and *central time*, t_0 , is analogous to the calculation of the centre-of-mass of an extended body. Here, the *signal power*, S_{kl} , in each time-frequency pixel serves as the ‘mass’ term and the time/frequency associated with each pixel serves as the ‘position’ term. That is,

$$\begin{aligned} f_0 &= \sum_{k,l} S_{kl} f_k / \sum_{k,l} S_{kl}, \\ t_0 &= \sum_{k,l} S_{kl} t_l / \sum_{k,l} S_{kl}. \end{aligned} \quad (2.7)$$

The *signal-to-noise ratio* (SNR), ρ , is defined in a similar way to the total power:

$$\rho^2 = \sum_{k,l} \frac{S_{kl}}{\mu_k} / r. \quad (2.8)$$

Finally, the *duration*, d , and *bandwidth*, b , of the burst event can be estimated from the extent of the burst event in the time/frequency plane as

$$\begin{aligned} d &= \max(t_l) - \min(t_l), \\ b &= \max(f_k) - \min(f_k). \end{aligned} \quad (2.9)$$

2.2. Quality of the parameter estimation

In this section, the accuracy of the parameter estimation is demonstrated by doing software injections into Gaussian white noise, and by comparing the parameters of the

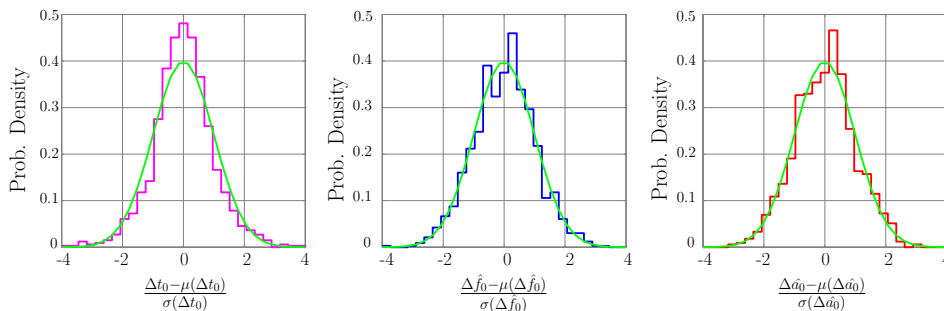


Figure 2.1.: Distribution of the errors in estimating the central time, central frequency and RSS amplitude of the injected sine-Gaussian waveforms. The errors in the frequency and amplitude estimation are normalised by the injected value of the parameters; i.e., $\hat{\Delta f}_0 = \Delta f_0 / f_{\text{cen}}$ and $\hat{\Delta a} = \Delta a / h_{\text{RSS}}$. Injections are done with Nine different values of h_{RSS} such that the SNR of the injections ranges from $\simeq 5$ to $\simeq 300$ (see Figure 2.2). Sample mean and standard deviation of each of the 9 populations are estimated separately. Each error is converted into a reduced normal variable by subtracting the corresponding sample mean and by normalising by the corresponding standard deviation. Also plotted are the probability densities of the standard normal distributions.

injected waveforms with those estimated by mHACR. The injected waveforms are sine-Gaussians of the form

$$h(t) = h_{\text{RSS}} \left(\frac{2f_{\text{cen}}^2}{\pi} \right)^{1/4} \sin [2\pi f_{\text{cen}}(t - t_{\text{cen}})] \exp \left[\frac{-(t - t_{\text{cen}})^2}{\tau^2} \right], \quad (2.10)$$

where f_{cen} is the central frequency of the waveforms and t_{cen} is the time corresponding to the peak amplitude. The envelope width is set as $\tau = 2/f_{\text{cen}}$. The corresponding quality factor is $Q \equiv \sqrt{2}\pi f_{\text{cen}}\tau = 8.9$. The quantity h_{RSS} is the root-sum-squared (RSS) amplitude, given by

$$\left[\int_{-\infty}^{\infty} h^2(t) dt \right]^{1/2} = h_{\text{RSS}}. \quad (2.11)$$

Nine different values of h_{RSS} are used for the injections such that the SNR of the injections ranges from $\simeq 5$ to $\simeq 300$, and the central frequency is randomly chosen from the interval (432, 3008) Hz. Since the injections are done with nine different values of h_{RSS} , we expect the errors in the estimation of each parameter to fall into a multivariate normal distribution of 9 dimensions. The sample mean and standard deviation of each of the 9 populations are estimated separately. The errors are converted into standard normal variables by subtracting the sample mean from each sample and by normalising by the standard deviation. Distributions of the errors (after subtracting the mean and normalising by the standard deviation) are plotted in Figure 2.1, along with the probability density of a normal distribution with mean 0 and variance 1. The figure shows the error distributions of three parameters – the estimated central frequency f_0 , central time t_0 and the RSS amplitude $a = \sqrt{P_{\text{tot}}}$. The standard deviation of the errors in the estimation of these parameters are plotted as a function of the SNR of the triggers

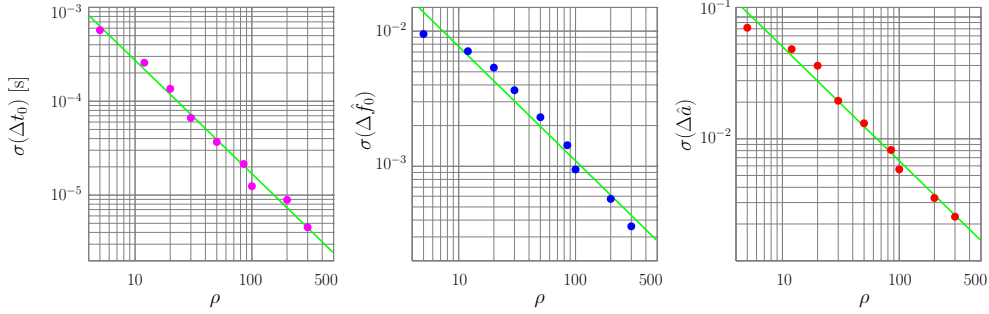


Figure 2.2.: Standard deviation of the distribution of the errors (fractional errors in the case of f_0 and a) in estimating the parameters of the injected sine-Gaussian waveforms, plotted as a function of the SNR of the triggers. Also shown are power-law fits to the data.

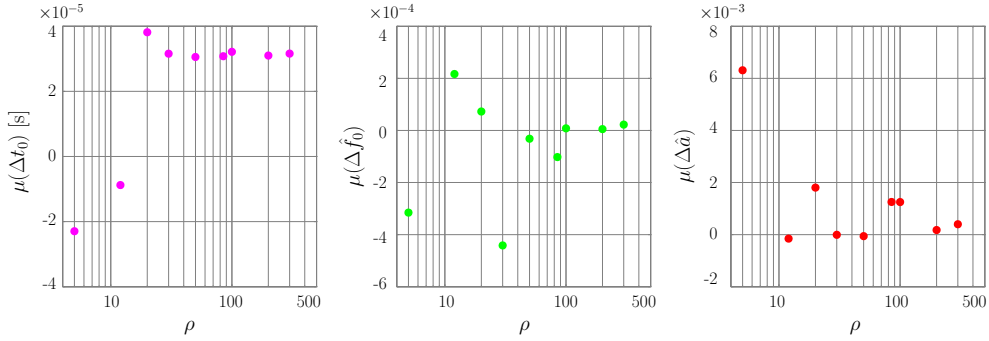


Figure 2.3.: Mean errors (fractional errors in the case of f_0 and a) in the parameter estimation, plotted as a function of the SNR of the triggers.

in Figure 2.2. It can be seen that, to a very good approximation, the errors fall into normal distributions whose standard deviation is a monotonically decreasing function of the SNR. Figure 2.3 shows the mean errors in the parameter estimation which are indications of the systematic biases in the parameter estimation. The left panel shows a small bias in the estimation of t_0 . But this is smaller, even, than the sampling period of the data used in the simulations ($\simeq 61\mu s$), and can be safely ignored.

2.3. Application of mHACR in the detector characterisation of GEO 600

In GEO 600, an online monitoring system is developed in order to routinely track the instrument status and sensitivity. This is a modified version [132] of the online characterisation system described in [151]. The first level of the characterisation system consists of a number of ‘monitor’ algorithms designed for tracking the data quality information, sensitivity and stationarity of the detector noise etc. The next level is a database sys-

tem where the results (often called ‘meta data’) acquired by the monitor algorithms are stored. As a third level, these results are passed through an automated visualization pipeline to produce online web pages [152] on a regular basis. These reports are generated three times per day and are of fixed format so as to allow quick comparison between one report and another. The contents of each summary report include noise-spectral densities of the calibrated detector outputs, sensitivity of the detector data in detecting certain prototype binary inspiral systems and some ad-hoc burst waveforms, basic data quality information such as lock status, maintenance mode, etc., time evolution of the detector model parameters used for calibration of the data, glitch rates of the main GW channel as well as many auxiliary channels, reported saturations of data acquisition channels etc.

Given the sensitivity of GEO 600, the most promising source are astrophysical sources of transient burst signals. Thus the emphasis is given on the characterisation of the data directed towards burst searches. The stationarity of the data is assessed by looking at the trigger rates produced by mHACR in the main GW channel. Apart from the time-frequency plots of the mHACR triggers, histograms of the distribution of various trigger parameters (like central time, central frequency, SNR etc.) are also produced. Similar information is extracted from mHACR triggers on a number of auxiliary channels recording the instrumental and environmental status. This information, apart from providing the experimentalists some indication on the possible physical origin of these glitches in the interferometer, help the data analysts to identify potential *veto channels*.

Several *veto methods* (see Section 3.1 of Chapter 3 for an overview) are employed in GEO 600 in order to reduce the rate of candidate burst triggers. Each of them makes use of the mHACR triggers in some way or other. In the *physical instrumental veto method* described in Chapters 3 and 4, mHACR triggers coincident in the GW channel H and an auxiliary channel X are selected for performing the veto analysis. In the *null-stream veto* described in Chapter 5, parameters of the mHACR triggers in channel H and the null-stream channel H_{null} are compared in order to see if the triggers are consistent with the expected coupling of GWs into these channels. In the *statistical veto method* described in [143], those mHACR triggers in channels H and X which lie in a particular coincidence window in the parameter space are vetoed.

3. Physical instrumental vetoes for gravitational-wave burst triggers

3.1. The search for transient, unmodelled gravitational-wave bursts

The search for transient, unmodelled gravitational-wave bursts is performed using detection algorithms which are tuned to detect a large morphology of short-lived burst waveforms. Since current interferometric detectors are highly complex instruments, the detector output typically contains a large number of noise transients, or ‘glitches’, of instrumental/environmental origin which cause the detection algorithms to generate spurious triggers. One of the main challenges in the burst data analysis is to distinguish these spurious bursts from actual GW bursts. Since the expected GW signals are unmodelled, it is practically impossible to distinguish these false alarms from actual GW bursts based on their signal characteristics. One way of dealing with this issue is to require that the triggers be coincident (within a time window) in multiple detectors located at different parts of the world. Although this ‘coincidence requirement’ reduces the list of candidate triggers by a considerable amount, it does not completely cure the problem. While coincident instrumental bursts in multiple detectors are highly improbable, long data-taking runs using multiple detectors can produce a large number of random coincidences [72]. It is thus very important to develop robust techniques to distinguish between true GW bursts and spurious instrumental bursts which are coincident in different detectors — popularly known as *veto* techniques.

Since a number of environmental and instrumental noise sources can potentially couple to the main detector output, many such noise sources are continuously recorded along with the data from the main detector output. The measurement points for time-series data within the detector are referred to as ‘channels’. One class of veto methods is based on identifying triggers in the ‘gravitational-wave channel’ (the main detector output) which are coincident with triggers in an instrumental/environmental noise channel. The ‘coincidence windows’ are chosen such that the accidental (random) coincidence rate between the two channels is limited to an acceptable amount. See [72, 142, 143, 144] for some recent work on such ‘statistical vetoes’. Another class of ‘physical vetoes’ is based on our understanding of how a GW should, or should not, appear in certain channels [138, 139, 140]. Moreover, a number of ‘waveform consistency tests’ between multiple detectors are also employed in the burst searches [128, 126, 125, 123, 127].

In this chapter, we formulate and demonstrate a veto strategy which makes use of our understanding of the physical coupling of various detector subsystems to the detector

output. This method is different from the physical veto methods discussed above in the sense that, here we use the knowledge of the coupling mechanism involved in transporting glitches from a particular subsystem to the main detector output. The main idea behind this method is that the noise in an instrumental channel X can be transferred to the GW channel H ¹ using the transfer function from X to H , provided the noise coupling is linear and the transfer function is unique. If a non-stationarity in channel H is causally related to one in channel X , the two have to be consistent with the transfer function. We formulate two methods for testing the consistency between the burst triggers in channel X and channel H . One method makes use of the *null stream* constructed from channel H and the transferred channel X , and the second involves cross-correlating the two.

3.2. Vetoes using known instrumental couplings

3.2.1. Noise transfer

Let $x(t)$ and $h(t)$ denote the time-series data measured at the input and output of a linear, time-invariant system. The input and output of the system are related by the transfer function $T^{\text{XH}}(s)$ of the system, defined as [153]

$$T^{\text{XH}}(s) \equiv \frac{H(s)}{X(s)}, \quad (3.1)$$

where $H(s)$ and $X(s)$ represent the Laplace transforms of $x(t)$ and $h(t)$, respectively, and the complex variable s represents a point in the Laplace space. i.e.,

$$\begin{aligned} X(s) &\equiv \int_0^\infty x(t) e^{-st} dt, \\ H(s) &\equiv \int_0^\infty h(t) e^{-st} dt. \end{aligned} \quad (3.2)$$

Although the transfer function $T^{\text{XH}}(s)$ is formally defined in the Laplace space, for the purpose of this method, it is easier to work in the Fourier domain. If $\tilde{x}(f)$ and $\tilde{h}(f)$ are the Fourier transforms of $x(t)$ and $h(t)$, respectively, the equivalent relation in the Fourier domain is given by

$$T^{\text{XH}}(f) \equiv \frac{\tilde{h}(f)}{\tilde{x}(f)}. \quad (3.3)$$

Throughout this thesis, we denote the (Fourier domain) transfer function from a subsystem X to the detector output H by $T^{\text{XH}}(f)$.

Let x_i and h_i denote the discretely sampled time-series data recorded in the instrumental/environmental channel X and the GW channel H , respectively. We denote the

¹Throughout this document, channel X refers to the measurement point for time-series data from a detector subsystem/environmental noise source X , and channel H refers to the main detector output (the GW channel).

corresponding discrete Fourier transforms (DFT) by \tilde{x}_k and \tilde{h}_k , respectively, where k indexes the frequency bins. If $P_k^{\text{XH}} \equiv \overline{\tilde{x}_k \tilde{h}_k^*}$ is the cross-power spectral density of x_i and h_i , and $P_k^{\text{XX}} \equiv \overline{\tilde{x}_k \tilde{x}_k^*}$ is the power spectral density of x_i , where the ‘bars’ indicate ensemble averages, the transfer function T_k^{XH} can be computed as:

$$T_k^{\text{XH}} = \frac{P_k^{\text{XH}}}{P_k^{\text{XX}}}. \quad (3.4)$$

In practice, the transfer function from the subsystem X to H can be estimated by injecting noise into X mimicking the way in which the noise in X would couple into H , and measuring P_k^{XH} and P_k^{XX} simultaneously² [154]. This is done in such a way that the injected noise from X completely dominates channel H , so that the noise in X and H are coherent, and the contributions from other noise sources are negligible. The measured transfer function represents our phenomenological understanding of the physical coupling of a detector subsystem to the main detector output. If the coupling of noise between channel X and H is linear and the transfer function is time-invariant, the Fourier transform of the noise measured in channel X at any time can be *transferred* to channel H , by using the transfer function

$$\tilde{x}'_k = \tilde{x}_k T_k^{\text{XH}}. \quad (3.5)$$

In the following section, we formulate a method to veto noise transients originating within the detector subsystems whose coupling to the GW channel can be estimated.

3.2.2. A veto strategy using known instrumental couplings

We can think of \tilde{x}_k and \tilde{h}_k as components of two vectors $\tilde{\mathbf{x}}$ and $\tilde{\mathbf{h}}$ defined in two N -dimensional linear vector spaces. In the mathematical sense, Eq.(3.5) maps $\tilde{\mathbf{x}}$ to the space of $\tilde{\mathbf{h}}$. In the physical sense, this means that if a noise transient originates in X , one can predict how it will appear in H . If there exists a noise transient in H at the same time³, we can compare it with the above prediction. If a noise transient in the channel H is causally related to one in channel X , the data vectors $\tilde{\mathbf{x}}$ and $\tilde{\mathbf{h}}$ have to be consistent with the transfer function. This allows us to formulate a powerful strategy to veto noise transients originating within a particular detector subsystem.

The basic idea is the following: firstly, we identify time-coincident burst triggers in channels X and H , allowing a liberal time window for coincidence. We compute the DFTs of two short segments of data in channels X and H . The length of these segments (typically a few tens of milliseconds) is chosen so as to encompass only the noise transient under investigation. If these two noise vectors are *consistent* with the transfer function, as given by Eq.(3.4), it is highly likely that the noise transient originates in X , and

²The transfer function can also be computed based on physical models of the systems, provided accurate and complete models exist.

³The time-coincidence window should be chosen according to the typical time scale of the transients that we are concerned with. We use a time window of a few tens of milliseconds since the current searches for GW bursts seek to detect bursts of duration $\ll 1$ sec.

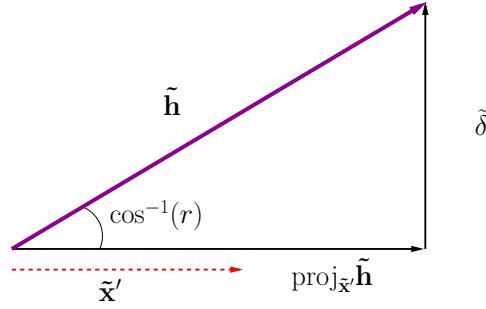


Figure 3.1.: Schematic diagram of the linear vector space in which the analysis methods are formulated.

we veto the trigger. On the other hand, if the two noise vectors are *inconsistent* with the transfer function, we conclude that this particular noise transient in H does not have its origin in X . In the following subsections, we construct two different statistics which can be used to make this decision. One statistic is based on constructing a *null stream* between channel H and the ‘transferred’ channel X ; i.e., if the noise transient originates in subsystem X , and is sensed by channel X , it is possible to construct a linear combination of the two data streams that does not contain any excess power. The second statistic is based on the cross-correlation of the noise in channel H with the transferred noise in channel X .

In the following two subsections, we assume that the data streams x_i and h_i are drawn from zero-mean Gaussian distributions. Also, we assume that the transfer function from X to H is accurately measured/calculated and is time-invariant.

The linear vector space in which the analysis methods are formulated is schematically illustrated in Figure 3.1.

3.2.3. Test statistic: using null-stream

The null-stream between $\tilde{\mathbf{h}}$ and $\tilde{\mathbf{x}}'$ is the component of the vector $\tilde{\mathbf{h}}$ orthogonal to $\tilde{\mathbf{x}}'$. This can be constructed using the Gram-Schmidt orthogonalisation [155]:

$$\tilde{\boldsymbol{\delta}} = \tilde{\mathbf{h}} - \text{proj}_{\tilde{\mathbf{x}}'} \tilde{\mathbf{h}}, \quad (3.6)$$

where we define the projection operator as

$$\text{proj}_{\tilde{\mathbf{u}}} \tilde{\mathbf{v}} \equiv \frac{\langle \tilde{\mathbf{v}}, \tilde{\mathbf{u}} \rangle}{\langle \tilde{\mathbf{u}}, \tilde{\mathbf{u}} \rangle} \tilde{\mathbf{u}}. \quad (3.7)$$

In the above expression $\langle \tilde{\mathbf{v}}, \tilde{\mathbf{u}} \rangle$ denotes the inner product between the vectors $\tilde{\mathbf{v}}$ and $\tilde{\mathbf{u}}$:

$$\langle \tilde{\mathbf{v}}, \tilde{\mathbf{u}} \rangle \equiv \text{Re} \sum_{k=m}^{m+M} \tilde{v}_k \tilde{u}_k^*. \quad (3.8)$$

If the noise transient originates in X , it will completely disappear in $\tilde{\delta}$. If the components of \mathbf{x} and \mathbf{h} are generated by zero-mean Gaussian processes, the real and imaginary parts of $\tilde{\delta}_k$ in each frequency bin will be distributed according to a Gaussian distribution of mean zero and variance σ_k^2 . Following [114], we compute the excess-power statistic from $\tilde{\delta}$:

$$\epsilon = \sum_{k=m}^{m+M} P_k, \quad P_k = \frac{|\tilde{\delta}_k|^2}{\sigma_k^2}. \quad (3.9)$$

It can be shown that ϵ will follow a χ^2 distribution of $2M$ degrees of freedom in the case of a non-windowed DFT. But in the case of a windowed DFT, P_k are not *independent* χ^2 variables, and hence ϵ will *not* follow a χ^2 distribution [156]. But to a very good approximation, ϵ will follow a Gamma distribution with scale parameter α and shape parameter β . These parameters are related to the mean, μ_ϵ , and variance, σ_ϵ^2 , of the distribution of ϵ by

$$\alpha = \left(\frac{\mu_\epsilon}{\sigma_\epsilon}\right)^2, \quad \beta = \frac{\sigma_\epsilon^2}{\mu_\epsilon}. \quad (3.10)$$

In order to estimate the parameters of the Gamma distribution, we generate a population of ϵ from stationary data surrounding the burst (using the same DFT-length and bandwidth). From that population, μ_ϵ and σ_ϵ^2 can be estimated, and hence α and β .

If ϵ computed from the segment of data containing the burst is less than a threshold, we veto the trigger. The threshold τ corresponding to a *rejection probability* (probability that a ‘causal’ trigger is vetoed) Φ can be found from

$$\Phi = \int_0^\tau \Gamma(x; \alpha, \beta) dx, \quad (3.11)$$

where $\Gamma(x; \alpha, \beta)$ is the probability density of the Gamma distribution with parameters α and β .

3.2.4. Test statistic: using cross-correlation

In this section, we construct another statistic to test the consistency of the noise vectors $\tilde{\mathbf{x}}'$ and $\tilde{\mathbf{h}}$. The linear cross-correlation coefficient between two vectors $\tilde{\mathbf{x}}'$ and $\tilde{\mathbf{h}}$ is the cosine of the angle between them:

$$r = \text{Re} \frac{\langle \tilde{\mathbf{x}}', \tilde{\mathbf{h}} \rangle}{\|\tilde{\mathbf{x}}'\| \|\tilde{\mathbf{h}}\|}, \quad (3.12)$$

where $\|\mathbf{u}\|$ denotes magnitude of the vector \mathbf{u} . If the noise transient in channel H indeed originates in X , $\tilde{\mathbf{x}}'$ and $\tilde{\mathbf{h}}$ should display a high correlation. On the other hand, if the noise transient does not originate in X , the vector $\tilde{\mathbf{x}}'$ and $\tilde{\mathbf{h}}$ will be randomly oriented, and hence the linear cross-correlation coefficient r will tend to be small in absolute value. This can be converted to the normally distributed variable z by the Fisher transformation [157]:

$$z = \frac{1}{2} \ln \left(\frac{1+r}{1-r} \right). \quad (3.13)$$

The new variable z will be approximately normally distributed with mean zero and standard deviation $1/\sqrt{M-3}$ (see Eq.(3.8) for the definition of M).

If z is greater than, or equal to, a threshold λ , we veto the trigger. The threshold giving an *accidental veto probability* (probability that a trigger is accidentally vetoed) of ψ can be calculated from

$$\psi = \int_{\lambda}^{\infty} f(x; \mu, \sigma^2) dx, \quad (3.14)$$

where $f(x; \mu, \sigma^2)$ is the probability density of the normal distribution with mean $\mu = 0$ and variance $\sigma^2 = 1/(M-3)$.

If the data vectors $\tilde{\mathbf{h}}$ and $\tilde{\mathbf{x}}$ are computed using windowed DFTs, the variance of the distribution of z will not be given by $\sigma^2 = 1/(M-3)$. In order to estimate the variance of the distribution of z , we generate a population of z from stationary data surrounding the burst (using the same DFT-length and bandwidth). From that population, σ^2 is estimated, and the veto threshold is computed using Eq.(3.14).

3.2.5. Implementation

Two sets of burst triggers are generated by running an ETG on channels X and H . We take a set of triggers that are coincident in channels X and H , allowing a liberal time window for coincidence.

In the case of the null-stream method, the data is divided into a number of segments of length L . The test statistic, ϵ , is computed from the segment of data containing the burst. It is well-known that the maximum signal-to-noise ratio (SNR) for the excess power statistic is achieved when the time-frequency volume used to compute the statistic is equal to the actual time-frequency volume of the signal [114]. Since the duration and bandwidth of the burst is estimated by the ETG itself, this information is used to decide on the length (L) of the data-segment used to compute $\tilde{\delta}$ and the bandwidth over which the integration is carried out in Eq.(6.15). Consequently, the frequency resolution of the DFT used in the analysis is in general different for each trigger, and hence, so are the dimension of the vectors $\tilde{\mathbf{h}}$ and $\tilde{\mathbf{x}}$. It is then required that the discrete transfer-function vector should also have the same dimension. To achieve this, we store a high-resolution transfer function and interpolate it to the required frequency resolution. It was found that the analysis can be sensitive to the errors in the interpolation, since the interpolation can smear out the detailed features in the transfer function. Since, the lower the frequency resolution the higher are the errors, we set up a minimum frequency resolution of 16 Hz for the analysis. In order to achieve this, the minimum length of the data segment used to compute the DFT is set to be $1/16$ s \simeq 60 ms. Parameters of the Gamma distribution are estimated from segments of data neighboring the one containing the burst, but excluding that segment. The trigger is vetoed if $\epsilon \leq \tau$, where the threshold, τ , giving a particular rejection probability, Φ , is calculated using Eq.(3.11).

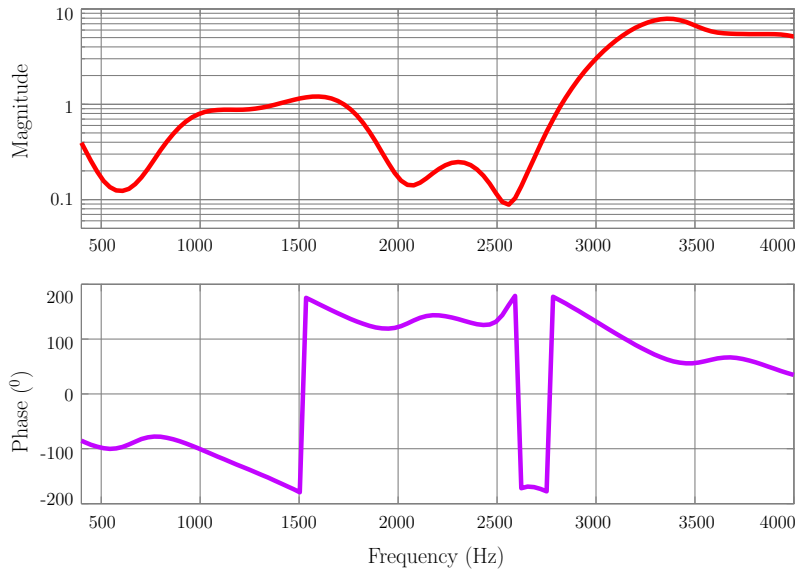


Figure 3.2.: Transfer function from channel X to channel H used for the simulations.

In the case of the cross-correlation method, a short segment of the data (of length L) encompassing the burst is used to compute the cross-correlation statistic z . The rest of the data segments are used to estimate the expected variance, σ^2 , of z in the case of random correlation. Again, the time-frequency volume of the data used to compute the statistics is decided making use of the information supplied by the ETG. The veto threshold, λ , corresponding to a prescribed accidental veto probability, ψ , can be calculated using Eq.(3.14).

3.3. Software injections

In the null-stream method, the veto threshold is set based on a specific rejection probability, while in the cross-correlation method, the threshold corresponds to a specific accidental veto probability. Since these are different aspects of the veto method, let us clarify the terminology. The rejection probability is the probability that a trigger originating from channel X (a ‘causal’ trigger) is vetoed using the method described above, while the accidental veto probability is the probability that a ‘non-causal’ trigger in channel H is accidentally vetoed using the method.

In order to demonstrate that the fraction of ‘causal’ and ‘accidental’ coincident triggers that are vetoed using these methods is consistent with the predictions given by Eqs. (3.11) and (3.14) we simulate two different populations of bursts in channels X and H . One set of such software injections is done in such a way that the injected burst waveforms are consistent with the transfer function from X to H . The second set of injections is done in such a way that the injected bursts in the two channels have random parameters (so that the waveforms in channels X and H are, in general, inconsistent

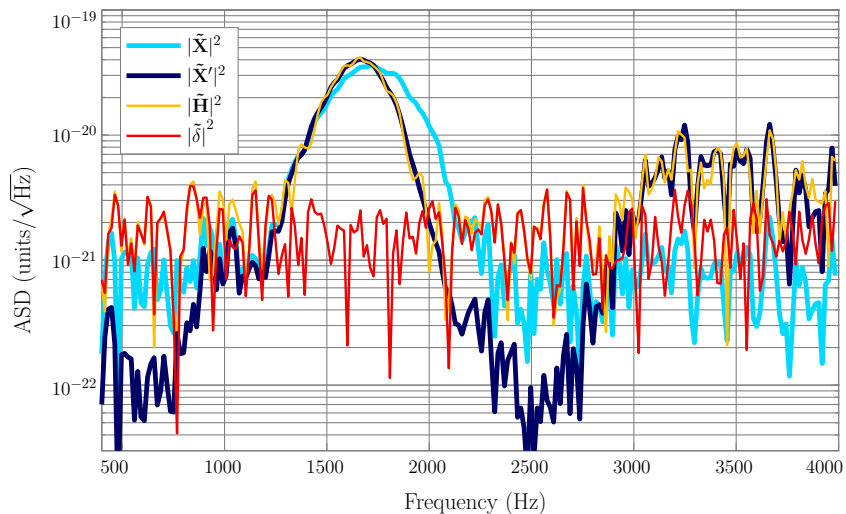


Figure 3.3.: Amplitude spectral densities of \mathbf{x} , \mathbf{x}' , \mathbf{h} and $\tilde{\delta}$ in the presence of a sine-Gaussian injection. It can be seen that $\tilde{\delta}$ contains no trace of the injected signal. The injected sine-Gaussian has a central frequency of 1715 Hz and SNR of 140 in channel X .

with the transfer function from X to H). We conveniently term the first set of injections as ‘causal injections’ and the second set of injections as ‘random injections’.

3.3.1. Causal injections

We generate a data stream of Gaussian white noise and inject Gaussian-modulated sinusoidal waveforms in to it; this forms our channel X . This data stream is filtered using a time-domain filter and some extra noise is added to it. This constitutes our channel H (the ‘extra’ noise being the component of \mathbf{h} orthogonal to \mathbf{x}'). The frequency response of the filter is the transfer function from X to H . The transfer function used in this simulation is shown in Figure 3.2, which is quite similar to one particular transfer function measured in GEO 600. The injected sine-Gaussians are of the form:

$$s(t) = s_{\text{RSS}} \left(\frac{2f_0^2}{\pi} \right)^{1/4} \sin [2\pi f_0(t - t_0)] \exp [-(t - t_0)^2/\tau^2], \quad (3.15)$$

where f_0 is the central frequency of the waveforms and t_0 is the time corresponding to the peak amplitude. We setup the envelope width as $\tau = 2/f_0$. The corresponding quality factor is $Q \equiv \sqrt{2}\pi f_0 \tau = 8.9$ and bandwidth is $\Delta f = f_0/Q \simeq 0.1f_0$. The quantity s_{RSS} is the root-sum-squared (RSS) amplitude:

$$\left[\int_{-\infty}^{\infty} s^2(t) dt \right]^{1/2} = s_{\text{RSS}}. \quad (3.16)$$

The s_{rss} is varied so that the SNR⁴ of the injections ranges from $\simeq 6$ to $\simeq 500$ in channel X , and the central frequency is randomly chosen from the interval (432 Hz, 3008Hz).

As an illustration, the amplitude spectral densities of \mathbf{x} , \mathbf{x}' , \mathbf{h} and $\tilde{\delta}$ in the presence of a particular sine-Gaussian injection are shown in Figure 3.3. The injected sine-Gaussian has a central frequency of 1715 Hz and SNR of 140 in channel X . As expected, $\tilde{\delta}$ contains no trace of the injected signal.

The fraction of vetoed events among the injections is plotted against the rejection probability corresponding to the chosen threshold in Figure 3.4 (left). It can be seen that the fraction of vetoed injections is in very good agreement with the chosen rejection probability.

3.3.2. Random injections

We inject two populations of sine-Gaussian waveforms with randomly selected parameters into two data streams of white noise, so that the waveforms in channels X and H are, in general, inconsistent with the transfer function from X to H . We then try to veto these triggers using the transfer function from X to H after choosing a veto threshold. The analysis is repeated after choosing different veto thresholds. The fraction of vetoed injections is plotted against the accidental veto probability corresponding to the chosen veto threshold in the right hand side of Figure 3.4. It can be seen that the fraction of vetoed injections is in good agreement with the chosen accidental veto probability.

3.4. An alternative method: ‘trigger mapping’

Although the above described methods are rigorous and make use of the complete information contained in the data, they can be computationally expensive because they require reprocessing of the time-series data from the two channels. It may be noted that the whole data stream is processed by the ETG in the first place and a condensed form of the information about the burst waveform is stored (which is often known as ‘meta-data’). In this section, we develop a strategy to veto the spurious triggers in channel H by comparing them with the set of triggers in channel X , making use of the transfer function from X to H as well as the information extracted by the ETG. Although this method is not as rigorous as the previous ones, the advantage is that this does not require the reprocessing of time-series data and hence is computationally inexpensive.

Let $\{\mathbf{E}_X\}$ and $\{\mathbf{E}_H\}$ denote the set of burst triggers in channel X and channel H , respectively. Let us assume that each event, \mathbf{E} , is parametrized by its central frequency E^f , amplitude E^a and time of occurrence E^t . It is useful to think of \mathbf{E} as a point in a three-dimensional parameter space with coordinates (E^a, E^f, E^t) . Using the transfer

⁴The SNR, ρ , of a burst trigger is defined by $\rho^2 \equiv 2 \int (|\tilde{s}(f)|^2 / |\tilde{n}(f)|^2) df$ where $\tilde{s}(f)$ and $\tilde{n}(f)$ represent the Fourier transforms of the signal and the underlying noise, respectively, and the integration is carried out over the bandwidth (positive frequencies) of the burst waveform.

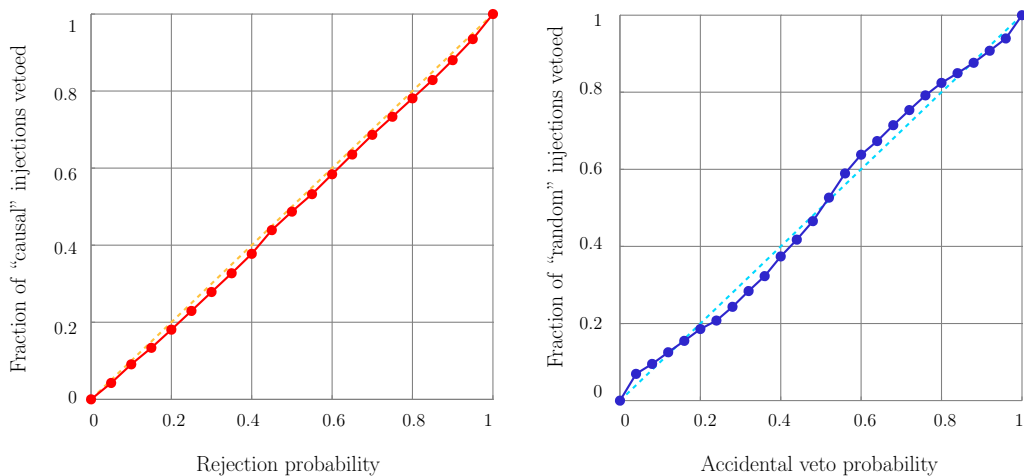


Figure 3.4.: [Left]: Fraction of causal injections vetoed by the null-stream method, plotted against the rejection probability corresponding to the chosen threshold. [Right]: Fraction of random injections vetoed by the cross-correlation method, plotted against the accidental veto probability corresponding to the chosen threshold. The dashed lines correspond to the case where the test statistics exactly fall in to the expected distributions.

function from X to H , we can predict how a certain event \mathbf{E}_X would appear in H . In other words, we map the event \mathbf{E}_X to the space of \mathbf{E}_H , making use of the transfer function from X to H . In order to veto an event \mathbf{E}_H in channel H , we check whether any of the ‘mapped’ \mathbf{E}_X triggers are consistent with \mathbf{E}_H in time of occurrence, central frequency and amplitude. Indeed, the precise definitions of these parameters depend upon the ETG, and hence we make use of these definitions in order to map the burst triggers from one channel to the other.

3.4.1. Mapping the burst triggers

The burst detection algorithm called mHACR [143] is used to generate the burst triggers. mHACR makes a time-frequency map of the data and identifies time-frequency pixels containing excess power which are statistically unlikely to be associated with the underlying noise distribution. mHACR then proceeds to cluster the neighboring pixels containing excess power to form an ‘event’. The central frequency and time of occurrence of the burst event are estimated by a weighted averaging of the pixel coordinates. This is equivalent to the calculation of the center of mass of an extended object where the signal power in a pixel serves as the ‘mass’ term. mHACR also estimates the total power contained in all the pixels belonging to a particular event, and the peak power of the event. The square root of the total power is taken as the characteristic amplitude E_X^a of the event.

The ETG does not reproduce the complete morphology of a burst waveform. Instead,

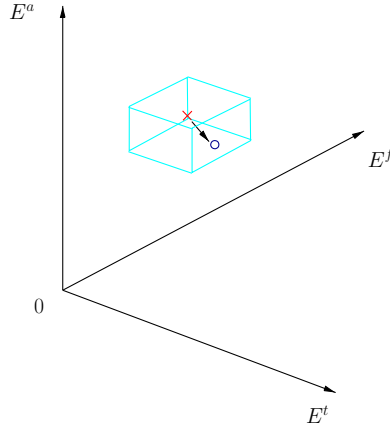


Figure 3.5.: A schematic diagram of the parameter space of burst triggers. The cross represents a trigger in channel H and the circle represents a trigger in channel X , mapped to channel H . A distance vector \mathbf{w} is drawn from one point to another. The consistency volume chosen to veto the trigger is also shown.

the ETG tries to parametrize the waveform using a set of quantities like the central frequency, amplitude, bandwidth, duration, etc. Considering the fact that we are mostly looking at short-lived, band-limited bursts, we approximate the power spectrum of the underlying burst waveform in channel X to a Gaussian function. For example, the power spectrum of the waveform associated with a trigger \mathbf{E}_X is approximated as a Gaussian function $G(f)$ such that

$$\int_{f_1}^{f_2} G(f) df = (E_X^a)^2, \quad (3.17)$$

where the limits of integration are defined by bandwidth E_X^b of the burst, i.e., $f_1 = E_X^f - E_X^b/2$ and $f_2 = E_X^f + E_X^b/2$. Since the peak power of the burst is also estimated by the ETG, the ‘spread’ of the Gaussian function can be calculated by solving Eq.(3.17). The power spectrum is deformed by the transfer function $T^{\text{XH}}(f)$ when the glitch makes its way to channel H ; this we denote by

$$\hat{G}(f) = G(f) |T^{\text{XH}}(f)|^2. \quad (3.18)$$

Given the transfer function $T^{\text{XH}}(f)$, the burst triggers in channel X can be mapped to channel H in the following way:

$$E_X^{a'} = \left[\int_{f_1}^{f_2} \hat{G}(f) df \right]^{1/2}, \quad (3.19)$$

$$E_X^{t'} = E_X^t + \frac{\int_{f_1}^{f_2} \hat{G}(f) \lambda(f) df}{\int_{f_1}^{f_2} \hat{G}(f) df}, \quad (3.20)$$

$$E_X^{f'} = \frac{\int_{f_1}^{f_2} \hat{G}(f) f df}{\int_{f_1}^{f_2} \hat{G}(f) df}. \quad (3.21)$$

In the above expression, $\lambda(f)$ is the frequency-normalized phase-delay (time-lag) of the transfer function $T^{\text{XH}}(f)$. i.e.,

$$\lambda(f) = \frac{1}{2\pi f} \phi(T^{\text{XH}}(f)). \quad (3.22)$$

where $\phi(\cdot)$ denotes the phase of a complex quantity.

3.4.2. Identifying consistent events

In order to veto a trigger, \mathbf{E}_H , in channel H , we check whether any of the ‘mapped’ triggers (\mathbf{E}'_X) from channel X , are ‘sufficiently close’ to it. To be explicit, we define a vector, \mathbf{w} , connecting the two points in the parameter space of H triggers,

$$\mathbf{w} \equiv \mathbf{E}_H - \mathbf{E}'_X, \quad (3.23)$$

and require that it has a sufficiently small ‘length’. This length is assigned to the vector by calculating the fractional volume enclosed by a three-dimensional Gaussian envelope of width $\sigma(\mathbf{w})$. This is explained below.

Let $\Delta\mathbf{E}$ denote the errors in the ETG in the estimation of parameters associated with the event \mathbf{E} . In the absence of any systematic biases, the errors $\Delta\mathbf{E}$ can be assumed to be drawn from multivariate Normal distributions of zero mean and standard deviation $\sigma(\Delta\mathbf{E})$, where the standard deviation is an monotonically decreasing function of the SNR. $\sigma(\Delta\mathbf{E})$ can be estimated by injecting known waveforms into the data and comparing the trigger parameters estimated by the ETG to the actual parameters of the injected waveforms.

Once the errors $\Delta\mathbf{E}_X$ associated with \mathbf{E}_X are estimated, they can be mapped to the space of H triggers using Eq.(3.19-3.21) by a linear approximation of the error propagation [158]. Then the components of \mathbf{w} will be distributed according to Normal distributions of zero mean and the following variance:

$$\sigma^2(\mathbf{w}) = \sigma^2(\Delta\mathbf{E}_H) + \sigma^2(\Delta\mathbf{E}'_X), \quad (3.24)$$

where $\Delta\mathbf{E}'_X$ denotes the errors $\Delta\mathbf{E}_X$, mapped to the space of H triggers. Thus the joint probability density of the vector \mathbf{w} comprising the three random variables (w^a, w^f, w^t) is given by the three-dimensional Gaussian function

$$f(\mathbf{w}) = \frac{1}{(2\pi)^{3/2} \sigma(w^f) \sigma(w^a) \sigma(w^t)} \exp\left(-\frac{1}{2} \mathbf{w}^T \mathbf{C}^{-1} \mathbf{w}\right), \quad (3.25)$$

where \mathbf{w}^T denotes the transpose of \mathbf{w} . Assuming that the errors are uncorrelated, we write the covariance matrix \mathbf{C} as,

$$\mathbf{C} = \begin{bmatrix} \sigma^2(w^f) & 0 & 0 \\ 0 & \sigma^2(w^a) & 0 \\ 0 & 0 & \sigma^2(w^t) \end{bmatrix}. \quad (3.26)$$

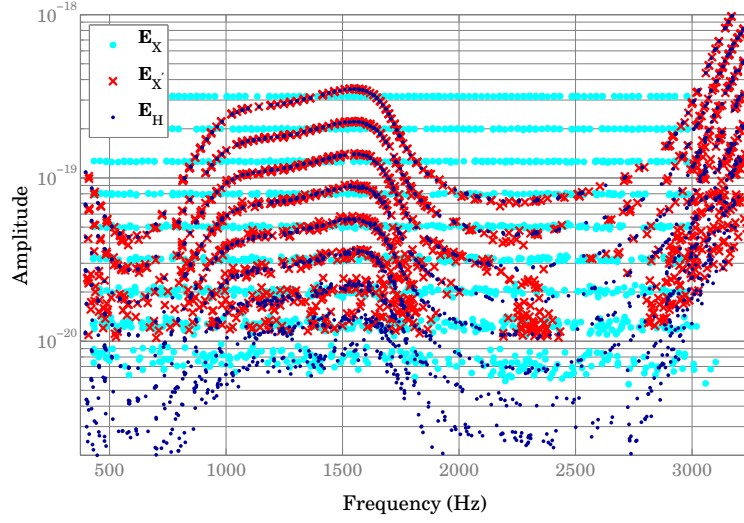


Figure 3.6.: The RSS amplitude, E^a , of the burst events plotted against the central frequency, E^f . Shown in the figure are three population of events: events in channel X (\mathbf{E}_X); channel X events mapped to channel H (\mathbf{E}'_X); and events in channel H (\mathbf{E}_H).

This enables us to set a threshold for \mathbf{w} for vetoing an event \mathbf{E}_H . In order to veto an event, we require that

$$|\mathbf{w}| \leq \boldsymbol{\tau}. \quad (3.27)$$

The components (τ^a, τ^t, τ^f) of the ‘threshold vector’ $\boldsymbol{\tau}$ are related to the rejection probability Φ by

$$\Phi = 8 \int_0^{\tau^f} \int_0^{\tau^a} \int_0^{\tau^t} f(\mathbf{w}) dw^f dw^a dw^t. \quad (3.28)$$

It can be seen that, by choosing a particular threshold vector $\boldsymbol{\tau}$, we are defining a consistency volume around each burst trigger in channel H . If one of the mapped triggers from channel X falls into this volume, we veto the H trigger. This is schematically illustrated in Figure 3.5.

The studies performed on the quality of the parameter estimation of mHACR are described in Chapter 2. The standard deviation of mHACR errors in estimating the parameters of the sine-Gaussian waveforms are given there as a function of the SNR of the triggers.

3.4.3. Software injections

We simulate two populations of bursts in channel X and H , as described in Section 6.2.1. The two data streams are processed by mHACR and two sets of triggers $\{\mathbf{E}_X\}$ and $\{\mathbf{E}_H\}$ are generated. The X triggers are mapped to channel H using the transfer function from

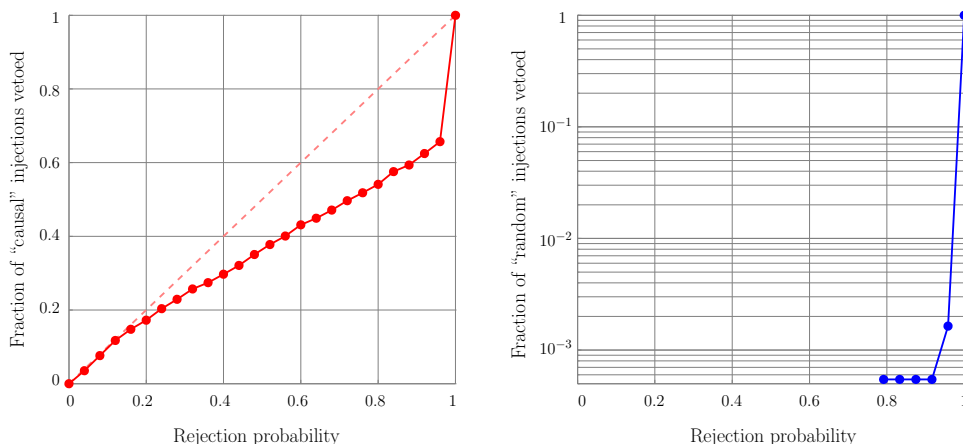


Figure 3.7.: [Left]: Fraction of ‘causal’ injections vetoed, plotted against the rejection probability corresponding to the chosen threshold. [Right]: Fraction of ‘random’ injections vetoed, plotted against the rejection probability corresponding to the chosen threshold.

X to H . Figure 3.6 shows the characteristic amplitudes E^a of the three population of triggers (\mathbf{E}_X , \mathbf{E}'_X and \mathbf{E}_H) plotted against the central frequency E^f . The injected events in channel X span 9 different amplitudes. The \mathbf{E}'_X triggers and \mathbf{E}_H triggers can be seen to fall nicely into the shape of the transfer function.

The veto analysis is repeated with different thresholds. The estimated veto efficiency is plotted against the rejection probability corresponding to the chosen thresholds in Figure 3.7. Although the estimated rejection efficiency roughly agrees with the predicted rejection probability, the effect of relying on a number of assumptions can be immediately seen. One of possible reason for the discrepancy could be that, contrary to the assumption, the parameters have a non-zero correlation.

We also make a plausible estimation of the accidental-veto probability by injecting sine-Gaussian waveforms with random parameters into the two data streams and performing the veto analysis. The estimated accidental veto probability is plotted in Figure 3.7 (right) as a function of the rejection probability. This exercise suggests that $\sim 70\%$ of the causal injections can be vetoed at the cost of an accidental-veto probability $\sim 1\%$.

3.5. Summary

One of the most challenging problems in the search for unmodelled GW bursts using ground-based detectors is to distinguish between actual GW bursts and spurious instrumental bursts that trigger the detection algorithms. In this chapter, we have presented a robust strategy to veto certain classes of instrumental glitches that appear at the output of these detectors. This veto method is ‘physical’ in the sense that, in order to veto a burst trigger, we make use of our knowledge of the coupling of different detector

subsystems to the main detector output. The main idea behind this method is that the noise in an instrumental channel X can be transferred to the detector output (channel H) using the transfer function from X to H , provided the noise coupling is linear and the transfer function is unique. If a non-stationarity in channel H is causally related to one in channel X , the two have to be consistent with the transfer function. We have formulated two methods for testing the consistency between the burst triggers in channel X and channel H . One method makes use of the null stream constructed from channel H and the transferred channel X , and the second involves cross-correlating the two. We have also proposed a less-rigorous, but computationally inexpensive alternative to the above methods. In this method, the parameters of the triggers in channel X are compared to the parameters of the triggers in channel H to see whether a trigger in channel X can explain a trigger in channel H . In order to demonstrate these methods, we have performed software injections of burst waveforms into Gaussian noise.

The ‘trigger mapping’ veto needs to make certain assumptions about the power spectrum of the glitch in channel X . The assumption that we made in this chapter, that the power spectrum can be approximated by a Gaussian function, should be verified against real-life glitches. It might also be possible to make assumptions which are closer to reality, using better parametrization of the underlying waveforms.

4. Physical instrumental vetoes: application to GEO 600 data

4.1. The ‘real-life’ scenario

In this chapter, we discuss the implementation of the instrumental veto method proposed in the previous chapter in the data characterisation of the GEO 600 detector. Noise in GEO 600, like in other present-generation laser interferometric detectors, is not perfectly Gaussian, and exhibits non-Gaussian tails in the distribution. Also, the assumption we made in the previous chapter that the transfer function is time invariant is strictly not true. Transfer functions in actual detectors can vary in time. The slow temporal variation of the transfer function can be taken into account by making repeated measurements of the transfer function and tracking its evolution by continuously injecting and measuring spectral lines at certain frequencies (see [154]). But the non-stationarities of the transfer function on short time scales are hard to track.

Considering these ‘real-life’ effects, it may not be wise to use the ‘ideal-case’ relations given by Eqs.(3.11) and (3.14) to compute the veto thresholds corresponding to a certain rejection probability/accidental veto probability. For instance, due to the imperfect transfer function, the null stream $\tilde{\delta}$ can contain some ‘residual bursts’, and, as a result, the excess power statistic computed from $\tilde{\delta}$ will not fall into the expected Gamma distribution.

Here, we demonstrate a more general formulation of the veto method which admits non-Gaussian tails in the noise distribution and other real-life effects. We also demonstrate the efficiency of the veto by injecting instrumental glitches in the hardware of the GEO 600 detector. The *veto safety* is demonstrated by performing GW-like hardware injections. We also show an example application of this method using 5 days of data from the fifth science run of GEO 600.

4.1.1. Implementation

In the real-life scenario, as discussed earlier, even if the excess power statistic computed from $\tilde{\delta}$ does not fall into the expected distribution, if the glitch actually originates in subsystem X , we do expect the excess power statistic ϵ_δ computed from $\tilde{\delta}$ to be smaller than the same (ϵ_h) computed from \tilde{h} . If the ratio $s \equiv \epsilon_h/\epsilon_\delta$ is greater than a threshold, it is likely that the trigger originates in X , and we veto the trigger. The veto threshold corresponding to a certain accidental veto probability is calculated as described below.

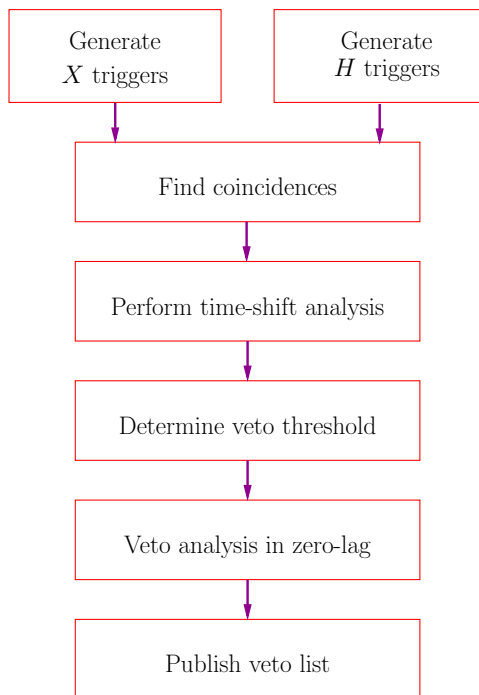


Figure 4.1.: Block diagram of the veto pipeline.

We time shift x_i with respect to h_i to destroy the causal relationship between the two data streams¹. The coincident triggers in the time-shifted data streams are identified and the ‘excess-power ratio’, s , for each coincident trigger is calculated. n such time shifts are performed to get better statistics from the data. A threshold, τ_s , is chosen such that only an acceptable number of coincident triggers in the time-shifted analysis have $s \geq \tau_s$. This threshold τ_s is used to veto the triggers in the ‘zero-lag’ analysis (without time shifting the data). The time-shifted analysis can also be used to calculate the veto threshold λ for the analysis using the cross-correlation statistic. Here, we choose a threshold λ such that only an acceptable number of coincident triggers have $z \geq \lambda$ in the time-shifted analysis and use this threshold to do the zero-lag analysis. The veto pipeline is schematically illustrated in Figure 4.1.

4.1.2. Caveats

It is worth stressing that this veto method relies on the linearity in the coupling of the noise from the detector subsystem X to the detector output, and can not be used where the coupling is nonlinear. This method also assumes that the transfer function from X to H is unique, and channel X accurately senses the disturbances in X . In other words, this technique can only be applied to systems that exhibit a linear coupling through a set

¹Time shift analysis is commonly employed in burst searches in order to estimate the accidental consistency, or ‘background’ rate. See, for example, [72]

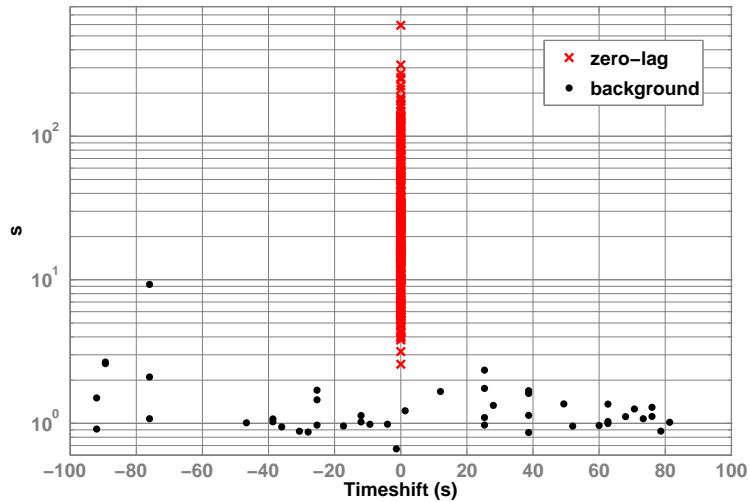


Figure 4.2.: Time shift analysis on instrumental-glitch-like hardware injections performed in the Φ_{MI} channel. The horizontal axis shows the time shift applied between x_i and h_i , and the vertical axis shows the excess-power ratio s . The (black) dots correspond to the coincident triggers in the time-shifted analysis and the (red) crosses correspond to the ones in the zero-lag analysis.

path, or multiple paths that are fixed. An environmental monitor will often fail to meet this requirement, unless the sensors are exceptionally well placed, because each local disturbance could couple differently into the monitor and to the GW channel, meaning that a different transfer function would be needed for each physical point of origin for the disturbance.

4.2. Analysis on hardware-injected burst signals

4.2.1. Injections mimicking instrumental bursts

In order to test this veto method, we injected around 300 sine-Gaussian burst signals over a period of one hour into four subsystems of GEO 600, whose couplings to H were known and well understood; the injections were performed serially, one subsystem after another. The four subsystems we chose are listed below. These descriptions are technical and concise. For more information, refer to [159].

Laser amplitude noise (P_{ref}): We make bursts of laser amplitude noise by injecting glitches into the laser amplitude stabilisation loop. We detect these glitches by measuring the light power reflected from the power-recycling cavity in the data acquisition system as channel P_{ref} .

Laser frequency noise (E_{ref}): We make bursts of laser frequency noise by adding glitches

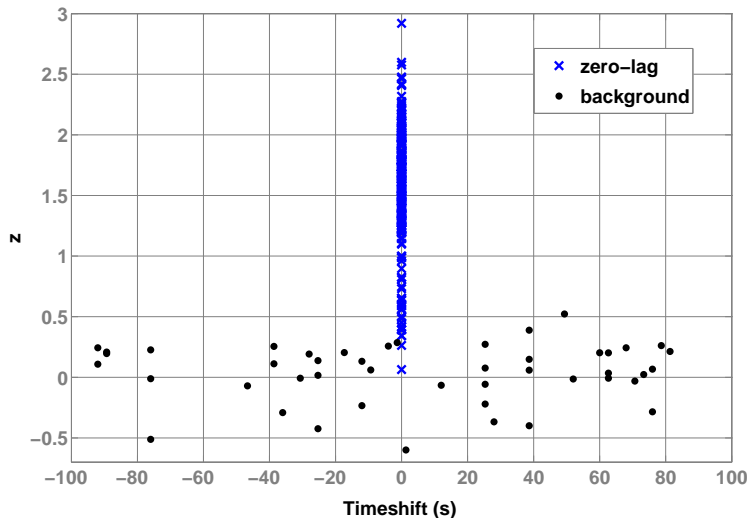


Figure 4.3.: Same as in Figure 4.2, except that the vertical axis shows the cross-correlation statistic z . The (black) dots correspond to the coincident triggers in the time-shifted analysis and the (blue) crosses correspond to the ones in the zero-lag analysis.

to the error-point of the Michelson common-mode control servo which keeps the power-recycling resonant by adjusting the frequency of the master laser. The recording of this error-point in the data acquisition system serves as the veto channel, E_{ref} .

Michelson oscillator phase noise (Φ_{MI}): The Michelson differential arm-length in GEO 600 is controlled by imposing phase-modulation side-bands on the light entering the interferometer. A heterodyne readout scheme is then used to derive an error signal which is fed back to the end mirrors of the Michelson to keep it on a dark fringe. We make glitches in the phase of the oscillator used to add the modulation sidebands by driving the voltage-frequency-control input of the crystal oscillator used to create this modulation signal. We phase-lock a reference crystal oscillator to the main crystal oscillator and the error-point of the phase-locked loop, which is sensitive to phase fluctuations on both oscillator signals, is recorded in the data acquisition system as Φ_{MI} and serves as a sensitive measurement of the phase noise on the main Michelson modulation sidebands.

Michelson oscillator amplitude noise (A_{MI}): The amplitude of the the main crystal oscillator is also stabilised to a quiet DC reference. We can add signals to the error-point of this stabilisation servo so as to impose additional amplitude noise on the main Michelson modulation signal. We added glitch signals in to this control loop and recorded its error-point in the data acquisition system as A_{MI} to serve as a veto channel.

Burst triggers in the veto channel and the GW channel are generated using the mHACR [143] burst detection algorithm. mHACR belongs to the class of time-frequency detection algorithms that make a time-frequency map of the data and identify time-frequency pixels

containing excess power which are statistically unlikely to be associated with the underlying noise distribution. For a detailed description of the algorithm and its performance, see Chapter 2. However, we remind the reader that the details of the burst detection algorithm are immaterial as far as this veto method is concerned. The burst ETG is only used to identify the coincident triggers in the two channels, and any ETG with proper time estimation of the burst event should serve this purpose.

Coincident triggers in the two channels are identified using a time window of ± 10 ms. The results of the time shift analysis on the hardware injections performed in the Φ_{MI} are shown in Figures 4.2 and 4.3. The horizontal axis shows the time shift applied between x_i and h_i . The vertical axis in Figure 4.2 shows the excess-power ratio $s \equiv \epsilon_{\text{h}}/\epsilon_{\delta}$. The (black) dots correspond to the coincident triggers in the time-shifted analysis and the (red) crosses correspond to the ones in the zero-lag analysis. From this, a veto threshold of 2.35 is chosen which corresponds to an accidental veto rate of 1 per day. All the coincident triggers in the zero lag are vetoed using this threshold. The vertical axis in Figure 4.3 shows the (transformed) cross-correlation statistic z . The (black) dots correspond to the coincident triggers in the time-shifted analysis and the (blue) crosses correspond to the ones in the zero-lag analysis. The veto threshold corresponding to an accidental veto rate of 1 per day is 0.27, which resulted in vetoing 99% of the coincident triggers in the zero-lag.

The veto analysis is performed on all the four channels in which the hardware injections are done. Results of the analysis are summarised in Table 4.1. It can be seen that only $\sim 5\%$ of the coincident triggers in the time-shifted analysis are vetoed, while more than 90% of the coincident triggers in the zero-lag are vetoed. This implies that the accidental rate of the veto is only $\sim 5\%$ of that of the standard statistical veto (using a time window of ± 10 ms) for almost the same veto efficiencies.

Veto channel	Threshold		Veto fraction		
	τ_s	λ	ξ	χ_s	χ_z
E_{ref}	2.51	0.33	4.48×10^{-2}	0.90	0.90
P_{ref}	1.94	0.23	5.45×10^{-2}	1.00	1.00
Φ_{MI}	2.35	0.27	6.12×10^{-2}	1.00	0.99
A_{MI}	1.50	0.26	4.62×10^{-2}	0.97	0.97

Table 4.1.: Summary of the veto analysis on hardware injections mimicking instrumental bursts. τ_s and λ are the chosen veto thresholds on the excess-power ratio s and the cross-correlation statistic z , respectively. ξ is the fraction of *coincident* events that are vetoed in the time-shifted analysis. The fraction of coincident events vetoed in the zero-lag using the s statistic is denoted by χ_s , while the same using the z statistic is denoted by χ_z . The chosen thresholds correspond to an accidental veto rate of 1 per day.

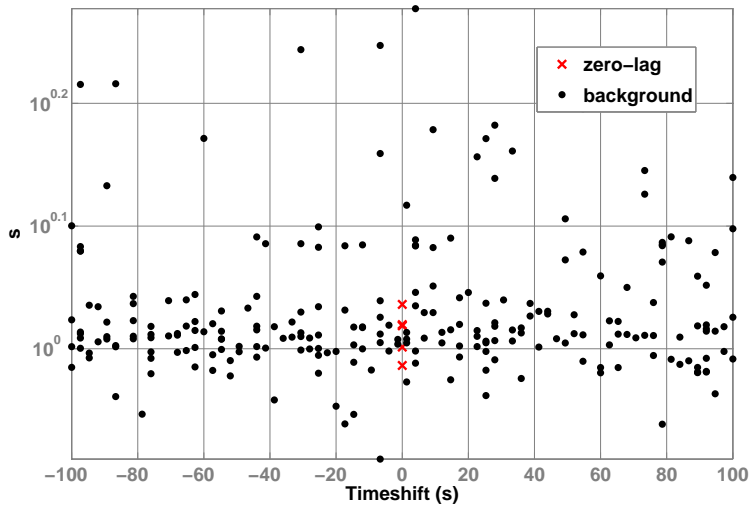


Figure 4.4.: Time shift analysis on the GW-like hardware injections. E_{ref} is used as the veto channel. The horizontal axis shows the time shift applied between x_i and h_i , and the vertical axis shows the excess-power ratio s . The (black) dots correspond to the coincident triggers in the time-shifted analysis and the (red) crosses correspond to the ones in the zero-lag analysis.

4.2.2. Injections mimicking gravitational-wave bursts

Some of the interferometer channels are sensitive to GWs to some non-negligible level. This raises the question of *veto safety* while using interferometer channels as veto channels. i.e., we have to make sure that we do not veto actual GW bursts which are coincident in the two channels. We argue that, since actual GW bursts are not causally related to the instrumental channels, the coincident triggers in channels X and H will not be consistent with the transfer function from X to H and hence, will not be vetoed using this method. Although the four channels under investigation in this paper are not expected to show any non-negligible sensitivity to GWs, there can be unexpected couplings, for example, through electrical faults or cross couplings in the data acquisition system. It is therefore prudent to explicitly demonstrate the safety of this veto method by doing GW-like hardware injections.

Hardware injections are performed by injecting signals into the electrostatic actuators used to control the differential-arm-length degree of freedom of GEO 600. For the test described here, around 300 sine-Gaussian bursts were injected with varying amplitudes and with central frequencies in the range 200 to 1300 Hz.

Figures 4.4 and 4.5 show the results of the veto analysis performed on the GW-like hardware injections. E_{ref} is used as the veto channel. It can be seen that neither of the test statistics (s or z) in the zero-lag analysis shows any excess significance over the corresponding time-shifted analysis. The veto thresholds corresponding to an accidental

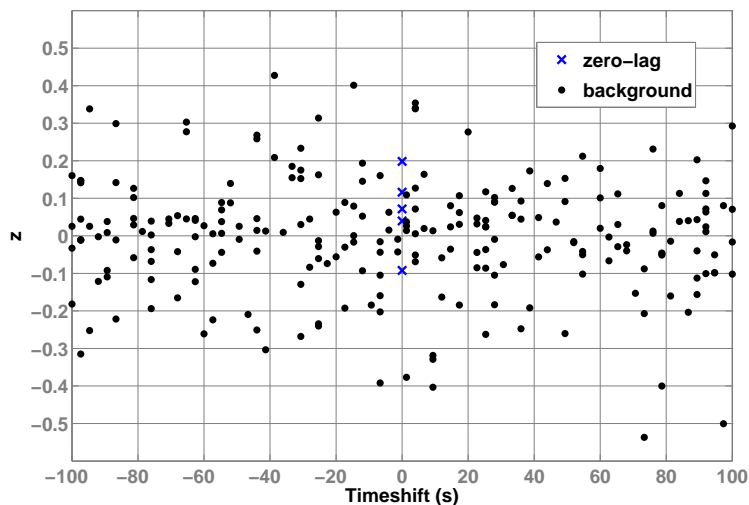


Figure 4.5.: Same as in Figure 4.4, except that the vertical axis shows the cross-correlation statistic z . The (black) dots correspond to the coincident triggers in the time-shifted analysis and the (blue) crosses correspond to the ones in the zero-lag analysis.

rate of 1 per day are $\tau_s = 1.64$ and $\lambda = 0.35$. Using these thresholds, we do not veto any of the injections.

4.3. An example application

GEO 600 participated full time in the Fifth Science Run (S5 run) in coincidence with the LIGO detectors from May 2006 to October 2006. The first few weeks of H data contained an additional population of glitches identified as coming from the laser frequency stabilisation control loop. These excess glitches had central frequencies typically around 2 kHz. In fact, the glitches were broad-band in the frequency stabilisation loop, but the coupling of frequency noise to H is most prominent around 2 kHz and so this is where we see the excess noise in H . The identification and repair of the source of these glitches took several weeks. So we identified an appropriate measure (E_{ref}) of the frequency-noise glitches that could be used as a veto channel (see Sec. 4.2.1 to see how this channel is derived).

Veto analysis is performed on 5 days of data from the period described above (in the frequency range of 400 Hz – 2kHz). Burst triggers in the two channels are generated by the mHACR burst-detection algorithm. Coincident triggers within the two channels are identified using a time window of ± 10 ms for time-coincidence. Only triggers with signal-to-noise ratio ≥ 6 are considered for this analysis. Out of 5326 triggers in the GW channel, 2048 triggers were found to be coincident with the E_{ref} channel. The accidental rate of the veto is estimated by doing 76 time shifts (from -100s to 100s). Figure 4.6

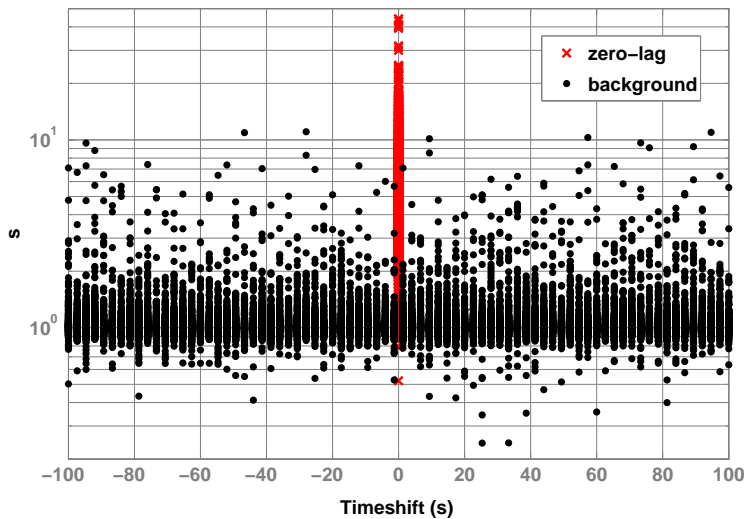


Figure 4.6.: Time-shifted analysis on 5 days of data from the Fifth science run of GEO 600 using E_{ref} as the veto channel. The horizontal axis shows the time shift applied between x_i and h_i , and the vertical axis shows the excess-power ratio s . The black dots correspond to the coincident triggers in the time-shifted analysis and the red crosses correspond to the ones in the zero-lag analysis.

shows the excess-power ratio s computed from the coincident triggers plotted against the applied time shift between the data streams, while Figure 4.7 shows the cross-correlation statistic z plotted against the time shift. The dots correspond to the coincident triggers from the time-shifted analysis and the crosses correspond to those from the zero-lag analysis. We choose an accidental veto rate of 1 per day. The thresholds on the two statistics are estimated from the time-shifted analysis. This corresponds to a threshold of $\tau_s = 2.25$ for the excess-power ratio s and a threshold of $\lambda = 0.54$ for the cross-correlation statistic z . In the analysis using the null-stream, all coincident triggers with $s \geq \tau_s$ are vetoed, while in the analysis using the cross-correlation statistic, all triggers with $z \geq \lambda$ are vetoed. It was found that 88% of the coincident triggers are vetoed using the null-stream method and 92% of the coincident triggers are vetoed using the cross-correlation method. These correspond to 34% and 35% of the total number of H triggers in the data.

Histograms of the two test statistics s and z computed from the coincident triggers are plotted in Figure 4.8 and 4.9. The plots on the left show the distributions of the test statistics computed from the time-shifted analysis, normalised by the number of time shifts applied. These are the expected distributions of s and z in the absence of any causal relation between triggers in X and H (for the given data set). Histograms on the right show the distributions of s and z computed from the zero-lag analysis. Two different populations are clearly visible in these plots. One population (centered around 1 in the histograms of s ; centered around zero in the histograms of z) corresponds to the triggers which are accidentally time-coincident in the channels X and H , while the

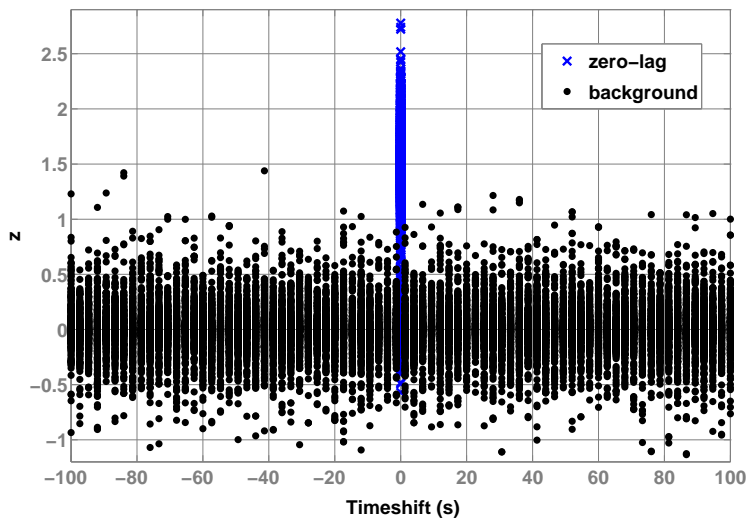


Figure 4.7.: Same as in Figure 4.6, except that the vertical axis shows the cross-correlation statistic z . The black dots correspond to the coincident triggers in the time-shifted analysis and the blue crosses correspond to the ones in the zero-lag analysis.

other population (centered around 6 in the histogram of s ; centered around 1.6 in the histogram of z) corresponds to triggers in H which are causally related to the ones in X . It is interesting to note that this method is able to distinguish clearly between these two populations. The reader may note that the number of accidental coincidences in the time-shifted analysis is $\sim 35\%$ larger than that in the zero-lag analysis. This can be explained in the following way: the veto analysis has shown that around 35% of the triggers in channel H are causally related to E_{ref} . These ‘causal’ triggers will fall into the populations on the right in the zero-lag analysis (centered around 6 in the histograms of s ; centered around 1.6 in the histograms of z). But, since the accidental coincidence rate is directly proportional to the total number of triggers, the presence of these causal triggers in the data would increase the coincidence rate in the time-shifted analysis by $\sim 35\%$, thus explaining the excess-coincidences that we observe.

Figure 4.10 shows a time-frequency plot of the mHACR triggers from 5 days of GEO 600 data. The green circles correspond to the coincident triggers (in channel H) which are vetoed using the null-stream method and the black dots correspond to the ones which are vetoed using the cross-correlation method. The red crosses correspond to the coincident triggers which are not vetoed by any of the methods.

A summary of the analyses performed using different accidental veto rates are given in Table 4.2. Also, in Figure 4.11, we plot the fraction of coincident events that are vetoed in the zero-lag (a measure of the efficiency of the veto) against the fraction of the coincident triggers which are vetoed in the time-shifted analysis (a measure of the accidental veto probability). This plot can be thought of as a *receiver operating characteristic* [160] plot for this analysis, and can be used to choose thresholds which

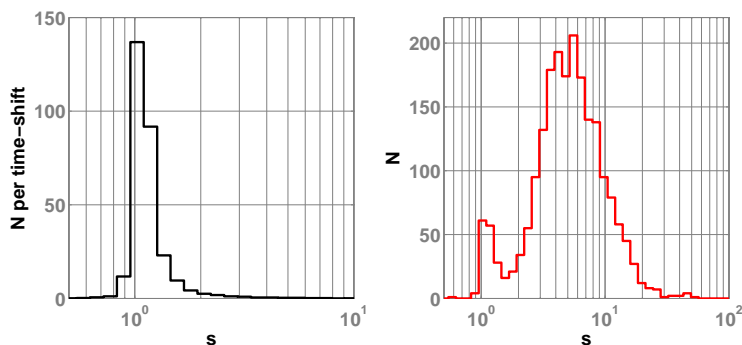


Figure 4.8.: Histograms of the excess-power ratio s computed from the time-shifted analysis (left) and the zero-lag analysis (right).

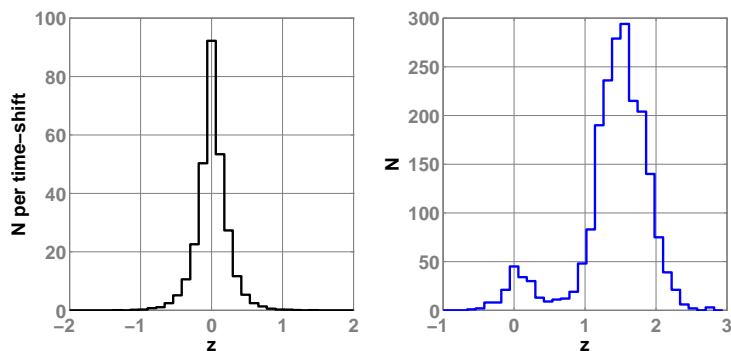


Figure 4.9.: Histograms of the cross-correlation statistic z computed from the time-shifted analysis (left) and the zero-lag analysis (right).

correspond to acceptable values of veto efficiency and accidental veto rate/probability. In the figure, the solid curve corresponds to the analysis using null-stream and the dashed curve corresponds to the analysis using cross correlation. It can be seen that, for high values of accidental veto probability, the two methods perform equally well. But for low values of accidental veto probability ($< 2 \times 10^{-2}$), the curve corresponding to the null-stream analysis starts to fall off, and the cross-correlation analysis continues to perform well.

Figure 4.12 provides a rough comparison between the abilities of the two test statistics (s and z) in vetoing the instrumental glitches. The horizontal axis shows the excess-power ratio s and the vertical axis shows the cross-correlation statistic z computed from the coincident triggers. The vertical (red) and horizontal (blue) lines in the plot correspond to the veto thresholds τ_s and λ on the two statistics, respectively. Triggers on the right of the vertical line are vetoed by s , and those above the horizontal line are vetoed by z . 33.5% of the total number of H triggers are vetoed by both methods. There exists a small population ($\sim 1\%$ of the total number of H triggers) which is vetoed by z ; but

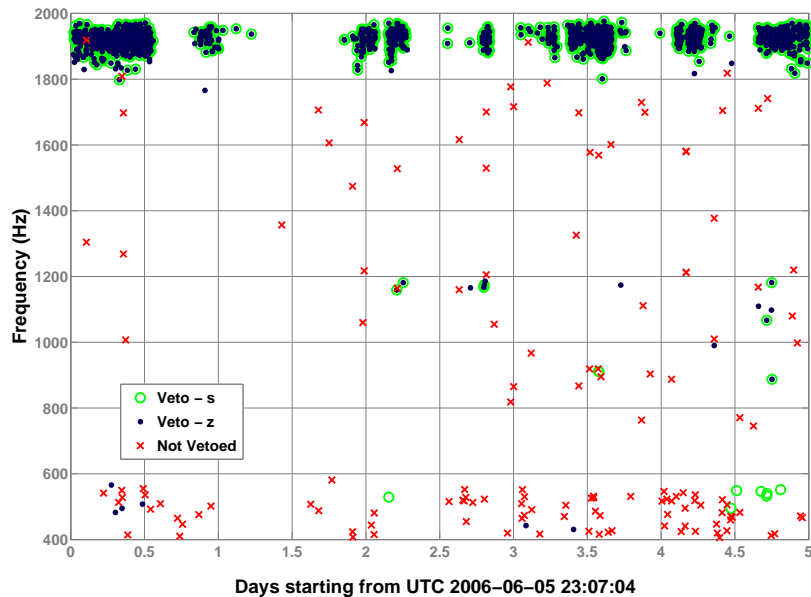


Figure 4.10.: A time-frequency plot of mHACR triggers from 5 days of GEO 600 data. The horizontal axis shows the time and the vertical axis shows the frequency of the the burst triggers in channel H , as estimated by mHACR. Only those triggers which are coincident with E_{ref} are plotted. The (green) circles correspond to coincident triggers which are vetoed using the null-stream method, and the (black) dots correspond to the ones which are vetoed using the cross-correlation method. Coincident triggers which are not vetoed by any of the methods are indicated by (red) crosses. The chosen veto thresholds correspond to one accidental veto per day.

not by s , which suggests that z is a more sensitive statistic than s . But this may not be taken as a general indication that the cross-correlation is a more sensitive method than the null stream. One can construct alternative statistics using the null stream, which could be more sensitive than s . One possible alternative is $\epsilon_{\delta}/\epsilon_{\text{opt}}$, where ϵ_{opt} is the excess power statistic computed from the optimal combination [161, 162] of the noise vectors $\tilde{\mathbf{h}}$ and $\tilde{\mathbf{x}}'$. We leave this as future work.

4.4. Summary and outlook

We proposed a veto method which makes use of the information on the physical coupling of different detector subsystems to the main detector output. We also demonstrated this method using the data of the GEO 600 detector. By performing hardware injections mimicking instrumental glitches, we showed that glitches originating in a detector subsystem can be vetoed using the transfer function from the subsystem to the detector output. We also addressed the issue of veto safety by performing hardware injections

Accidental rate	Threshold		Veto fraction		
	τ_s	λ	ξ	χ_s	χ_z
day ⁻¹	2.25	0.54	1.73×10^{-2}	0.88	0.92
week ⁻¹	5.09	0.86	2.47×10^{-3}	0.45	0.90
month ⁻¹	7.40	1.11	5.93×10^{-4}	0.23	0.85

Table 4.2.: Summary of the veto analysis on 5 days of data from GEO 600. τ_s and λ are the chosen veto thresholds on the excess-power ratio s and the cross-correlation statistic z , respectively. ξ is the fraction of *coincident* events that are vetoed in the time-shifted analysis. The fraction of coincident events vetoed in the zero-lag using the s statistic is denoted by χ_s , while the same using the z statistic is denoted by χ_z . The chosen veto thresholds correspond to the accidental veto rates tabulated in the first column.

mimicking GW bursts into GEO 600, and by showing that such injections are *not* vetoed. Finally, we used this strategy to veto glitches in the data from the fifth science run of GEO 600, using the laser frequency noise channel as the veto channel. The analysis was performed on 5 days of GEO 600 data from the second month of the science run. Of the 5326 triggers in the GW channel, 35% were vetoed with an accidental rate of 1 per day using the cross-correlation method, while 34% of the triggers were vetoed using the null-stream method.

The method relies on linearity in the coupling of the noise from a detector subsystem to the detector output, and the measurability/calculability and uniqueness of the transfer function. The assumption of linear coupling is valid as far as many detector subsystems in the large-scale interferometers are concerned. Strictly speaking, this method also requires time-invariant transfer functions. The way to track down slow temporal variations in the transfer functions is discussed in the literature. The formulation that we have developed was found to be robust against non-stationarities of short time scales in the transfer functions, and non-Gaussian tails in the noise distribution.

When possible, using physical information has clear advantages over relying only on statistical correlations. The method that was proposed here is a fully coherent way of testing the consistency of the glitches in the GW channel with those in an instrumental channel. We hope that this will serve as a first step for developing a class of ‘physical instrumental vetoes’ for present and future detectors.

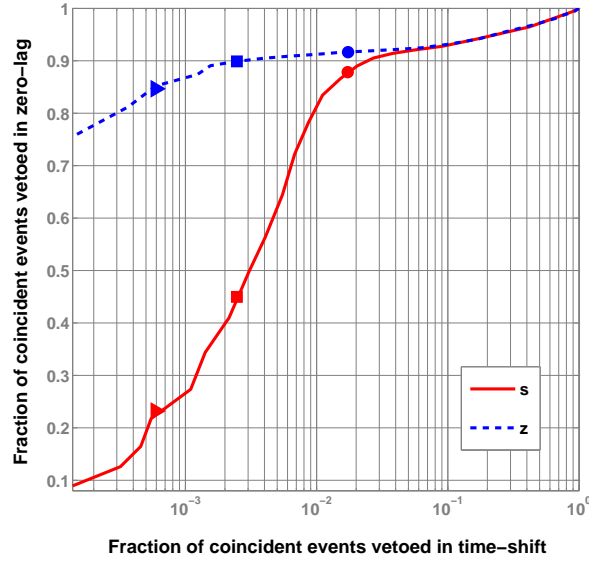


Figure 4.11.: Fraction of coincident triggers that are vetoed in the zero-lag plotted against the fraction of the coincident triggers that are vetoed in the time-shifted analysis. The solid curve corresponds to the analysis using null-stream and the dashed curve corresponds to the analysis using cross-correlation. The triangles, the squares, and the dots correspond to accidental veto rates of 1 per month, 1 per week, and 1 per day, respectively.

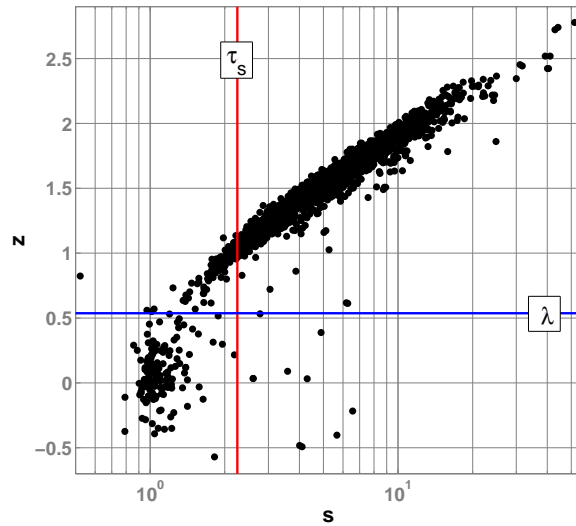


Figure 4.12.: Excess-power ratio s (horizontal axis) computed from the coincident triggers plotted against the cross-correlation statistic z (vertical axis). The vertical (red) and horizontal (blue) lines correspond to the veto thresholds τ_s and λ on the two statistics, respectively.

5. A null-stream veto for GEO 600

5.1. Introduction

The optical layout of the gravitational-wave detector GEO 600 is based on a standard Michelson interferometer with the addition of two mirrors: the power-recycling mirror and the signal-recycling mirror. This so-called *dual-recycled* optical scheme is used to enhance the sensitivity of the detector (see [163] and [164] for details).

The use of signal recycling and a heterodyne readout scheme means that gravitational-wave signal can be extracted optimally from the detector output only at one frequency by selecting an appropriate demodulation phase of the output signal. This means that, for any other frequency, the gravitational-wave information will be spread between two orthogonal demodulation quadratures of the output.

In GEO 600, both output quadratures are calibrated to strain since, in general, the noise components of each output quadrature are different. This calibration is done in the time-domain by injecting calibration lines into the differential length-control actuators of the Michelson interferometer. These calibration lines produce, at least at those frequencies, known strain signals. From the measurement of these calibration lines in the detector output, the response function of the detector is determined periodically on-line. The inverse of this response function is used to compute time-domain filters which are used to filter the detector outputs, $P(t)$ and $Q(t)$, to produce two estimates of the detected strain, $h_P(t)$ and $h_Q(t)$. Details of the calibration method used at GEO 600 are given in [165, 166].

If we consider that both $h_P(t)$ and $h_Q(t)$ contain the same gravitational wave signal, $h(t)$, together with different noise components, $N_P(t)$ and $N_Q(t)$, such that

$$h_P(t) = h(t) + N_P(t), \quad (5.1)$$

$$h_Q(t) = h(t) + N_Q(t), \quad (5.2)$$

then we can recover the best estimate of the underlying signal, $h(t)$, by optimally combining $h_P(t)$ and $h_Q(t)$. Details of this combining method are given in [162].

We can also construct a *null stream* from $h_P(t)$ and $h_Q(t)$ by

$$h_{\text{null}}(t) = h_P(t) - h_Q(t), \quad (5.3)$$

which will yield a data stream that contains no gravitational wave signal to a level consistent with the relative calibration accuracy of $h_P(t)$ and $h_Q(t)$.

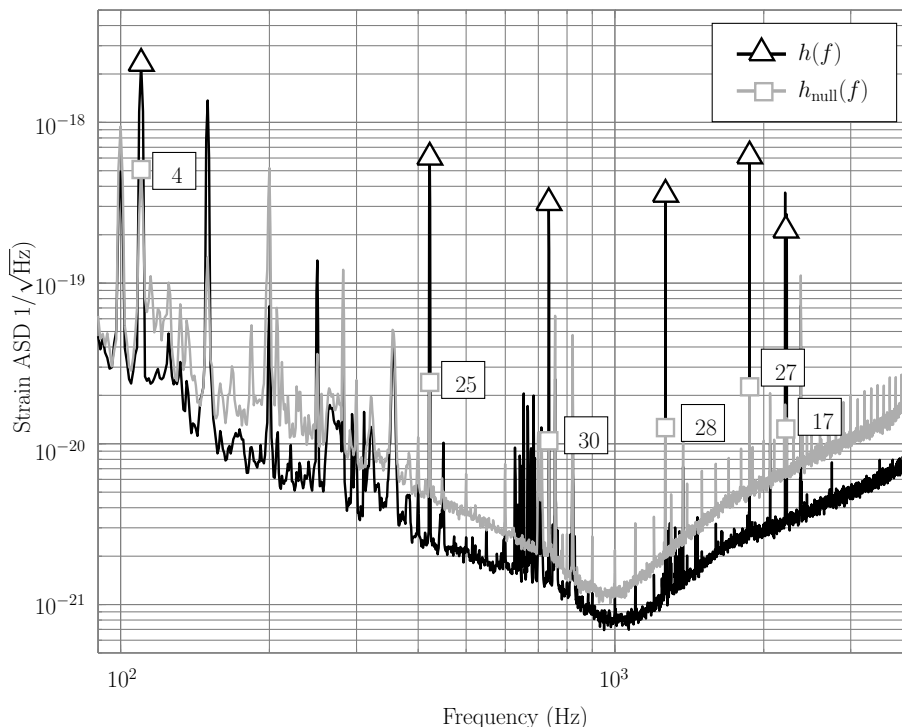


Figure 5.1.: Amplitude spectral densities of the $h(t)$ and $h_{\text{null}}(t)$ outputs of GEO 600. Calibration lines are marked for the two spectra, and the ratio of the calibration line amplitudes in $h(t)$ and $h_{\text{null}}(t)$ are indicated in the boxes.

Figure 5.1 shows snapshot amplitude spectral density estimates of both $h(t)$ and $h_{\text{null}}(t)$ from the same stretch of data; the injected calibration lines are highlighted. We can see that the calibration lines (and hence any gravitational wave signal), appear significantly suppressed in the null stream. We can also see that since the amplitude of the calibration lines is not zero in the null stream, there is a relative error in the calibration of the two output quadratures of the order of 5% over most of the frequency band.

We can search for burst signals in this null stream, as we do in the $h(t)$ data. If a coincident signal is found in both the null stream and the $h(t)$ stream, with a relative amplitude that is *inconsistent* with it being a gravitational wave signal, then we can veto it. In this chapter, we develop a strategy which can be used to veto spurious triggers in the search for transient, unmodelled gravitational-wave bursts. This veto method is studied in the following sections using software injections into data from GEO 600. The ‘false-veto’ (false-dismissal) probability and veto efficiency is estimated as a function of an amplitude consistency threshold. The ‘safety’ of the veto is demonstrated by performing hardware injections mimicking gravitational-wave bursts into GEO 600, and by showing that such injections are vetoed. This method is then applied with a particular threshold to a long stretch of GEO 600 data. It may be noted that, while the veto strategy proposed in this chapter relies on the physical properties of the grav-

Parameter	Min	Max
h_{rss}	5×10^{-21}	5×10^{-20}
f_0 (Hz)	900	2000
τ (s)	0.01	0.1

Table 5.1.: The ranges of the waveform parameters used in the series of software injections.

itational waves (the way they couple into $h(t)$ and the null stream), it does not make any assumptions about the model of the waveforms and is, in this sense, very robust.

5.2. Signal injection and detection

In order to study the false-veto probability and efficiency of such a veto method, we used software injections into the two detector outputs, $P(t)$ and $Q(t)$, prior to the calibration routine being applied. The signals injected were sine-Gaussians of the form

$$s(t) = h_{\text{rss}} \left(\frac{2f_0^2}{\pi} \right)^{1/4} \sin[2\pi f_0(t - t_0)] \exp \left[-\frac{(t - t_0)^2}{2\tau^2} \right], \quad (5.4)$$

where h_{rss} is the root-sum-squared (RSS) amplitude of the waveform such that the total integrated power in the waveform is equal to h_{rss}^2 , f_0 is the central frequency of the waveform, t_0 is the time corresponding to the peak amplitude, and τ sets the duration of the signal.

In order to detect these signals in both the $h(t)$ channel and the null stream, and to generate lists of transient events, we used the mHACR burst detection algorithm (see Chapter 2 for more details about this algorithm).

In all of the experiments detailed below (unless stated otherwise), the parameters of the sine-Gaussian injections were allowed to vary in the ranges shown in Table 5.1. These parameter ranges lead to injected signals that span a sensible range of signal-to-noise ratio (SNR) in the detector strain signal: not too small as to be undetectable by mHACR, and not too big as to be unrealistic. Figure 5.2 shows two examples of injected events; one showing a typically small SNR injection, and one showing a typically large SNR injection.

We only apply the veto to events which are coincident events in $h(t)$ and $h_{\text{null}}(t)$. These coincident events are selected from the two event lists by applying time- and frequency-consistency windows, Δt and Δf , respectively. The size of each of these windows was selected using software injections into the strain signal. Figure 5.3 shows efficiency-false alarm curves (see the following discussion) for these two tunable parameters, Δt and Δf , generated by comparing the detected events to the injected events from a particular set of 200 random injections using the parameter ranges indicated in Table 5.1. These events were injected into the two uncalibrated detector output streams with relative amplitudes such that the amplitudes in the two calibrated output streams, $h_P(t)$ and

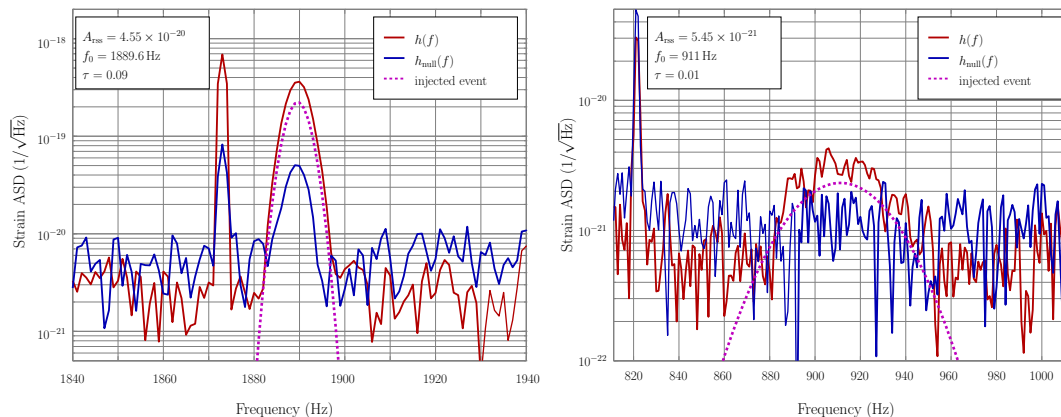


Figure 5.2.: Two example injected events into the data. The amplitude spectral density estimates are computed from 1 second of data with no averaging and using a Hann window. The parameters of the injected waveform are shown in the legend. The left plot shows an event with a high SNR; the right plot, one with a low SNR.

$h_Q(t)$, are equal. From these injections, 193 were detected by mHACR in the $h(t)$ stream.

The efficiency of the time/frequency windows is defined as the fraction of triggers in $h(t)$ that was found to be consistent with the triggers in $h_{\text{null}}(t)$ with a given choice of time/frequency windows. Similarly, the false alarm probability is the fraction of $h(t)$ triggers which are found to be *accidentally* coincident with triggers in $h_{\text{null}}(t)$. This can be estimated by shifting the time or frequency of $h_{\text{null}}(t)$ triggers by a non-zero amount and by applying the time and frequency windows on these time/frequency shifted triggers. In order to make a more precise estimate, one can make a number of time/frequency shifts and take the mean value of consistent triggers as the false alarm probability (see, for example, [143]). Since a rough estimation is sufficient for our purpose, we estimate this by doing a single time/frequency shift. The reader is cautioned at this point that the efficiency and false alarm probability of the consistency windows should not be confused with the *veto efficiency* and *false-veto* probability, which will be discussed later.

The curves shown in Figure 5.3 give the false alarm probability and efficiency of the time and frequency selection of these 193 detected events. The false alarm curve for each parameter is generated by time or frequency shifting the detected events by 1.1 seconds and 10.2 Hz respectively prior to making the time and frequency cut; those that pass the consistency test are considered a false alarm. From this experiment, we chose a time consistency window of 40 ms and a frequency consistency of 6 Hz to apply to the $h(t)$ and $h_{\text{null}}(t)$ event lists when using the mHACR algorithm in the experiments detailed in the rest of this chapter.

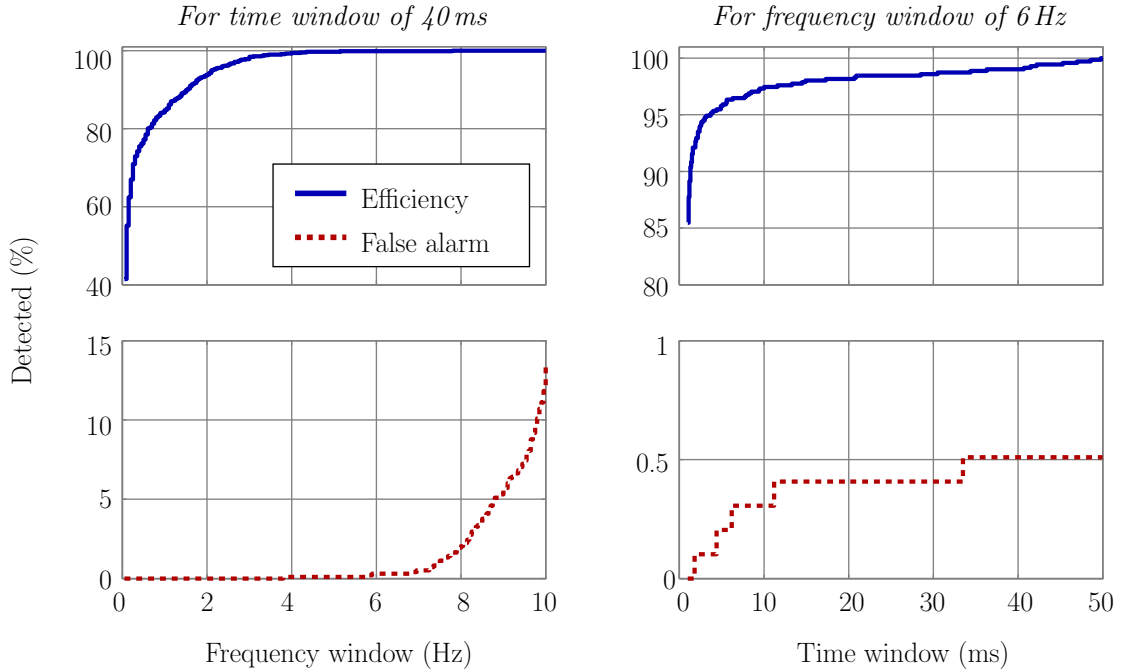


Figure 5.3.: False alarm and efficiency plots for the time and frequency cuts (Δt and Δf) applied to events detected by mHACR. From these plots, a frequency window of 6 Hz and a time window of 40 ms was chosen for the null-stream experiments. Here ‘efficiency’ refers to the percentage of coincident events that are expected to pass the consistency test; ‘false-alarm’ refers to the percentage of non-coincident events which are falsely taken to be coincident when applying the consistency test.

5.3. The amplitude consistency test

We compute the ratio of the amplitude of events in $h(t)$ and $h_{\text{null}}(t)$ that are time and frequency consistent. If the ratio, A_h/A_{null} , of a particular event is below a certain threshold, A_{thresh} , then we veto the event.

The value of the threshold, A_{thresh} , can be determined in two ways: a loose condition can be set by observing the amplitude of the calibration lines in the amplitude spectra of $h(t)$ and $h_{\text{null}}(t)$. Figure 5.1 shows the ratio of the calibration line amplitudes in $h(t)$ and $h_{\text{null}}(t)$ as a function of frequency. From this we could set a threshold of around 25 – the mean of the ratios. This is only one of the different ways in which we can set the threshold. We can determine a much more stringent test by performing software injections and looking at the efficiency of the veto and the false-veto probability as a function of the threshold we apply.

5.3.1. Veto efficiency and false-veto probability studies

Four different sets of injections were performed into the two uncalibrated detector-output data streams of GEO 600 in order to carry out the 4 experiments detailed in this section. In each set, 200 sine-Gaussian waveforms were injected into 2000 seconds of data. The time interval between injections was allowed to vary (randomly) between 0 and 10 seconds. The waveform parameters were randomly chosen from the ranges given in Table 5.1. The mHACR algorithm was then used to detect events in both $h(t)$ and $h_{\text{null}}(t)$.

In all four experiments, a time and frequency consistency cut (using the windows discussed above) was applied to these two event lists to preferentially select the injected events. These two shorter lists were then tested for amplitude consistency for various values of A_{thresh} .

Strain-like injections. For this experiment, the waveforms were injected with relative amplitudes consistent with the signals being from a gravitational-wave source. In other words, the injections into the two *uncalibrated* data streams were performed in such a way that they will be identical (up to the level of the calibration accuracy) in the *calibrated* $h_P(t)$ and $h_Q(t)$ strain outputs. Typical detector response functions for P and Q were used to generate the signals to add to the two uncalibrated data streams. These detector response functions are not necessarily those used to calibrate the $P(t)$ and $Q(t)$ time-series, thus mimicking the possible effects of calibration errors. In order to detect the injections in the null stream, the range of amplitudes of the injections had to be increased by a factor 5 compared to the values given in Table 5.1. From the 200 injections, 197 were detected in the $h(t)$ stream, and 99 were detected in the $h_{\text{null}}(t)$ stream. From these two lists, 99 events were found to be time and frequency consistent.

Figure 5.4 shows the result of applying the veto to the two time and frequency consistent events lists as a function of threshold. Since we expect the vast majority of the time-frequency consistent events to be GW-like events, any events that are vetoed are attributed to the false-veto probability of the method for that particular threshold.

Single output-channel events. One test of the efficiency of the veto method can be done by performing injections into the two uncalibrated detector outputs that are discrete in time, i.e., injected into either detector output, but not both. This simulates those real-life events that couple into the two detector outputs after the demodulation process where the two signal paths are separated. Of the 200 injected events, 169 were detected in the $h(t)$ stream, and 178 were detected in the null stream. Out of these events, 165 were found to be time and frequency consistent.

The efficiency curve for this class of events, generated from these two event lists, is labeled ‘Single channel events’ in Figure 5.4. Such events always appear in the null stream with a higher amplitude than in the $h(t)$ stream since the null stream contains all the signal whereas the $h(t)$ stream gets a share of the power from both

calibrated strain outputs (see [162] for details). Because of this, we expect these signals to be vetoed with a very high efficiency.

Equal amplitude events. This class of injections are simultaneous and have equal amplitude in both of the *uncalibrated* detector output signals. Such events could arise due to a coupling in the data acquisition system where a third channel couples transient signals into both detector output signals prior to digitization. Of the 200 injected events, 189 were detected in the $h(t)$ stream, and 182 were detected in the null stream. Out of these events, 172 were found to be time and frequency consistent.

The efficiency curve for this type of events is labeled ‘Equal events’ in Figure 5.4. Events such as these should appear slightly stronger in $h(t)$ stream than in the null stream since the signal in the null stream is reduced by the ratio of the two optical transfer functions at the frequency of the event. Since this ratio is, for most frequencies, of the order 2 or less (see [166] for typical optical transfer functions of GEO 600), we would expect to efficiently veto them.

Random amplitude, simultaneous events. The final class of signals studied are simultaneous in both uncalibrated detector outputs, but have a random relative amplitude in each. For these injections, a single waveform was selected at random using the parameter ranges given in Table 5.1. Two copies of this waveform were then injected in the the two uncalibrated detector output signals, with each being multiplied by a different random scaling factor selected from the range 0.1 to 10 prior to injection.

This type of signal would be symptomatic of a noise source that couples at the detector output, either before or after the demodulation process, but in a way that means the ratio of the two coupling paths is arbitrary and may depend on other external influences. One example of this may be pickup that depends on cable positions or signal sizes. Of the 200 injected events, 175 were detected in the $h(t)$ stream, and 178 were detected in the null stream. Of the events of these two lists, 160 were found to be time and frequency consistent. The efficiency curve for this type of events is labeled ‘Time-consistent events’ in Figure 5.4.

5.3.2. Setting the consistency threshold

From Figure 5.4, we can safely set a threshold for this veto method of $A_{\text{thresh}} = 5$. The threshold was chosen to be as high as possible (to maximize the efficiency) for a false-dismissal (false-veto) probability of less than 1%. From this figure, we can see that we expect to get a false-veto probability of around 1% and an efficiency (at least for the type of signals explored so far) of almost 100%.

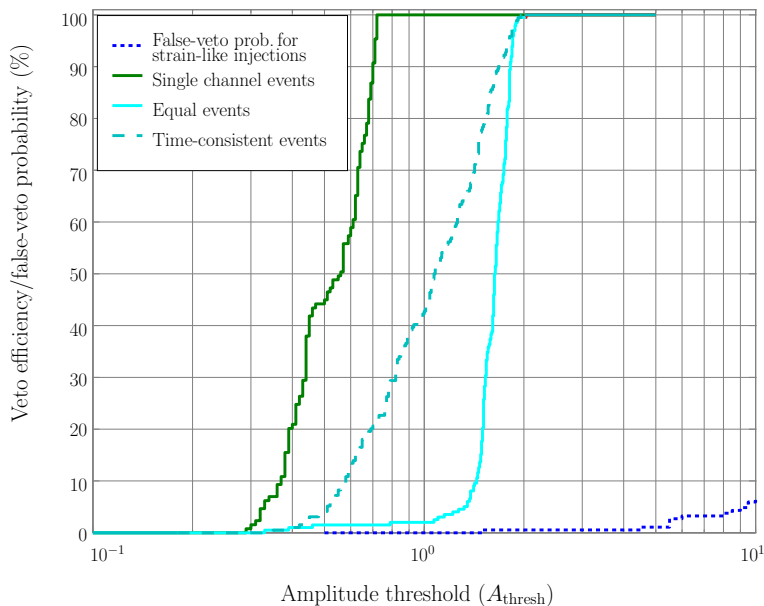


Figure 5.4.: The false-veto and efficiency curves for the null-stream veto. The efficiency curves are computed for different cases of signal injection—see text for details.

5.3.3. Demonstrating veto safety: hardware injections

This section once again demonstrates the *veto safety* by showing that signals consistent with actual gravitational-wave bursts are not vetoed using this method. This is done by performing hardware injections into GEO 600. Sine-Gaussian waveforms were injected into the electrostatic actuators used to control the differential-arm-length degree of freedom of the detector. For the test described here, around 300 sine-Gaussian bursts were injected with varying amplitudes and with central frequencies in the range 200 to 1300 Hz.

Figure 5.5 shows a time-frequency plot of mHACR triggers in $h(t)$ and $h_{\text{null}}(t)$ channels at the time of hardware injections. 302 triggers were detected in channel h and 51 triggers were detected in channel h_{null} . It is evident from the plot that not many injections are detected in h_{null} . Only one trigger is found to be coincident between h and h_{null} using the time and frequency windows described in Section 5.2. The amplitude ratio A_h/A_{null} computed from this set of coincident triggers is 33.9, which is well above the threshold ($A_{\text{thresh}} = 5$) that we chose to veto the triggers. To summarise, none of the triggers from the hardware injections are vetoed, which demonstrates the high safety of the veto.

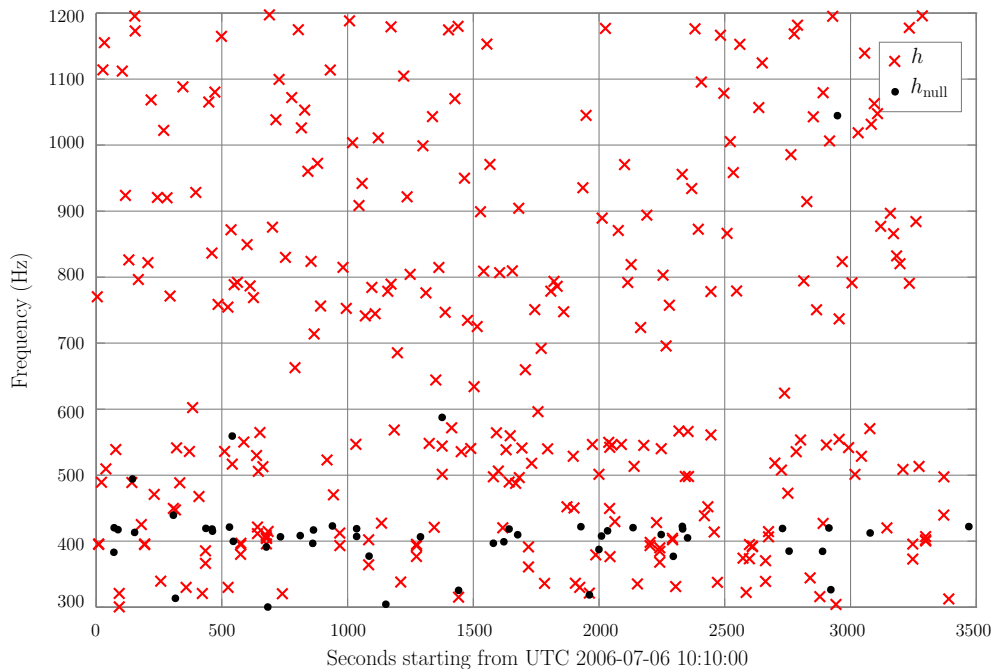


Figure 5.5.: Time-frequency plot of mHACR triggers from hardware injections. The (red) crosses denote burst events in channel h and the (black) dots denote events in channel h_{null} .

5.4. Example application to GEO 600 data

The veto method was applied to a long stretch (22 hours) of calibrated data from GEO 600. For the entire duration, the detector was locked and operating normally.

The mHACR algorithm was run on the $h(t)$ and $h_{\text{null}}(t)$ data streams for this time. A total of 141766 events were found in $h(t)$, 42380 in $h_{\text{null}}(t)$. Of these, 1086 events were found to be time and frequency consistent using the consistency windows described in Section 5.2.

The amplitude consistency veto was applied to these two reduced event lists with a threshold of 5. From this we would expect to falsely veto around 10 events. All 1086 of the time and frequency consistent events were found to be inconsistent in amplitude for being a gravitational wave, and were hence vetoed. Figure 5.6 shows a short section of the events from the 22 hours of data.

We can see immediately that the majority of vetoed events have a central frequency around 370 Hz; this is true for the entire 22 hour data stretch. At this frequency, the output noise of the detector is dominated by features which are believed to be acoustically or seismically driven resonances of some of the optical mounts that steer the output beam to the main output photo-detector. For such events, the veto method seems to be very efficient, as the software injections would suggest.

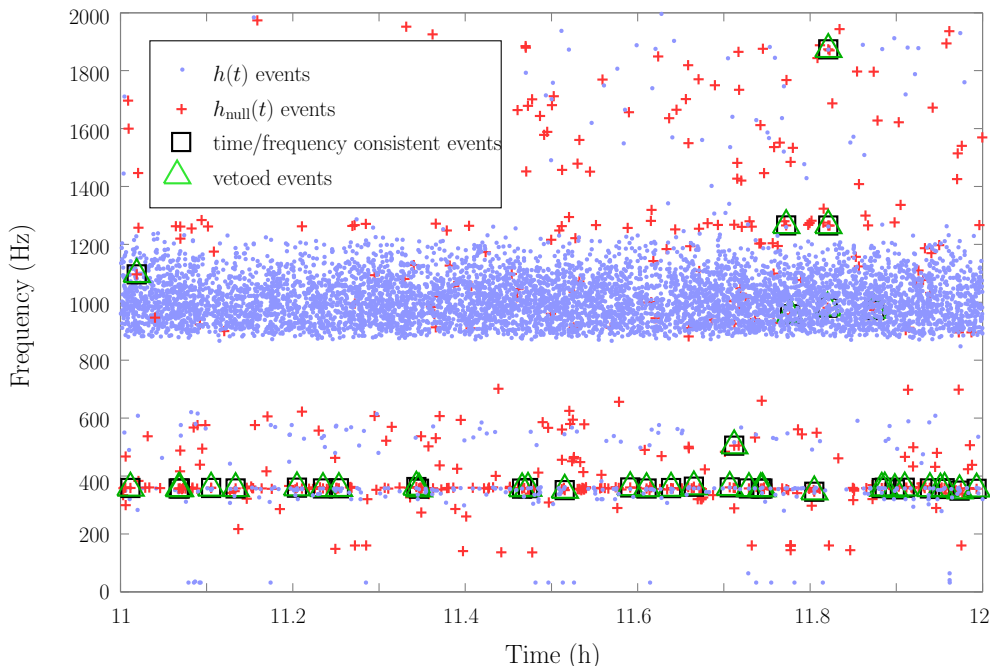


Figure 5.6.: A time-frequency map of the events detected by mHACR in $h(t)$ and $h_{\text{null}}(t)$ for a 1 hour data stretch of GEO 600. Those events that were found to be time and frequency consistent between the two lists are marked with boxes; those that were subsequently vetoed are marked with triangles.

The other (few) events that are vetoed could be false vetoes, although the number of vetoes out-with 370 Hz band suggests that at least some of them are not. In addition, the fact that a large concentration of the events around 1 kHz are detected in $h(t)$ but not in $h_{\text{null}}(t)$ suggests that these instrumental bursts pass through the detector in a similar way to gravitational waves and hence appear with similar amplitudes in the two calibrated output streams (most probably frequency noise originating in the laser subsystem).

5.5. Summary

The null-stream output of GEO 600 has been used to generate a list of transient events that can be used to veto those events detected in the main strain output of GEO 600. By using software injections, an amplitude-ratio threshold has been determined that can be used to compare the amplitude of events in the $h(t)$ data stream to those events detected in the null stream. Software injections which are *inconsistent* with gravitational-wave bursts are performed, and events that were found to be time and frequency consistent in the two event lists could be vetoed with $\sim 100\%$ efficiency for a false-veto probability of 1%. The veto safety is demonstrated by performing hardware injections mimicking actual gravitational-wave bursts into GEO 600, and by showing that the injections are

not vetoed. In addition, this method was applied to a short section of the detector data and it was possible to veto a significant fraction of events that appeared clustered around 370 Hz in the detector output.

One possible way to improve the performance of this method would be to have a threshold that is frequency-dependent. Currently, the relative calibration accuracy of the two detector outputs is different for different frequencies, varying from about 20% at low frequencies, to around 5% at high frequencies. This means that the suppression of gravitational wave events in the null stream, and hence the threshold needed to robustly test them, is also a function of frequency.

While the results presented in this chapter are based on the trigger events produced by the mHACR algorithm, the principles should apply for any algorithm used to generate the event lists. However, it is clear that the chosen amplitude consistency threshold may be different when different trigger generation algorithms are used.

Part II.

Data analysis for coalescing compact binaries and unmodelled-burst sources

6. Null-stream veto for two co-located detectors

6.1. Introduction

Given the time-series data from a network of gravitational-wave (GW) detectors, one can find a particular linear combination of the data streams such that it does not contain any trace of GWs. The idea of this *null stream* was proposed by Gürsel and Tinto in their classic work [146]. Gürsel and Tinto proposed that the null stream can be used to solve the ‘inverse problem’ of GW bursts, i.e., to compute the unknown quantities (two sky positions and two polarizations) associated with the gravitational waveform from the responses of three broad-band detectors.

Recently, there has been a lot of interest in the null stream in the GW community. The main reason for this rejuvenated interest is that the first generation of ground-based interferometric GW detectors [7, 8, 9, 10] have started acquiring scientifically interesting data. Among the most promising astrophysical sources of GWs for these ground-based detectors are the transient, unmodelled astrophysical phenomena like supernovae explosions, Gamma-ray bursts and black hole/neutron star mergers – popularly known as ‘unmodelled bursts’. Most of the algorithms currently used in burst searches are time-frequency detection algorithms that look for short-lived excitations of power in the ‘time-frequency map’ constructed from the data [114, 116, 117]. Since present-day interferometric GW detectors are highly complex instruments, the data often contains lots of noise transients which trigger the burst detection algorithms. It is almost impossible to distinguish these spurious instrumental bursts from actual GW bursts using any physical model of the GW bursts. Thus, burst data analysis is usually performed as a coincidence analysis between multiple detectors. Although this ‘coincidence requirement’ considerably reduces the list of candidate burst triggers, one month of data can potentially produce hundreds of multi-detector random coincidences. So, it becomes absolutely necessary to have additional ‘waveform consistency tests’ that distinguish actual GW bursts from noise transients. A cross-correlation statistic that is formulated in [125] is already being used as a coherent waveform consistency test in the search for GW bursts in the data of LIGO detectors. This is making use of the fact that all the LIGO detectors are (approximately) aligned parallel to each other.

Recently, it was proposed by Wen and Schutz [126] that the null stream can be used to distinguish between actual GW triggers and spurious noise transients in a search for GW bursts using any general network of detectors. The main idea is that, if the

coincident triggers correspond to an actual GW burst, the null stream constructed at the time of the triggers will contain no trace of the burst, and, will fall into an expected noise distribution. On the other hand, if the coincident triggers correspond to spurious instrumental bursts, the bursts will not necessarily cancel out in the null stream, and the null stream will contain some excess power. Many authors have proposed similar, but non-equivalent ways of implementing this. The veto method described in this chapter is based on the *excess power* statistic [114], which was first used by [126] in this context. For an alternative implementation, see [127]. A similar veto strategy using the null stream constructed from the two calibrated output quadratures of GEO 600 [9] detector is already being used to veto the burst triggers from GEO 600. This is discussed in Chapter 5 of this thesis.

It was soon realised that the biggest source of error in the null-stream analysis comes from the fact that the detector data are *not* perfectly calibrated, for various technical reasons. In such cases, the null stream constructed from the data containing actual GW bursts will contain some residual signal and will deviate from the expected noise distribution. This chapter tries to address such practical issues connected with the implementation of the null-stream veto in the burst-data-analysis using a network consisting of two co-located interferometric detectors, like the two LIGO detectors [7] in Hanford, WA, USA. The detectors are assumed to have calibration uncertainties and correlated noise components. Section 6.2 briefly reviews the veto method in the case of two co-located detectors. In Section 6.3, we estimate the effect of calibration uncertainties in the null-stream veto, and in Section 6.3, we lay out and demonstrate a formulation to overcome this effect. An example application of the veto into the data of LIGO Hanford detectors is described in Section 6.4 ¹.

6.2. The null-stream veto

In the case of detectors placed widely apart, the null stream is a function of the antenna patterns, and hence, the source-position [146]. But in the case of two co-located detectors, the null stream is particularly simple. If $h_1(t)$ and $h_2(t)$ denote the properly calibrated time-series data from the two detectors, the null stream is just [126]:

$$n(t) = h_1(t) - h_2(t), \quad (6.1)$$

or, in discrete notation

$$n_j = h_{1j} - h_{2j}, \quad (6.2)$$

where h_{1j} and h_{2j} are the discretely sampled versions of $h_1(t)$ and $h_2(t)$. At the time of a set of coincident triggers, we construct the null-stream n_j . Let \tilde{N}_k denote the discrete Fourier transform (DFT) of n_j computed using L samples of the data. We assume that the real and imaginary parts of \tilde{N}_k are drawn from a multivariate Gaussian distribution

¹These results are not fully reviewed by the LIGO Scientific Collaboration.

of mean zero ² and variance σ_k^2 . Following [114, 126], we compute the excess power statistic from the null-stream:

$$\epsilon = \sum_{k=m}^{m+M} P_k, P_k = \frac{|\tilde{N}_k|^2}{\sigma_k^2}. \quad (6.3)$$

It can be shown that ϵ will follow a χ^2 distribution of $2M$ degrees of freedom in the case of a non-windowed DFT. But in the case of a windowed DFT, P_k are not *independent* χ^2 variables, and hence ϵ will *not* follow a χ^2 distribution [156]. But, we note that the χ^2 distribution is a special case of the Gamma distribution. It can be shown that, to a very good approximation, ϵ will follow a Gamma distribution with scale parameter α and shape parameter β . These parameters are related to the mean μ_ϵ and variance σ_ϵ^2 of the distribution of ϵ by

$$\alpha = \left(\frac{\mu_\epsilon}{\sigma_\epsilon}\right)^2, \quad \beta = \frac{\sigma_\epsilon^2}{\mu_\epsilon}. \quad (6.4)$$

In order to estimate the parameters of the expected Gamma distribution, we generate a population of ϵ from stationary data (i.e., data not containing the burst event under investigation, but surrounding it). To be explicit, we divide the data in to a number of segments each length L and compute ϵ from each of these segments. From that population, μ_ϵ and σ_ϵ^2 can be estimated, and hence α and β .

It is known that the maximum signal-to-noise ratio (SNR) for the excess power statistic is achieved when the time-frequency volume used to compute the statistic is equal to the actual time-frequency volume of the signal [114]. Since the duration and bandwidth of the burst is estimated by the burst detection algorithm itself, this information is used to decide on the length (L) of the data used to compute \tilde{N}_k and the bandwidth over which P_k is summed over.

If the ϵ computed from the segment containing the burst is greater than a threshold, we veto the trigger. The threshold, τ , giving a false-dismissal (‘false-veto’) probability of γ can be found from

$$\gamma = \int_\tau^\infty f(x; \alpha, \beta) dx, \quad (6.5)$$

where $f(x; \alpha, \beta)$ is the probability density of the Gamma distribution with parameters α and β .

6.2.1. Software injections

Let us define some terminology. The false-dismissal probability is the *probability* of an actual GW burst being falsely vetoed, and the ‘false-veto fraction’ is the fraction of GW bursts that are *actually* vetoed using this method. As a sanity check, we estimate the false-veto fraction by injecting some prototype gravitational waveforms into two data

²If the real and imaginary parts of \tilde{N}_k are drawn from a non-zero-mean Gaussian distribution, one can always convert them to mean-zero Gaussian variables by subtracting the sample mean μ_k from them.

streams of Gaussian white noise and by performing the analysis. If all of our assumptions are true, the fraction of vetoed events among the injections should be equal to the chosen false-dismissal probability.

The injected waveforms are Gaussian-modulated sinusoidal waveforms, of the form:

$$\hat{h}(t) = \hat{h}_{\text{RSS}} \left(\frac{2f_0^2}{\pi} \right)^{1/4} \sin [2\pi f_0(t - t_0)] \exp [-(t - t_0)^2/\tau^2], \quad (6.6)$$

where f_0 is the central frequency of the waveform (randomly chosen from the set $\{153, 235, 361, 554, 849, 1053, 1245, 1534, 1856\}$ Hz) and t_0 is the time corresponding to the peak amplitude. We setup the envelope width as $\tau = 2/f_0$, which gives durations of approximately 1-20 ms. The corresponding quality factor is $Q \equiv \sqrt{2}\pi f_0\tau = 8.9$ and the bandwidth is $\Delta f = f_0/Q \simeq 0.1f_0$. The quantity \hat{h}_{RSS} is the root-sum-squared (RSS) amplitude:

$$\left[\int_{-\infty}^{\infty} \hat{h}^2(t) dt \right]^{1/2} = \hat{h}_{\text{RSS}}. \quad (6.7)$$

The \hat{h}_{RSS} is randomly chosen from the logarithmically-spaced interval $(5 \times 10^{-22}, 1 \times 10^{-19})$. The amplitude spectral density (ASD) of the noise in the two data streams is chosen to be $1 \times 10^{-22}/\sqrt{\text{Hz}}$ and $2 \times 10^{-22}/\sqrt{\text{Hz}}$ ³. We define the combined SNR, ρ , by

$$\rho^2 = \rho_1^2 + \rho_2^2, \quad (6.8)$$

where ρ_1 and ρ_2 are the optimal SNRs⁴ in detecting the bursts in the two data streams, and quote this quantity while discussing the results.

The veto analysis is performed with different thresholds. The fraction of vetoed events is plotted against the false-dismissal probability corresponding to the chosen threshold in Figure 6.1 (left). It can be seen that the estimated false-veto fraction is in very good agreement with the predicted false-dismissal probability.

6.3. Calibration uncertainties

So far, we have been assuming that the two data streams are perfectly calibrated. But, due to various limitations in the calibration procedure, the calibration of present-day interferometers can be subject to uncertainties of a few percent in amplitude and a few degrees in phase. This means that the null stream constructed from the data containing actual GW triggers can contain some residual signal, and the computed statistic can vary from the expected distribution. This will result in a different false-dismissal probability than the one predicted by the hypothesis test.

³These values roughly correspond to the sensitivities of the two LIGO detectors in Hanford.

⁴The optimal SNR, ρ , in detecting a signal $h(t)$ buried in the noise is defined by $\rho^2 = 4 \int_0^\infty |\tilde{H}(f)|^2 df / S_n(f)$ where $\tilde{H}(f)$ is the Fourier transform of the signal and $S_n(f)$ is the one-sided PSD of the detector noise.

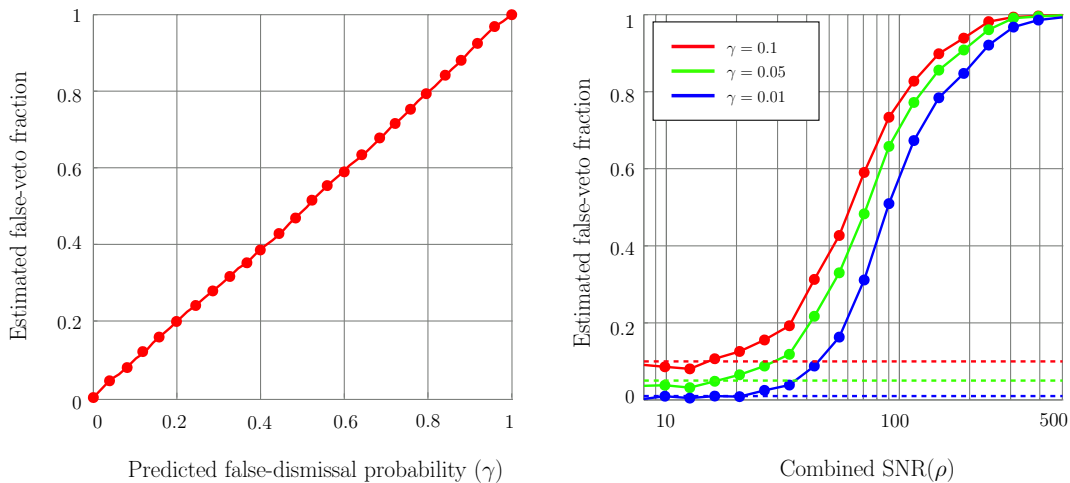


Figure 6.1.: [*Left*]: Estimated false-veto fraction plotted against the predicted false-dismissal probability, assuming that the two detectors are perfectly calibrated. [*Right*]: Estimated false-veto fraction in the presence of $\pm 10\%$ calibration uncertainty, plotted against the combined SNR of the injections, for three different values of the predicted false-dismissal probability (γ). The three dashed lines show the predicted values of the false-dismissal probability in the absence of calibration uncertainties.

It can be shown that we see approximately the same residual signal power in the null stream for both a 10% relative amplitude error and a 10 degree relative phase error; therefore, in principle, we need to consider both of these effects. However, it is not easy to conceive of a simple model for the possible relative phase error between two co-located detectors (since such errors most probably arise due to inaccuracies in the calibration process and will therefore be frequency dependent)⁵. It is, however, easy to think of a simple model for one possible source of relative amplitude calibration error. Suppose we know the absolute calibration of each detector to some accuracy. If the two detectors have identical optical configurations and if they are calibrated using similar methods, it is quite possible that the relative calibration error between the two detectors will be independent of frequency. We explore a way to deal with this type of error in the rest of this chapter.

As a simple model, we assume that the frequency-dependence of the calibration error is negligible, and that the calibration error is a constant scaling factor over short time-scales (of the order of seconds). In the context of this analysis, we can assume that one detector is perfectly calibrated and the other is calibrated with a wrong scaling factor,

⁵One another possible source of relative phase error would be a time-offset between the two data streams. Although it is unlikely that such an error exists at any significant level, it would be possible to include this in the following analysis if necessary.

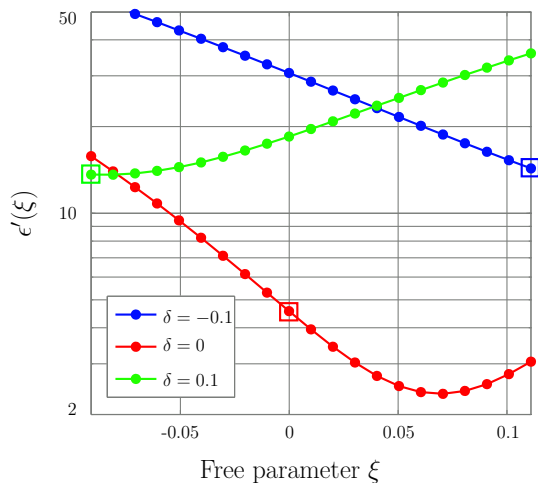


Figure 6.2.: The excess-power statistic $\epsilon'(\xi)$ constructed from null stream $n'(t; \xi)$ plotted against the free parameter ξ , for three different values of δ . We assume that the maximum expected absolute value of δ is 0.1. $\epsilon'(-\delta/(1+\delta))$ for each curve is marked with a square. It can be seen that the minimum value of $\epsilon'(\xi)$ is less than, or equal to $\epsilon'(-\delta/(1+\delta))$.

i.e.,

$$\begin{aligned} h_1(t) &= n_1(t) + \hat{h}(t), \\ h_2(t) &= n_2(t) + (1 + \delta) \hat{h}(t), \end{aligned} \quad (6.9)$$

where $n_1(t)$ and $n_2(t)$ are the detector noises in which a gravitational waveform $\hat{h}(t)$ is present. δ is the relative calibration error which is assumed to be a real quantity and is constant over short time-scales.

In order to estimate the effect of calibration error in the false-dismissal probability, injections are done simulating a relative calibration error of $\delta = \pm 0.1$ between the two data streams. The fraction of the vetoed events among the injections is shown in the right plot of Figure 6.1 as a function of the combined SNR of the injections. Different curves in the plot represent three different values of the predicted false-dismissal probability (γ). It can be seen that the estimated false-veto fraction raises to alarmingly high values for strong signals.

6.3.1. Dealing with calibration uncertainties

In this section we formulate a strategy to reduce the effect of calibration errors in the false-dismissal probability. We construct the following linear combination of the data streams by introducing a free parameter, ξ , in the null-stream construction, i.e.,

$$n'(t; \xi) = h_1(t) - (1 + \xi) h_2(t). \quad (6.10)$$

Substituting for $h_1(t)$ and $h_2(t)$ from Eq.(6.9) gives,

$$n'(t; \xi) = n(t; \xi) - (\delta + \xi + \xi \delta) \hat{h}(t), \quad (6.11)$$

where

$$n(t; \xi) = n_1(t) - (1 + \xi) n_2(t), \quad (6.12)$$

is the ‘perfect’ null stream. We can ‘tune’ the parameter ξ such that the residual signal disappears in Eq.(6.11). This is accomplished by minimizing the ‘excess power’ in $n'(t; \xi)$ by varying ξ over an interval.

As described in Section 6.2, the null stream $n(t; \xi)$ is divided into a number of short segments and the DFT of each segment is computed. It may be noted that in all segments except the one containing the burst, $n'(t; \xi) = n(t; \xi)$, because the signal is absent in these segments. We denote the DFT of $n(t; \xi)$ and $n'(t; \xi)$ by $\tilde{N}_k(\xi)$ and $\tilde{N}'_k(\xi)$, respectively. The mean, $\mu_k(\xi)$, and variance, $\sigma_k^2(\xi)$, of $\tilde{N}_k(\xi)$ are estimated from the neighboring segments of the one containing the burst. These are the moments of the expected distribution of $\tilde{N}'_k(\xi)$ *in the absence of the burst*. $\tilde{N}_k(\xi)$ is converted to a mean-zero Gaussian variable by subtracting the sample mean $\mu_k(\xi)$ from it. The test statistic $\epsilon'(\xi)$ is computed from the segment of $n'(t; \xi)$ containing the burst:

$$\epsilon'(\xi) = \sum_{k=m}^{m+M} P'_k(\xi), \quad P'_k(\xi) = \frac{|\tilde{N}'_k(\xi)|^2}{\sigma_k^2(\xi)}. \quad (6.13)$$

We minimize $\epsilon'(\xi)$ by varying ξ over an interval (ξ_{\min}, ξ_{\max}) ⁶. The boundary of the parameter-space can be fixed as

$$\xi_{\min} = \frac{-\delta_{\max}}{1 + \delta_{\max}}, \quad \xi_{\max} = \frac{\delta_{\max}}{1 - \delta_{\max}}, \quad (6.14)$$

where $\pm\delta_{\max}$ is the maximum expected value of the calibration uncertainty. When $\xi \rightarrow -\delta/(1 + \delta)$, the residual signal in the null stream cancels out, and $\epsilon'(\xi) \rightarrow \epsilon(\xi)$, where

$$\epsilon(\xi) = \sum_{k=m}^{m+M} P_k(\xi), \quad P_k(\xi) = \frac{|\tilde{N}_k(\xi)|^2}{\sigma_k^2(\xi)}, \quad (6.15)$$

which falls in to an expected Gamma distribution in the case of GW bursts.

Since ϵ is quadratic in \tilde{N}'_k , apart from $|\tilde{N}_k|^2$ and $|(\delta + \xi + \xi \delta) \hat{H}_k|^2$, it contains also the cross-terms. This means that the minimum value of $\epsilon'(\xi)$ could be less than $\epsilon(\xi)$. This is illustrated in Figure 6.2, for three different values of δ . Thus, the obtained false-dismissal probability could be less than what is predicted by the hypothesis test. Since the cross-terms depend upon the actual value of δ , this adds an error-bar to the false-dismissal probability. *But it may be noted that the actual false-dismissal probability is always less than (or equal to) what is predicted by the hypothesis test.*

⁶It is important to note that we minimise the *excess-power*, $\epsilon'(\xi)$, in the null stream, and not the *total power*, $n'^2(t; \xi)$. In the later case, if there are correlated noise in $h_1(t)$ and $h_2(t)$, ξ can take values which will minimise the correlated noise components in $n'(t; \xi)$ instead of the residual signal.

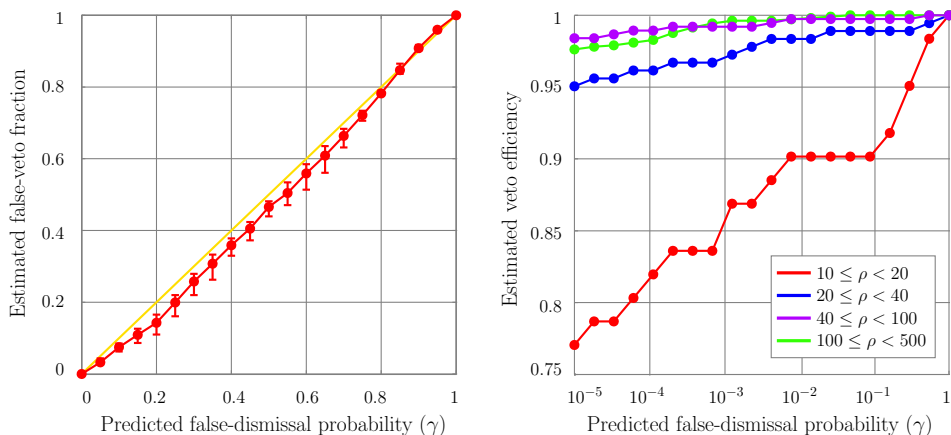


Figure 6.3.: [Left]: Estimated false-veto fraction plotted against the predicted false-dismissal probability. The relative calibration between $h_1(t)$ and $h_2(t)$ is assumed to be between $-0.1 \leq \delta \leq 0.1$. [Right]: Rejection power of the veto plotted against the predicted false-dismissal probability. Each curve in the plot corresponds to a particular range of SNR.

6.3.2. Software injections with simulated calibration errors

We generate two data streams with a simulated relative calibration error δ according to Eq.(6.9) and perform the veto analysis, assuming that $|\delta_{\max}| = 0.1$. The minimisation of $\epsilon(\xi)$ is carried out using an optimised minimisation algorithm. The analysis is performed for three different values (-0.1, 0, 0.1) of δ and the false-veto fractions corresponding to different thresholds are estimated in each case (in all cases, we assumed that $|\delta_{\max}| = 0.1$). The mean value (among the three simulations) of the false-veto fraction corresponding to each threshold is plotted against the corresponding false-dismissal probability in Figure 6.3 (left). The extremum values corresponding to each threshold are used to generate the error-bars. It can be seen that the estimated false-veto fraction is always less than or equal to the predicted false-dismissal probability.

The real figure-of-merit of a veto method is its ability to reject spurious events with a given false-dismissal probability. But, given that the probability density of the noise transients are not known *a priori*, there is no rigorous way of estimating the ‘rejection power’ of the veto. The best we can do is to estimate the ability of the veto to reject a given glitch population. As a plausible estimation, we inject a population of sine-Gaussian waveforms with random parameters into two data streams. We then perform the veto analysis after choosing different thresholds. The estimated rejection power is plotted against the false-dismissal probability in Figure 6.3 (right). Since the ‘excess power’ in the null stream is proportional to the individual SNRs of the bursts in the two data streams, the rejection power is also proportional to the SNR. Each curve in the figure corresponds to a particular range of SNR ρ (see Eq.(6.8)). This suggests that veto efficiencies of $\geq 90\%$ can be achieved with a false-dismissal probability of $\simeq 1\%$ for spurious noise transients with $\rho \geq 10$.

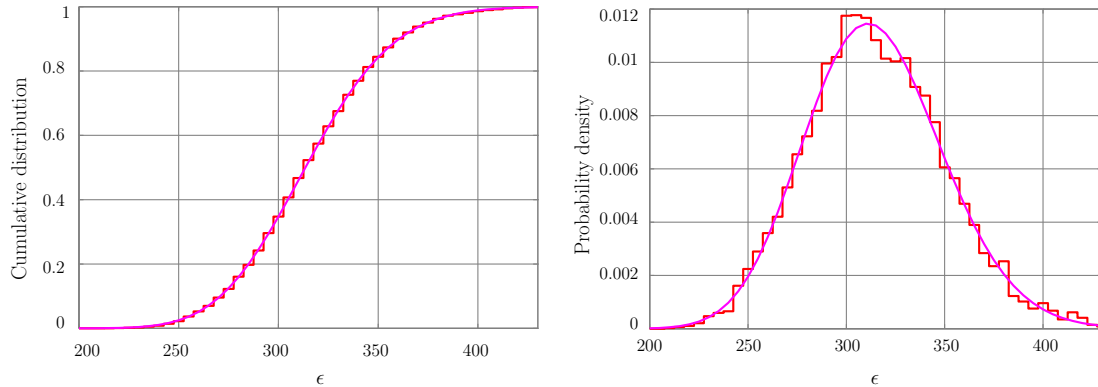


Figure 6.4.: Cumulative distribution (left) and the probability density (right) of the test statistic ϵ calculated from H1-H2 playground data. Also shown are the cumulative distribution (left) and probability density (right) of the expected Gamma distribution. These correspond to injections performed with no calibration errors.

6.4. Example application to LIGO data

This section presents an application of the null-stream veto method to the data of the two co-located LIGO detectors (henceforth, H1 and H2) in Hanford. Data used in this analysis was taken as part of the Fourth Science Run (S4) of the LIGO detectors. Software injections performed on the ‘playground data’ in order to verify the method are presented first. Then we proceed to describe the veto analysis performed on the triggers generated by the *Waveburst* event trigger generator [117], and summarize the main results.

6.4.1. Data conditioning

The $h(t)$ data from the LIGO detectors contains a large amount of low-frequency noise which can cause a huge amount of spectral leakage when the DFT is computed from short chunks of data (say, 32 ms). In order to minimize this effect, the data is whitened using a 6th order high-pass filter before computing the DFT. An Infinite Impulse Response filter of order 6 is applied to the data with corner frequency 64 Hz. Apart from this, 11 ‘notch’ filters are applied in order to suppress strong spectral lines in the data. These narrow-band filters are applied at frequencies where strong spectral lines are present, i.e., at 18, 30, 36, 60, 180, 344, 349, 688, 698, 1144 and 1160 Hz.

6.4.2. Software injections

The first set of injections is performed assuming *no* calibration error, i.e., we assume that the detector data is perfectly calibrated so that the two data streams contain

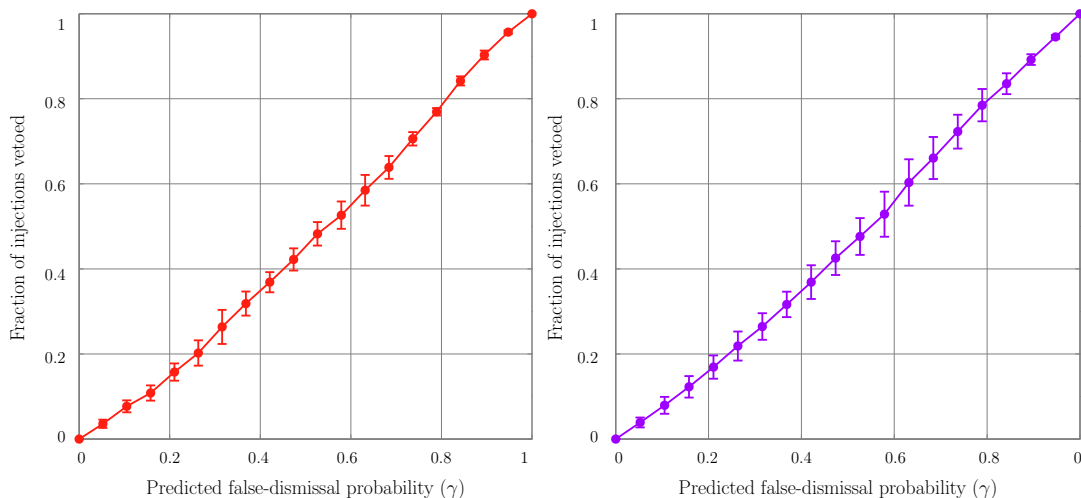


Figure 6.5.: Left panel shows the fraction of vetoed sine-Gaussian injections plotted against the predicted false-veto probability. Right panel shows the same plot using band-limited white-noise burst injections. The injections are done simulating a relative calibration error $-0.1 \leq \delta \leq 0.1$.

exactly the same signal. The injections are done in S4 playground data using sine-Gaussian waveforms and band-limited white-noise bursts (BLWNB). Parameters chosen for the sine-Gaussian injections are specified in Section 6.2.1. The parameter range of the central frequency and h_{rss} of the BLWNB injections are chosen to be same as in the case of sine-Gaussian injections. Duration and bandwidth are chosen to be $2/f_0$ s and $f_0/10$ Hz, respectively. For this set of injections, a fixed number of frequency bins (M in Eq.(6.15)) are used to calculate the excess-power statistic so that the parameters of the expected Gamma distribution remain the same for all the injections.

Null stream is constructed as per Eq.(6.1) and the excess-power statistic ϵ is computed using Eq.(6.15). Figure 6.4 shows the cumulative distribution (left) and probability density (right) of the distribution of ϵ computed from the sine-Gaussian injections. The cumulative distribution and probability density of the expected Gamma distribution are overlaid in the plots. This verifies that the test statistic falls into the expected distribution in the absence of calibration errors.

Now we proceed to do another set of injections mimicking the calibration errors. Two data streams are generated with a simulated relative calibration error δ according to Eq.(6.9). Veto analysis described in Section 6.3 is performed assuming a maximum (unknown) calibration error $|\delta_{\text{max}}| = 0.1$. Injections are performed with three different values (-0.1, 0, 0.1) of δ and the false-veto fractions corresponding to different thresholds are estimated in each case (assuming $|\delta_{\text{max}}| = 0.1$ in all cases). The mean value (among the three set of injections) of the false-veto fraction is plotted against the corresponding false-dismissal probability in Figure 6.5. The left panel corresponds to the sine-Gaussian injections and the right panel corresponds to the band-limited white-noise

burst injections. In each panel, the extremum values (among the three set of injections) of false-veto fraction corresponding to each threshold are used to generate the error-bars. This again verifies that the estimated false-veto fraction is always less than or equal to the predicted false-dismissal probability.

6.4.3. Null-stream veto analysis on *Waveburst* triggers

Null-stream veto analysis was performed on S4 Waveburst triggers produced in the LIGO-only search, assuming a relative calibration error of $\epsilon = \pm 10\%$ between $h_1(t)$ and $h_2(t)$. Only those triggers which are found to be coincident in the *time-shifted* analysis were used for the veto analysis (the ‘*background*’ triggers). Parameters of the expected Gamma distribution are estimated from 64 seconds of data around the trigger-centers. Data conditioning was done as described in Section 6.4.1.

Out of 3659 coincident triggers in the background, 69% was vetoed using the null-stream method with a false-dismissal probability of 1%. Figure 6.6 makes a rough comparison of the efficiency of the null-stream veto with the ‘H1-H2 amplitude cut’ [72]. In the latter method, all the triggers with amplitude ratio $h_{\text{RSS}1}/h_{\text{RSS}2}$ greater than 2 or less than 0.5 are vetoed (where $h_{\text{RSS}1}$ and $h_{\text{RSS}2}$ are the RSS amplitudes of the triggers in H1 and H2, respectively) because they are highly inconsistent with the expectation from actual GW signals⁷. The horizontal axis of Figure 6.6 reports the false-dismissal probability γ with which the coincident triggers are vetoed using the null-stream method while the vertical axis reports the H1-H2 amplitude ratio. The (red) dashed vertical line corresponds to $\gamma = 1\%$, which means that the triggers on the left of this line can be vetoed with $\gamma < 1\%$. The (green) horizontal lines correspond to the amplitude ratios 0.5 and 2. Triggers with amplitude ratio less than 0.5 and greater than 2 are vetoed using the amplitude cut. Out of the 3659 coincident triggers, 53% are vetoed using the amplitude cut. 41% of the triggers are vetoed by both methods and 81% are vetoed by either of these methods.

This preliminary comparison is only done for illustrative purpose. The reader is warned that the veto efficiencies of the two methods quoted here may not be compared directly. The amplitude cuts chosen here need not correspond to a false-dismissal probability of 1%, the chosen value for the null-stream analysis.

6.5. Summary

The null-stream constructed from the data of multiple GW detectors can be used to distinguish between actual GW triggers and spurious noise transients in the search for GW bursts using a network of detectors. The biggest source of error in the analysis comes from the fact that the present-day detectors are subject to calibration uncertainties. In this chapter we have proposed an implementation of the null-stream veto in the search for GW bursts in the data of two co-located interferometers. We estimated the effect

⁷For actual GW signals, we expect that $h_{\text{RSS}1}/h_{\text{RSS}2} \simeq 1$.

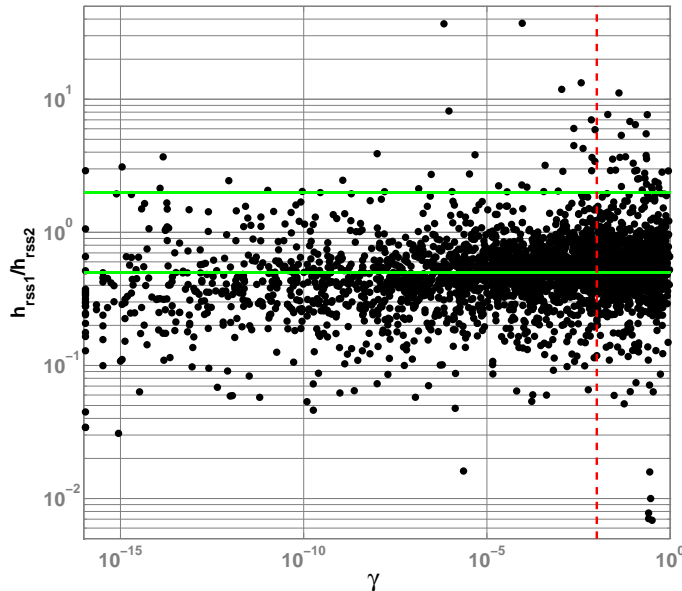


Figure 6.6.: Comparison of the null-stream veto analysis with the H1-H2 amplitude cut. The horizontal axis shows the false-dismissal probability of the null-stream in vetoing the coincident triggers, while the vertical axis shows the ratio of the h_{rss} of the coincident triggers in H1 and H2. The (red) dashed vertical line corresponds to a false-dismissal probability γ of 1%, and the triggers on the left of this line can be vetoed with $\gamma < 1\%$. The (green) horizontal lines correspond to the amplitude ratios ($h_{\text{rss}1}/h_{\text{rss}2}$) 0.5 and 2. Triggers with amplitude ratio less than 0.5 and greater than 2 are vetoed using the amplitude cut.

of calibration uncertainties in the veto analysis by performing software injections in Gaussian noise with simulated calibration errors. A strategy is proposed to minimize this effect, assuming a simple model for the amplitude calibration-error and neglecting the errors in the phase calibration. This is done by introducing an additional free parameter in the null-stream combination and minimizing the excess-power in the null-stream. We compared the estimated fraction of falsely-vetoed GW-like injections with the predicted false-dismissal probability and found that the estimated fraction has a good agreement with the prediction. We also estimated the rejection power of the veto as a function of the false-dismissal probability by injecting random waveforms into the two data streams. Finally, an example application of the veto method to the data of the two co-located LIGO detectors in Hanford is presented.

7. A template bank for gravitational waveforms from coalescing binary black holes

7.1. Introduction

As discussed in Chapter 1, among the most promising sources detectable by the ground-based gravitational-wave (GW) observatories are coalescing compact binaries consisting of black holes (BHs) and/or neutron stars spiraling toward each other as they lose orbital energy and angular momentum through gravitational-wave emission. The gravitational-wave signal from coalescing binaries is conventionally split into three parts: inspiral, merger and ring down. In the first stage, the two compact objects, usually treated as point masses, move in quasi-circular orbits (eccentricity, if present initially, is quickly radiated away). This part of the waveform is described very well by the post-Newtonian (PN) approximation of general relativity. In this approximation the Einstein equations are solved in the near zone (which contains the source) using an expansion in terms of the (small) velocity of the point masses. In the far zone, the vacuum equations are solved assuming weak gravitational fields, and these two solutions are matched in the intermediate region [88, 89, 90].

The PN approximation breaks down as the two compact objects approach the ultra-relativistic regime and eventually merge with each other. Although various resummation methods, such as Padé [167] and effective-one-body (EOB) approaches [168], have been developed to extend the validity of the PN approximation, unambiguous waveforms in the merger stage must be calculated numerically in full general relativity. Recent breakthroughs in numerical relativity [93, 94, 95] have allowed many groups [93, 94, 95, 169, 170, 171, 172, 173] to evolve BH binaries fully numerically for the last several orbits through the plunge to single BH formation. The field is now rapidly developing the capability to routinely evolve generic black-hole binary configurations in the comparable-mass regime, and to accurately extract the gravitational-wave signal. Important milestones include simulations of unequal-mass binaries and calculations of the gravitational recoil effect and the evolution of black-hole binaries with spin [174, 175, 176, 177, 178, 179, 180, 181, 182, 183, 184].

Comparisons with post-Newtonian results are essential for data analysis efforts, and several groups have published results showing good agreement of various aspects of non-spinning simulations with post-Newtonian predictions (see e.g. [185, 186, 187, 188,

189, 190, 191, 192]), and first results for certain configurations with spin have also become available [193, 194]. In order to overcome phase inaccuracies in long evolutions, significant progress has been made by the Caltech-Cornell group using spectral codes [195, 196], and by the Jena group using higher (sixth) order finite differencing [197]. Methods to reduce the eccentricity to around 10^{-3} (so far only for equal-mass binaries) have been presented by the Caltech-Cornell group [196], and the Jena group [198] (using initial parameters from PN solutions that take into account radiation reaction). Current numerical waveforms can be generated for the last ($\lesssim 10$) orbits, and these waveforms can be joined continuously with analytic PN inspiral waveforms to obtain one full signal. This was done in [187, 189, 190, 199]. Indeed, there are no fundamental obstructions to generating the whole waveform, including long inspiral over hundreds of orbits, by solving the full Einstein equations numerically. But, not only would this be computationally prohibitive with current methods, it is also unnecessary: the PN formalism is known to work very well in the weak-field regime (when the BHs are well-separated), and is a low-cost and perfectly adequate substitute to fully general relativistic solutions in that regime.

The numerically generated part of the gravitational-wave signal from coalescing binaries also includes the final stage of the coalescence, when a single perturbed black hole is formed and it rapidly loses its deviations from a Kerr black hole via gravitational waves. This part of the signal can be decomposed as a superposition of exponentially damped modes, and is called quasi-normal mode ‘ring down’, by analogy with the vibrations of a bell. The detectable part of the ring down is rather short and only a few modes (if not only the dominant one) are expected to be important/detectable by initial ground-based observatories. This will not be true, however, for the advanced detectors [200] and certainly it is not the case for LISA, the planned space-borne gravitational-wave observatory. Indeed, the majority of the signal-to-noise ratio (SNR) comes from the quasi-normal mode ringing of binary systems with a total mass above a few $10^6 M_{\odot}$ [35]. For LISA, and also perhaps for the next generation of ground based detectors, it will be possible to detect several quasi-normal modes and test the ‘no hair’ theorem, according to which all modes are functions of a BH’s mass and spin [33, 34, 35].

Joining analytically modeled inspiral with numerically generated merger and ring down allows us to produce the complete gravitational-wave signal from coalescing binaries, and to use it in the analysis of detector data. There are several benefits to using the whole signal in searches. The most obvious one is the increase in SNR in a fully coherent matched filtering search. Increase in SNR implies increase in the event rate and improvement in the parameter estimation. Including the inspiral, merger and ring down parts in a template waveform also means that the waveform has a more complex structure. This extra complexity will also bring about some improvement in the parameter estimation [201] and possibly also a reduction in the false alarm rate in analysis of the data from the ground-based network of detectors. This is because it is in general harder for the noise to mimic a complex signal¹. For LISA, the detection of inspiralling

¹At least we expect this to happen for those binaries for which both the inspiral and the merger contribute significantly to SNR.

super-massive black holes is not a problem; the SNR is expected to be so large that we expect some signals to be visible by eye in LISA data. However, using the full signal for LISA data analysis is equally important because the full signal is essential in estimating parameters of the binary with the required accuracy. This is important not only from the astrophysical point of view, but also because we need to subtract loud signals from the data in order to detect/analyze other signals. Imperfect signal removal due to errors in the parameter estimation will result in large residuals and will adversely affect subsequent analyses. Improved parameter estimation will also enable GW observations (in conjunction with electromagnetic observations) to constrain important cosmological parameters, most importantly the equation of state of dark energy [202, 201].

7.1.1. Summary and organisation of this chapter

The numerical waveforms described above are still computationally expensive and cannot be used directly to densely cover the parameter space of the binary BHs that will be searched over by matched filtering techniques. A promising alternative is to use the post-Newtonian and numerical-relativity waveforms to construct an analytic model that sufficiently accurately mimics a true signal [190, 199]. This chapter proposes a two-parameter family of template waveforms which can match physical signals from non-spinning binaries in quasi-circular orbits with fitting factors above 99%. These waveforms are explicitly parametrized by the physical parameters of the binary. This two-dimensional template family is shown to be not only ‘*effectual*’ in detecting the signals from binary BH coalescences, but also ‘*faithful*’ in estimating the parameters of the binary. This family of template waveforms can be used to densely cover the parameter space of the binary, thus avoiding the computational burden of generating numerical waveforms in each grid point in the parameter space. The effectualness and faithfulness (see Section 7.3 for definitions) of the template family are computed in the context of three different ground-based detectors: namely, Initial LIGO, Virgo and Advanced LIGO. We also compare the sensitivity of a search which coherently includes all three (inspiral, merger and ring down) stages of the BH coalescence with other template-based searches which look for each stage separately.

The ‘target signals’ used in this work are constructed by matching the numerical-relativity waveforms to a particular family (*TaylorT1* approximant [107]) of post-Newtonian waveforms, but this choice is by no means necessary. Indeed, we expect that more robust ways of constructing post-Newtonian approximants, such as the effective one-body approach [168] or Padé resummation approach [167], will give better agreement with numerical-relativity (NR) waveforms. But the purpose of this work is to explicitly prescribe a general procedure to produce phenomenological waveforms, and to construct interpolated template banks using these parametrized waveforms. It is shown that, given the number of numerical wave cycles employed, even a simple PN choice like TaylorT1 leads to very faithful and effectual templates, and significantly increases the possible range of gravitational-wave searches. The use of improved PN approximants will require a smaller number of NR cycles, thereby further reducing computational cost for

template construction.

This chapter is structured as follows. Section 7.2 summarizes the methods of current numerical-relativity simulations, including a setup of the initial data that allows an unambiguous comparison with post-Newtonian results, and the wave extraction techniques. Waveform generation using the *restricted* post-Newtonian approximation is briefly outlined in Section 7.3. This section also reviews the main data-analysis techniques and defines notations that are used in the subsequent sections. A phenomenological template family parametrized only by the masses of the two individual black holes is constructed in Section 7.4. First we combine restricted 3.5PN waveforms [91] with results from NR simulations to construct ‘hybrid’ waveforms for the quasi-circular inspiral of non-spinning binaries with possibly unequal masses. A phenomenological family of templates is then introduced in the frequency domain. Initially the template family is parametrized by 10 phenomenological parameters. We then find a unique mapping of these 10 parameters to the two physical parameters: namely, the total mass M and the symmetric mass ratio $\eta \equiv M_1 M_2 / M^2$, so that the template family is just two-dimensional. The resulting templates have remarkably high fitting factors with target waveforms. The faithfulness of the templates and the bias in the estimation of the parameter of the binary are also computed here. A comparison of the sensitivity of the search using the proposed template family with other existing template-based searches is also presented. Finally, the main results are summarised in Section 7.5. Some details of the calculations involved are described in Appendices A and B. Geometrical units are adopted throughout this chapter: $G = c = 1$.

7.2. Numerical simulations and wave extraction

Numerical simulations were performed with the BAM [171] and CCATIE [183] codes. Both codes evolve black-hole binaries using the ‘moving-puncture’ approach [94, 95]. The method involves setting up initial data containing two black holes via a Brill-Linquist-like wormhole construction [203], where the additional asymptotically flat end of each wormhole is compactified to a point, or ‘puncture’. A coordinate singularity exists at the puncture, but can be stably evolved using standard finite-difference techniques, and is protected by causality from adversely affecting the physically relevant external space-time. This prescription allows black holes to be constructed on a 3D Cartesian numerical grid without recourse to excision techniques, and also provides a simple way to generate any number of moving, spinning black holes [204, 205]. Given an initial configuration of two black holes, the data are evolved using a conformal and traceless ‘3+1’ decomposition of Einstein’s equations [206, 207, 208]. In addition the gauge is evolved using the ‘1+log’ [209, 210] and ‘ Γ -driver’ equations [211, 210] and the coordinate singularity in the conformal factor is dealt with by evolving either the regular variable $\chi = \psi^{-4}$ [94] (in BAM) or $\phi = \ln \psi$ (in CCATIE), which diverges ‘slowly’ enough so as not lead to numerical instabilities. The standard moving puncture approach consists of all these techniques, and causes the ‘punctures’ to quickly assume a cylindrical asymptotics [212], and allows them to move across the numerical grid. This method has been found to

allow accurate, stable simulations of black holes over many (> 10) orbits through merger and ring down.

In the initial data construction we must specify the masses, locations and momenta of the two black holes (spinning black holes are not considered in this work). The mass of each black hole, M_i , is specified in terms of the Arnowitt-Deser-Misner (ADM) mass at each puncture. This corresponds to the mass at the other asymptotically flat end which is, to a very good approximation, equal to irreducible mass of the apparent-horizon mass [213, 214, 215]

$$M_i = \sqrt{\frac{A_i}{16\pi}}. \quad (7.1)$$

where A_i is the area of the apparent horizon. We assume that this mass is the same as the mass used in post-Newtonian formulas. This assumption is really expected to be true only in the limit where the black holes are infinitely far apart and stationary. As such we consider any error in this assumption as part of the error due to starting the simulation at a finite separation. The important point is that a binary with horizon masses M_1 and M_2 should be compared with a post-Newtonian system with the same mass parameters. This allows us to provide the same overall scale $M = M_1 + M_2$ for both numerical and post-Newtonian waveforms, and is crucial for comparison and matching.

The initial momenta of the black holes are chosen to correspond approximately to quasi-circular (low eccentricity) inspiral. For equal-mass evolutions performed with the CCATIE code, parameters for quasi-circular orbit were determined by minimizing an effective potential for the binary [216, 217, 183]. For the unequal-mass simulations performed with the BAM code [175], initial momenta were specified by the 3PN-accurate quasi-circular formula given in Section VII of [171]. For the longer unequal-mass simulations performed with higher-order spatial finite-difference methods [197] and used for verification, the initial momenta were taken from a PN prescription that takes radiation reaction into account to reduce the initial eccentricity to below $e \approx 10^{-3}$ [198].

The Einstein equations are solved numerically with standard finite-difference techniques. Spatial derivatives are calculated at fourth- or sixth-order accuracy, and the time evolution is performed with a fourth-order Runge-Kutta integration. Mesh refinement is used to achieve high resolution around the punctures and low resolutions far from the black holes, allowing the outer boundary to be placed very far (at least $> 300M$) from the sources. Full details of the numerical methods used in the two codes are given in [171] for BAM and [183] for CCATIE.

In the wave-zone, sufficiently far away from the source, the spacetime metric can be accurately described as a perturbation of a flat background metric. Let h_{ab} denote the metric perturbation where a, b denote spacetime indices, and t be the time coordinate used in the numerical simulation to foliate the spacetime by spatial slices. Working in the transverse-traceless (TT) gauge, all the information about the radiative degrees of freedom is contained in the spatial part h_{ij} of h_{ab} , where i, j denote spatial indices. Let us use a coordinate system (x, y, z) on a spatial slice so that the z -axis is parallel to the total angular momentum of the binary system at the starting time. Let ι be the

inclination angle from the z -axis, and let ϕ be the phase angle and r the radial distance coordinates so that (r, ι, ϕ) are standard spherical coordinates in the wave-zone.

The radiative degrees of freedom in h_{ab} can be written in terms of two polarizations h_+ and h_\times :

$$h_{ij} = h_+(\mathbf{e}_+)_{ij} + h_\times(\mathbf{e}_\times)_{ij}, \quad (7.2)$$

where $\mathbf{e}_{+,\times}$ are the basis tensors for transverse-traceless tensors in the wave frame

$$(\mathbf{e}_+)_{ij} = \hat{\iota}_i \hat{\iota}_j - \hat{\phi}_i \hat{\phi}_j, \quad \text{and} \quad (\mathbf{e}_\times)_{ij} = \hat{\iota}_i \hat{\phi}_j + \hat{\iota}_j \hat{\phi}_i. \quad (7.3)$$

Here $\hat{\iota}$ and $\hat{\phi}$ are the unit vectors in the ι and ϕ directions, respectively, and the wave propagates in the radial direction.

In our numerical simulations, the gravitational waves are extracted by two distinct methods. The first one uses the Newman-Penrose Weyl tensor component Ψ_4 [218, 219] which is a measure of the outgoing transverse gravitational radiation in an asymptotically flat spacetime. In the wave-zone it can be written in terms of the complex strain $\mathbf{h} = h_+ - ih_\times$ as [96],

$$\mathbf{h} = \lim_{r \rightarrow \infty} \int_0^t dt' \int_0^{t'} dt'' \Psi_4. \quad (7.4)$$

An alternative method for wave extraction determines the waveform via gauge-invariant perturbations of a background Schwarzschild spacetime, via the Zerilli-Moncrief formalism (see [220] for a review). In terms of the even ($Q_{\ell m}^+$) and odd ($Q_{\ell m}^\times$) parity master functions, the gravitational wave strain amplitude is then given by

$$\mathbf{h} = \frac{1}{\sqrt{2}r} \sum_{\ell, m} \left(Q_{\ell m}^+ - i \int_{-\infty}^t Q_{\ell m}^\times(t') dt' \right) Y_{\ell m}^{-2} + \mathcal{O}\left(\frac{1}{r^2}\right). \quad (7.5)$$

Results from the BAM code have used the Weyl tensor component Ψ_4 and Eq. (7.4), with the implementation described in [171]. While the CCATIE code computes waveforms with both methods, the AEI-CCT waveforms used here were computed using the perturbative extraction and Eq. (7.5). Beyond an appropriate extraction radius (that is, in the wave-zone), the two methods for determining \mathbf{h} are found to agree very well for moving-puncture black-hole evolutions of the type considered here [179].

It is useful to discuss gravitational radiation fields in terms of spin-weighted $s = -2$ spherical harmonics $Y_{\ell m}^s$, which represent symmetric tracefree 2-tensors on a sphere, and in this work we will only consider the dominant $\ell = 2$, $m = \pm 2$ modes (see [188] for the higher ℓ contribution in the unequal-mass case), with basis functions

$$\begin{aligned} Y_{2-2}^{-2} &\equiv \sqrt{\frac{5}{64\pi}} (1 - \cos \iota)^2 e^{-2i\phi}, \\ Y_{22}^{-2} &\equiv \sqrt{\frac{5}{64\pi}} (1 + \cos \iota)^2 e^{2i\phi}. \end{aligned} \quad (7.6)$$

Our ‘input’ numerical relativity waveforms thus correspond to the projections

$$\mathbf{h}_{\ell m} \equiv \langle Y_{\ell m}^{-2}, \mathbf{h} \rangle = \int_0^{2\pi} d\phi \int_0^\pi \overline{\mathbf{h}} Y_{\ell m}^{-2} \sin\theta d\theta, \quad (7.7)$$

of the complex strain \mathbf{h} , where the bar denotes complex conjugation. In the cases considered here, we have equatorial symmetry so that $\mathbf{h}_{22} = \overline{\mathbf{h}_{2-2}}$, and

$$\mathbf{h}(t) = \sqrt{\frac{5}{64\pi}} e^{2i\phi} \left((1 + \cos\iota)^2 \mathbf{h}_{22}(t) + (1 - \cos\iota)^2 \overline{\mathbf{h}_{22}(t)} \right). \quad (7.8)$$

In this work, the binary is assumed to be optimally-oriented, so that $\iota = 0$. Thus

$$\mathbf{h}(t) = 4 \sqrt{\frac{5}{64\pi}} \mathbf{h}_{22}(t) \approx 0.6308 \mathbf{h}_{22}(t). \quad (7.9)$$

7.3. Post-Newtonian waveforms and introduction to data-analysis concepts

This section introduces notation that will be used later in this chapter and describe briefly the main data-analysis techniques currently used in gravitational-wave astronomy.

7.3.1. Restricted post-Newtonian waveforms

We use the restricted PN waveform at mass-quadrupole order, which has a phase equal to twice the orbital phase up to highest available order in the adiabatic approximation, and amplitude accurate up to leading order. The corresponding \mathbf{h} is given by

$$\mathbf{h} = \frac{\eta M}{r} v^2(t) e^{2i\phi} \left[(1 + \cos\iota)^2 e^{-i\varphi(t)} + (1 - \cos\iota)^2 e^{i\varphi(t)} \right] \quad (7.10)$$

where $M \equiv M_1 + M_2$ is the total mass, $\eta \equiv M_1 M_2 / M^2$ is the symmetric mass ratio, r is the observation radius, ι is the inclination angle; the quantity $v(t)$ is an expansion parameter, defined by $v = (M\dot{\varphi}/2)^{1/3}$ with $\varphi(t)$ equal to twice the adiabatic orbital phase. The *waveform* seen by the detector is given by

$$s(t) = 4\eta \frac{M}{r} A v^2(t) \cos[\varphi(t) + \varphi_0], \quad (7.11)$$

where, for short-lived signals (i.e., with duration much shorter than the earth rotation time, as well as de-phasing time scale due to Doppler shifts induced by earth motion and rotation), A and φ_0 are numerical constants depending on the relative position and orientation of the source relative to the detector, as well as the antenna pattern functions of the detector. In PN theory, the adiabatic phase $\varphi(t)$ is determined by the following ordinary differential equations (also called the *phasing formula*):

$$\frac{d\varphi}{dt} = \frac{2v^3}{M}, \quad \frac{dv}{dt} = -\frac{\mathcal{F}(v)}{ME'(v)}. \quad (7.12)$$

In these expressions, $E'(v) = dE(v)/dv$ where $E(v)$ is the binding energy (per unit mass) of the system, and $\mathcal{F}(v)$ is the GW luminosity. $E(v)$ and $\mathcal{F}(v)$ are computed as post-Newtonian expansions in terms of v [221]. Currently, the binding energy function $E(v)$ has been calculated to v^6 (3PN) accuracy by a variety of methods [222, 223, 224, 225, 226, 227, 228, 229]. The flux function $\mathcal{F}(v)$, on the other hand, has been calculated to v^7 (3.5PN) accuracy [230, 91] up to now only by the multipolar-post-Minkowskian method and matching to a post-Newtonian source [221].

The inspiralling phase is usually pushed up to the point where the adiabatic evolution of circular orbits breaks down due to the lack of further stable circular orbits. In the test-mass limit, the last (or innermost) stable circular orbit (ISCO) can be computed exactly (at $6M$ in Schwarzschild coordinates). For comparable-mass binaries, on the other hand, the ISCO cannot always arise unambiguously from PN theories. In adiabatic models, the maximum-binding-energy condition (referred to as MECO, or the maximum binding energy circular orbit, [231]) can be used in place of the ISCO. This condition is reached when the derivative of the orbital binding energy with respect to orbital frequency vanishes. As a consequence, in this work, the waveforms are evolved in time up to MECO: $E'(v) = 0$. It may be noted that the ISCO and MECO may not be physically meaningful beyond the test-mass limit, but they make convenient cutoff criteria. The appropriate region of validity of PN waveforms can only be determined by comparison with fully general relativistic results, such as the numerical simulations that we discussed earlier.

Given $E(v)$ and $\mathcal{F}(v)$, one can construct different, but equivalent in terms of accuracy, approximations to the phasing by choosing to retain the involved functions or to re-expand them. Indeed, the different PN models which describe the GW signal from inspiralling binaries agree with each other in the early stages of inspiral; but start to deviate in the late inspiral. The classification and explicit form of various models is nicely summarized in [107]. The PN waveforms used in this work are obtained by numerically solving Eqs. (8.1), called the *TaylorT1* approximant.

7.3.2. Introduction to matched filtering

Since we can model the signal reasonably well, it is natural to employ matched filtering (which is the optimal detection strategy for a signal of known shape in the stationary Gaussian noise) to search for the gravitational-wave signal. Suppose the detector's data $x(t)$ contains noise $n(t)$, and possible signal $s(t)$, i.e., $x(t) = n(t) + s(t)$. Assuming n to be stationary Gaussian noise, it is convenient to work in the Fourier domain, because the statistical property of the noise is completely characterized by its power spectral density $S_n(f)$, which is given by (here we use a *single-sided* spectrum)

$$\langle \tilde{n}(f) \tilde{n}^*(f') \rangle = \frac{1}{2} S_n(f) \delta(f - f'), \quad (7.13)$$

where $\tilde{n}(f)$ is the Fourier Transform of $n(t)$

$$\tilde{n}(f) \equiv \int_{-\infty}^{\infty} n(t) e^{-2\pi i f t} dt, \quad (7.14)$$

and $\langle \dots \rangle$ denotes taking the expectation value. Based on the detector noise spectrum, we introduce a Hermitian inner product:

$$(g|h) \equiv 2 \int_0^{\infty} \frac{\tilde{g}^*(f) \tilde{h}(f) + \tilde{g}(f) \tilde{h}^*(f)}{S_n(f)} df. \quad (7.15)$$

For the data x with known signal s , the optimal detection statistic is given by applying a template h with the same shape as s , or $h = \alpha s$:

$$\rho_{\text{opt}} \equiv (x|h). \quad (7.16)$$

The detectability of the signal is then determined by the SNR of ρ_{opt} ,

$$\frac{S}{N} = \frac{(s|h)}{\sqrt{\langle (h|n)(n|h) \rangle}} \Big|_{h=\alpha s} = (s|s)^{1/2}. \quad (7.17)$$

(Note that the SNR does not depend on the overall normalization of h .) In case the template h is not exactly of the same shape as s , the SNR will be reduced to

$$\frac{S}{N} = (s|s)^{1/2} \mathcal{M}, \quad (7.18)$$

where $\mathcal{M} \leq 1$ is the *match* of the template to the signal, given by

$$\mathcal{M}[s, h] \equiv \frac{(s|h)}{\sqrt{(s|s)(h|h)}} \equiv (\hat{s}|\hat{h}), \quad (7.19)$$

and where a hat denotes a normalized waveform. For more details, the reader is referred to Ref. [232].

7.3.3. Template banks, effectualness and faithfulness

We now consider the more realistic problem of attempting to detect a family of waveforms $s(\boldsymbol{\theta})$, parametrized by a vector of physical parameters $\boldsymbol{\theta} \in \Theta$, using a family of templates $h(\boldsymbol{\lambda})$ parametrized by a vector of parameters $\boldsymbol{\lambda} \in \Lambda$. We first introduce the concepts of *physical template bank* and *phenomenological template bank*. Roughly speaking, physical template banks are constructed from well-motivated physical models (e.g., approximation up to a certain order) [233], while phenomenological banks are constructed in an ad-hoc manner to mimic the desired physical signals with high accuracy. For physical banks, the vectors $\boldsymbol{\theta}$ and $\boldsymbol{\lambda}$ consists of the same set of *physical parameters*, while for phenomenological banks, the vector $\boldsymbol{\lambda}$ usually contains *phenomenological parameters*, which can be larger or smaller in number than the physical parameters.

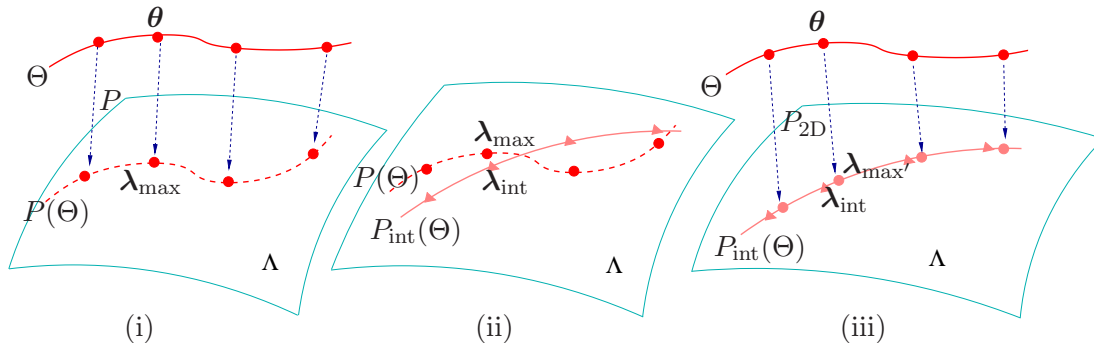


Figure 7.1.: Construction of the phenomenological template bank: (i) mapping physical signals (solid curve) into a sub-manifold (dashed curve, with example templates marked by dots) of a larger-dimensional template bank (curved surface), (ii) obtaining a lower-dimensional phenomenological bank with the same number of parameters as physical parameters, through interpolation (solid curve on the curved surface, with example templates marked by triangles), and (iii) Estimating the bias of the lower-dimensional interpolated bank by mapping physical signals into the bank (with images of example signals marked by dots).

Two phenomenological template families [112, 113] are used currently in the search for BH binaries in LIGO data [71, 234]. They each represent a different motivation for introducing phenomenological banks: (i) when we have uncertainty in the signal model, we can produce a template bank with larger detection efficiency by introducing extra (phenomenological) parameters (BCV1, [112]) so that $\dim(\Lambda) > \dim(\Theta)$; (ii) when the true signal depends on too many parameters and is too difficult to search over, it is sometimes possible to come up with a model with fewer (phenomenological) parameters ($\dim(\Lambda) < \dim(\Theta)$) and still high fitting factors (BCV2, [113]).

The detection efficiency of a template bank towards a specific signal $s(\theta)$ can be measured by the threshold SNR above which the detection probability exceeds a certain minimum (usually 50%), while the false-alarm probability is kept below a certain maximum (usually 1% for one-year data). The threshold value depends (logarithmically, in the case of Gaussian noise) on the number of statistically independent templates, and (inverse-proportionally) on the *fitting factor* (FF) [235]:

$$\text{FF}[h; \theta] \equiv \max_{\lambda} \mathcal{M}[s(\theta), h(\lambda)] \equiv \mathcal{M}[s(\theta), h(\lambda_{\max})]. \quad (7.20)$$

A bank with high FF is said to be *effectual*. Typically, we require that the total mismatch between the template and true signal (including the effects of both the fitting factor and the discreteness of the template bank) to not exceed 3%. We shall see that this requirement is easily met by our template bank.

It is natural to associate every point θ in the physical space Θ with the best matched point $\lambda_{\max} \in \Lambda$. This leads to a mapping $P : \Theta \mapsto \Lambda$ defined by

$$P(\theta) = \lambda_{\max}. \quad (7.21)$$

This mapping will play a key role in the construction of our template bank. We will assume the mapping P to be single-valued, i.e., given a target signal, the best-matched template is unique. This mapping is schematically illustrated in the left panel of Figure 7.1.

For a physical template bank with θ and λ the same set of parameters (which we use θ to denote), it is *most convenient* to identify the best-match parameter θ_{\max} as the estimation of the original parameter θ . In general this will lead to a systematic bias

$$\Delta\theta = \theta_{\max} - \theta = P(\theta) - \theta. \quad (7.22)$$

A bank with a small bias (as defined above) is said to be *faithful*.

However, if we assume no uncertainty in the true waveforms (thereby excluding the case of BCV1), then as long as P is invertible, a non-faithful physical or phenomenological bank can always be *converted into* a faithful bank by the re-parametrization

$$h_{\text{faithful}}(\theta) \equiv h \circ P(\theta) \quad (7.23)$$

where we have used the standard notation $h \circ P(\theta) \equiv h(P(\theta))$. In other words, each template λ in the image set of physical signals $P(\Theta)$ is labeled by physical parameters $\theta = P^{-1}(\lambda)$. For this reason, we require P to be invertible. It is quite conceivable that for physical banks, P should be invertible, if the physical bank does not fail to describe the true waveforms too dramatically (and of course assuming the true waveform does contain independent information about the physical parameters θ). In this way, *all reasonable physical banks can be made faithful*.

By contrast, if for some phenomenological bank (e.g., BCV2 if we only take into account the intrinsic parameters of the bank), P is a many-to-one map, with $P(\theta_1) = P(\theta_2)$ for some $\theta_1 \neq \theta_2$. Then for a physical signal with parameter θ_1 , the template bank h_{faithful} would achieve the same best match at both θ_1 and θ_2 , making physical parameter determination non-unique. In this case, we can simply keep using the phenomenological bank $h(\lambda)$; once a detection is made with λ_{\max} , the a set of parameters $P^{-1}(\lambda_{\max})$ would be the best knowledge we have about the physical parameters of the source. (In practice, statistical uncertainty also applies to λ_{\max} .)

7.4. A phenomenological template family for black-hole coalescence waveforms

7.4.1. Strategy for constructing the phenomenological bank

In our situation, since it is expensive to generate the entire physical bank of templates using numerical simulations, we first construct a highly effectual 10-dimensional phenomenological bank (motivated by the format of PN waveforms), with effectualness confirmed by computing its FF with a relatively small number of ‘target signals’. Since we are considering only non-spinning black holes, the physical parameter space Θ is the

set of all masses and symmetric mass ratios (M, η) that we wish to consider. As we shall see shortly, for our case the phenomenological parameter space Λ is a 10-dimensional space. Our templates will be denoted by

$$h(\boldsymbol{\lambda}) = h_{10\text{D}}(\boldsymbol{\lambda}). \quad (7.24)$$

According to the discussion above [Eqs. (7.21)–(7.23)], if the mapping $P : \Theta \mapsto \Lambda$ can indeed be obtained and inverted, then a faithful two-dimensional (2D) phenomenological bank can be constructed as

$$h_{2\text{D}}^{\text{faithful}}(\boldsymbol{\theta}) = h_{10\text{D}} \circ P(\boldsymbol{\theta}). \quad (7.25)$$

However, if our aim was to know P exactly, then in principle we would have to calculate accurate numerical waveforms for every (M, η) and to calculate the corresponding $\boldsymbol{\lambda}$ in each case. This is obviously not practical, and we shall instead compute P at a few chosen points in Θ and interpolate to obtain an approximation to P . The detailed steps are as follows:

- i. While confirming effectualness of the ten-dimensional (10D) bank, we simultaneously obtain N (a number manageable in terms of computational costs) data points for the mapping P ,

$$\boldsymbol{\lambda}_{\text{max}}^{(n)} = P(\boldsymbol{\theta}^{(n)}), \quad n = 1, 2, \dots, N \quad (7.26)$$

which gives discrete points on the 2D manifold $P(\Theta)$. This is depicted by the left panel of Figure 7.1.

- ii. Using these discrete points, we perform a smooth interpolation of P denoted by P_{int} . The form of P_{int} is motivated by PN waveforms, but with expansion coefficients determined by interpolation:

$$P_{\text{int}}(\boldsymbol{\theta}) = \boldsymbol{\lambda}_{\text{int}}. \quad (7.27)$$

This gives us a 2D phenomenological bank,

$$h_{2\text{D}}(\boldsymbol{\theta}) = h_{10\text{D}} \circ P_{\text{int}}(\boldsymbol{\theta}). \quad (7.28)$$

This is depicted by the middle panel of Figure 7.1. Due to the discrete choice of target waveforms, the constrained form of P_{int} , and numerical errors (in the target waveforms as well as in searching for best-fit parameters), the interpolation will have errors, even at the sample points. This means the 2D bank will have slightly lower effectualness than the 10D bank.

- iii. We re-test the effectualness of this 2D bank. Note that there will be a new mapping $P_{2\text{D}}$ which maps the physical parameters to the best fit parameters of this 2D bank. We therefore find the best-matched parameters $\boldsymbol{\lambda}_{\text{max}'}^{(n)}$, therefore obtaining discrete samples of the mapping $P_{2\text{D}}$:

$$\boldsymbol{\lambda}_{\text{max}'}^{(n)} = P_{2\text{D}}(\boldsymbol{\theta}^{(n)}), \quad (7.29)$$

yielding a systematic bias of

$$\Delta\boldsymbol{\theta}^{(n)} = P_{\text{int}}^{-1}(\boldsymbol{\lambda}_{\text{max}}^{(n)}) - \boldsymbol{\theta}^{(n)}. \quad (7.30)$$

This is depicted in the right panel of Figure 7.1.

In this work, we construct the 2D template bank $h_{2\text{D}}(\boldsymbol{\theta})$ and estimate the systematic bias $\Delta\boldsymbol{\theta}^{(n)}$ in the estimation of parameters $\boldsymbol{\theta}$, as described above. But, it is also possible to construct an interpolation $P_{2\text{D int}}$ from the data points of $P_{2\text{D}}$ so that we can construct a fully faithful (no systematic bias) bank (up to interpolation error)

$$h_{2\text{D}}^{\text{faithful}}(\boldsymbol{\theta}) = h_{10\text{D}} \circ P_{\text{int}} \circ P_{2\text{D int}}(\boldsymbol{\theta}). \quad (7.31)$$

7.4.2. Constructing the ‘target signals’

The ultimate aim of this work is to create a family of *analytical* waveforms that are very close to the gravitational waveforms produced by coalescing binary black holes. As a first step, we need to construct a set of ‘target signals’ containing all the three (inspiral, merger and ring down) stages of the binary black hole coalescence. Although numerical relativity, in principle, is able to produce gravitational waveforms containing all these stages, the numerical simulations are heavily constrained by their high computational cost. It is therefore necessary, at the present time, to use results from post-Newtonian theory to extend the waveforms obtained from numerical relativity.

A set of ‘hybrid waveforms’ is produced by matching the PN and NR waveforms in an overlapping time interval $t_1 \leq t < t_2$. The obvious assumption involved in this procedure is that such an overlapping region exists and that in it both approaches yield the correct waveforms. These hybrid waveforms are assumed to be the target signals that we want to detect in the data of GW detectors.

The NR and PN waveforms are given by Eq. (7.8) and Eq. (7.10), respectively (with $\iota = 0$). The (complex) time-domain waveform $\mathbf{h}(t, \boldsymbol{\mu})$ from a particular system is parametrized by a set of ‘extrinsic parameters’ $\boldsymbol{\mu} = \{\varphi_0, t_0\}$, where φ_0 is the initial phase and t_0 is the start time of the waveform. The PN waveforms $\mathbf{h}^{\text{PN}}(t, \boldsymbol{\mu})$ are matched with the NR waveforms $\mathbf{h}^{\text{NR}}(t, \boldsymbol{\mu})$ by minimizing the integrated squared absolute difference, δ , between the two waveforms, i.e.,

$$\delta \equiv \int_{t_1}^{t_2} \left| \mathbf{h}^{\text{PN}}(t, \boldsymbol{\mu}) - a \mathbf{h}^{\text{NR}}(t, \boldsymbol{\mu}) \right|^2 dt. \quad (7.32)$$

The minimization is carried out over the extrinsic parameters $\boldsymbol{\mu}$ of the PN waveform and an amplitude scaling factor a , while keeping the ‘intrinsic parameters’ (M and η) of both the PN and NR waveforms the same². The hybrid waveforms are then produced

²Here the amplitude scaling factor a is introduced because of two reasons. (i) The short NR waveforms used to construct the phenomenological template family (see the following discussion in this section)

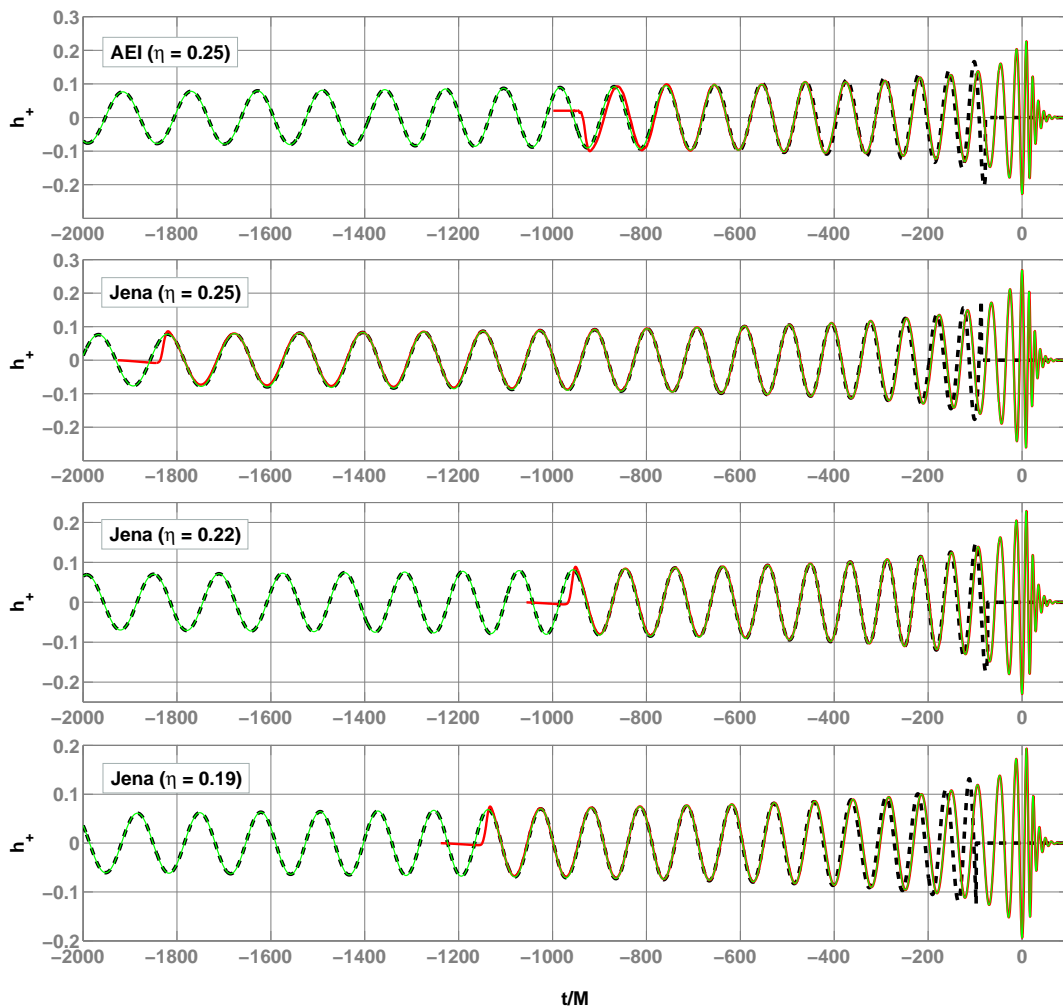


Figure 7.2.: NR waveforms (thick/red), the ‘best-matched’ 3.5PN waveforms (dashed/black), and the hybrid waveforms (thin/green) from three binary systems. The top panel corresponds to $\eta = 0.25$ NR waveform produced by the AEI-CCT group. The second, third and fourth panels, respectively, correspond to $\eta = 0.25, 0.22$ and 0.19 NR waveforms from produced by the Jena group. In each case, the matching region is $-750 \leq t/M \leq -550$ and we plot the real part of the complex strain (the ‘+’ polarization).

by combining the ‘best-matched’ PN waveforms and the NR waveforms in the following way:

$$\mathbf{h}^{\text{hyb}}(t, \boldsymbol{\mu}) \equiv a_0 \tau(t) \mathbf{h}^{\text{NR}}(t, \boldsymbol{\mu}) + (1 - \tau(t)) \mathbf{h}^{\text{PN}}(t, \boldsymbol{\mu}_0) \quad (7.33)$$

where $\boldsymbol{\mu}_0$ and a_0 denote the values of $\boldsymbol{\mu}$ and a for which δ is minimized, and τ is a weighting function, defined as

$$\tau(t) \equiv \begin{cases} 0 & \text{if } t < t_1 \\ \frac{t-t_1}{t_2-t_1} & \text{if } t_1 \leq t < t_2 \\ 1 & \text{if } t_2 \leq t. \end{cases} \quad (7.34)$$

In this work, two families of hybrid waveforms are used. Both are produced by matching 3.5 PN TaylorT1 waveforms with NR waveforms. The first set is constructed by using long (> 10 inspiral cycles) NR waveforms. This include equal-mass ($\eta = 0.25$) NR waveforms produced by the AEI-CCT group using their CCATIE code employing fourth-order finite differencing to compute spatial derivatives, and equal and unequal-mass ($\eta = 0.19, 0.22, 0.25$, or $M_1/M_2 = 1, 2, 3$) waveforms produced by the Jena group using their BAM code employing sixth-order finite differencing and PN-motivated initial-data parameters. The second set of hybrid waveforms is constructed by using NR waveforms produced by the Jena group using their BAM code employing fourth-order finite differencing. These are short waveforms (~ 4 inspiral cycles) densely covering a wide parameter range ($0.16 \leq \eta \leq 0.25$). We use the second set of hybrid waveforms to construct the phenomenological family and to test its efficiency in detecting signals from black hole coalescences, and use the first set of hybrid waveforms (which are closer to the actual signals) to verify our results.

The former family of hybrid waveforms is shown in Figure 7.2. The NR waveforms from three different simulations ($\eta = 0.25, 0.22, 0.19$) done by AEI and Jena groups are matched with 3.5PN inspiral waveforms over the matching region $-750 \leq t/M \leq -550$. The hybrid waveforms are constructed by combining the above as per Eq. (7.33) and Eq. (7.34).

The robustness of the matching procedure can be tested by computing the overlaps between hybrid waveforms constructed with different matching regions. If the overlaps are very high, this can be taken as an indication of the robustness of the matching procedure. A more detailed discussion of this will be presented in [236].

were extracted at a finite extraction radius. This introduces some error in the amplitude of the NR waveforms. (ii) Since the ‘long and accurate’ NR waveforms (see the following discussion) are extrapolated to an infinite extraction radius, we expect the amplitude of these waveforms to be correct within numerical accuracy of the simulations. But, it turns out that the *restricted* PN waveform has an amplitude which is inconsistent with the NR waveform by roughly constant factor $6 \pm 2\%$ in the frequency range we consider here [191]. For simplicity, we take the amplitude of the restricted PN waveform as the amplitude scale for the hybrid waveforms. It should be noted that, since we use normalised templates, the errors introduced by this ($< 10\%$) do not affect the fitting factors or the detection statistic. But the horizon distances computed in Section 7.4.6 can have an error up to 10% due to this choice.

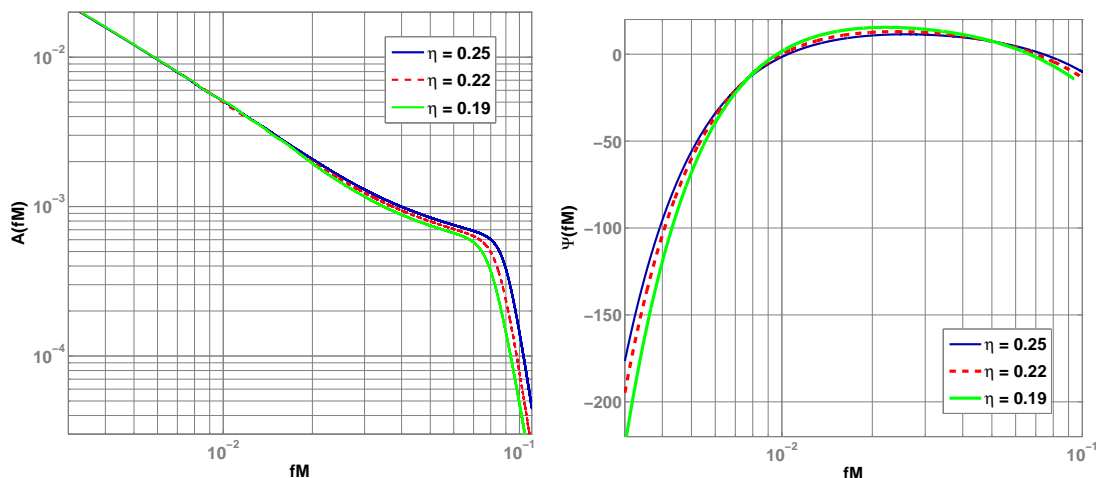


Figure 7.3.: Fourier domain magnitude (left) and phase (right) of the (normalized) hybrid waveforms. For the phase the leading order linear in time part has already been subtracted. Symmetric mass-ratio η of each waveform is shown in the legends. These waveforms are constructed by matching 3.5PN waveforms with the long NR waveforms produced by the Jena group.

Figure 7.3 shows the hybrid waveforms of different mass-ratios in the Fourier domain. In particular, the panel on the left shows the amplitude of the waveforms in the Fourier domain, while the panel on the right shows the phase. These waveforms are constructed by matching 3.5PN waveforms with the long NR waveforms produced by the Jena group. In the next section, we will try to parametrize these Fourier domain waveforms in terms of a set of phenomenological parameters.

7.4.3. Parametrizing the hybrid waveforms

We propose a phenomenological parametrization to the hybrid waveforms in the Fourier domain. Template waveforms in the Fourier domain are of particular preference because, (i) a search employing Fourier domain templates is computationally inexpensive compared to one using time domain templates (ii) parametrization of the hybrid waveforms is easier in the Fourier domain (iii) the explicit frequency-domain parametrization makes the subsequent calculation of many useful objects, such as the Fisher information matrix, much easier.

We take our motivation from the restricted post-Newtonian approximation to model the amplitude of the inspiral stage of the hybrid waveform, i.e., the amplitude is approximated to leading order as a power law $f^{-7/6}$ in terms of the Fourier frequency f (as follows straight from adding leading order radiation reaction to Newtonian dynamics). The amplitude of the merger stage is empirically approximated as a power law $f^{-2/3}$ (consistent with the observation of [187]), while the amplitude of the ring down stage is known to be a Lorentzian function around the quasi-normal mode ring down frequency.

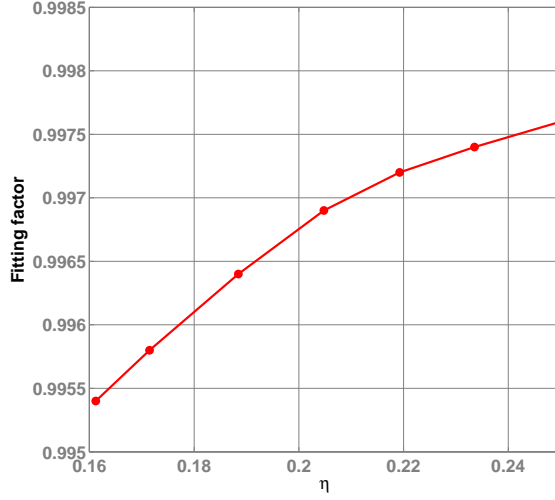


Figure 7.4.: Fitting factors of the hybrid waveforms with the phenomenological waveform family. Horizontal axis shows the symmetric mass ratio of the binary. Fitting factors are calculated assuming a white noise spectrum, and hence are independent of the mass of the binary.

Similarly, we take our motivation from the stationary phase approximation (see, for example, [42]) of the inspiral waveform to write the Fourier domain phase of the hybrid waveform as a series expansion in powers of f . As we shall see later, this provides an excellent approximation of the phase of the hybrid waveform.

Phenomenological waveforms

The phenomenological waveforms in the Fourier domain are written as

$$u(f) \equiv A_{\text{eff}}(f) e^{i\Psi_{\text{eff}}(f)}. \quad (7.35)$$

where $A_{\text{eff}}(f)$ is the amplitude of the waveform in the frequency domain, which is written in terms of a set of ‘amplitude parameters’ $\alpha = \{f_{\text{merg}}, f_{\text{ring}}, \sigma, f_{\text{cut}}\}$ as

$$A_{\text{eff}}(f) \equiv C \begin{cases} (f/f_{\text{merg}})^{-7/6} & \text{if } f < f_{\text{merg}} \\ (f/f_{\text{merg}})^{-2/3} & \text{if } f_{\text{merg}} \leq f < f_{\text{ring}} \\ w \mathcal{L}(f, f_{\text{ring}}, \sigma) & \text{if } f_{\text{ring}} \leq f < f_{\text{cut}} \end{cases} \quad (7.36)$$

where f_{cut} is the cutoff frequency of the template and f_{merg} is the frequency at which the power-law changes from $f^{-7/6}$ to $f^{-2/3}$ (as noted previously in [187] for the equal-mass case). C is a numerical constant whose value depends on the relative orientations of the

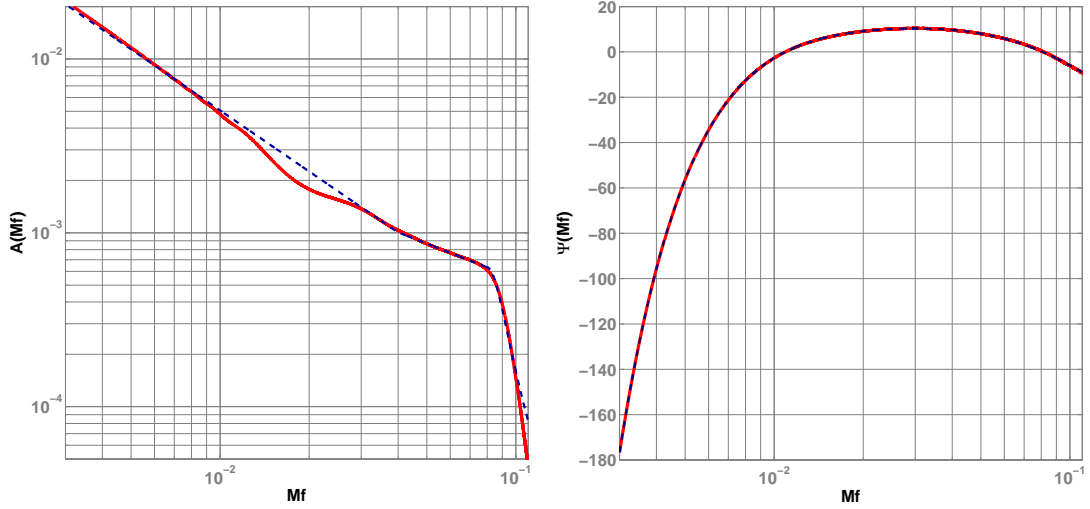


Figure 7.5.: Hybrid waveforms (solid lines) in the frequency domain, and the ‘best-matched’ phenomenological waveforms (dashed lines). The left panel shows the Fourier domain magnitude, while the right panel shows the phase. For the phase the leading order linear in time part has already been subtracted. These waveforms correspond to a binary with $\eta = 0.25$, and are constructed from the ‘short’ NR waveforms produced by the Jena group (see Section 7.4.2). The ‘dip’ in the left panel at $Mf \simeq 2 \times 10^{-2}$ is due to the small eccentricity present in the first few cycles of the NR waveform.

interferometer and the binary orbit as well as the physical parameters of the binary (see below). Also, in the above expression,

$$\mathcal{L}(f, f_{\text{ring}}, \sigma) \equiv \left(\frac{1}{2\pi} \right) \frac{\sigma}{(f - f_{\text{ring}})^2 + \sigma^2/4}, \quad (7.37)$$

represents a Lorentzian function of width σ centered around f_{ring} . The normalization constant w is chosen in such a way that $A_{\text{eff}}(f)$ is continuous across the ‘transition’ frequency f_{ring} , i.e.,

$$w \equiv \frac{\pi\sigma}{2} \left(\frac{f_{\text{ring}}}{f_{\text{merg}}} \right)^{-2/3}. \quad (7.38)$$

Taking our motivation from the stationary-phase approximation of the gravitational-wave phase, the effective phase $\Psi_{\text{eff}}(f)$ is written as an expansion in powers of f ,

$$\Psi_{\text{eff}}(f) = 2\pi f t_0 + \varphi_0 + \sum_{k=0}^7 \psi_k f^{(k-5)/3}, \quad (7.39)$$

where t_0 is the time of arrival, φ_0 is the frequency-domain phase offset, and $\boldsymbol{\psi} = \{\psi_0, \psi_2, \psi_3, \psi_4, \psi_6, \psi_7\}$ are the ‘phase parameters’, that is the set of phenomenological parameters describing the phase of the waveform.

The numerical constant C in Eq. (7.36) can be determined by comparing the amplitude of the phenomenological waveforms with that of the restricted post-Newtonian waveforms in the frequency domain.

In the restricted post-Newtonian approximation, the Fourier transform of the gravitational signal from an optimally-oriented binary located at an effective distance d can be written as in Eq. (B.1). We expect that in the inspiral stage ($f < f_{\text{merg}}$) of our phenomenological waveforms the amplitude will be equal to that of the post-Newtonian waveforms as given in Eq. (B.1). Thus, in the case of an optimally-oriented binary, the numerical constant C can be computed as

$$C = \frac{M^{5/6} f_{\text{merg}}^{-7/6}}{d \pi^{2/3}} \left(\frac{5\eta}{24} \right)^{1/2}. \quad (7.40)$$

This ‘physical’ scaling will be useful when we estimate the sensitivity of a search using this template family (see Section 7.4.6 and Appendix B).

We now compute the fitting factors of the hybrid waveforms with the family of phenomenological waveforms by maximizing the overlaps over all the parameters, i.e., $\{\alpha, \psi, \varphi_0, t_0\}$ of the phenomenological waveforms. While doing this, we also find the parameters, α_{max} and ψ_{max} , of the ‘best-matched’ phenomenological waveforms. This calculation is described in detail in Appendix A.

We first take a few (seven) hybrid waveforms coarsely spaced in the parameter range $0.16 \leq \eta \leq 0.25$, and compute the fitting factors and the best-matched phenomenological parameters. These samples in the parameter space are used to construct the interpolated template bank (see next subsection). We then test the effectualness and faithfulness of the template bank using all (~ 30) hybrid waveforms finely spaced in the parameter space.

The fitting factors are shown in Figure 7.4. These are calculated assuming a white noise spectrum for the detector noise. It is quite apparent that the fitting factors are always greater than 0.99, thus underlining the effectiveness of the phenomenological waveforms in reproducing the hybrid ones. Also, as an example, in Figure 7.5, the hybrid waveform from $\eta = 0.25$ binary is plotted in Fourier domain along with the ‘best-matched’ phenomenological waveform.

From phenomenological to physical parameters

It is possible to parametrize the phenomenological waveforms having the largest overlaps with the hybrid waveforms in terms of the physical parameters of the hybrid waveforms. Figure 7.6 shows the amplitude parameters α_{max} of the best-matched phenomenological waveforms plotted against the physical parameters of the binary. Similarly, the phase parameters ψ_{max} of the best-matched phenomenological waveforms are plotted against the physical parameters of the binary in Figure 7.7.

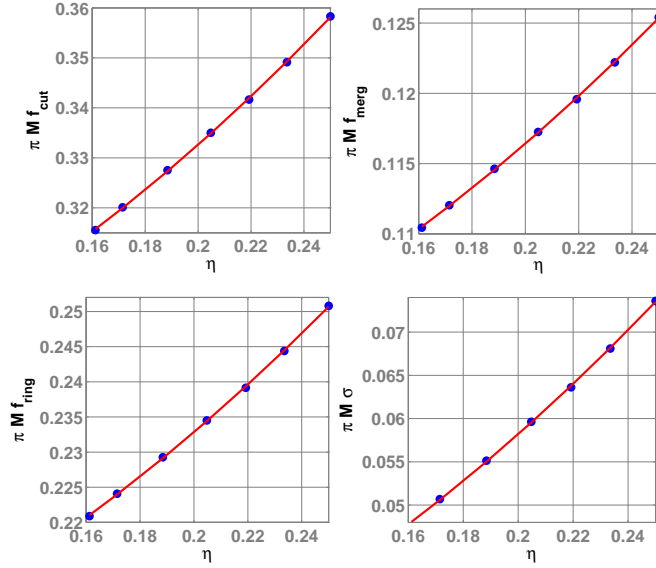


Figure 7.6.: Best-matched amplitude parameters α_{\max} in terms of the physical parameters of the binary (assuming white noise spectrum). The horizontal axis shows the symmetric mass-ratio of the binary. Quadratic polynomial fits α_{int} to the data points are also shown.

It can be seen that α_{\max} and ψ_{\max} can be written as quadratic polynomials in terms of the physical parameters (M and η) of the hybrid waveforms as:

$$\begin{aligned}\alpha_{j \text{ int}} &= \frac{a_j \eta^2 + b_j \eta + c_j}{\pi M}, \\ \psi_{k \text{ int}} &= \frac{x_k \eta^2 + y_k \eta + z_k}{\eta (\pi M)^{(5-k)/3}},\end{aligned}\tag{7.41}$$

where a_j, b_j, c_j , $j = 0 \dots 3$ and x_k, y_k, z_k , $k = 0, 2, 3, 4, 6, 7$ are the coefficients of the quadratic polynomials used to fit the data given in Figures 7.6 and 7.7. These coefficients are listed in Tables 7.1 and 7.2. It may be noted at this point that Figures 7.6 and 7.7 correspond to the mapping $P : \boldsymbol{\theta}^{(n)} \rightarrow \boldsymbol{\lambda}_{\max}^{(n)}$ that we have introduced in Section 7.4.1, and Eq. (7.41) to the interpolation P_{int} of P .

Using the empirical relations given in Eq. (7.41), we can rewrite the effective amplitude

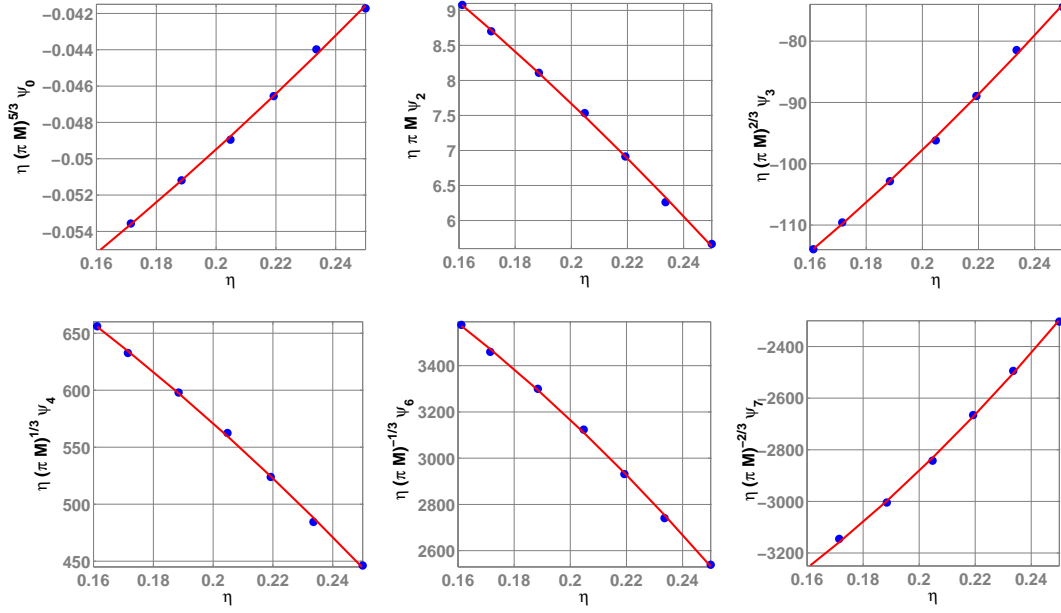


Figure 7.7.: Best-matched phase parameters ψ_{\max} in terms of the physical parameters of the binary (assuming white noise spectrum). The horizontal axis shows the symmetric mass-ratio of the binary. Quadratic polynomial fits ψ_{int} to the data points are also shown.

and phase of the waveforms in terms of M and η as:

$$A_{\text{eff}}(f) \equiv C \begin{cases} \left(\frac{\pi M f}{a_0 \eta^2 + b_0 \eta + c_0} \right)^{-7/6} & \text{if } f < \frac{a_0 \eta^2 + b_0 \eta + c_0}{\pi M} \\ \left(\frac{\pi M f}{a_0 \eta^2 + b_0 \eta + c_0} \right)^{-2/3} & \text{if } \frac{a_0 \eta^2 + b_0 \eta + c_0}{\pi M} \leq f < \frac{a_1 \eta^2 + b_1 \eta + c_1}{\pi M} \\ w \mathcal{L} \left(f, \frac{a_1 \eta^2 + b_1 \eta + c_1}{\pi M}, \frac{a_2 \eta^2 + b_2 \eta + c_2}{\pi M} \right) & \text{if } \frac{a_1 \eta^2 + b_1 \eta + c_1}{\pi M} \leq f < \frac{a_3 \eta^2 + b_3 \eta + c_3}{\pi M}, \end{cases}$$

$$\Psi_{\text{eff}}(f) = 2\pi f t_0 + \varphi_0 + \frac{1}{\eta} \sum_{k=0}^7 (x_k \eta^2 + y_k \eta + z_k) (\pi M f)^{(k-5)/3}, \quad (7.42)$$

where the constant C is given by Eq.(7.40). This family of parametrized waveforms is used to create a two-dimensional template bank of non-spinning waveforms. This template family can be seen as a two-dimensional sub-manifold (parametrized by M and η) embedded in a higher dimensional manifold (of the phenomenological waveforms).

7.4.4. Effectualness and faithfulness

In order to measure the accuracy of our parametrized templates we compute their overlap with the ‘target signals’ (the hybrid waveform). To check the faithfulness of our phenomenological templates, we compute their overlap with the target signal maximizing it over the extrinsic parameters (time-of-arrival and the initial phase). The effectualness of the parametrized waveforms is assessed by computing fitting factors with the target signals (computing the overlap maximized over both extrinsic and intrinsic parameters). Faithfulness is a measure of how good the template waveform is in both detecting a signal and estimating its parameters. However, effectualness is aimed at finding whether or not an approximate template model is good enough in detecting a signal without reference to its use in estimating the parameters.

The effectualness and the faithfulness of the template family are computed for three different noise spectra. The one-sided noise power spectral density (PSD) of the Initial LIGO detector is given in terms of a dimensionless frequency $x = f/f_0$ by [237]

$$S_h(f) = 9 \times 10^{-46} [(4.49x)^{-56} + 0.16x^{-4.52} + 0.52 + 0.32x^2], \quad (7.43)$$

where $f_0 = 150$ Hz; while the same for Virgo reads [237]

$$S_h(f) = 10.2 \times 10^{-46} [(7.87x)^{-4.8} + 6/17x^{-1} + 1 + x^2], \quad (7.44)$$

where $f_0 = 500$ Hz. For Advanced LIGO [237],

$$S_h(f) = 10^{-49} \left[x^{-4.14} - 5x^{-2} + 111 \left(\frac{1 - x^2 + x^4/2}{1 + x^2/2} \right) \right], \quad (7.45)$$

where $f_0 = 215$ Hz.

Faithfulness is computed by maximizing the overlaps over the extrinsic parameters t_0 and φ_0 only, which can be done trivially [238]. Effectualness is computed by maximizing both intrinsic and extrinsic parameters of the binary. The maximization over the intrinsic parameters is performed with the aid of the Nelder-Mead downhill simplex algorithm [239].

The effectualness of the template waveforms with the hybrid waveforms is plotted in Figure 7.8 for three different noise spectral densities. The corresponding faithfulness is plotted in Figure 7.9. It is evident that, having both values always greater than 0.99, the proposed template family is both effectual and faithful.

We also calculate the systematic bias in the estimation of parameters while maximizing the overlaps over the intrinsic parameters of the binary. The bias in the estimation of the parameters θ is defined in Eq.(7.30).

The percentage biases in estimating the total mass M , mass ratio η , and chirp mass $M_c = M\eta^{3/5}$ of the binary are plotted in Figures 7.10, 7.11, and 7.12, respectively. This preliminary investigation suggests that the bias in the estimation of M and η using the proposed template family is $< 3\%$, while the same in estimating M_c is $< 6\%$.

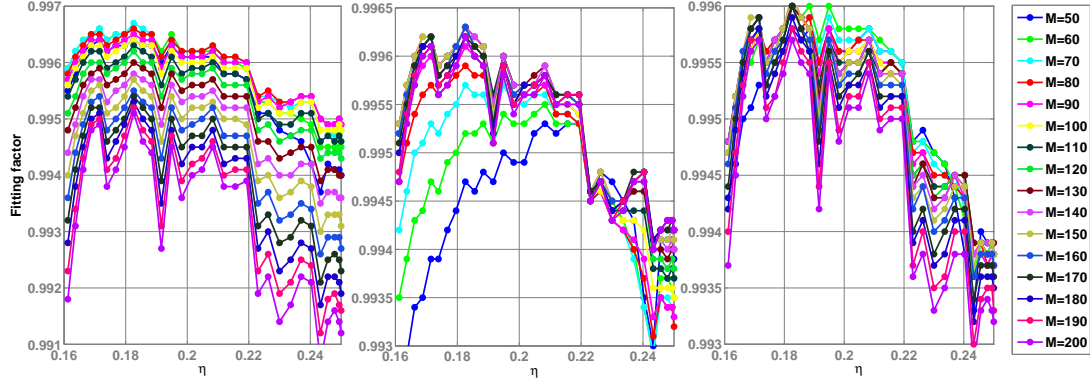


Figure 7.8.: Fitting factor of the (two-dimensional) template family computed using three different noise spectra. The panel in the left correspond to the Initial LIGO noise PSD, the one in the middle to the Virgo noise PSD and the one in the right to the Advanced LIGO noise PSD. The horizontal axis reports the symmetric mass ratio η of the binary and the legends display the total mass M (in units of M_\odot).

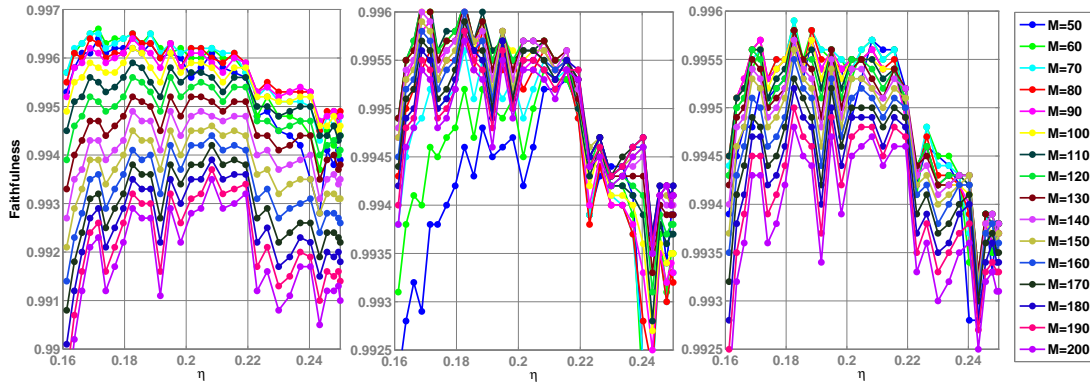


Figure 7.9.: Same as in Figure 7.8, except that the plots show the faithfulness of the (two-dimensional) template family.

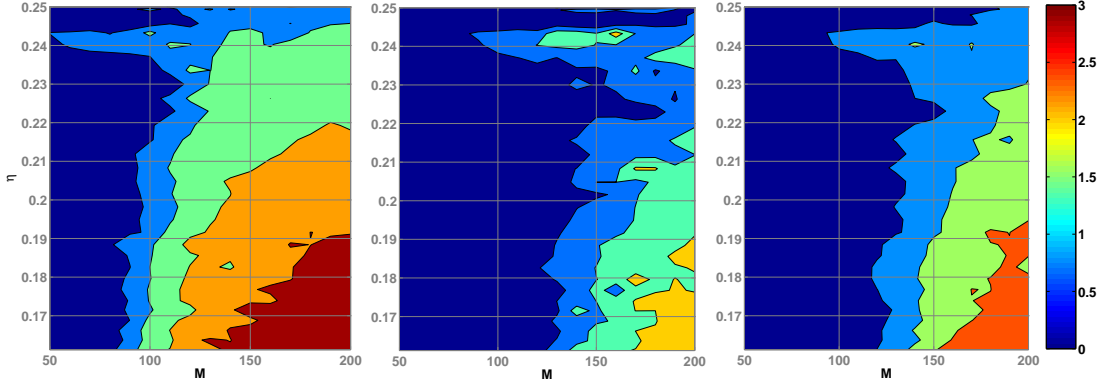


Figure 7.10.: Bias in the estimation of M . Horizontal axis reports the total mass M (in units of M_\odot) and vertical axis reports the symmetric mass ratio η of the binary. Colors in the plot corresponds to the percentage bias, $|\Delta M|/M \times 100$. The left panel corresponds to the Initial LIGO noise PSD, the middle panel to the Virgo noise PSD and the right panel to the Advanced LIGO noise PSD.

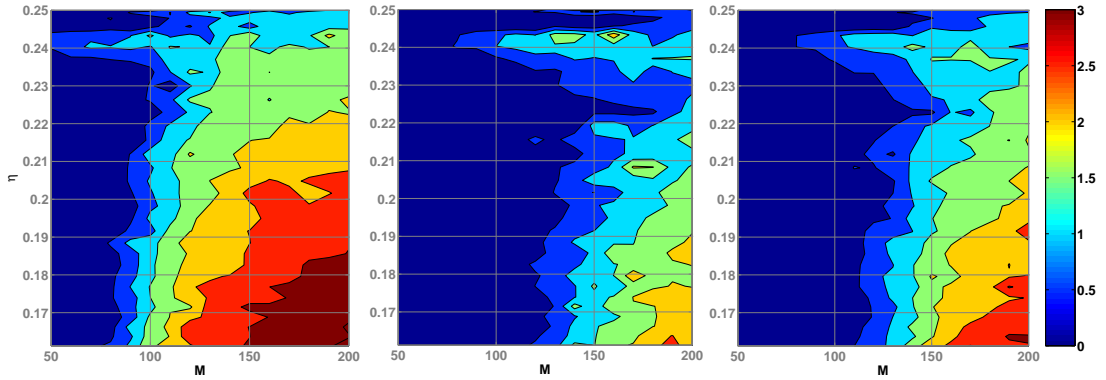


Figure 7.11.: Same as in Figure 7.10, except that the plots show the percentage bias $|\Delta\eta|/\eta \times 100$ in the estimation of η .

Parameter	a_k	b_k	c_k
f_{merg}	2.9740×10^{-1}	4.4810×10^{-2}	9.5560×10^{-2}
f_{ring}	5.9411×10^{-1}	8.9794×10^{-2}	1.9111×10^{-1}
σ	5.0801×10^{-1}	7.7515×10^{-2}	2.2369×10^{-2}
f_{cut}	8.4845×10^{-1}	1.2848×10^{-1}	2.7299×10^{-1}

Table 7.1.: Polynomial coefficients of the best-matched amplitude parameters. The first column lists the amplitude parameters α_{int} . Eq.(7.41) shows how these parameters are related to the coefficients a_k, b_k, c_k .

Parameter	x_k	y_k	z_k
ψ_0	1.7516×10^{-1}	7.9483×10^{-2}	-7.2390×10^{-2}
ψ_2	-5.1571×10^1	-1.7595×10^1	1.3253×10^1
ψ_3	6.5866×10^2	1.7803×10^2	-1.5972×10^2
ψ_4	-3.9031×10^3	-7.7493×10^2	8.8195×10^2
ψ_6	-2.4874×10^4	-1.4892×10^3	4.4588×10^3
ψ_7	2.5196×10^4	3.3970×10^2	-3.9573×10^3

Table 7.2.: Polynomial coefficients of the best-matched phase parameters. The first column lists the phase parameters ψ_{int} . Eq.(7.41) shows how these parameters are related to the coefficients x_k, y_k, z_k .

7.4.5. Verification of the results using more accurate hybrid waveforms

As we have discussed in Section 7.4.2, the hybrid waveforms used for constructing the template waveforms are produced by matching rather short (~ 4 inspiral cycles) NR waveforms with PN waveforms. We have also produced a few hybrid waveforms by matching PN waveforms with long (> 10 inspiral cycles) and highly accurate (sixth-order finite differencing and low eccentricity) NR waveforms. This set of hybrid waveforms (which are closer to the ‘actual signals’) can be used to verify the efficacy of the template waveforms in reproducing these more accurate signals.

Figure 7.13 shows the fitting factors of the two-dimensional template family with the ‘more accurate’ hybrid waveforms. The fitting factors are computed, as before, using the Initial LIGO (left), Virgo (middle) and Advanced LIGO (right) noise spectra. The high fitting factors (although smaller than the same obtained in the previous section) with the hybrid waveforms once again underline the efficacy of the template waveforms in reproducing the hybrid ones. It is indeed expected that the template family will have better overlaps with the hybrid waveforms described in the previous section (those constructed from ‘short’ NR waveforms), because the polynomial coefficients given in Tables 7.1 and 7.2 are optimized for these hybrid waveforms. When more ‘long and accurate’ NR waveforms are available in the future, the polynomial coefficients given in the tables can be optimized for the corresponding family of ‘more accurate’ hybrid waveforms. In any case, since the fitting factors are already very high, we don’t expect

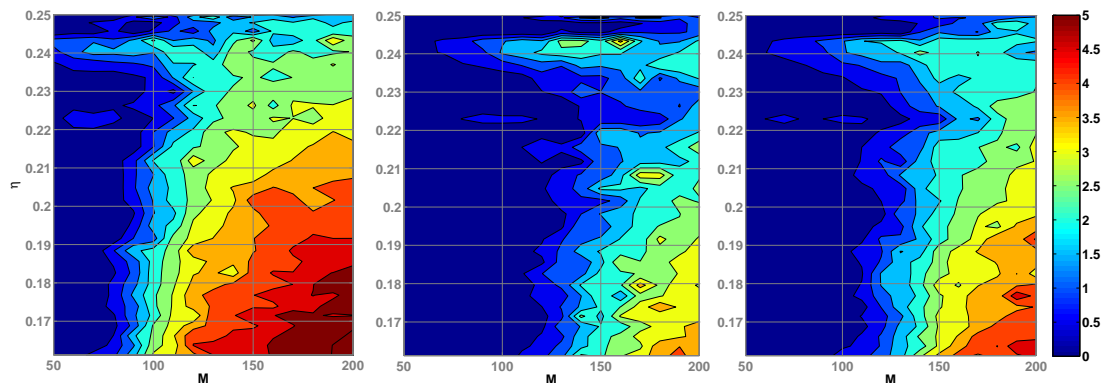


Figure 7.12.: Same as in Figure 7.10, except that the plots show the percentage bias $|\Delta M_c|/M_c \times 100$ in the estimation of $M_c = M\eta^{3/5}$.

any significant improvements.

7.4.6. The astrophysical range and comparison with other searches

The template family proposed in this chapter can be used for coherently searching for all the three stages (inspiral, merger, and ring-down) of the binary black hole coalescence, thus making this potentially more sensitive than searches which look at the three stages separately. Figure 7.14 compares the sensitivity of the searches using different template families. What is plotted here are the distances at which an optimally-oriented, equal-mass binary would produce an optimal SNR of 8 at the Initial LIGO (left plot), Virgo (middle plot) and Advanced LIGO (right plot) noise spectra. In each plot, the thin solid (blue) line corresponds to a search using PN templates truncated at the innermost stable circular orbit (ISCO) of the Schwarzschild geometry having the same mass as the total mass M of the binary; the dashed (purple) line to a search using ring-down templates [240]; the dot-dashed (black) line to a search using effective one body [168] waveform templates truncated at the light ring of the corresponding Schwarzschild geometry, and the solid line to a search using all three stages of the binary coalescence using the template bank proposed here. The computation is described in detail in Appendix B. The horizontal axis reports the total-mass of the binary, while the vertical axis the distance in Mpc. It is quite evident that, for a substantial range of total mass ($100 \lesssim M/M_\odot \lesssim 300$ for Initial LIGO, $200 \lesssim M/M_\odot \lesssim 500$ for Virgo, $150 \lesssim M/M_\odot \lesssim 400$ for Advanced LIGO), the ‘coherent search’ using the new template family is significantly more sensitive than any other search considered here.

However, while this looks promising, it is important to treat Figure 7.14 as only a preliminary assessment; fitting factors are not the only consideration for a practical search strategy. It is also very important to consider issues which arise when dealing with real data. For example, false alarms produced by noise artifacts might well determine the true sensitivity of the search, and these artifacts will inevitably be present in real

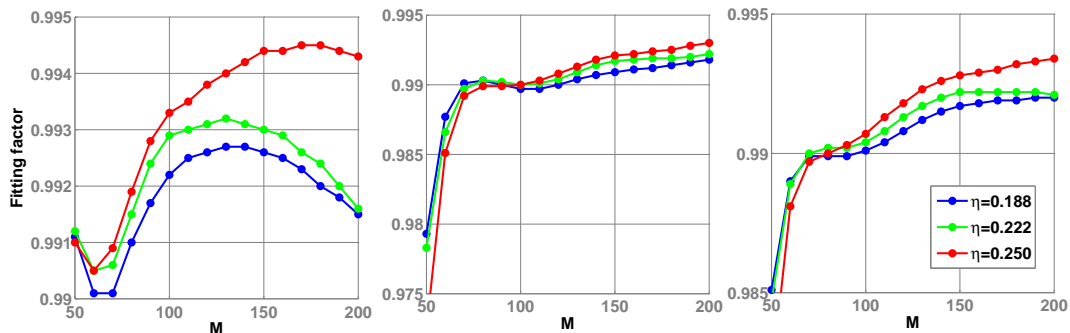


Figure 7.13.: Fitting factor of the (two-dimensional) template family with ‘more accurate’ hybrid waveforms (see Section 7.4.5). The overlaps are computed using three different noise spectra. The panel in the left corresponds to the Initial LIGO PSD, the one in the middle to the Virgo noise PSD and the one in the right to the Advanced LIGO noise PSD. The horizontal axis represents the total mass M (in units of M_{\odot}) and the legends display the symmetric mass ratio η of the binary.

data. This is however beyond the scope of the present work, and further investigation is required before we can properly assess the efficacy of our phenomenological template bank in real-life searches.

7.5. Summary and outlook

Making use of the recent results from numerical relativity a phenomenological waveform family is proposed, which can model the inspiral, merger and ring-down stages of the coalescence of non-spinning binary black holes in quasi-circular orbits. We first constructed a set of hybrid waveforms by matching the NR waveforms with analytical PN waveforms. Then, we constructed analytical phenomenological waveforms which approximated the hybrid waveforms. The proposed family of phenomenological waveforms was found to have fitting factors larger than 0.99 with the hybrid waveforms. It was also shown that this phenomenological waveform family can be parametrized solely in terms of the physical parameters (M and η) of the binary, so that the template bank is, in the end, two dimensional. We estimated the ‘closeness’ of this two-dimensional template family with the family of hybrid waveforms in the detection band of three ground-based GW detectors, namely Initial LIGO, Virgo and Advanced LIGO. We estimated the effectualness (larger overlaps with the target signals for the purpose of detection) and faithfulness (smaller biases in the estimation of the parameters of the target signals) of the template family. Having both types of overlap always greater than 0.99, the two dimensional template family is found to be both effectual and faithful in the detection band of these ground-based detectors.

This phenomenological waveform family can be used to densely cover the parameter

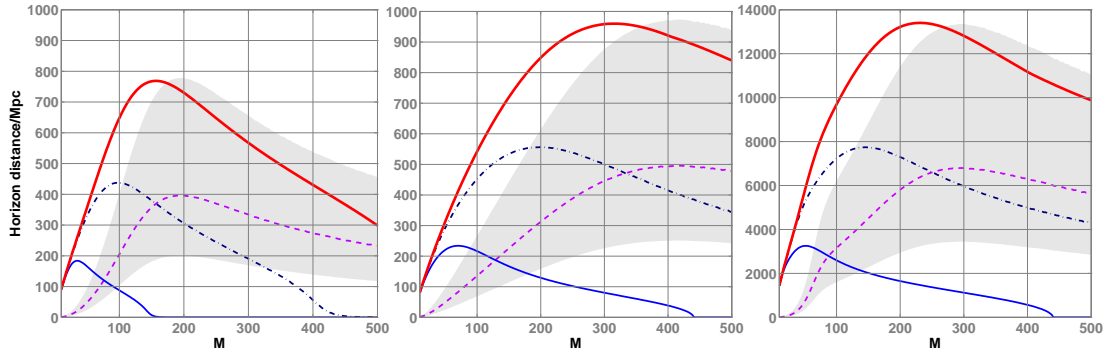


Figure 7.14.: Distance to optimally located and oriented equal-mass binaries which can produce an optimal SNR of 8 at the Initial LIGO (left plot), Virgo (middle plot) and Advanced LIGO (right plot) noise spectra. Horizontal axis reports the total mass of the binary (in units of M_{\odot}) and vertical axis reports the distance in Mpc. In each plot, the thin solid (blue) line corresponds to a search using standard PN templates truncated at ISCO, the dotted-dashed (black) line to a search using effective one body waveform templates truncated at the light ring, the the dashed (purple) line to a search using ring-down templates, and the thick solid (red) line to a search using the template family proposed in this chapter. The ring down horizon distance is computed assuming that $\epsilon = 0.7\%$ of the black hole mass is radiated in the ring down stage, while the Kerr parameter $a = 0.69$ is known from the numerical simulation. Since the value of ϵ has some amount of uncertainty in it, a shaded region is also included in the plot corresponding to $0.18\% \leq \epsilon \leq 2.7\%$.

space of the binary, avoiding the computational cost of generating numerical waveforms at every grid point in the parameter space. The sensitivity of a search using this template family is compared with other searches. For a substantial mass-range, the search using all the three stages of the binary black hole coalescence was found to be significantly more sensitive than any other template-based searches considered in this work. This might enable us to do a more sensitive search for intermediate-mass black-hole binaries using ground-based GW detectors.

A number of practical issues need to be addressed before we can employ this template family in an actual search for GW signatures. The first issue will be how to construct a bank of templates sufficiently densely spaced in the parameter space so that the loss in the event rate because of the mismatch between the signal and template is restricted to an acceptable amount (say, 10%). The explicit frequency domain parametrization of the proposed template family makes it easier to adopt the formalism proposed by Owen [108] in laying down the templates using a metric in the parameter space. Work is ongoing to compare the metric formalism adopted to the proposed template family and other ways of laying out the templates, for example a ‘stochastic’ template bank [241]. Also, this explicit parametrization makes it easier to employ additional signal-based vetoes, such as the ‘chi-square test’ [136]. This will also be explored in a forthcoming work.

Since this template bank is also a faithful representation of the target signals considered, we expect that, for a certain mass-range, a search which coherently includes all three stages of the binary coalescence will bring about remarkable improvement in the estimation of parameters of the binary. This may be especially important for LISA data analysis in estimating the parameters of super massive black hole binaries. This is also being explored in an ongoing work [201].

It is worth pointing out that the family of target signals (the hybrid waveforms) that we have considered in this chapter is not unique. One can construct alternate families of hybrid waveforms by matching PN waveforms computed using different approximations with NR waveforms. Also, owing to the differences in initial data and accuracy of numerical techniques, the NR waveforms from different simulations can also be slightly different. Thus, the coefficients listed in Tables 7.1 and 7.2 have a unique meaning only related to this particular family of target waveforms. But we expect that the general parametrization that we propose in this work will hold for the whole family of non-spinning black hole coalescence waveforms from quasi-circular inspiral. As mentioned in the Introduction, the purpose of this work is to explicitly prescribe a general procedure to construct interpolated template banks using parametrized waveforms which mimics actual signals from binary black hole coalescence (as predicted by numerical relativity and analytical methods).

Nevertheless, it may be noted that most of the PN waveforms constructed using different approximations are known to be very close to each other (see, for example, [107]). Also, we expect that NR waveforms from different simulations will converge as the accuracy of numerical simulations improves (see, for example, [242]). Thus, since different families of PN and NR waveforms, which are the ‘ingredients’ for constructing our target signals, are very close to each other, we expect that the phenomenological waveform family

proposed in this work, in its present form, will be sufficiently close to other families of target signals for the purpose of detecting these signals. As a preliminary illustration of this, the fitting factors of the template waveforms with a different family of hybrid waveforms (constructed from longer and more accurate NR waveforms) are computed, and was shown to be very high. This will be explored in detail in a forthcoming work.

Part III.

Modelling of coalescing compact binaries

8. New class of post-Newtonian approximants to the waveform templates of inspiralling compact binaries

8.1. Introduction

The late-time dynamics of astronomical binaries consisting of neutron stars and/or black holes is dominated by relativistic motion and nonlinear general relativistic effects. The component bodies would be accelerated to velocities close to half the speed of light before they plunge towards each other, resulting in a violent event during which the source would be most luminous in the gravitational-wave (GW) window. Such events are prime targets of interferometric GW detectors like LIGO, Virgo, GEO 600 and TAMA 300, that are currently taking data at unprecedented sensitivity levels and bandwidths [243, 244, 245, 246].

Binary coalescences are the end state of a long period of adiabatic dynamics in which the orbital frequency of the system changes as a result of gravitational radiation back-reaction, but the change in frequency per orbit is negligible compared to the orbital frequency itself. This *inspiral* stage of the coalescing binary is of particular interest to the GW searches, because the gravitational waveforms from the inspiralling stage can, in principle, be well-modelled by the post-Newtonian (PN) approximation of general relativity. This allows the data analysts to use the *matched filtering* technique to extract these signals buried in the detector noise. Matched filtering, which can be shown to be the optimal filter in detecting any known signal buried in the noise, involves cross correlating the data with a template of the signal waveform. The effectiveness of matched filtering depends on how well the phase evolution of the waveform is known. Thus, for the purpose of the detection of these signals, it is sufficient to use the so-called *restricted* PN approximation to quasi-circular inspiral. This keeps the crucial phase information to the best order of approximation available, but restricts the amplitude to be Newtonian and the harmonic to the second harmonic of the orbital frequency.

In the adiabatic approximation of the calculation of GW phasing, the inspiralling orbit is approximated as an adiabatic perturbation of many quasi-circular orbits with a specific conserved energy associated with each orbit. The time evolution of the GW phase is computed from the *energy balance argument*. i.e., the difference in binding energy

between consecutive orbits is equated to the energy flux of GWs emitted by the system. There are different ways of casting the *phasing formula* – the formula that gives the phase of the emitted gravitational wave as a function of time and the parameters of the system. These different approaches make use of the post-Newtonian expansions of the binding energy and gravitational wave luminosity of the system¹. Indeed, the adiabatic inspiral phase is well-modelled by the post-Newtonian approximation to Einstein’s equations; but this approximation becomes less accurate close to the merger phase.

8.1.1. Standard approach to phasing formula

In the post-Newtonian approximation, the binding energy and the GW luminosity are computed as series expansions in terms of v/c , where v is the post-Newtonian expansion parameter describing the velocity in the system and c is the speed of light. (For the rest of this chapter we use units in which $G = c = 1$).

Given the *specific* gravitational binding energy $E(v)$ (i.e. the binding energy per unit mass) of the system and its luminosity $\mathcal{F}(v)$, the phasing of gravitational waves can be computed using the following ordinary, coupled differential equations:

$$\frac{d\varphi}{dt} = \frac{2v^3}{m}, \quad \frac{dv}{dt} = -\frac{\mathcal{F}(v)}{mE'(v)}, \quad (8.1)$$

where $E'(v) = dE(v)/dv$ and $m = m_1 + m_2$ is the total mass of the binary. The phasing obtained by numerically solving the above set of differential equations is called the *TaylorT1* approximant [247]. If the detector’s motion can be neglected during the period when the wave passes through its bandwidth then the response of the interferometer to arbitrarily polarized waves from an inspiralling binary is given by

$$h(t) = \frac{4A\eta m}{D} v^2(t) \cos[\varphi(t) + \varphi_C], \quad (8.2)$$

where $\varphi(t)$ is defined so that it is zero when the binary coalesces at time $t = t_C$, φ_C is the phase of the signal at t_C , $\eta = m_1 m_2 / m^2$ is the symmetric mass ratio, D is the distance to the source and A is a numerical constant whose value depends on the relative orientations of the interferometer and the binary orbit. It suffices to say for the present purpose that for an optimally oriented source $A = 1$.

One can compute the Fourier transform $H(f)$ of the waveform given in Eq. (8.2) using the stationary phase approximation:

$$H(f) = \frac{4Am^2}{D} \sqrt{\frac{5\pi\eta}{384}} v_f^{-7/2} e^{i[2\pi f t_C - \varphi_C + \psi(f) - \pi/4]}, \quad (8.3)$$

¹In the case of binaries consisting of spinning bodies in eccentric orbit one additionally requires equations describing the evolution of the individual spins and the orbital angular momentum, but this complication is unimportant for our purposes.

where the phase of the Fourier transform obeys a set of differential equations given by

$$\frac{d\psi}{df} = 2\pi t, \quad \frac{dt}{df} = -\frac{\pi m^2 E'(v_f)}{3v_f^2 \mathcal{F}(v_f)}. \quad (8.4)$$

In the above expressions, including the post-Newtonian expansions of the energy and flux functions, the parameter $v_f = (\pi m f)^{1/3}$. The waveform Eq.(8.3) computed by numerically solving the differential equations Eq.(8.4) is called *TaylorF1* [247] approximant.

Before we proceed further, let us recall the notation used in post-Newtonian theory to identify different orders in the expansion. In the conservative dynamics of the binary, wherein there is no dissipation, the energy is expressed as a post-Newtonian expansion in $\epsilon = (v/c)^2$, with the dominant order termed Newtonian or 0PN and a correction at order $\epsilon^n = (v/c)^{2n}$, $n = 1, 2, \dots$, called n PN, with the dynamics involving only even powers of $\sqrt{\epsilon} = (v/c)$. When dissipation is added to the dynamics, then the equation of motion will have terms of both odd and even powers of v/c . Thus, a correction of order $(v/c)^m$ is termed as $(m/2)$ PN.

In the adiabatic approximation of a test-particle orbiting a Schwarzschild black hole, the energy function $E(v)$ is exactly calculable analytically, while the flux function $\mathcal{F}(v)$ is exactly calculable numerically [248, 249, 250, 251]. In addition, $\mathcal{F}(v)$ has been calculated analytically to 5.5PN order [252] by black hole perturbation theory [253]. In contrast, in the case of a general binary including bodies of comparable masses, the energy function $E(v)$ has been calculated recently to 3PN accuracy by a variety of methods [222, 254, 255, 223, 224, 225, 226, 256, 227, 228, 229]. The flux function $\mathcal{F}(v)$, on the other hand, has been calculated to 3.5PN accuracy [257, 258, 259, 258, 260, 259, 261, 262, 230, 92, 91, 263, 264] up to now only by the multipolar-post-Minkowskian method and matching to a post-Newtonian source [221].

The standard approach to the calculation of GW phasing is based on the PN expansions of the binding energy (energy function) and GW luminosity (flux function) truncated at the *same relative* PN order [265]. At the lowest order, it uses only the leading terms in the energy (Newtonian) and flux (quadrupolar) functions. For higher order phasing, the energy and flux functions are retained to the same relative PN orders. For example, at 3PN phasing, both the energy and flux functions are given to the same *relative* 3PN order beyond the leading Newtonian order. We refer to this usual physical treatment of the phasing of GWs computed in the adiabatic approximation, and used in the current searches for the radiation from inspiralling compact binaries, as the *standard adiabatic* approximation. We will denote the n PN standard adiabatic approximant as $T(E_{[n]}, \mathcal{F}_n)$, where $[p]$ denotes the integer part of p .

8.1.2. Complete phasing of the adiabatic inspiral: an alternative

As a prelude to go beyond the standard adiabatic approximation, let us consider the phasing of the waves in terms of the equations of motion of the system. To this end, it is

natural to order the PN approximation in terms of its dynamics or acceleration. From the viewpoint of the dynamics, the leading order standard adiabatic approximation is equivalent to using the 0PN (corresponding to 0PN conserved energy) and 2.5PN (corresponding to the Newtonian or 0PN flux) terms in the acceleration ignoring the intervening 1PN and 2PN terms. A complete, mathematically consistent treatment of the acceleration, however, should include *all* PN terms in the acceleration up to 2.5PN, *without any gaps*. We refer to the dynamics of the binary, and the resulting waveform, arising from the latter as the 0PN *complete non-adiabatic* approximation. In contrast, the waveform arising from the former choice, with gaps in the acceleration at 1PN and 2PN, is referred to as the 0PN *standard non-adiabatic* approximation. Extension to higher-order phasing is obvious. At 1PN the standard non-adiabatic approximation would involve acceleration terms at orders 0PN, 1PN, 2.5PN and 3.5PN, whereas the complete non-adiabatic approximation would additionally involve the 2PN and 3PN acceleration terms.

Finally, we propose a simple extension of the above construction to generate a new class of approximants in the adiabatic regime. To understand the construction let us examine the lowest order case. Given the 0PN flux (leading to an acceleration at 2.5PN), one can choose the energy function at 2PN (equivalent to 2PN conservative dynamics) instead of the standard choice 0PN (equivalent to 0PN or Newtonian conservative dynamics). This is the adiabatic analogue of the complete non-adiabatic approximant². Extension to higher PN orders follows naturally. For instance, corresponding to the flux function at 1PN (1.5PN), the dissipative force is at order 3.5PN (4PN), and, therefore, the conservative dynamics, and the associated energy function, should be specified up to order 3PN (4PN). In general, given the flux at n PN-order, a corresponding complete adiabatic approximant is constructed by choosing the energy function at order $[n + 2.5]$ PN, where as mentioned before, $[p]$ denotes the integer part of p . We refer to the dynamics of the binary and the resulting waveform arising from such considerations, as the *complete adiabatic* approximation. We will denote the n PN *complete adiabatic* approximant as $T(E_{[n+2.5]}, \mathcal{F}_n)$.

Before moving ahead the following point is worth emphasizing: The standard adiabatic phasing is, by construction, consistent in the *relative PN* order of its constituent energy and flux functions, and thus *unique* in its ordering of the PN terms. Consequently, one can construct different nonequivalent, but consistent, approximations as discussed in Ref. [247] by choosing to retain the involved functions or re-expand them. The complete adiabatic phasing, on the other hand, is constructed so that it is consistent in spirit with the underlying dynamics, or acceleration, rather than with the relative PN orders of the energy and flux functions. Consequently, it has a unique meaning only when the associated energy and flux functions are used *without any further re-expansions* when working out the phasing formula. As a result, though the complete non-adiabatic approximant is more consistent than the standard non-adiabatic approximant in treating the PN accelerations, in the adiabatic case there is no rigorous sense in which one can

² In this case one may also choose the energy function to 3PN accuracy and construct a complete approximant leading to 3PN acceleration

claim that either of the approximants is more consistent than the other. The important point, as we shall see is that, not only are the two approximants *not* the same but the new complete adiabatic approximants are closer to the exact solution than the standard adiabatic approximants.

These new approximants should be of some interest. They are simple generalizations of the standard adiabatic approximants coding information of the PN dynamics beyond the standard approximation without the need for numerical integration of the equations of motion. They should be appropriate approximants to focus on when one goes beyond the adiabatic picture and investigates the differences stemming from the use of more complete equations of motion.

In the case of comparable mass binaries, the energy function is currently known up to 3PN order and hence it would be possible to compute the complete adiabatic phasing of the waves to only 1PN order. One is thus obliged in practice to follow the standard adiabatic approximation to obtain the phasing up to 3.5PN order. Consequently, it is a relevant question to ask how ‘close’ are the complete and standard adiabatic approximants. The standard adiabatic approximation would be justified if we can verify that it produces in most cases a good lower bound to the mathematically consistent, but computationally more demanding, complete adiabatic approximation. In this work, we compare the standard and complete models by explicitly studying their overlaps with the exact waveform which can be computed in the adiabatic approximation of a test mass motion in a Schwarzschild spacetime. The availability, in this case, of the exact (numerical) and approximate (analytical) waveforms to as high a PN order as v^{11} , allows one to investigate the issue exhaustively, and provides the main motivation for the present analysis. Assuming that the comparable mass case is qualitatively similar and a simple η -distortion of the test mass case would then provide a plausible justification for the standard adiabatic treatment of the GW phasing employed in the literature³.

8.1.3. What this study is about

We will use the *effectualness* and *faithfulness* (see below) to quantify how good the various approximation schemes are. There are at least three different contexts in which one can examine the performance of an approximate template family relative to an exact one. Firstly, one can think of a mathematical family of approximants and examine its convergence towards some exact limit. Secondly, one can ask whether this mathematical family of approximants correctly represents the GWs from some physical system. Thirdly, how does this family of approximate templates converge to the exact solution in the sensitive bandwidth of a particular GW detector. In the context of GW data analysis, the third context will be relevant and studied in this chapter. Although there is no direct application to GW data analysis, equally interesting is the mathematical

³Note, however, that the view that the comparable mass case is just a η -distortion of the test mass approximation is not universal. In particular, Blanchet [266] has argued that the dynamics of a binary consisting of two bodies of comparable masses is very different from, and possibly more accurately described by post-Newtonian expansion than, the test mass case.

question concerning the behavior of different approximations, and the waveforms they predict, in the strongly non-linear regime of the dynamics of the binary, which is also studied in this work. The latter obviously does not require the details of the detector-sensitivity and it is enough to study the problem assuming a flat power spectral density (i.e. a *white-noise* background) for the detector noise.

To summarize, our approach towards the problem will be two-pronged. First, we will study the problem as a general mathematical question concerning the nature of templates defined using PN approximation methods. We shall deal with two families of PN templates – the standard adiabatic and complete adiabatic approximants – and examine their closeness, defined by using effectualness and faithfulness, to the exact waveform defined in the adiabatic approximation. Since this issue is a general question independent of the characteristics of a particular GW detector, we first study the problem assuming the white-noise case. Having these results, we then proceed to see how and which of these results are applicable to the noise spectra of three detectors, namely the Initial LIGO, Advanced LIGO, and Virgo. During the course of this study, we also attempt to assess the relative importance of improving the accuracy of the energy and flux functions by studying the overlaps of the PN templates constructed from different orders of energy and flux functions with the exact waveform. It should be kept in mind that this work is solely restricted to the inspiral part of the signal and neglects the plunge and quasi-normal mode ringing phases of the binary [267, 268, 269, 247, 270, 271, 272].

8.1.4. Effectualness and faithfulness

In order to measure the accuracy of our approximate templates we shall compute their overlap with a fiducial exact signal. We shall consider two types of overlaps [167, 273, 247, 274]. The first one is the *faithfulness* which is the overlap of the approximate template with the exact signal computed by keeping the intrinsic parameters (e.g. the masses of the two bodies) of both the template and the signal to be the same but maximizing over the extrinsic (e.g. the time-of-arrival and the phase at that time) parameters. i.e., if h is the exact signal and $u(\boldsymbol{\mu}, \boldsymbol{\nu})$ is a template family parametrised by a set of intrinsic parameters $\boldsymbol{\mu}$ and extrinsic parameters $\boldsymbol{\nu}$, the faithfulness is defined by

$$\mathbb{F} = \max_{\boldsymbol{\nu}} \frac{\langle h, u(\boldsymbol{\mu}, \boldsymbol{\nu}) \rangle}{\sqrt{\langle h, h \rangle} \sqrt{\langle u(\boldsymbol{\mu}, \boldsymbol{\nu}), u(\boldsymbol{\mu}, \boldsymbol{\nu}) \rangle}}, \quad (8.5)$$

where the inner product is defined as

$$\langle h, u(\boldsymbol{\mu}, \boldsymbol{\nu}) \rangle = 4 \operatorname{Re} \int_{f_{\text{low}}}^{f_{\text{cut}}} \frac{\tilde{h}(f) \tilde{u}^*(f; \boldsymbol{\mu}, \boldsymbol{\nu})}{S_h(f)} df. \quad (8.6)$$

In the above expression, $\tilde{h}(f)$ and $\tilde{u}(f; \boldsymbol{\mu}, \boldsymbol{\nu})$ denote the Fourier transforms of the (time-domain) exact signal and the template waveform, $S_h(f)$ is the one-sided power spectral density (PSD) of the detector noise, and, f_{low} and f_{cut} denote the lower and upper cutoff frequencies of the template waveform.

The second type of overlap that we consider is the *effectualness* (also called *fitting factor*, FF) which is the overlap of the approximate template with the exact signal computed by maximizing the overlap over both the intrinsic and extrinsic parameters. i.e.,

$$\text{FF} = \max_{\boldsymbol{\nu}, \boldsymbol{\mu}} \frac{\langle h, u(\boldsymbol{\mu}, \boldsymbol{\nu}) \rangle}{\sqrt{\langle h, h \rangle} \sqrt{\langle u(\boldsymbol{\mu}, \boldsymbol{\nu}), u(\boldsymbol{\mu}, \boldsymbol{\nu}) \rangle}}. \quad (8.7)$$

Faithfulness is a measure of how good is the template waveform in both detecting a signal and measuring its parameters. However, effectualness is aimed at finding whether or not an approximate template model is good enough in detecting a signal without reference to its use in estimating the parameters. As in previous studies, we take overlaps greater than 96.5% to be indicative of a good approximation.

8.1.5. Noise spectra of the interferometers

The performance of the standard and complete adiabatic approximants are studied using the noise spectra of three different interferometric detectors, namely Initial LIGO, Advanced LIGO and Virgo. Analytical fits of the design noise spectra of these interferometers are given in the literature. We use these analytical fits for our calculations. These are plotted in Figure 8.1

The one-sided noise PSD (per Hz) of the initial LIGO is given in terms of a dimensionless frequency $x = f/f_0$ by [247],

$$S_h(x) = 9 \times 10^{-46} [(4.49x)^{-56} + 0.16x^{-4.52} + 0.52 + 0.32x^2], \quad (8.8)$$

where $f_0 = 150$ Hz and the PSD rises steeply above a lower cut-off $f_c = 40$ Hz. The one-sided PSD of Virgo is given by [247]

$$S_h(f) = 3.24 \times 10^{-46} [(6.23x)^{-5} + 2x^{-1} + 1 + x^2], \quad (8.9)$$

where $f_0 = 500$ Hz; while the same for the Advanced LIGO reads [44, 275]

$$S_h(f) = 10^{-49} \left[x^{-4.14} - 5x^{-2} + 111 \left(\frac{1 - x^2 + x^4/2}{1 + x^2/2} \right) \right], \quad (8.10)$$

where $f_0 = 215$ Hz.

8.1.6. Organization of this chapter

In the next section we study the test-mass waveforms in the adiabatic approximation. We discuss the construction of the exact energy and flux functions as well as the respective T-approximants. The overlaps of various standard adiabatic and complete adiabatic approximants are also compared in this section. Section 8.3 explores the extension of the results in the comparable mass case. It presents the energy and flux functions which are the crucial inputs for the construction of the fiducial ‘exact’ waveform as well as the

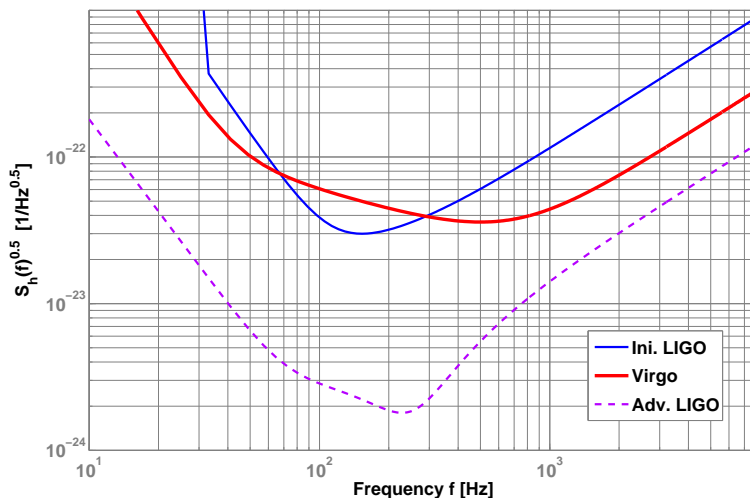


Figure 8.1.: Amplitude noise spectral densities of three ground-based interferometric detectors.

approximate waveforms followed by a discussion of the results. In the last section we summarize our main conclusions.

One of the main conclusions of this study is that the effectualness of the test-mass approximants significantly improves in the complete adiabatic approximation at PN orders below 3PN. However, standard adiabatic approximants of order ≥ 3 PN are nearly as good as the complete adiabatic approximants for the construction of effectual templates. In the comparable mass case the problem can be only studied at the lowest two PN orders. No strong conclusions can be drawn as in the test mass case. Still, the trends indicate that the standard adiabatic approximation provides a good lower bound to the complete adiabatic approximation for the construction of both effectual and faithful templates at PN orders ≥ 1.5 PN. From the detailed study of test-mass templates we also conclude that, provided the comparable mass case is qualitatively similar to the test mass case, neither the improvement of the accuracy of energy function from 3PN to 4PN nor the improvement of the accuracy of flux function from 3.5PN to 4PN will result in a significant improvement in effectualness in the comparable mass case. As far as faithfulness is concerned, it is hard to reach any conclusion. To achieve the target sensitivity of 0.965 in effectualness corresponding to a 10% loss in the event-rate, standard adiabatic approximants of order 2PN and 3PN are required for the $(10M_{\odot}, 10M_{\odot})$ and $(1.4M_{\odot}, 1.4M_{\odot})$ binaries, respectively, when restricting to only the inspiral phase. (Be warned that this is not a good approximation in the BH-BH case since the approach to the plunge and merger lead to significant differences.)

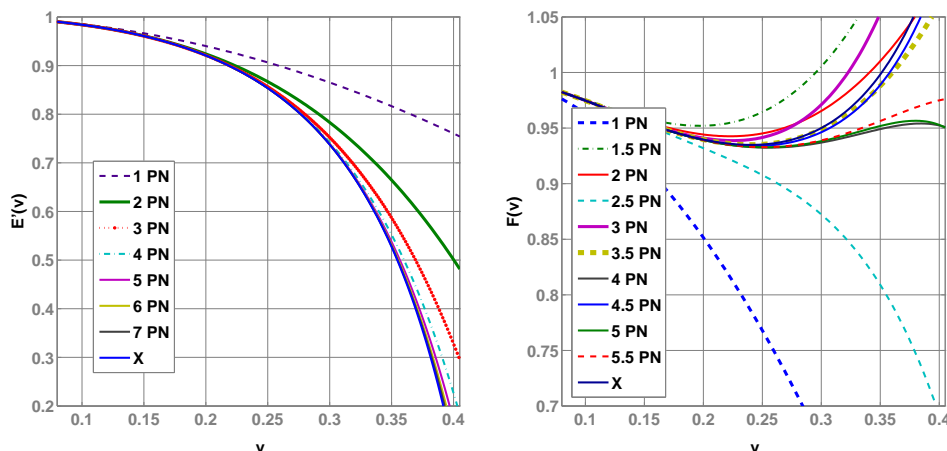


Figure 8.2.: Various T-approximants of Newton-normalized (v -derivative of) energy function $E'_T(v)/E'_N(v)$ [left], and flux function $\mathcal{F}_T(v)/\mathcal{F}_N(v)$ [right] in the test mass limit along with the exact functions (denoted by X).

8.2. Test mass waveforms in the adiabatic approximation

Our objective is to compare the *effectualness* (i.e. larger overlaps with the exact signal) and *faithfulness* (i.e. smaller bias in the estimation of parameters) of the standard adiabatic $T(E_{[n]}, \mathcal{F}_n)$ and complete adiabatic $T(E_{[n+2.5]}, \mathcal{F}_n)$ approximants. The exact waveform is constructed by numerically integrating the phasing formula in the time-domain [*TaylorT1* approximant, cf. Eqs. (8.1) and (8.2)]. Both the exact and approximate waveforms are terminated at $v_{\text{iso}} = 1/\sqrt{6}$, which corresponds to $F_{\text{iso}} \simeq 43$ Hz for the $(1M_\odot, 100M_\odot)$ binary, $F_{\text{iso}} \simeq 86$ Hz for the $(1M_\odot, 50M_\odot)$ binary and $F_{\text{iso}} \simeq 399$ Hz for the $(1M_\odot, 10M_\odot)$ binary⁴. The lower frequency cut-off of the waveforms is chosen to be $F_{\text{low}} = 20$ Hz.

In this study, we restrict to approximants TaylorT1 and TaylorF1 since they do not involve any further re-expansion in the phasing formula and hence there is no ambiguity when we construct the phasing of the waves using approximants with unequal orders of the energy and flux functions.

8.2.1. The energy function

In the case of a test-particle m_2 moving in circular orbit in the background of a Schwarzschild black hole of mass m_1 , where $m_2/m_1 \rightarrow 0$, the energy function $E(x)$

⁴Here, v_{iso} is the velocity at the last stable circular orbit of Schwarzschild geometry having the same mass as the total mass $m_1 + m_2$ of the binary, and F_{iso} is the GW frequency corresponding to it.

in terms of the invariant argument $x \equiv v^2$ is given by

$$E_{\text{exact}}(x) = \eta \frac{1 - 2x}{\sqrt{1 - 3x}}, \quad (8.11)$$

The associated v -derivative entering the phasing formula is

$$E'_{\text{exact}}(v) = 2v \left. \frac{dE(x)}{dx} \right|_{x=v^2} = -\eta v \frac{(1 - 6v^2)}{(1 - 3v^2)^{3/2}}. \quad (8.12)$$

We use the above exact $E'(v)$ to construct the exact waveform in the test-mass case. In order to construct various approximate PN templates, we Taylor-expand $E'_{\text{exact}}(v)$ and truncate it at the necessary orders.

$$E'_{7PN}(v) = -\eta v \left[1 - \frac{3v^2}{2} - \frac{81v^4}{8} - \frac{675v^6}{16} - \frac{19845v^8}{128} - \frac{137781v^{10}}{256} - \frac{1852389v^{12}}{1024} - \frac{12196899v^{14}}{2048} + \mathcal{O}(v^{16}) \right]. \quad (8.13)$$

Different T-approximants of the energy function $E'_T(v)$ along with $E'_{\text{exact}}(v)$ are plotted in Figure 8.2 [left].

8.2.2. The flux function

In the test-particle limit, the exact gravitational-wave flux has been computed numerically with good accuracy [249]. We will use this flux function (see Figure 8.2 [right]), along with the energy function given by Eq. (8.12), to construct an exact waveform in the test-mass case. In the test-particle limit, the GW flux is also known analytically to 5.5PN order from black hole perturbation theory [252] and given by

$$\mathcal{F}(v) = \frac{32}{5} \eta^2 v^{10} \left[\sum_{k=0}^{11} A_k v^k + \left(\sum_{m=6}^{11} B_m v^m \right) \ln v + \mathcal{O}(v^{12}) \right], \quad (8.14)$$

where the various coefficients A_k and B_k are [252],

$$\begin{aligned} A_0 &= 1, \quad A_1 = 0, \quad A_2 = -\frac{1247}{336}, \quad A_3 = 4\pi, \quad A_4 = -\frac{44711}{9072}, \quad A_5 = -\frac{8191\pi}{672}, \\ A_6 &= \frac{6643739519}{69854400} + \frac{16\pi^2}{3} - \frac{1712\gamma}{105} - \frac{1712\ln 4}{105}, \quad A_7 = -\frac{16285\pi}{504}, \\ A_8 &= -\frac{323105549467}{3178375200} + \frac{232597\gamma}{4410} - \frac{1369\pi^2}{126} + \frac{39931\ln 2}{294} - \frac{47385\ln 3}{1568}, \\ A_9 &= \frac{265978667519\pi}{745113600} - \frac{6848\gamma\pi}{105} - \frac{13696\pi\ln 2}{105}, \\ A_{10} &= -\frac{2500861660823683}{2831932303200} + \frac{916628467\gamma}{7858620} - \frac{424223\pi^2}{6804} - \frac{83217611\ln 2}{1122660} + \frac{47385\ln 3}{196}, \\ A_{11} &= \frac{8399309750401\pi}{101708006400} + \frac{177293\gamma\pi}{1176} + \frac{8521283\pi\ln 2}{17640} - \frac{142155\pi\ln 3}{784}, \end{aligned}$$

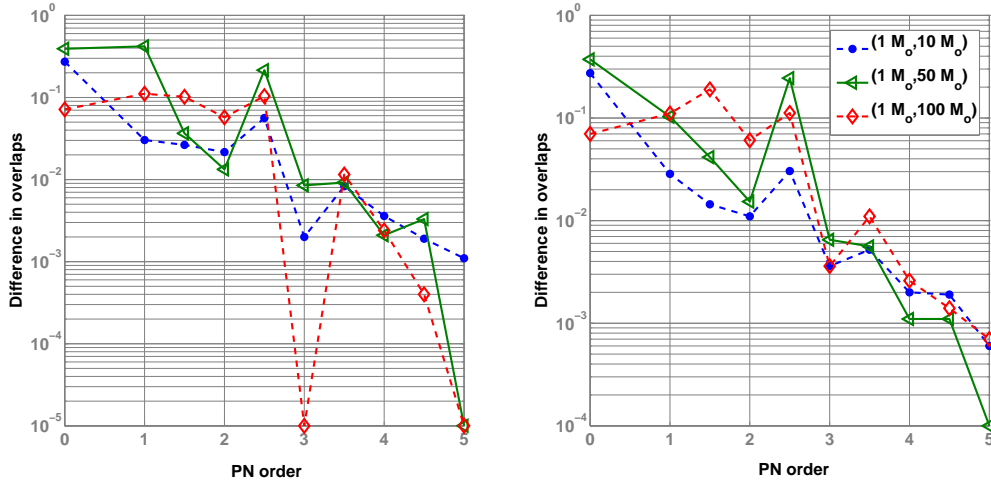


Figure 8.3.: The difference, $FF_C - FF_S$, in the effectualness of complete adiabatic and standard adiabatic templates in the test mass limit. Overlaps are calculated assuming a flat spectrum for the detector noise (white noise). Plots on the left correspond to TaylorT1 approximants, while plots on the right correspond to TaylorF1 approximants.

$$\begin{aligned}
 B_6 &= -\frac{1712}{105}, \quad B_7 = 0, \quad B_8 = \frac{232597}{4410}, \quad B_9 = \frac{-6848\pi}{105}, \\
 B_{10} &= \frac{916628467}{7858620}, \quad B_{11} = \frac{177293\pi}{1176}.
 \end{aligned} \tag{8.15}$$

We will use the energy and flux functions given by Eq. (8.13) – Eq. (8.15) to construct various approximate templates by truncating the expansions at the necessary order. The different T-approximants of the flux function $\mathcal{F}_T(v)$ along with the (numerical) exact flux $\mathcal{F}_{\text{exact}}(v)$ are plotted in Figure 8.2 [right].

8.2.3. Comparison of standard and complete adiabatic approximants

We present the results of our study in the test mass limit in four parts. In the first part we discuss our conclusions on the mathematical problem of the closeness of the standard adiabatic and complete adiabatic template families with the family of exact waveforms in the adiabatic approximation. In the next part we exhibit our results in the case of three ground-based detectors. In the third part we compare the relative importance of improving the accuracy of the energy and flux functions. Finally, in the fourth part we compare the total number of GW cycles and the number of useful cycles accumulated by various standard adiabatic and complete adiabatic approximants.

Table 8.1.: Effectualness of standard (S) and complete (C) adiabatic templates in the test mass limit. Overlaps are calculated assuming a flat spectrum for the detector noise (white noise).

Order (n)	TaylorT1		TaylorF1	
	S	C	S	C
$(1M_{\odot}, 10M_{\odot})$				
0PN	0.6250	0.8980	0.6212	0.8949
1PN	0.4816	0.5119	0.4801	0.5086
1.5PN	0.9562	0.9826	0.9448	0.9592
2PN	0.9685	0.9901	0.9514	0.9624
2.5PN	0.9362	0.9924	0.9298	0.9602
3PN	0.9971	0.9991	0.9677	0.9713
3.5PN	0.9913	0.9996	0.9636	0.9688
4PN	0.9937	0.9973	0.9643	0.9663
4.5PN	0.9980	0.9999	0.9671	0.9690
5PN	0.9968	0.9979	0.9661	0.9667
$(1M_{\odot}, 50M_{\odot})$				
0PN	0.5809	0.9726	0.5917	0.9644
1PN	0.4913	0.9107	0.4841	0.5871
1.5PN	0.9466	0.9832	0.9370	0.9785
2PN	0.9784	0.9917	0.9719	0.9872
2.5PN	0.7684	0.9833	0.7326	0.9772
3PN	0.9861	0.9946	0.9821	0.9886
3.5PN	0.9902	0.9994	0.9858	0.9914
4PN	0.9975	0.9996	0.9903	0.9914
4.5PN	0.9967	1.0000	0.9902	0.9913
5PN	0.9994	0.9994	0.9913	0.9914
$(1M_{\odot}, 100M_{\odot})$				
0PN	0.8515	0.9231	0.8318	0.9017
1PN	0.8059	0.9169	0.7874	0.8980
1.5PN	0.8963	0.9981	0.7888	0.9788
2PN	0.9420	0.9993	0.9178	0.9785
2.5PN	0.8819	0.9858	0.8610	0.9730
3PN	0.9965	0.9959	0.9756	0.9792
3.5PN	0.9885	1.0000	0.9690	0.9800
4PN	0.9968	0.9992	0.9769	0.9795
4.5PN	0.9996	1.0000	0.9787	0.9801
5PN	0.9992	0.9991	0.9790	0.9797

Table 8.2.: Faithfulness of standard (S) and complete (C) adiabatic templates in the test mass limit. Overlaps are calculated assuming a flat spectrum for the detector noise (white noise).

Order (n)	TaylorT1		TaylorF1	
	S	C	S	C
$(1M_{\odot}, 10M_{\odot})$				
0PN	0.6124	0.1475	0.6088	0.1446
1PN	0.1322	0.1433	0.1350	0.1461
1.5PN	0.5227	0.4005	0.5241	0.3967
2PN	0.7687	0.5707	0.7680	0.5689
2.5PN	0.4735	0.5268	0.4748	0.5278
3PN	0.8629	0.8165	0.8932	0.8277
3.5PN	0.9309	0.9979	0.9194	0.9609
4PN	0.9174	0.9303	0.9087	0.9176
4.5PN	0.9525	0.9744	0.9330	0.9415
5PN	0.9370	0.9392	0.9225	0.9241
$(1M_{\odot}, 50M_{\odot})$				
0PN	0.2045	0.4683	0.2104	0.4750
1PN	0.1182	0.1446	0.1236	0.1508
1.5PN	0.3444	0.3947	0.3505	0.3866
2PN	0.5518	0.6871	0.5535	0.6827
2.5PN	0.2874	0.3561	0.2933	0.3625
3PN	0.9420	0.6317	0.9334	0.6222
3.5PN	0.6689	0.9681	0.6695	0.9632
4PN	0.6693	0.7227	0.6701	0.7230
4.5PN	0.7829	0.9242	0.7827	0.9229
5PN	0.7275	0.7417	0.7276	0.7420
$(1M_{\odot}, 100M_{\odot})$				
0PN	0.2098	0.4534	0.2208	0.4641
1PN	0.1395	0.1901	0.1432	0.1994
1.5PN	0.3260	0.7869	0.3399	0.7700
2PN	0.4377	0.8528	0.4506	0.8486
2.5PN	0.2787	0.4001	0.2918	0.4133
3PN	0.7579	0.8407	0.7570	0.8194
3.5PN	0.5740	0.9425	0.5805	0.9383
4PN	0.6129	0.7112	0.6236	0.7159
4.5PN	0.7286	0.9689	0.7308	0.9632
5PN	0.6972	0.7409	0.7027	0.7500

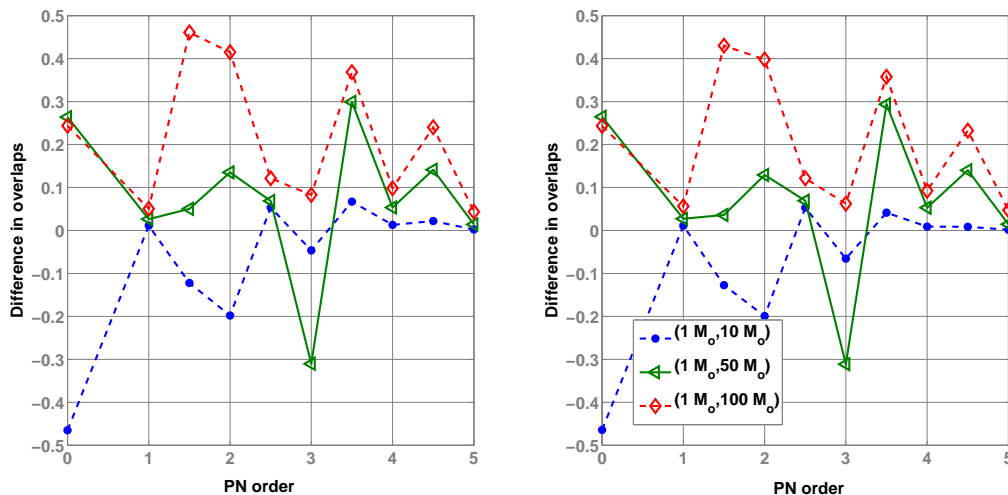


Figure 8.4.: The difference, $\mathbb{F}_C - \mathbb{F}_S$, in the faithfulness of complete adiabatic and standard adiabatic templates in the test mass limit. Overlaps are calculated assuming a flat spectrum for the detector noise (white noise). Plots on the left correspond to TaylorT1 approximants, while plots on the right correspond to TaylorF1 approximants.

White-noise case

First, we explore the general question of the closeness of the standard adiabatic and complete adiabatic templates to the exact waveform assuming flat power spectral density for the detector noise. The effectualness and faithfulness of various standard and complete adiabatic approximants are tabulated in Tables 8.1 and 8.2, respectively. These values correspond to three archetypal binaries with component masses ($1M_\odot, 10M_\odot$), ($1M_\odot, 50M_\odot$) and ($1M_\odot, 100M_\odot$). Also, in Figure 8.3, we plot the difference, $\mathbb{F}\mathbb{F}_C - \mathbb{F}\mathbb{F}_S$, in the effectualness between the complete and standard approximants. The difference, $\mathbb{F}_C - \mathbb{F}_S$, in faithfulness between the complete and standard approximants are plotted in Figure 8.4.

The central result of this study is that *complete adiabatic approximants bring about a remarkable improvement in the effectualness for all systems at low PN orders ($< 3PN$)*. The complete adiabatic approximants converge to the adiabatic exact waveform at lower PN orders than the standard adiabatic approximants. This indicates that at these orders general relativistic corrections to the conservative dynamics of the binary are quite important contrary to the assumption employed in the standard post-Newtonian treatment of the phasing formula. On the other hand, the difference in effectualness between the standard and complete adiabatic approximants at orders greater than 3PN is very small. Thus, *if we have a sufficiently accurate (order $\geq 3PN$) T -approximant of the flux function, the standard adiabatic approximation is nearly as good as the complete adiabatic approximation for construction of effectual templates*. But at all orders the

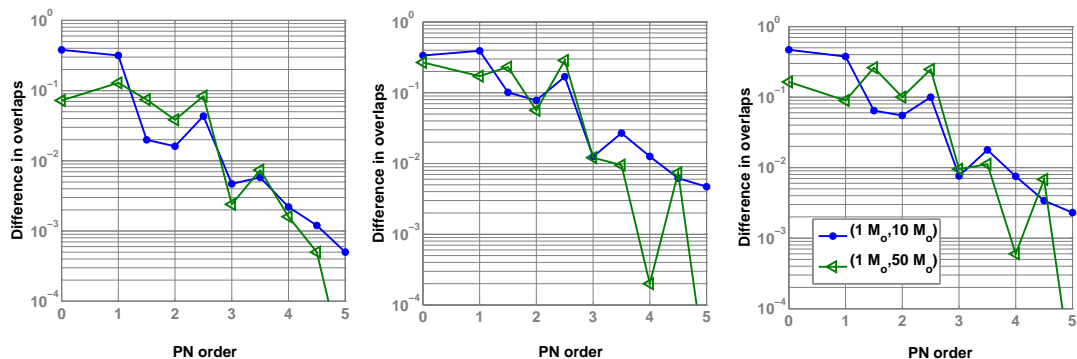


Figure 8.5.: The difference, $FF_C - FF_S$, in the effectualness between complete adiabatic and standard adiabatic templates in the test mass limit. The plots correspond to overlaps calculated using three different noise spectra — Initial LIGO (left), Virgo (middle), and Advanced LIGO (right).

standard adiabatic approximation provides a lower bound to the complete adiabatic approximation for the construction of *effectual* templates.

The faithfulness of both the approximants fluctuates as we go from one PN order to the next and is generally much smaller than our target value of 0.965. The fluctuation continues all the way up to 5PN order reflecting the oscillatory approach of the flux function to the exact flux function at different PN orders. It is again interesting to note that complete adiabatic approximants are generally more faithful than the standard adiabatic approximants.

Initial LIGO, Virgo and Advanced LIGO studies

Having addressed the general question concerning the closeness of standard adiabatic and complete adiabatic templates to the exact waveforms, we now compare the overlaps in the specific cases of three ground-based detectors, namely, Initial LIGO, Virgo and Advanced LIGO. The effectualness and faithfulness of various standard and complete adiabatic approximants in the test mass limit are tabulated in Tables 8.3 and 8.4. Also, the difference, $FF_C - FF_S$, in the effectualness between complete adiabatic and standard adiabatic templates is plotted in Figure 8.5, while the difference $\mathbb{F}_C - \mathbb{F}_S$, in the faithfulness is plotted in Figure 8.6.

As in the case of white noise, here too we see that standard adiabatic approximants of order less than 3PN have considerably lower overlaps than the corresponding complete adiabatic approximants, and that the difference in overlaps between standard adiabatic and complete adiabatic approximants of order ≥ 3 PN is very small. Thus, as in the white-noise case, if we have a sufficiently accurate (order ≥ 3 PN) T-approximant of the flux function, the standard adiabatic approximation is nearly as good as the complete adiabatic approximation for the construction of effectual templates. Unlike in

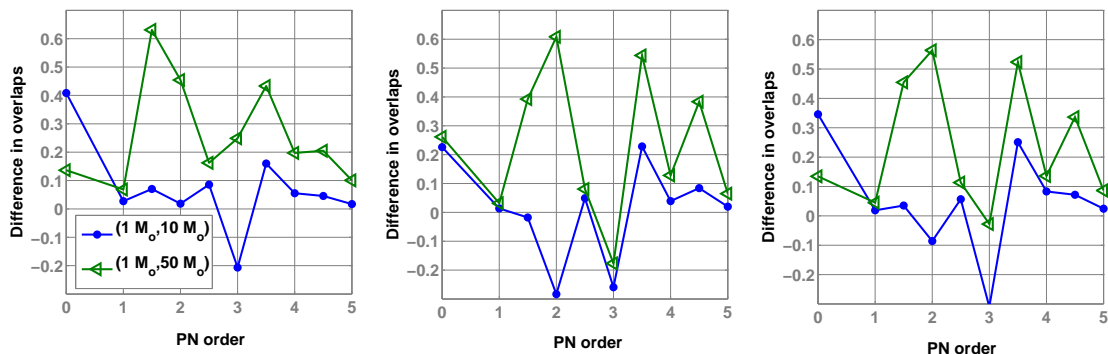


Figure 8.6.: The difference, $\mathbb{F}_C - \mathbb{F}_S$, in the faithfulness between complete adiabatic and standard adiabatic templates in the test mass limit. The plots correspond to overlaps calculated using three different noise spectra — Initial LIGO (left), Virgo (middle), and Advanced LIGO (right).

the white-noise case, in the case of real interferometer noise spectra, the plots and Table 8.4 indicate that the faithfulness of PN templates generally improves in the complete adiabatic treatment, for almost all orders studied. But there are some cases of anomalous behavior. In the next subsection we will try to understand the reason for these anomalous cases where the complete approximants perform worse than the standard.

We also calculate the bias in the estimation of parameters while maximizing the overlaps over the intrinsic parameters of the binary. The (percentage) bias in the estimation of the parameter p is defined as

$$\sigma_p \equiv \frac{|p_{\max} - p|}{p} \times 100, \quad (8.16)$$

where p_{\max} is the value of the parameter p which gives the maximum overlap. Along with the maximized overlaps (effectualness), the bias in the estimation of the parameters m and η are also quoted in Table 8.3. It can be seen that at lower PN orders (order < 3 PN) the complete adiabatic approximants show significantly lower biases. Even at higher PN orders complete adiabatic approximants are generally less-biased than the corresponding standard adiabatic approximants.

Understanding the results

Table 8.5 summarizes the PN orders showing the anomalous behavior (i.e. the complete approximants being less faithful than the standard approximants) for the different noise spectra studied by us. The best-sensitivity bandwidth of each detector is shown in brackets⁵. The left-most column in the table shows the flattest noise spectrum and the

⁵It should be noted that there is no rigorous definition for the ‘best-sensitivity’ bandwidth. We define it as the bandwidth where the detector’s effective noise amplitude $h = \sqrt{fS_h(f)}$ is within a factor of two of its lowest value.

Table 8.3.: Effectualness of standard (S) and complete (C) adiabatic approximants in the test mass limit. Percentage biases σ_m and σ_η in determining parameters m and η are given in brackets.

Order (n)	$(1M_\odot, 10M_\odot)$		$(1M_\odot, 50M_\odot)$	
	S	C	S	C
Initial LIGO				
0PN	0.5910 (12, 5.7)	0.9707 (36, 45)	0.8748 (24, 29)	0.9471 (19, 14)
1PN	0.5232 (22, 105)	0.8397 (125, 69)	0.8101 (28, 104)	0.9392 (19, 40)
1.5PN	0.9688 (52, 51)	0.9887 (8.3, 15)	0.9254 (21, 4.1)	0.9996 (6.7, 20)
2PN	0.9781 (18, 25)	0.9942 (0.4, 0.6)	0.9610 (18, 16)	0.9993 (7.5, 16)
2.5PN	0.9490 (96, 68)	0.9923 (26, 32)	0.9104 (21, 6.9)	0.9940 (8.3, 0.7)
3PN	0.9942 (0.3, 1.1)	0.9989 (3.7, 6.2)	0.9968 (11, 21)	0.9992 (2.6, 10)
3.5PN	0.9940 (6.9, 11)	0.9998 (0.6, 1.4)	0.9923 (13, 19)	0.9997 (2.4, 5.2)
4PN	0.9974 (6.2, 11)	0.9996 (3.9, 6.9)	0.9979 (8.8, 13)	0.9995 (3.5, 4.3)
4.5PN	0.9988 (3.3, 5.5)	1.0000 (0.8, 1.6)	0.9995 (7.1, 14)	1.0000 (0.9, 1.9)
5PN	0.9992 (4.0, 6.9)	0.9997 (3.5, 5.7)	0.9994 (5.2, 7.7)	0.9990 (2.6, 2.4)
Advanced LIGO				
0PN	0.4281 (9.2, 2.6)	0.8960 (32, 42)	0.6461 (27, 22)	0.8099 (48, 54)
1PN	0.3498 (28, 8.9)	0.7258 (156, 75)	0.6200 (25, 123)	0.7093 (27, 13)
1.5PN	0.9010 (48, 49)	0.9653 (11, 21)	0.6919 (27, 20)	0.9532 (2.0, 8.7)
2PN	0.9266 (14, 20)	0.9814 (2.6, 4.2)	0.8835 (31, 39)	0.9833 (6.3, 13)
2.5PN	0.8917 (89, 66)	0.9913 (26, 31.7)	0.6720 (26, 6.2)	0.9194 (17, 21)
3PN	0.9913 (0.7, 1.6)	0.9989 (3.9, 7.3)	0.9645 (8.4, 16)	0.9740 (1.4, 1.4)
3.5PN	0.9816 (4.5, 7.4)	0.9994 (0.4, 0.3)	0.9875 (14, 23)	0.9987 (2.0, 3.9)
4PN	0.9895 (4.2, 7.1)	0.9970 (3.0, 5.3)	0.9967 (9.5, 16)	0.9973 (4.4, 6.9)
4.5PN	0.9965 (2.1, 3.6)	0.9999 (0.8, 1.6)	0.9932 (6.1, 11)	1.0000 (0.9, 1.9)
5PN	0.9954 (2.9, 5.2)	0.9977 (2.6, 4.0)	0.9986 (5.7, 9.9)	0.9960 (3.6, 6.2)
Virgo				
0PN	0.3894 (42, 41)	0.7256 (0.8, 3.8)	0.6004 (50, 25)	0.8689 (51, 56)
1PN	0.2956 (11, 6.5)	0.6876 (187, 80)	0.5498 (51, 30)	0.7217 (52, 28)
1.5PN	0.8474 (31, 37)	0.9487 (12, 22)	0.7308 (56, 53)	0.9619 (1.1, 6.9)
2PN	0.8933 (9.9, 15)	0.9711 (3.0, 4.6)	0.9291 (34, 43)	0.9854 (5.4, 12)
2.5PN	0.8179 (69, 59)	0.9864 (26, 32)	0.6579 (49, 41)	0.9446 (19, 23)
3PN	0.9845 (0.6, 1.5)	0.9970 (3.8, 7.3)	0.9697 (7.4, 14)	0.9818 (1.5, 1.5)
3.5PN	0.9722 (4.3, 7.2)	0.9991 (0.4, 0.3)	0.9885 (14, 22)	0.9980 (1.9, 3.8)
4PN	0.9829 (4.1, 7.1)	0.9955 (2.9, 5.2)	0.9971 (9.5, 16)	0.9973 (4.4, 6.9)
4.5PN	0.9937 (2.0, 3.5)	0.9999 (0.8, 1.6)	0.9926 (6.0, 11)	1.0000 (0.9, 1.9)
5PN	0.9920 (3.0, 5.3)	0.9967 (2.6, 4.1)	0.9987 (5.7, 10)	0.9960 (3.5, 6.2)

Table 8.4.: Faithfulness of standard (S) and complete (C) adiabatic templates in the test mass limit.

Order (n)	$(1M_{\odot}, 10M_{\odot})$		$(1M_{\odot}, 50M_{\odot})$	
	S	C	S	C
Initial LIGO				
0PN	0.2186	0.6272	0.2134	0.3498
1PN	0.1342	0.1615	0.1511	0.2196
1.5PN	0.3788	0.4492	0.2915	0.9223
2PN	0.7449	0.7633	0.3613	0.8157
2.5PN	0.3115	0.3970	0.2608	0.4233
3PN	0.9633	0.7566	0.7194	0.9686
3.5PN	0.8385	0.9984	0.4941	0.9273
4PN	0.8356	0.8909	0.5960	0.7934
4.5PN	0.9395	0.9851	0.7594	0.9644
5PN	0.8960	0.9129	0.7344	0.8350
Advanced LIGO				
0PN	0.1456	0.4915	0.1608	0.2955
1PN	0.0853	0.1041	0.1159	0.1609
1.5PN	0.2711	0.3063	0.2187	0.6735
2PN	0.6998	0.6140	0.2765	0.8403
2.5PN	0.2143	0.2710	0.1961	0.3094
3PN	0.8889	0.5791	0.7252	0.6971
3.5PN	0.7476	0.9985	0.3852	0.9087
4PN	0.7314	0.8144	0.4404	0.5761
4.5PN	0.9001	0.9718	0.5714	0.9078
5PN	0.8273	0.8518	0.5303	0.6166
Virgo				
0PN	0.1384	0.3644	0.1265	0.3881
1PN	0.0682	0.0818	0.0887	0.1205
1.5PN	0.2524	0.2348	0.1859	0.5783
2PN	0.7451	0.4617	0.2514	0.8597
2.5PN	0.2003	0.2496	0.1612	0.2420
3PN	0.8339	0.5745	0.7978	0.6210
3.5PN	0.7684	0.9968	0.3821	0.9259
4PN	0.7501	0.7892	0.4024	0.5306
4.5PN	0.8753	0.9595	0.5298	0.9132
5PN	0.8033	0.8232	0.4968	0.5617

Table 8.5.: PN orders showing anomalous behavior in the context of different noise spectra. The best-sensitivity bandwidth of each detector is shown in brackets. Label A corresponds to the $(1M_{\odot}, 10M_{\odot})$ binary and label B to the $(1M_{\odot}, 50M_{\odot})$ binary.

White-noise		Virgo (50-400 Hz)		Advanced LIGO (60-300 Hz)		Initial LIGO (80-200 Hz)	
A	B	A	B	A	B	A	B
0PN							
1.5PN		1.5PN					
2PN		2PN		2PN			
3PN	3PN	3PN	3PN	3PN	3PN	3PN	

right-most column shows the narrowest one.

In order to understand the anomalous behavior shown at certain PN orders, we compare the approximants of the $\mathcal{F}(v)/E'(v)$ function with the corresponding exact function. Figure 8.7 shows the standard and complete approximants of $\hat{\mathcal{F}}(v)/\hat{E}'(v)$ along with the exact functions, where a ‘hat’ indicates the corresponding Newton-normalized quantity. These results show that, while the complete approximants are far superior to the standard approximants in modelling the late-inspiral, the early inspiral is better modelled by the standard approximants at these PN orders. In the case of the $(1M_{\odot}, 10M_{\odot})$ binary, the 0PN standard approximant is closer to the exact function than the corresponding complete approximant in the frequency region 20-50 Hz. But, since none of the detectors is sensitive in this frequency band, this effect shows up in the white-noise case only. Similarly the 1.5PN and 2PN standard approximants are closer to the exact function in the frequency regions 20-60 Hz and 20-80 Hz, respectively. But the 1.5PN approximant does not show the anomalous behavior in the case of the Advanced LIGO and Initial LIGO because the 20-60 Hz region does not fall in the best-sensitivity bandwidth of these detectors. The anomalous behavior exhibited by the 3PN approximant can be understood in a similar way. It should be noted that the final stages of the inspiral is much better modelled by the complete approximants (see the top panel of Figure 8.7).

Accuracy of energy function Vs. flux function

In this section, we study the relative importance of improving the accuracy of the energy function and the flux function. We take all possible combinations of T-approximants of energy and flux functions, construct PN templates and calculate the overlap of these templates with the exact waveform. In all cases, the exact waveform is constructed as described in the previous section. The effectualness (left) and faithfulness (right) of various PN approximants corresponding to the $(1M_{\odot}, 10M_{\odot})$ binary are plotted in Figure 8.8 while the same quantities corresponding to the $(1M_{\odot}, 50M_{\odot})$ binary are plotted in Figure 8.9.

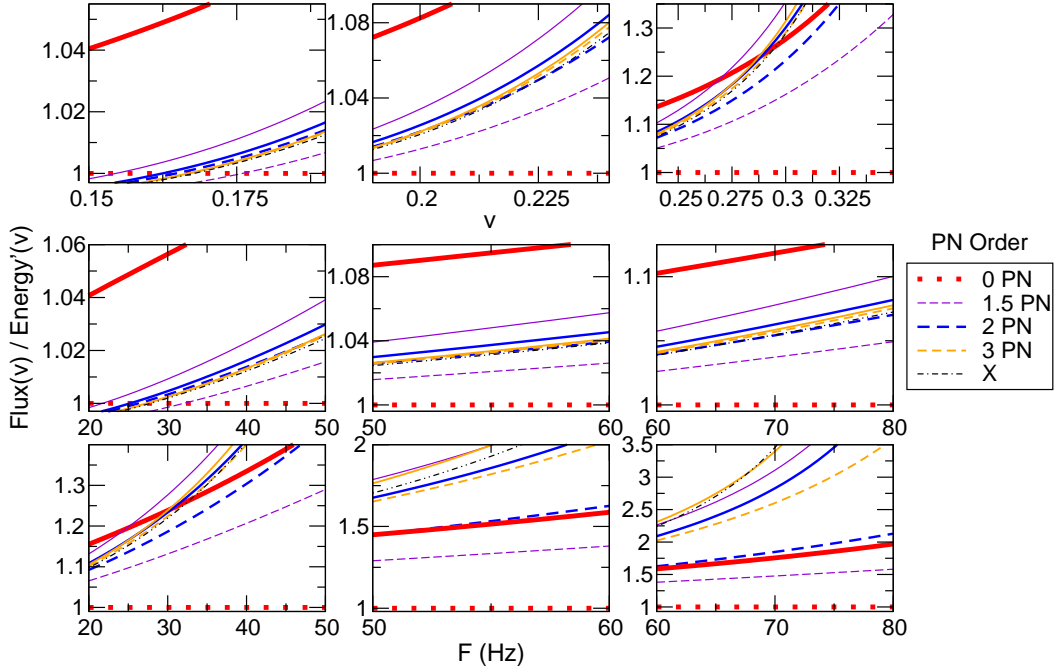


Figure 8.7.: Top panel shows the approximants of $\hat{\mathcal{F}}(v)/\hat{E}'(v)$ plotted as a function of v . Dashed lines indicate standard approximants and solid lines indicate the corresponding complete approximants. Middle and bottom panels show the same approximants plotted as a function of the GW frequency $F = v^3/\pi m$ in the case of the $(1M_{\odot}, 10M_{\odot})$ binary and the $(1M_{\odot}, 50M_{\odot})$ binary, respectively.

In most of the cases, TaylorT1 and TaylorF1 templates show trends of smoothly increasing overlaps as the accuracy of the energy function is increased keeping the accuracy of the flux function constant. This is because the T-approximants of the energy function smoothly converge to the exact energy as we go to higher orders (see the left plot of Figure 8.2). On the other hand, if we improve the accuracy of the flux function for a fixed order of energy, the overlaps do not show such a smoothly converging behavior. This can be understood in terms of the oscillatory nature of the T-approximants of the flux function. For example, templates constructed from 1PN and 2.5PN flux functions can be seen to have considerably lower overlaps than the other ones. This is because of the poor ability of the 1PN and 2.5PN T-approximants to mimic the behavior of the exact flux function (see the right plot of Figure 8.2). This inadequacy of the 1PN and 2.5PN T-approximants is prevalent in both test mass and comparable mass cases. Hence it is not a good strategy to use the T-approximants at these orders for the construction of templates. On the other hand, 3.5PN and 4.5PN T-approximants are greatly successful in following the exact flux function in the test mass case, and consequently lead to larger overlaps.

We have found that in the test mass case if we improve the accuracy of energy function

8.2 Test mass waveforms in the adiabatic approximation

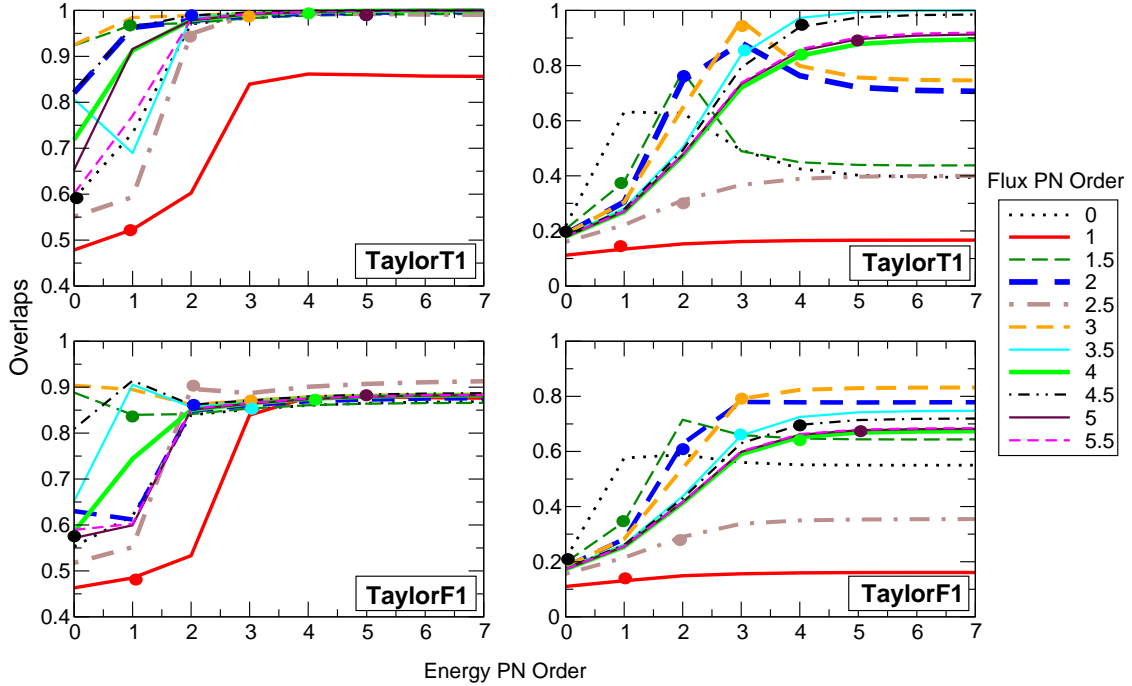


Figure 8.8.: Effectualness (left panels) and faithfulness (right panels) of various test mass TaylorT1 and TaylorF1 templates in detecting a signal from a $(1M_{\odot}, 10M_{\odot})$, calculated for the initial LIGO noise PSD. The horizontal axis reports the order $[n]$ of the energy function, while the legends report the order n of the flux function. Each line shows how the overlaps are evolving as a function of the accuracy of the energy function. Standard adiabatic approximants $T(E_{[n]}, \mathcal{F}_n)$ are marked with thick dots.

from 3PN to 4PN, keeping the flux function at order 3PN, the increase in effectualness (respectively, faithfulness) is $\simeq 0.36\%$ (-16%). The same improvement in the energy function for the 3.5PN flux will produce an increase of $\simeq 0.36\%$ (13%). On the other hand, if we improve the accuracy of flux function from 3.5PN to 4PN, keeping the energy function at order 3PN, the increase in effectualness (respectively, faithfulness) is $\simeq -0.17\%$ (-12%). The values quoted are calculated using the TaylorT1 method for the $(1M_{\odot}, 10M_{\odot})$ binary for the initial LIGO noise PSD. The effectualness trends are similar in the case of the $(1M_{\odot}, 50M_{\odot})$ binary also. *If the comparable mass case is qualitatively similar to the test mass case, this should imply that neither the improvement in the accuracy of the energy function from 3PN to 4PN nor the improvement in the accuracy of the flux function from 3.5PN to 4PN will produce significant improvement in the effectualness in the comparable mass case.* The trends in the faithfulness are very different for different binaries so that it is hard to make any statement about the improvement in faithfulness.

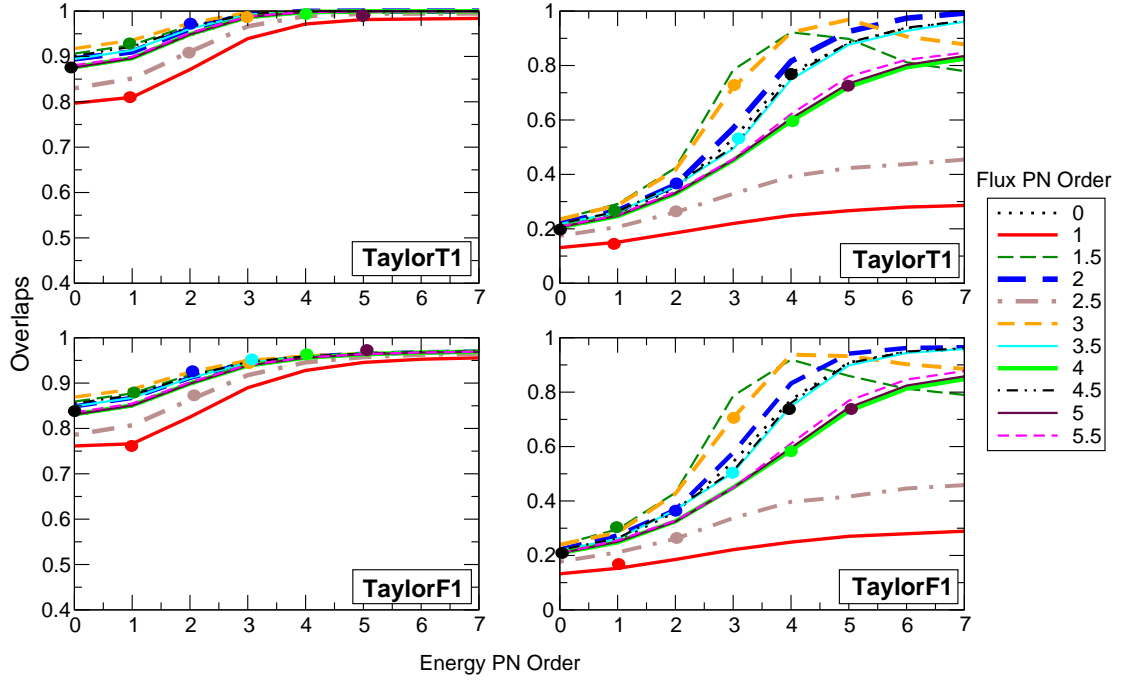


Figure 8.9.: Same as in Figure 8.8 except that the plot correspond to a $(1M_{\odot}, 50M_{\odot})$ binary.

Number of gravitational wave cycles

The number of GW cycles accumulated by a template is defined as [273]

$$\mathcal{N}_{\text{tot}} \equiv \frac{1}{2\pi} (\varphi_{\text{lso}} - \varphi_{\text{low}}) = \int_{F_{\text{low}}}^{F_{\text{lso}}} dF \frac{N(F)}{F}, \quad (8.17)$$

where φ_{lso} and φ_{low} are the GW phases corresponding to the last stable orbit and the low frequency cut-off, respectively, and $N(F) \equiv F^2/\dot{F}$ is the *instantaneous number of cycles* spent near some instantaneous frequency F (as usual, \dot{F} is the time derivative of F). However, it has been noticed that [273], the large number \mathcal{N}_{tot} is not significant because the only really *useful* cycles are those that contribute most to the signal-to-noise ratio (SNR). The number of *useful cycles* is defined as [273]

$$\mathcal{N}_{\text{useful}} \equiv \left(\int_{F_{\text{low}}}^{F_{\text{lso}}} \frac{df}{f} w(f) N(f) \right) \left(\int_{F_{\text{low}}}^{F_{\text{lso}}} \frac{df}{f} w(f) \right)^{-1}, \quad (8.18)$$

where $w(f) \equiv a^2(f)/h_n^2(f)$. If $S_n(f)$ is the two-sided PSD of the detector noise, $h_n(f)$ is defined by $h_n^2(f) \equiv f S_n(f)$, while $a(f)$ is defined by $|H(f)| \simeq a(t_f)/[\dot{F}(t_f)]^{1/2}$ where $H(f)$ is the Fourier transform of the time-domain waveform $h(t)$ (See Eqs.(8.2) and (8.3)) and t_f is the time when the instantaneous frequency $F(t)$ reaches the value f of the Fourier variable.

The total numbers of GW cycles accumulated by various standard and complete adiabatic approximants in the test mass limit are tabulated in Table 8.6 along with the number of useful cycles calculated for the initial LIGO noise PSD. We use Eq.(8.4) to calculate \dot{F} and numerically evaluate the integrals in Eq.(8.18) to compute the number of useful cycles. In order to compute the total number of cycles, we numerically evaluate the integral in Eq.(8.17)

It can be seen that all complete adiabatic approximants accumulate fewer number of (total and useful) cycles than the corresponding standard adiabatic approximants. This is because the additional conservative terms in the complete adiabatic approximants add extra acceleration to the test mass which, in the presence of radiation reaction, would mean that the test body has to coalesce faster, and therefore such templates accumulate fewer number of cycles. Notably enough, approximants (like 3PN and 4.5PN) producing the highest overlaps with the exact waveform, accumulate the closest number of cycles as accumulated by the exact waveform. This is indicative that the phase evolution of these approximants is closer to that of the exact waveform. On the other hand, the fractional absolute difference in the number of cycles of the approximants producing the lowest overlaps (like 0PN, 1PN and 2.5PN) as compared to the exact waveform is the largest, which indicates that these templates follow a significantly different phase evolution.

In order to illustrate the correlation between the number of (total/useful) cycles accumulated by an approximant and its overlap with the exact waveform, we introduce a quantity $\delta\mathcal{N}_n = \frac{|\mathcal{N}_n - \mathcal{N}_{\text{exact}}|}{\mathcal{N}_{\text{exact}}}$ which is the fractional absolute difference between the number of (total/useful) cycles accumulated by a template and the exact waveform. Here \mathcal{N}_n and $\mathcal{N}_{\text{exact}}$ are the number of (total/useful) cycles accumulated by the n PN approximant and exact waveform, respectively. In Figure 8.10, we plot $\delta\mathcal{N}_n$ of various standard adiabatic and complete adiabatic approximants against the corresponding overlaps in the case of a $(1M_\odot, 10M_\odot)$ binary.

The following points may be noted while comparing the results quoted here for the number of cycles with those of other works, e.g. Refs. [276, 230, 275]. As emphasized in Ref. [247] one can get very different results for the phasing depending on whether one consistently re-expands the constituent energy and flux functions or evaluates them without re-expansion. In the computation of the number of useful cycles different authors treat the function \dot{F} differently, some re-expand and others do not, leading to differences in the results. The other important feature we would like to comment upon is a result that appears, at first, very counter-intuitive. It is the fact that in some cases the number of useful GW cycles is greater than the total number of GW cycles! A closer examination reveals that while for most cases of interest this does not happen, in principle its occurrence is determined by the ratio $f_r \equiv F_{\text{low}}/F_{\text{iso}}$. To understand this in more detail let us consider the ratio \mathcal{N}_r of the number of useful cycles to the total number of cycles in the case of white-noise (in a frequency band F_{low} to F_{iso}) for which

$$\mathcal{N}_r \equiv \frac{\mathcal{N}_{\text{useful}}}{\mathcal{N}_{\text{tot}}} = \frac{5}{12} f_r^{1/3} \frac{1 - f_r^{4/3}}{1 - f_r^{1/3}}. \quad (8.19)$$

Table 8.6.: Number of GW cycles accumulated by various standard (S) and complete (C) adiabatic approximants in the test mass limit. The number of useful cycles calculated for the initial LIGO noise PSD is also shown in brackets. The chosen low-frequency cut-off is 40Hz.

Order n	$(1M_{\odot}, 10M_{\odot})$		$(1M_{\odot}, 50M_{\odot})$		$(1M_{\odot}, 100M_{\odot})$	
	S	C	S	C	S	C
0PN	481 (92.3)	424 (74.6)	118 (110)	77.8 (64.4)	13.6	6.7
1PN	560 (117)	526 (102)	180 (186)	124 (104)	25.7	10.6
1.5PN	457 (81.7)	433 (71.8)	88.8 (76.3)	58.5 (38.2)	8.4	2.3
2PN	447 (77.7)	440 (74.0)	77.0 (61.8)	62.5 (41.5)	6.1	2.6
2.5PN	464 (84.5)	454 (79.6)	96.8 (85.5)	74.5 (50.5)	9.7	2.9
3PN	442 (74.7)	440 (73.3)	64.5 (45.2)	58.1 (35.5)	3.4	1.6
3.5PN	445 (76.1)	442 (74.5)	68.7 (49.7)	60.6 (36.8)	4.0	1.4
4PN	445 (75.8)	443 (75.2)	66.4 (45.1)	62.9 (39.0)	2.9	1.6
4.5PN	443 (75.1)	442 (74.5)	63.7 (42.0)	60.0 (35.6)	2.5	1.2
5PN	444 (75.3)	443 (75.0)	63.8 (40.9)	62.2 (37.8)	2.1	1.4
Exact	442 (74.1)		59.1 (34.3)		0.9	

For $f_r \ll 1$, $\mathcal{N}_r < 1$. However, as f_r increases to about $f_r = 0.52$, \mathcal{N}_r transits from being less than one to becoming greater than one! Essentially this arises due to the details of the scaling of the various quantities involved and the point of transition depends on the PN order and the precise form of the noise PSD. For $f_r \simeq 1$, the calculation of useful cycles does not make much physical sense. This explains the absence of $\mathcal{N}_{\text{useful}}$ results for the $(1M_{\odot}, 100M_{\odot})$ binary in Table 8.6.

8.3. Comparable mass waveforms

Until recently, in the case of comparable mass binaries there was no *exact* waveform available. But recently, a series of breakthroughs has occurred in numerical simulations of binary black hole systems [93, 94, 95] and it has become possible to calculate the gravitational waveforms from coalescing binary black holes by exactly solving the Einstein’s equations. It is possible, in principle, to take these waveforms as the ‘exact’ waveforms, and to compute the closeness of the standard and complete adiabatic template families with this family of exact waveforms. But, although several different numerical relativity groups have come up with binary black hole simulations which produce qualitatively similar results using independent codes [277, 278, 185, 279, 171, 195, 178, 280], there are several issues like the accuracy and convergence of numerical simulations that have to be sorted out before we can use these waveforms as the exact waveforms in our study (see Chapter 7 for some related discussion). Moreover, the high computational cost makes it unfeasible, as of now, to produce gravitational waveforms lasting several tens of orbits, which are required for a study like this. So, what we do here is to compare the

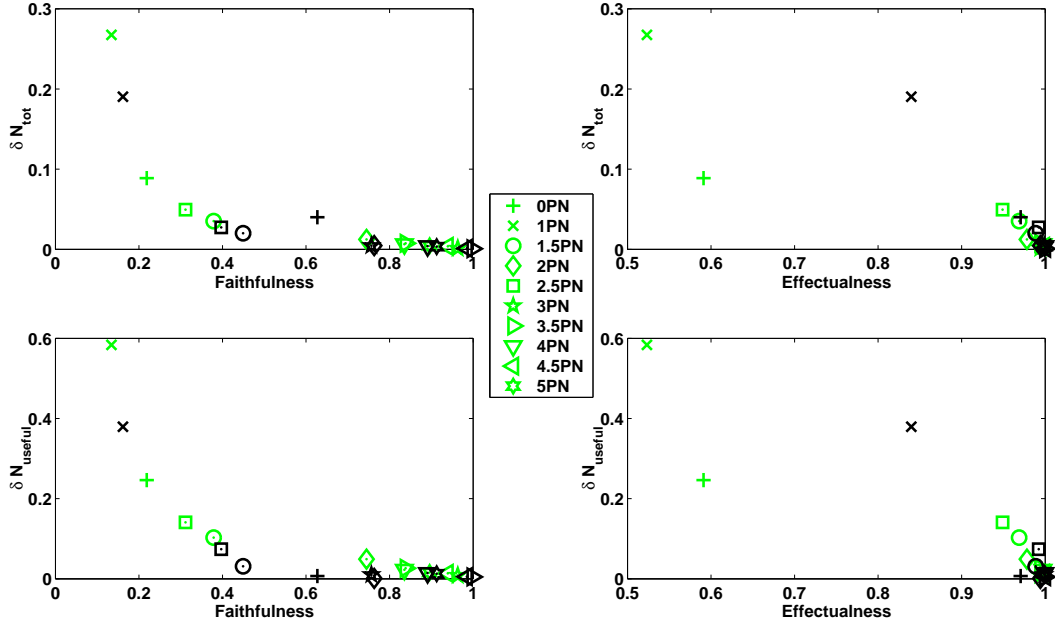


Figure 8.10.: The fractional absolute difference $\delta\mathcal{N}_n$ between the number of cycles accumulated by various approximants and the exact waveform, plotted against the corresponding overlaps. Standard adiabatic approximants are marked with lighter markers and complete adiabatic approximants are marked with darker markers. Top panels show $\delta\mathcal{N}_n$ for the total number of cycles and bottom panels show $\delta\mathcal{N}_n$ for the number of useful cycles. The number of useful cycles are calculated for the initial LIGO noise PSD and the low frequency cut-off is chosen to be 40Hz. The plotted results are for a $(1M_\odot, 10M_\odot)$ binary.

performance of the standard adiabatic and complete adiabatic templates by studying their overlaps with a plausible fiducial exact waveform family (see below).

We will consider all possible combinations of the T-approximants of the energy and flux functions, construct PN templates and calculate the overlaps of these templates with the fiducial ‘exact’ waveform. In all cases, the fiducial ‘exact’ waveform is constructed by numerically integrating the phasing formula in the time-domain (TaylorT1 approximant), and terminating both the ‘exact’ and approximate waveforms at $v_{lso} = 1/\sqrt{6}$, which corresponds to $F_{lso} \simeq 1570$ Hz for a $(1.4M_\odot, 1.4M_\odot)$ binary and $F_{lso} \simeq 220$ Hz for a $(10M_\odot, 10M_\odot)$ binary⁶. The lower frequency cut-off of the waveforms is chosen to be $F_{low} = 40$ Hz.

⁶Here also, v_{lso} is the velocity at the last stable circular orbit of the Schwarzschild geometry having the same mass as the total mass $m_1 + m_2$ of the binary. Strictly speaking, in the comparable mass case, v_{lso} at n PN order should be determined by solving $E'_n(v) = 0$ where $E'_n(v)$ is the v -derivative of the n th PN order energy function. Since we found that our results are qualitatively independent of such considerations, we stick to the choice in the test-mass limit.

8.3.1. The energy function

In the case of binaries with comparable masses, the energy function $E(x; \eta)$ has been computed at present up to 3PN accuracy [222, 254, 255, 223, 224, 225, 226, 256, 227, 228, 229].

$$\begin{aligned}
 E_{3PN}(x; \eta) &= -\frac{1}{2} \eta x \left[1 - \frac{1}{12} (9 + \eta) x - \frac{1}{8} \left(27 - 19\eta + \frac{\eta^2}{3} \right) x^2 \right. \\
 &+ \left. \left(\frac{-675}{64} + \left(\frac{209323}{4032} - \frac{205\pi^2}{96} - \frac{110\lambda}{9} \right) \eta - \frac{155}{96} \eta^2 - \frac{35}{5184} \eta^3 \right) x^3 \right. \\
 &+ \left. \mathcal{O}(x^4) \right], \tag{8.20}
 \end{aligned}$$

where $\lambda = -1987/3080 \simeq -0.6451$ [256, 227, 228, 229]. The corresponding $E'(v; \eta)$ appearing in the phasing formula reads,

$$\begin{aligned}
 E'_{3PN}(v; \eta) &= -\eta v \left[1 - \frac{1}{6} (9 + \eta) v^2 - \frac{3}{8} \left(27 - 19\eta + \frac{\eta^2}{3} \right) v^4 \right. \\
 &+ 4 \left(\frac{-675}{64} + \left(\frac{209323}{4032} - \frac{205\pi^2}{96} - \frac{110\lambda}{9} \right) \eta - \frac{155}{96} \eta^2 - \frac{35}{5184} \eta^3 \right) v^6 \\
 &+ \left. \mathcal{O}(v^8) \right]. \tag{8.21}
 \end{aligned}$$

We use this expression truncated at the necessary orders to construct the various approximate templates. To compute a fiducial ‘exact’ waveform, we use the exact energy function in the test mass limit supplemented by the finite mass corrections up to 3PN in the spirit of the hybrid approximation [281, 282]. In other words, the fiducial ‘exact’ energy $E'(v; \eta)$ will look like

$$\begin{aligned}
 E'_{\text{exact}}(v; \eta) &= -\eta v \left[\frac{-E'_{\text{exact}}(v)}{\eta v} - \frac{\eta}{6} v^2 - \frac{3}{8} \left(-19\eta + \frac{\eta^2}{3} \right) v^4 \right. \\
 &+ \left. 4 \left(\left(\frac{209323}{4032} - \frac{205\pi^2}{96} - \frac{110\lambda}{9} \right) \eta - \frac{155}{96} \eta^2 - \frac{35}{5184} \eta^3 \right) v^6 \right] \tag{8.22}
 \end{aligned}$$

where $E'_{\text{exact}}(v)$ is the v -derivative of the exact energy function in the test mass limit given by Eq. (8.12). The T-approximants of the energy function $E'_T(v; \eta)$ as well as the fiducial exact energy $E'_{\text{exact}}(v; \eta)$ are plotted in Figure 8.11 (left). The v_{lso} corresponding to the fiducial ‘exact’ energy function can be determined by solving $E'_{\text{exact}}(v; \eta) = 0$. This will yield a value $v_{\text{lso}}^{3\text{PN-hybrid}} \simeq 0.4294$ against the $v_{\text{lso}} \simeq 0.4082$ in the test-mass case (more precisely it is the v_{MECO} [270]). If the η -corrections are included only up to 2PN instead of 3PN, $v_{\text{lso}}^{2\text{PN-hybrid}} \simeq 0.4113$. It is worth pointing that $v_{\text{lso}}^{2\text{PN-Pade}} \simeq 0.4456$ [167] and it is not unreasonable to expect that, with 3PN η -corrections the differences between various different ways of determining the lso converge. (For the purposes of our analysis, we have checked that there is no drastic change in our conclusions due to these differences and hence we use uniformly the value $v_{\text{lso}} = 0.4082$).

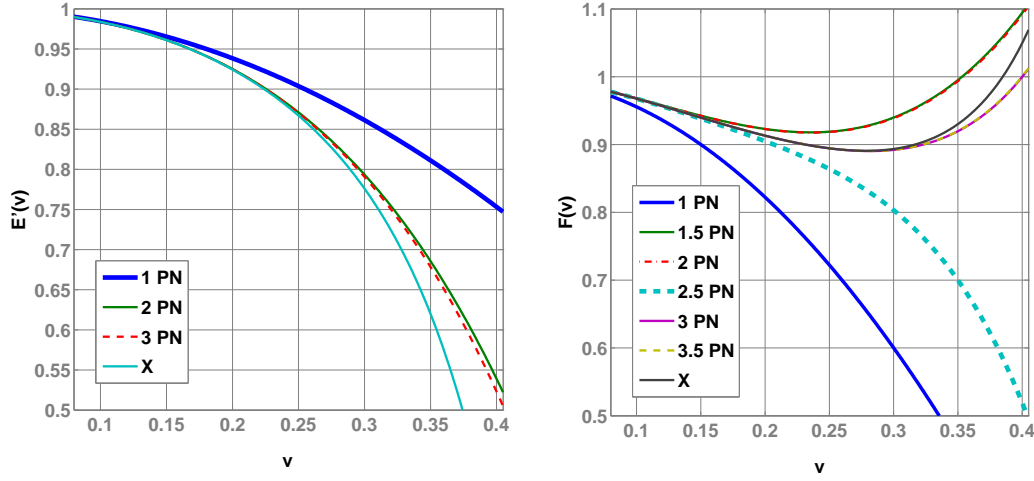


Figure 8.11.: Various T-approximants of Newton-normalized (v -derivative of) energy function $E'_T(v)/E'_N(v)$ (left) and flux function $\mathcal{F}_T(v)/\mathcal{F}_N(v)$ (right) in the comparable mass case, along with the corresponding fiducial ‘exact’ functions (denoted by X).

8.3.2. The flux function

The flux function in the case of comparable masses has been calculated up to 3.5PN accuracy [257, 258, 260, 259, 261, 262, 230], and is given by:

$$\mathcal{F}(v; \eta) = \frac{32}{5} \eta^2 v^{10} \left[\sum_{k=0}^7 A_k(\eta) v^k + B_6(\eta) v^6 \ln v + \mathcal{O}(v^8) \right], \quad (8.23)$$

where

$$\begin{aligned} A_0(\eta) &= 1, \quad A_1(\eta) = 0, \quad A_2(\eta) = -\frac{1247}{336} - \frac{35}{12} \eta, \quad A_3(\eta) = 4\pi, \\ A_4(\eta) &= -\frac{44711}{9072} + \frac{9271}{504} \eta + \frac{65}{18} \eta^2, \\ A_5(\eta) &= -\left(\frac{8191}{672} + \frac{583}{24} \eta \right) \pi, \\ A_6(\eta) &= \frac{6643739519}{69854400} + \frac{16\pi^2}{3} - \frac{1712}{105} \gamma \\ &\quad + \left(-\frac{11497453}{272160} + \frac{41\pi^2}{48} + \frac{176\lambda}{9} - \frac{88\Theta}{3} \right) \eta \\ &\quad - \frac{94403}{3024} \eta^2 - \frac{775}{324} \eta^3 - \frac{1712}{105} \ln 4, \\ A_7(\eta) &= \left(-\frac{16285}{504} + \frac{214745}{1728} \eta + \frac{193385}{3024} \eta^2 \right) \pi, \end{aligned}$$

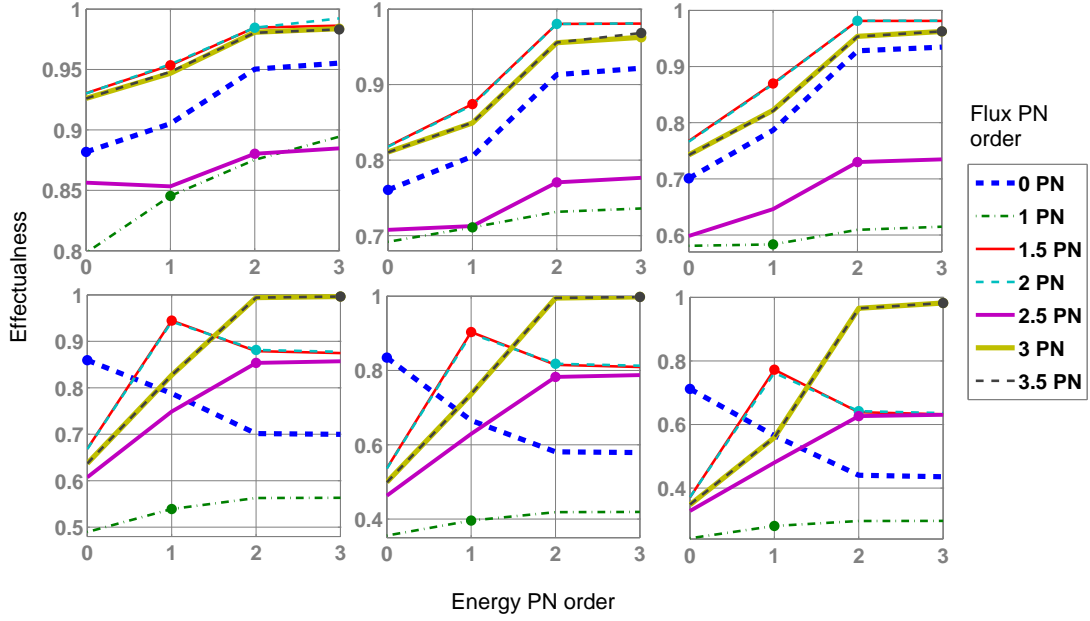


Figure 8.12.: Effectualness of various TaylorT1 templates in the comparable mass case. The horizontal axis reports the PN order $[n]$ of the energy function, while the legends report the PN order n of the flux function. Each line shows how the overlaps are evolving as a function of the accuracy of the energy function. Standard adiabatic approximants are marked with thick dots. The top panel corresponds to the $(10M_{\odot}, 10M_{\odot})$ binary and the bottom panel to the $(1.4M_{\odot}, 1.4M_{\odot})$ binary. Overlaps are calculated for the initial LIGO (left plots), Advanced LIGO (middle plots) and Virgo (right plots) noise spectra.

$$B_6(\eta) = -\frac{1712}{105}, \quad (8.24)$$

and the value of Θ has been recently calculated to be $-11831/9240 \simeq -1.28$ [91] by dimensional regularization.

To construct our fiducial ‘exact’ waveform, we will use the energy function given by Eq. (8.22) and the flux function

$$\begin{aligned} \mathcal{F}_{\text{exact}}(v; \eta) = & \frac{32}{5} \eta^2 v^{10} \left[\mathcal{F}_{\text{exact}}(v) - \sum_{k=0}^7 \left(A_k v^k + B_6 v^6 \ln v \right) \right. \\ & \left. + \sum_{k=0}^7 \left(A_k(\eta) v^k + B_6(\eta) v^6 \ln v \right) \right], \end{aligned} \quad (8.25)$$

where $\mathcal{F}_{\text{exact}}(v)$ is the Newton-normalized (numerical) exact flux in the test-mass limit. The expansion coefficients A_k ’s and B_6 refer to the test-mass case and $A_k(\eta)$ ’s and $B_6(\eta)$ refer to the comparable mass case. The exact flux function is thus constructed

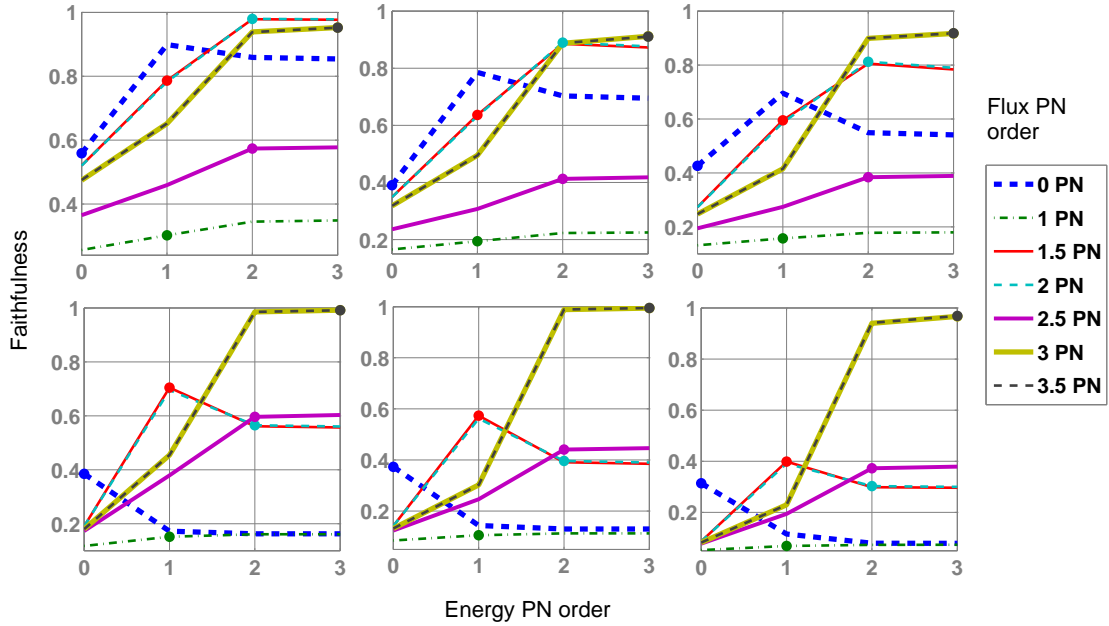


Figure 8.13.: Faithfulness of various TaylorT1 templates in the comparable mass case. The horizontal axis reports the PN order $[n]$ of the energy function, while the legends report the PN order n of the flux function. Each line shows how the overlaps are evolving as a function of the accuracy of the energy function. Standard adiabatic approximants are marked with thick dots. The top panes corresponds to the $(10M_{\odot}, 10M_{\odot})$ binary and the bottom panel to the $(1.4M_{\odot}, 1.4M_{\odot})$ binary. Overlaps are calculated for the initial LIGO (left plots), Advanced LIGO (middle plots) and Virgo (right plots) noise spectra.

by superposing all that we know in the test mass case from perturbation methods and the two body case by post-Newtonian methods. It supplements the exact flux function in the test body limit by all the η -dependent corrections known up to 3.5PN order in the comparable mass case. The T-approximants of the flux function $\mathcal{F}_T(v; \eta)$ and the fiducial exact flux $\mathcal{F}_{\text{exact}}(v; \eta)$ are plotted in Figure 8.11 (right).

8.3.3. Comparable mass results in the adiabatic approximation

The effectualness and faithfulness of various PN templates in the case of comparable mass binaries are plotted in Figure 8.12 and in Figure 8.13, respectively. The overlaps of the fiducial exact waveform are calculated with the TaylorT1 approximants using three different noise spectra — Initial LIGO, Advanced LIGO and Virgo. Let us note that in the case of comparable mass binaries the complete adiabatic approximants can be calculated, at present, at most up to 1PN order. The effectualness and faithfulness of various standard and complete adiabatic templates are also tabulated in Tables 8.7 and

8.8, respectively. From these tables, one can see that the complete adiabatic approximation generally improves the effectualness of the templates at 0PN and 1PN orders. But, as far as faithfulness is concerned, it is hard to conclude that one approximation is better than the other at these PN orders.

Even though complete adiabatic approximants are not calculated for higher PN orders, the general conclusion one can make from Figures 8.12 and 8.13 is that the complete adiabatic approximation of the phasing will not result in a significant improvement in overlaps if we have a flux function of order ≥ 1.5 PN. We, thus, conclude that, provided we have a sufficiently accurate (order ≥ 1.5 PN) T-approximant of the flux function, the standard adiabatic approximation provides a good lower bound to the complete adiabatic approximation for the construction of both effectual and faithful templates in the case of comparable mass binaries. It should be kept in mind that unlike the test mass case where the exact energy and flux functions are known leading to an exact waveform in the adiabatic approximation, in the comparable mass case we are only talking about *fiducial* energy and flux functions constructed from what is known. Probably, the fiducial waveform in this case has much less to do with the exact waveform predicted by general relativity.

Table 8.7 indicates that, to achieve the target sensitivity of 0.965 in effectualness corresponding to a 10% loss in the event-rate, standard adiabatic approximants of order 2PN and 3PN are required for the $(10M_{\odot}, 10M_{\odot})$ and $(1.4M_{\odot}, 1.4M_{\odot})$ binaries, respectively, when restricting to only the inspiral phase.

8.4. Summary and conclusion

The standard adiabatic approximation to the phasing of gravitational waves from inspiralling compact binaries is based on the post-Newtonian expansions of the binding energy and gravitational wave flux both truncated at the same relative post-Newtonian order. To go beyond the adiabatic approximation one must view the problem as the dynamics of a binary under conservative relativistic forces and gravitation radiation damping. In this viewpoint the standard approximation at leading order is equivalent to considering the 0PN and 2.5PN terms in the acceleration and neglecting the intermediate 1PN and 2PN terms. A complete treatment of the acceleration at leading order should include *all* PN terms up to 2.5PN. These define the *standard* and *complete non-adiabatic* approximants respectively. A new post-Newtonian *complete adiabatic* approximant based on energy and flux functions is proposed. At the leading order it uses the 2PN energy function rather than the 0PN one in the standard approximation so that heuristically, it does not miss any intermediate post-Newtonian terms in the acceleration. We have evaluated the performance of the standard adiabatic vis-a-vis complete adiabatic approximants, in terms of their *effectualness* (i.e. larger overlaps with the exact signal) and *faithfulness* (i.e. smaller bias in estimation of parameters). We restricted our study only to the inspiral part of the signal neglecting the plunge and quasi-normal mode ringing phases of the binary [268, 269, 247, 270, 271, 272]. We have studied the problem in the context of both the white-noise spectrum and real interferometer noise spectra.

Table 8.7.: Effectualness of standard (S) and complete (C) adiabatic approximants in the comparable-mass case. Waveforms are generated using the TaylorT1 method. Percentage biases σ_m and σ_η in determining parameters m and η are given in brackets.

Order n	$(10M_\odot, 10M_\odot)$		$(1.4M_\odot, 1.4M_\odot)$	
	S	C	S	C
Initial LIGO				
0PN	0.8815 (14, 0.2)	0.9515 (3.7, 0.1)	0.8636 (1.4, 0.2)	0.6993 (4.3, 0.2)
1PN	0.8457 (59, 0.1)	0.8957 (45, 12)	0.5398 (5.0, 0.1)	0.5639 (4.3, 0.2)
1.5PN	0.9536 (3.9, 0.3)		0.9516 (0.4, 0.2)	
2PN	0.9833 (0.4, 0.2)		0.8751 (0.0, 0.1)	
2.5PN	0.8728 (14, 0.1)		0.8517 (0.4, 0.1)	
3PN	0.9822 (1.5, 0.0)		0.9955 (0.0, 0.3)	
3.5PN	0.9843 (1.4, 0.0)		0.9968 (0.0, 0.3)	
Advanced LIGO				
0PN	0.7606 (8.5, 0.1)	0.9132 (5.0, 0.3)	0.8347 (1.4, 0.1)	0.5809 (4.3, 0.1)
1PN	0.7110 (57, 0.6)	0.7360 (39, 0.6)	0.3959 (6.1, 0.0)	0.4194 (5.0, 0.1)
1.5PN	0.8741 (2.4, 0.1)		0.9034 (0.0, 0.2)	
2PN	0.9803 (0.8, 0.2)		0.8179 (0.4, 0.0)	
2.5PN	0.7705 (7.3, 0.1)		0.7826 (0.4, 0.0)	
3PN	0.9626 (0.5, 0.0)		0.9981 (0.4, 0.3)	
3.5PN	0.9683 (1.3, 1.5)		0.9977 (0.4, 0.3)	
Virgo				
0PN	0.7009 (5.3, 0.0)	0.9280 (4.7, 0.9)	0.7119 (1.4, 0.1)	0.4405 (5.0, 0.0)
1PN	0.5834 (56, 0.3)	0.6148 (30, 0.2)	0.2808 (3.9, 0.1)	0.2968 (2.9, 0.0)
1.5PN	0.8698 (1.3, 0.0)		0.7724 (0.4, 0.7)	
2PN	0.9815 (0.8, 0.2)		0.6420 (0.0, 0.0)	
2.5PN	0.7299 (4.8, 0.0)		0.6266 (0.0, 0.1)	
3PN	0.9624 (0.5, 0.1)		0.9822 (0.0, 0.3)	
3.5PN	0.9627 (0.5, 0.1)		0.9823 (0.0, 0.3)	

Table 8.8.: Faithfulness of the standard (S) and complete (C) adiabatic templates in the comparable-mass case. The waveforms are generated using the TaylorT1 method.

Order	$(10M_{\odot}, 10M_{\odot})$		$(1.4M_{\odot}, 1.4M_{\odot})$	
n	S	C	S	C
Initial LIGO				
0PN	0.5603	0.8560	0.3783	0.1624
1PN	0.3026	0.3491	0.1520	0.1615
1.5PN	0.7949		0.7259	
2PN	0.9777		0.5565	
2.5PN	0.5687		0.5934	
3PN	0.9440		0.9888	
3.5PN	0.9522		0.9916	
Advanced LIGO				
0PN	0.3902	0.7030	0.3731	0.1300
1PN	0.1944	0.2248	0.1054	0.1128
1.5PN	0.6362		0.5735	
2PN	0.8895		0.3964	
2.5PN	0.4125		0.4407	
3PN	0.9117		0.9947	
3.5PN	0.9106		0.9952	
Virgo				
0PN	0.4262	0.5490	0.3138	0.0794
1PN	0.1574	0.1798	0.0686	0.0732
1.5PN	0.5950		0.3986	
2PN	0.8120		0.3027	
2.5PN	0.3842		0.3726	
3PN	0.9169		0.9668	
3.5PN	0.9177		0.9686	

The main result of this study is that the conservative corrections to the dynamics of a binary that are usually neglected in the standard treatment of the phasing formula are rather important at low PN orders. At the low PN orders, they lead to significant improvement in the overlaps between the approximate template and the exact waveform. In both the cases of white noise and real interferometer noise, we found that at low ($< 3\text{PN}$) PN orders the effectualness of the approximants significantly improves in the complete adiabatic approximation. However, standard adiabatic approximants of order $\geq 3\text{PN}$ are nearly as good as the complete adiabatic approximants for the construction of effectual templates.

In the white-noise case, the faithfulness of both the approximants fluctuates as we go from one PN order to the next and is generally much smaller than our target value of 0.965. The fluctuation continues all the way up to 5PN order probably reflecting the oscillatory approach of the flux function to the exact flux function with increasing PN order. Poor faithfulness also means that the parameters extracted using these approximants will be biased. It is again interesting to note that complete adiabatic approximants are generally more faithful than the standard adiabatic approximants. In the case of real interferometer noise spectra on the other hand, the faithfulness of the complete adiabatic approximants is vastly better at almost all orders.

To the extent possible, we also tried to investigate this problem in the case of comparable mass binaries by studying the overlaps of all the approximants with a fiducial exact waveform. It is shown that, provided we have a T-approximant of the flux function of order $\geq 1.5\text{PN}$, the standard adiabatic approximation provides a good lower bound to the complete adiabatic approximation for the construction of both effectual and faithful templates. This result is in contrast with the test mass case where we found that the complete adiabatic approximation brings about significant improvement in effectualness up to 2.5PN order and significant improvement in faithfulness at all orders. To achieve the target sensitivity of 0.965 in effectualness, standard adiabatic approximants of order 2PN and 3PN are required for the $(10M_{\odot}, 10M_{\odot})$ and $(1.4M_{\odot}, 1.4M_{\odot})$ binaries, respectively. Whether the complete adiabatic approximant achieves this at an earlier PN order is an interesting question. It is worth stressing that this result is relevant only for the family of inspiral waveforms. In the real physical case of BH-BH binaries the inspiral family may not be adequate because the contributions from the plunge, merger and ring down phases are also going to be significant [268]. This is an example of the second variety of questions one can study in this area referred to in our introduction related to whether a template family indeed represents the GWs from a specific astrophysical system.

During the course of this study, we also attempted to assess the relative importance of improving the accuracy of the energy function and the flux function by systematically studying the approach of the adiabatic PN templates constructed with different orders of the energy and the flux functions to the exact waveforms. From the study of test-mass templates we also conclude that, provided the comparable mass case is qualitatively similar to the test mass case, neither the improvement of the accuracy of energy function from 3PN to 4PN nor the improvement of the accuracy of flux function from 3.5PN to

4PN will result in a significant improvement in effectualness in the comparable mass case.

There is a limitation to our approach which we should point out: complete adiabatic models can be very well tested in the test mass where both approximate and exact expressions are available for the various quantities. However, complete models cannot be worked out to high orders in the comparable mass case since they need the energy function to be computed to 2.5PN order greater than the flux and currently the energy function is only known to 3PN accuracy. Also, we have used a fiducial exact waveform constructed from the approximants themselves. Though, in the present study we have used the new approximants to construct waveform templates, one can also envisage applications to discuss the dynamics of the binary using numerical integration of the equations of motion.

Appendix A.

Analytical calculation of the fitting factors

In Section 7.4.3 of Chapter 7, in order to find the fitting factor of our phenomenological bank to a hybrid waveform, as well as the best-matched parameters $(\boldsymbol{\alpha}_{\max}, \boldsymbol{\psi}_{\max})$, we need to perform a maximization of the overlap $\mathcal{M}(\boldsymbol{\alpha}, \boldsymbol{\psi})$ in a 12-dimensional space, which seems a challenging task at first sight, especially due to the oscillatory nature of the dependence of $\mathcal{M}(\boldsymbol{\alpha}, \boldsymbol{\psi})$ on the components of $\boldsymbol{\psi}$. However, due to the very high fitting factor, as well as the linear dependence of $\Psi_{\text{eff}}(\boldsymbol{\psi}; f)$ on $\boldsymbol{\psi}$, it is possible to design an analytic approximation to $\mathcal{M}(\boldsymbol{\alpha}, \boldsymbol{\psi})$ that is highly accurate and can be maximized over $\boldsymbol{\psi}$ analytically. In describing this approximation, we also include φ_0 and t_0 in $\boldsymbol{\psi}$, forming an 8-dimensional vector.

For a target hybrid waveform

$$\tilde{h}(f) = A(f) e^{i\Psi(f)}, \quad (\text{A.1})$$

and a phenomenological template

$$u(f) = A_{\text{eff}}(\boldsymbol{\alpha}; f) e^{i\Psi_{\text{eff}}(\boldsymbol{\psi}; f)}, \quad (\text{A.2})$$

the overlap $\mathcal{M}(\boldsymbol{\alpha}, \boldsymbol{\psi})$ can be broken into a product of two terms,

$$\mathcal{M}(\boldsymbol{\alpha}, \boldsymbol{\psi}) = \mathcal{M}_A(\boldsymbol{\alpha}) \mathcal{M}_P(\boldsymbol{\alpha}, \boldsymbol{\psi}) \quad (\text{A.3})$$

with

$$\mathcal{M}_A(\boldsymbol{\alpha}) \equiv \frac{1}{a} \int_0^\infty \frac{A_{\text{eff}}(\boldsymbol{\alpha}; f) A(f)}{S_h(f)} df \quad (\text{A.4})$$

and

$$\mathcal{M}_P(\boldsymbol{\alpha}, \boldsymbol{\psi}) \equiv \frac{1}{b} \int_0^\infty \frac{A_{\text{eff}}(\boldsymbol{\alpha}; f) A(f) \cos[\Delta\Psi(f)]}{S_h(f)} df \quad (\text{A.5})$$

where

$$\Delta\Psi(f) \equiv \Psi(f) - \Psi_{\text{eff}}(\boldsymbol{\psi}; f). \quad (\text{A.6})$$

In the above expressions, the normalization constants a and b are defined by

$$a^2 \equiv \int_0^\infty \frac{A^2(f)}{S_h(f)} df \int_0^\infty \frac{A_{\text{eff}}^2(\boldsymbol{\alpha}; f)}{S_h(f)} df, \quad (\text{A.7})$$

and

$$b \equiv \int_0^\infty \frac{A_{\text{eff}}(\boldsymbol{\alpha}; f)A(f)}{S_h(f)} df. \quad (\text{A.8})$$

If the phase difference $\Delta\Psi(f)$ is small, we can approximate $\cos \Delta\Psi \approx 1 - \Delta\Psi^2/2$, and rewrite \mathcal{M}_P as

$$\mathcal{M}_P \approx \mathcal{M}'_P \equiv 1 - \frac{1}{2b} \int_0^\infty \frac{A_{\text{eff}}(\boldsymbol{\alpha}; f)A(f)[\Delta\Psi(f)]^2}{S_h(f)} df. \quad (\text{A.9})$$

Since $\Psi_{\text{eff}}(\boldsymbol{\psi}; f)$ is a linear function in $\boldsymbol{\psi}$, minimizing \mathcal{M}'_P becomes a least-square fit with a weighting function

$$\mu(f) \equiv \frac{A_{\text{eff}}(\boldsymbol{\alpha}; f)A(f)}{S_h(f)}. \quad (\text{A.10})$$

More specifically, writing $\Psi_{\text{eff}}(\boldsymbol{\psi}; f)$ as in Eq.(7.39), i.e.,

$$\Psi_{\text{eff}}(\boldsymbol{\psi}; f) = \sum_j \psi_j f^{(5-j)/3}, \quad (\text{A.11})$$

we have

$$1 - \mathcal{M}'_P = \frac{1}{2} [\boldsymbol{\psi} \mathbf{A} \boldsymbol{\psi}^T - 2\mathbf{B} \boldsymbol{\psi}^T + D], \quad (\text{A.12})$$

where we have defined a matrix \mathbf{A} , a vector \mathbf{B} and a scalar constant D , such that

$$\begin{aligned} A_{ij} &\equiv \frac{1}{b} \int_0^\infty f^{(10-i-j)/3} \mu(f) df, \\ B_j &\equiv \frac{1}{b} \int_0^\infty f^{(5-j)/3} \Psi(f) \mu(f) df, \\ D &\equiv \frac{1}{b} \int_0^\infty \Psi^2(f) \mu(f) df. \end{aligned} \quad (\text{A.13})$$

The maximum of \mathcal{M}'_P is then equal to

$$\mathcal{M}'_{P \text{ max}} = 1 - \frac{1}{2} [D - \mathbf{B} \mathbf{A}^{-1} \mathbf{B}], \quad (\text{A.14})$$

reached at

$$\boldsymbol{\psi}_{\text{max}} = \mathbf{B} \mathbf{A}^{-1}. \quad (\text{A.15})$$

As a consequence, for each $\boldsymbol{\alpha}$, we are able to maximize $\mathcal{M}_P(\boldsymbol{\alpha}, \boldsymbol{\psi})$, and hence $\mathcal{M}(\boldsymbol{\alpha}, \boldsymbol{\psi})$, over $\boldsymbol{\psi}$ analytically. The original 12-dimensional maximization is then converted to a 4-dimensional maximization, only over the amplitude parameters, on which the overlap depends in a non-oscillatory way.

Appendix B.

Computing the horizon distance

This Appendix details the computation of the horizon distance of different searches discussed in Section 7.4.6 of Chapter 7.

B.1. Search using post-Newtonian templates

In the restricted post-Newtonian approximation, the Fourier transform of the gravitational signal from an optimally-oriented binary located at an effective distance d can be written in the following way:

$$h(f) = \frac{M^{5/6}}{d\pi^{2/3}} \left(\frac{5\eta}{24}\right)^{1/2} f^{-7/6} e^{i[2\pi ft_0 - \varphi_0 + \psi(f) - \pi/4]} \quad (\text{B.1})$$

where M is the total mass, η is the symmetric mass ratio, t_0 is the time of arrival and φ_0 is the initial phase. The phase $\psi(f)$ is computed using the stationary phase approximation.

The optimal SNR in detecting a known signal h buried in the noise is given by

$$\rho_{\text{opt}} = 2 \left[\int_0^\infty df \frac{h(f)^2}{S_h(f)} \right]^{1/2}, \quad (\text{B.2})$$

where $S_h(f)$ is the one-sided PSD of the noise. The optimal SNR in detecting the signal given in Eq.(B.1) can thus be computed as:

$$\rho_{\text{opt}} = \frac{M^{5/6}}{d\pi^{2/3}} \left(\frac{5\eta}{6}\right)^{1/2} \left[\int_{f_{\text{low}}}^{f_{\text{upp}}} df \frac{f^{-7/3}}{S_h(f)} \right]^{1/2}, \quad (\text{B.3})$$

where f_{low} is the low-frequency cutoff of the detector noise and f_{upp} is upper frequency cutoff of the template waveform. The effective distance to a binary which can produce an optimal SNR ρ_{opt} can be computed by inverting the above equation.

The standard post-Newtonian waveforms are truncated at $f_{\text{upp}} = f_{\text{ISCO}}$, where $f_{\text{ISCO}} = (6^{3/2}\pi M)^{-1}$ is the GW frequency corresponding to the innermost stable circular orbit (ISCO) of the Schwarzschild geometry with mass equal to the total mass M of the binary.

The effective one body (EOB) waveforms are truncated at $f_{\text{upp}} = f_{\text{LR}}$, where $f_{\text{LR}} = (3^{3/2}\pi M)^{-1}$ is the GW frequency corresponding to the light ring of the Schwarzschild geometry with mass M . Both of these quantities are computed assuming the test particle limit. It may be noted that, for the EOB waveforms, an analytical Fourier domain representation is not available. They cannot be expressed in the form given in Eq.(B.1). But for the purpose of the estimation of the horizon distance, these formulas give a reasonable approximation.

B.2. Search using ring down templates

The ring down portion of the GW signal from a coalescing binary, considering only the fundamental quasi-normal mode, corresponds to a damped sinusoid. This can be written as [283]

$$h_{\text{ring}}(t) = A_{\text{ring}} \exp\left[-\frac{\pi f_{\text{QNR}}(t-t_0)}{Q}\right] \times \cos(-2\pi f_{\text{QNR}}(t-t_0) + \varphi_0), \quad (\text{B.4})$$

where A_{ring} is the amplitude, t_0 is the start time of the ring down, φ_0 the initial phase, M is the mass of final black hole, f_{QNR} and Q are the central frequency and the quality factor of the ringing. For the fundamental mode, a good fit to the frequency f_{QNR} and quality factor Q , within an accuracy of 5%, is given by

$$f_{\text{QNR}} \approx [1 - 0.63(1-a)^{3/10}] \frac{1}{2\pi M}, \quad (\text{B.5})$$

$$Q \approx 2(1-a)^{-9/20}, \quad (\text{B.6})$$

where aM^2 is the spin angular momentum, and a is the Kerr parameter [283].

To compute the optimal SNR in detecting this signal present in the data, we proceed as in [284], assuming that for $t < t_0$, $h_{\text{ring}}(t)$ is identical to $t > t_0$ except for the sign in the exponential, and dividing by a correcting factor of $\sqrt{2}$ in amplitude to compensate for the doubling of power:

$$\bar{h}_{\text{ring}}(t) = \frac{A_{\text{ring}}}{\sqrt{2}} \exp\left[-\frac{\pi f_{\text{QNR}}|t-t_0|}{Q}\right] \times \cos(-2\pi f_{\text{QNR}}(t-t_0) + \varphi_0). \quad (\text{B.7})$$

Its Fourier transform then becomes

$$\begin{aligned} \tilde{\bar{h}}_{\text{ring}}(f) &= \frac{A_{\text{ring}} f_{\text{QNR}}}{\sqrt{2}\pi Q} e^{i2\pi f t_0} \left(\frac{e^{i\varphi_0}}{g^2 + 4(f - f_{\text{QNR}})^2} \right. \\ &\quad \left. + \frac{e^{-i\varphi_0}}{g^2 + 4(f + f_{\text{QNR}})^2} \right), \end{aligned} \quad (\text{B.8})$$

where $g = f_{\text{QNR}}/Q$.

In general, it is not easy to estimate A_{ring} , or the two polarization amplitudes; they depend upon the detailed evolution of the merger epoch, as well as variables such as the orientation of the final merged remnant. A reasonable hypothesis [285, 286, 287] is that their ratio follows the ratio of the inspiral polarization amplitudes. With this hypothesis, the overall amplitude of the signal from an optimally located and oriented binary, requiring that the ring down radiate some fraction ϵ of the system's total mass, becomes

$$A_{\text{ring}}^{\text{opt}} = \sqrt{\frac{5\epsilon}{4\pi}} \frac{M}{d} \frac{2}{\sqrt{M f_{\text{QNR}} Q F(Q)}} \quad (\text{B.9})$$

where $F(Q) = 1 + \frac{7}{24Q^2}$ and d is the distance to the source. The optimal SNR ρ can now be computed as

$$\rho_{\text{opt}} = 2 \left[\int_{f_{\text{low}}}^{f_{\text{upp}}} df \frac{|\tilde{h}_{\text{ring}}|^2}{S_h(f)} \right]^{1/2}, \quad (\text{B.10})$$

where f_{low} and f_{upp} are the lower and upper cutoff frequencies of the detector noise. As in the previous case, the horizon distance can be computed by inverting this equation.

B.3. Search using all the three stages of the binary black-hole coalescence

The phenomenological waveforms in the frequency domain are given in Eqs.(7.35– 7.40). The optimal SNR in detecting this signal can be computed as:

$$\begin{aligned} \rho_{\text{opt}} &= \frac{M^{5/6} f_{\text{merg}}^{-7/6}}{d \pi^{2/3}} \left(\frac{5\eta}{6} \right)^{1/2} \left[\int_{f_{\text{low}}}^{f_{\text{merg}}} df \frac{(f/f_{\text{merg}})^{-7/3}}{S_h(f)} \right. \\ &+ \int_{f_{\text{merg}}}^{f_{\text{ring}}} df \frac{(f/f_{\text{merg}})^{-4/3}}{S_h(f)} \\ &+ \left. \int_{f_{\text{ring}}}^{f_{\text{cut}}} df \frac{\mathcal{L}^2(f, f_{\text{ring}}, \sigma)}{S_h(f)} \right]^{1/2}, \quad (\text{B.11}) \end{aligned}$$

where $\mathcal{L}(f, f_{\text{ring}}, \sigma)$ is defined in Eq.(7.37), and $f_{\text{merg}}, f_{\text{ring}}, f_{\text{cut}}$ and σ are given by Eq.(7.41).

This equation can be inverted to calculate the effective distance to the optimally-oriented binary which can produce an optimal SNR ρ_{opt} .

Bibliography

- [1] K. S. Thorne, *Gravitational radiation: A new window onto the universe* (1997), [gr-qc/9704042](#).
- [2] R. A. Hulse and J. H. Taylor, *Discovery of a pulsar in a binary system*, *Astrophys. J.* **195**, L51 (1975).
- [3] J. Taylor, *Binary Pulsars and Relativistic Gravity*, *Rev. Mod. Phys.* **66**, 711 (1994).
- [4] I. Stairs, *Testing General Relativity with Pulsar Timing*, *Living Rev. Relativity* **6** (2003).
URL <http://www.livingreviews.org/lrr-2003-5>
- [5] M. Burgay, N. D'Amico, A. Possenti, R. Manchester, A. Lyne, B. C. Joshi, M. A. McLaughlin, M. Kramer, J. M. Sarkissian, C. F. V. Kalogera, C. Kim and D. R. Lorimer, *An increased estimate of the merger rate of double neutron stars from observations of a highly relativistic system*, *Nature* **426**, 531 (2003), [astro-ph/0312071](#).
- [6] M. Kramer et al., *Testing GR with the Double Pulsar: Recent Results* (2005), [astro-ph/0503386](#).
- [7] <http://www.ligo.caltech.edu>.
- [8] <http://www.virgo.infn.it>.
- [9] <http://www.geo600.uni-hannover.de>.
- [10] <http://tamago.mtk.nao.ac.jp>.
- [11] <http://www.auriga.lnl.infn.it>.
- [12] <http://www.roma1.infn.it/rog/nautilus>.
- [13] <http://sam.phys.lsu.edu>.
- [14] <http://www.roma1.infn.it/rog/explorer>.
- [15] <http://www.minigrail.nl>.
- [16] <http://lisa.jpl.nasa.gov>.
- [17] K. A. Postnov and L. R. Yungelson, *The Evolution of Compact Binary Star Systems*, *Living Reviews in Relativity* **9** 6 (2006).
URL <http://www.livingreviews.org/lrr-2006-6>

-
- [18] M. Shibata, K. Taniguchi and K. Uryu, *Merger of binary neutron stars with realistic equations of state in full general relativity*, Physical Review D (Particles, Fields, Gravitation, and Cosmology) **71** 8, 084021 (2005).
URL <http://link.aps.org/abstract/PRD/v71/e084021>
- [19] C. W. Helstrom, *Elements of signal detection and estimation*, Prentice-Hall, Inc., Upper Saddle River, NJ, USA (1995).
- [20] C. L. Fryer and K. C. New, *Gravitational Waves from Gravitational Collapse*, Living Reviews in Relativity **6** 2 (2003).
URL <http://www.livingreviews.org/lrr-2003-2>
- [21] K. D. Kokkotas and N. Stergioulas, *Gravitational waves from compact sources* (2005), [gr-qc/0506083](#).
- [22] C. L. Fryer, *Mass Limits For Black Hole Formation*, Astrophys. J. **522**, 413 (1999), [astro-ph/9902315](#).
- [23] B. Abbott et al., *Coherent searches for periodic gravitational waves from unknown isolated sources and Scorpius X-1: Results from the second LIGO science run* (2006), [gr-qc/0605028](#).
- [24] L. Bildsten, *Gravitational radiation and rotation of accreting neutron stars*, Astrophys. J. **501**, L89 (1998), [astro-ph/9804325](#).
- [25] B. Allen, *The stochastic gravity-wave background: Sources and detection* (1996), [gr-qc/9604033](#).
- [26] K. S. Thorne, *Gravitational waves* (1995), [gr-qc/9506086](#).
- [27] T. Regimbau and J. A. de Freitas Pacheco, *Cosmic background of gravitational waves from rotating neutron stars* (2001), [astro-ph/0105260](#).
- [28] T. Regimbau and B. Chauvineau, *Stochastic background from extra-galactic double neutron stars*, Class. Quant. Grav. **24**, S627 (2007), [arXiv:0707.4327\[gr-qc\]](#).
- [29] D. M. Coward, R. R. Burman and D. G. Blair, *Simulating a stochastic background of gravitational waves from neutron star formation at cosmological distances*, Mon. Not. Roy. Astron. Soc. **329**, 411 (2002).
- [30] A. R. Cooray, *Gravitational wave background of neutron star - white dwarf binaries*, Mon. Not. Roy. Astron. Soc. **354**, 25 (2004), [astro-ph/0406467](#).
- [31] C. M. Will, *The Confrontation between General Relativity and Experiment*, Living Reviews in Relativity **9** 3 (2006).
URL <http://www.livingreviews.org/lrr-2006-3>
- [32] C. M. Will, *Bounding the mass of the graviton using gravitational-wave observations of inspiralling compact binaries*, Phys. Rev. D **57**, 2061 (1998), [gr-qc/9709011](#).
- [33] O. Dreyer et al., *Black hole spectroscopy: Testing general relativity through gravitational wave observations*, Class. Quant. Grav. **21**, 787 (2004), [gr-qc/0309007](#).

- [34] E. Berti, A. Buonanno and C. M. Will, *Testing general relativity and probing the merger history of massive black holes with LISA*, *Class. Quant. Grav.* **22**, S943 (2005), [gr-qc/0504017](#).
- [35] E. Berti, V. Cardoso and C. M. Will, *On gravitational-wave spectroscopy of massive black holes with the space interferometer LISA*, *Phys. Rev.* **D73**, 064030 (2006), [gr-qc/0512160](#).
- [36] E. Poisson, *Measuring black-hole parameters and testing general relativity using gravitational-wave data from space-based interferometers*, *Phys. Rev. D* **54** 10, 5939 (1996).
- [37] F. D. Ryan, *Gravitational waves from the inspiral of a compact object into a massive, axisymmetric body with arbitrary multipole moments*, *Phys. Rev. D* **52** 10, 5707 (1995).
- [38] L. Blanchet and B. S. Sathyaprakash, *Signal analysis of gravitational wave tails*, *Class. Quantum Grav.* **11**, 2807 (1994).
- [39] L. Blanchet and B. S. Sathyaprakash, *Detecting the tail effect in gravitational wave experiments*, *Phys. Rev. Lett.* **74**, 1067 (1995).
- [40] K. G. Arun, B. R. Iyer, M. S. S. Qusailah and B. S. Sathyaprakash, *Testing post-Newtonian theory with gravitational wave observations*, *Class. Quantum Grav.* **23**, L37 (2006), [gr-qc/0604018](#).
- [41] K. G. Arun, B. R. Iyer, M. S. S. Qusailah and B. S. Sathyaprakash, *Probing the non-linear structure of general relativity with binary black holes*, *Phys. Rev. D* **74**, 024025 (2006), [gr-qc/0604067](#).
- [42] K. Thorne, *Gravitational radiation*, in S. Hawking and W. Israel, editors, *Three Hundred Years of Gravitation*, pp. 330–458, Cambridge University Press, Cambridge, U.K.; New York, U.S.A. (1987).
- [43] M. J. Benacquista, *Relativistic Binaries in Globular Clusters*, *Living Reviews in Relativity* **9** 2 (2006).
URL <http://www.livingreviews.org/lrr-2006-2>
- [44] C. Cutler and K. Thorne, *An Overview of Gravitational-Wave Sources*, in N. Bishop and S. Maharaj, editors, *Proceedings of GR-17*, World Scientific (2002).
- [45] N. Andersson and K. D. Kokkotas, *Towards gravitational-wave asteroseismology*, *Mon. Not. Roy. Astron. Soc.* **299**, 1059 (1998), [gr-qc/9711088](#).
- [46] B. F. Schutz, *Determining the Hubble constant from gravitational wave observations*, *Nature (London)* **323**, 310 (1986).
- [47] D. E. Holz and S. A. Hughes, *Using gravitational-wave standard sirens*, *Astrophys. J* **629**, 15 (2005), [astro-ph/0504616](#).
- [48] L. S. Finn, *Binary inspiral, gravitational radiation, and cosmology*, *Phys. Rev. D* **53** 6, 2878 (1996).

-
- [49] D. Chernoff and L. Finn, *Gravitational radiation, inspiraling binaries, and cosmology*, *Astrophys. J. Lett.* **411**, L5 (1993).
- [50] NASA ‘Beyond Einstein’ Program.
URL <http://universe.nasa.gov/program/vision.html>
- [51] C. Misner, K. Thorne and J. Wheeler, *Gravitation*, W.H. Freeman, San Francisco, U.S.A. (1973).
- [52] B. F. Schutz, *A First Course in General Relativity*, Cambridge University Press, Cambridge (UK) (1985, 1986).
- [53] P. Saulson, *Fundamentals of Interferometric Gravitational Wave Detectors*, World Scientific, Singapore; River Edge, U.S.A. (1994).
- [54] C. D. Ott, A. Burrows, L. Dessart and E. Livne, *A new mechanism for gravitational wave emission in core-collapse supernovae*, *Phys. Rev. Lett.* **96**, 201102 (2006), [astro-ph/0605493](#).
- [55] R. Drever, J. Hough, A. Munley, S.-A. Lee, R. Spero, S. Whitcomb, H. Ward, G. Ford, M. Hereld, N. Robertson, I. Kerr, J. Pugh, G. Newton, B. Meers, E. Brooks III and Y. Gürsel, *Gravitational wave detectors using laser interferometers and optical cavities: Ideas, principles and prospects*, in P. Meystre and M. Scully, editors, *Quantum Optics, Experimental Gravity, and Measurement Theory*, volume 94 of *NATO ASI Series, Series B*, pp. 503–514, Plenum Press, New York, U.S.A. (1983).
- [56] B. J. Meers, *Recycling in laser-interferometric gravitational-wave detectors*, *Phys. Rev. D* **38** 8, 2317 (1988).
- [57] D. Sigg, *Status of the LIGO detectors* (2007), Proceedings of the 7th Edoardo Amaldi Conference on Gravitational Waves.
- [58] F. Marion, *Status of Virgo* (2007), Proceedings of the 7th Edoardo Amaldi Conference on Gravitational Waves.
- [59] H. Grote, *The status of GEO 600* (2007), Proceedings of the 7th Edoardo Amaldi Conference on Gravitational Waves.
- [60] R. Takahashi, *Operational status of TAMA 300 with the seismic attenuation system* (2007), Proceedings of the 7th Edoardo Amaldi Conference on Gravitational Waves.
- [61] L. Taffarello, *Status report of Auriga detector* (2007), Proceedings of the 7th Edoardo Amaldi Conference on Gravitational Waves.
- [62] O. Usenko, *MiniGRAIL progress; Test of complete transducer chains down to mK temperatures* (2007), Proceedings of the 7th Edoardo Amaldi Conference on Gravitational Waves.
- [63] E. Coccia, *Status of the bar detectors Explorer and Nautilus* (2007), Proceedings of the 7th Edoardo Amaldi Conference on Gravitational Waves.

- [64] S. W. R. Adhikari, P. Fritschel, *Enhanced LIGO*, LIGO Technical Document LIGO-T060156-01-I (2006).
- [65] P. Fritschel, R. Adhikari and R. Weiss, *Enhancements to the LIGO S5 Detectors*, LIGO Technical Document LIGO-T050252-00-I (2005).
- [66] E. Gustafson, D. Shoemake, K. Strain and R. Weiss, *LSC White Paper on Detector Research and Development*, LIGO Technical Document T990080-00-D (1999).
URL <http://www.ligo.caltech.edu/docs/T/T990080-00.pdf>
- [67] R. Flaminio et al., *Advanced Virgo White Paper*, Virgo Technical Document VIR-NOT-DIR-1390-304 (2005).
URL <http://wwwcascina.virgo.infn.it/advirgo/docs/whitepaper.pdf>
- [68] B. Willke et al., *The GEO-HF project*, *Class. Quant. Grav.* **23**, S207 (2006).
- [69] K. Kuroda, *The status of LCGT*, *Class. Quant. Grav.* **23**, S215 (2006).
- [70] <http://www.ligo.org>.
- [71] B. Abbott et al., *Search for gravitational waves from binary inspirals in S3 and S4 LIGO data* (2007), [arXiv:0704.3368\[gr-qc\]](https://arxiv.org/abs/0704.3368).
- [72] B. Abbott et al., *Search for gravitational-wave bursts in LIGO data from the fourth science run* (2007), [arXiv:0704.0943\[gr-qc\]](https://arxiv.org/abs/0704.0943).
- [73] B. Abbott et al., *Search for Gravitational Waves Associated with 39 Gamma-Ray Bursts Using Data from the Second, Third, and Fourth LIGO Runs* (2007), [arXiv:0709.0766\[gr-qc\]](https://arxiv.org/abs/0709.0766).
- [74] B. Abbott et al., *Upper limits on gravitational wave emission from 78 radio pulsars*, *Phys. Rev.* **D76**, 042001 (2007), [gr-qc/0702039](https://arxiv.org/abs/gr-qc/0702039).
- [75] B. Abbott et al., *All-sky search for periodic gravitational waves in LIGO S4 data* (2007), [arXiv:0708.3818\[gr-qc\]](https://arxiv.org/abs/0708.3818).
- [76] B. Abbott et al., *Searching for a stochastic background of gravitational waves with LIGO*, *Astrophys. J.* **659**, 918 (2007), [astro-ph/0608606](https://arxiv.org/abs/astro-ph/0608606).
- [77] B. Abbott et al., *Upper limit map of a background of gravitational waves*, *Phys. Rev.* **D76**, 082003 (2007), [astro-ph/0703234](https://arxiv.org/abs/astro-ph/0703234).
- [78] B. Abbott et al., *Joint LIGO and TAMA300 search for gravitational waves from inspiralling neutron star binaries*, *Phys. Rev.* **D73**, 102002 (2006), [gr-qc/0512078](https://arxiv.org/abs/gr-qc/0512078).
- [79] B. Abbott et al., *Upper limits from the LIGO and TAMA detectors on the rate of gravitational-wave bursts*, *Phys. Rev.* **D72**, 122004 (2005), [gr-qc/0507081](https://arxiv.org/abs/gr-qc/0507081).
- [80] L. Baggio et al., *A Joint Search for Gravitational Wave Bursts with AURIGA and LIGO* (2007), [arXiv:0710.0497\[gr-qc\]](https://arxiv.org/abs/0710.0497).

-
- [81] B. Abbott et al., *First cross-correlation analysis of interferometric and resonant-bar gravitational-wave data for stochastic backgrounds*, Phys. Rev. **D76**, 022001 (2007), [gr-qc/0703068](#).
- [82] I. S. Heng, *Search for burst gravitational waves in LIGO-GEO S4 data* (2006), Presented at the 11th Gravitational-Wave Data Analysis Workshop, Potsdam, Germany.
- [83] G. Guidi, *Status report on joint LIGO-Virgo compact binary searches* (2007), Presented at the 7th Edoardo Amaldi Conference on Gravitational Waves, Sydney, Australia.
- [84] B. Whiting, *Stochastic Gravitational Wave Searches with LIGO and Virgo data* (2007), Presented at the 7th Edoardo Amaldi Conference on Gravitational Waves, Sydney, Australia.
- [85] I. Yakushin, *Coherent all-sky search for gravitational wave bursts with the LIGO, GEO and VIRGO detectors* (2007), Presented at the American Physical Society Meeting, Florida, USA.
- [86] D. Blair, editor, *The Detection of Gravitational Waves*, Cambridge University Press, Cambridge, U.K., New York, U.S.A. (1991).
- [87] J. Hough and S. Rowan, *Gravitational Wave Detection by Interferometry (Ground and Space)*, Living Reviews in Relativity **3** 3 (2000).
URL <http://www.livingreviews.org/lrr-2000-3>
- [88] V. Fock, *Theory of space, time and gravitation*, Pergamon, London (1959).
- [89] L. Blanchet and T. Damour, *Radiative gravitational fields in general relativity I. general structure of the field outside the source*, Phil. Trans. Roy. Soc. Lond. **A320**, 379 (1986).
- [90] R. V. Wagoner and C. M. Will, *PostNewtonian Gravitational Radiation from Orbiting Point Masses*, Astrophys. J. **210**, 764 (1976).
- [91] L. Blanchet, T. Damour, G. Esposito-Farèse and B. R. Iyer, *Gravitational radiation from inspiralling compact binaries completed at the third post-Newtonian order*, Phys. Rev. Lett. **93**, 091101 (2004), [gr-qc/0406012](#).
- [92] K. G. Arun, L. Blanchet, B. R. Iyer and M. S. S. Qusailah, *The 2.5PN gravitational wave polarisations from inspiralling compact binaries in circular orbits*, Class. Quantum Grav. **21**, 3771 (2004), erratum-ibid. **22**, 3115 (2005), [gr-qc/0404185](#).
- [93] F. Pretorius, *Evolution of binary black hole spacetimes*, Phys. Rev. Lett. **95**, 121101 (2005), [gr-qc/0507014](#).
- [94] M. Campanelli, C. O. Lousto, P. Marronetti and Y. Zlochower, *Accurate evolutions of orbiting black-hole binaries without excision*, Phys. Rev. Lett. **96**, 111101 (2006), [gr-qc/0511048](#).

- [95] J. G. Baker, J. Centrella, D.-I. Choi, M. Koppitz and J. van Meter, *Gravitational wave extraction from an inspiraling configuration of merging black holes*, Phys. Rev. Lett. **96**, 111102 (2006), [gr-qc/0511103](#).
- [96] S. A. Teukolsky, *Perturbations of a Rotating Black Hole. I. Fundamental Equations for Gravitational, Electromagnetic, and Neutrino-Field Perturbations*, Astrophys. J. **185**, 635 (1973).
- [97] M. Shibata and K. Uryu, *Gravitational waves from the merger of binary neutron stars in a fully general relativistic simulation*, Prog. Theor. Phys. **107**, 265 (2002), [gr-qc/0203037](#).
- [98] M. Shibata, K. Taniguchi and K. Uryu, *Merger of binary neutron stars with realistic equations of state in full general relativity*, Phys. Rev. **D71**, 084021 (2005), [gr-qc/0503119](#).
- [99] M. Shibata and K. Taniguchi, *Merger of binary neutron stars to a black hole: Disk mass, short gamma-ray bursts, and quasinormal mode ringing*, Phys. Rev. **D73**, 064027 (2006), [astro-ph/0603145](#).
- [100] M. Anderson et al., *Simulating binary neutron stars: dynamics and gravitational waves* (2007), [arXiv:0708.2720\[gr-qc\]](#).
- [101] M. Shibata and K. Uryu, *Merger of black hole - neutron star binaries: Nonspinning black hole case*, Phys. Rev. **D74**, 121503 (2006), [gr-qc/0612142](#).
- [102] L. Rezzolla (2007), Private communication.
- [103] A. Burrows, L. Dessart, E. Livne, C. D. Ott and J. Murphy, *Simulations of Magnetically-Driven Supernova and Hypernova Explosions in the Context of Rapid Rotation* (2007), [astro-ph/0702539](#).
- [104] A. Burrows, E. Livne, L. Dessart, C. Ott and J. Murphy, *A New Mechanism for Core-Collapse Supernova Explosions*, Astrophys. J. **640**, 878 (2006), [astro-ph/0510687](#).
- [105] C. D. Ott et al., *3D Collapse of Rotating Stellar Iron Cores in General Relativity including Deleptonization and a Nuclear Equation of State*, Phys. Rev. Lett. **98**, 261101 (2007), [astro-ph/0609819](#).
- [106] H. Dimmelmeier, C. D. Ott, H.-T. Janka, A. Marek and E. Mueller, *Generic gravitational wave signals from the collapse of rotating stellar cores*, Phys. Rev. Lett. **98**, 251101 (2007), [astro-ph/0702305](#).
- [107] T. Damour, B. R. Iyer and B. S. Sathyaprakash, *A comparison of search templates for gravitational waves from binary inspiral*, Phys. Rev. D **63**, 044023 (2001), erratum-ibid. **D 72** (2005) 029902, [gr-qc/0010009](#).
- [108] B. J. Owen, *Search templates for gravitational waves from inspiraling binaries: Choice of template spacing*, Phys. Rev. **D53**, 6749 (1996), [gr-qc/9511032](#).

-
- [109] B. S. Sathyaprakash and S. V. Dhurandhar, *Choice of filters for the detection of gravitational waves from coalescing binaries*, Phys. Rev. D **44** 12, 3819 (1991).
- [110] S. V. Dhurandhar and B. S. Sathyaprakash, *Choice of filters for the detection of gravitational waves from coalescing binaries. II. Detection in colored noise*, Phys. Rev. D **49** 4, 1707 (1994).
- [111] B. S. Sathyaprakash, *Filtering post-Newtonian gravitational waves from coalescing binaries*, Phys. Rev. D **50** 12, R7111 (1994).
- [112] A. Buonanno, Y. Chen and M. Vallisneri, *Detection template families for gravitational waves from the final stages of binary-black-hole inspirals. I: Nonspinning case*, Phys. Rev. **D67**, 024016 (2003), [gr-qc/0205122](#).
- [113] A. Buonanno, Y. Chen and M. Vallisneri, *Detecting gravitational waves from precessing binaries of spinning compact objects: Adiabatic limit*, Phys. Rev. **D67**, 104025 (2003), [gr-qc/0211087](#).
- [114] W. G. Anderson, P. R. Brady, J. D. E. Creighton and E. E. Flanagan, *An excess power statistic for detection of burst sources of gravitational radiation*, Phys. Rev. **D63**, 042003 (2001), [gr-qc/0008066](#).
- [115] W. G. Anderson, P. R. Brady, J. D. E. Creighton and E. E. Flanagan, *A power filter for the detection of burst sources of gravitational radiation in interferometric detectors*, Int. J. Mod. Phys. **D9**, 303 (2000), [gr-qc/0001044](#).
- [116] J. Sylvestre, *Time-frequency detection algorithm for gravitational wave bursts*, Phys. Rev. **D66**, 102004 (2002), [gr-qc/0210043](#).
- [117] S. Klimenko and G. Mitselmakher, *A wavelet method for detection of gravitational wave bursts*, Class. Quant. Grav. **21**, S1819 (2004).
- [118] T. Pradier et al., *An efficient filter for detecting gravitational wave bursts in interferometric detectors*, Phys. Rev. **D63**, 042002 (2001), [gr-qc/0010037](#).
- [119] T. Pradier et al., *About the detection of gravitational wave bursts*, Int. J. Mod. Phys. **D9**, 309 (2000), [gr-qc/0001062](#).
- [120] W. G. Anderson and R. Balasubramanian, *Time-frequency detection of gravitational waves*, Phys. Rev. **D60**, 102001 (1999), [gr-qc/9905023](#).
- [121] S. Chatterji, L. Blackburn, G. Martin and E. Katsavounidis, *Multiresolution techniques for the detection of gravitational-wave bursts*, Class. Quant. Grav. **21**, S1809 (2004), [gr-qc/0412119](#).
- [122] A. Pai, S. Dhurandhar and S. Bose, *A data-analysis strategy for detecting gravitational-wave signals from inspiraling compact binaries with a network of laser-interferometric detectors*, Phys. Rev. **D64**, 042004 (2001), [gr-qc/0009078](#).
- [123] S. Klimenko, S. Mohanty, M. Rakhmanov and G. Mitselmakher, *Constraint likelihood analysis for a network of gravitational wave detectors*, Phys. Rev. **D72**, 122002 (2005), [gr-qc/0508068](#).

- [124] K. Hayama, S. D. Mohanty, M. Rakhmanov and S. Desai, *Coherent network analysis for triggered gravitational wave burst searches*, Class. Quant. Grav. **24**, S681 (2007), [arXiv:0709.0940\[gr-qc\]](#).
- [125] L. Cadonati, *Coherent waveform consistency test for LIGO burst candidates*, Class. Quant. Grav. **21**, S1695 (2004), [gr-qc/0407031](#).
- [126] L. Wen and B. F. Schutz, *Coherent network detection of gravitational waves: The redundancy veto*, Class. Quant. Grav. **22**, S1321 (2005), [gr-qc/0508042](#).
- [127] S. Chatterji et al., *Coherent network analysis technique for discriminating gravitational-wave bursts from instrumental noise*, Phys. Rev. **D74**, 082005 (2006), [gr-qc/0605002](#).
- [128] P. Ajith, M. Hewitson and I. S. Heng, *Null-stream veto for two co-located detectors: Implementation issues*, Class. Quant. Grav. **23**, S741 (2006), [gr-qc/0604004](#).
- [129] S. D. Mohanty and S. V. Dhurandhar, *Hierarchical search strategy for the detection of gravitational waves from coalescing binaries*, Phys. Rev. D **54** 12, 7108 (1996).
- [130] A. S. Sengupta, S. Dhurandhar and A. Lazzarini, *A faster implementation of the hierarchical search algorithm for detection of gravitational waves from inspiraling compact binaries*, Phys. Rev. **D67**, 082004 (2003), [gr-qc/0301025](#).
- [131] <http://einstein.phys.uwm.edu/>.
- [132] M. H. (for the LIGO Scientific Collaboration), *Detector and data characterization at GEO 600*, Classical and Quantum Gravity **24** 19, S445 (2007).
URL <http://stacks.iop.org/0264-9381/24/S445>
- [133] F. Acernese et al., *Data quality studies for burst analysis of Virgo data acquired during Weekly Science Runs*, Classical and Quantum Gravity **24** 19, S415 (2007).
URL <http://stacks.iop.org/0264-9381/24/S415>
- [134] L. Cadonati, *Data Quality Vetos in LIGO S5 Searches for Gravitational Wave Transients* (2006), Presented at the 11th Gravitational-Wave Data Analysis Workshop, Potsdam, Germany. LIGO DCC number G060628-00.
- [135] E. Katsavounidis, *Glitch and veto studies in LIGO's S5 search for gravitational wave bursts* (2006), Presented at the 11th Gravitational-Wave Data Analysis Workshop, Potsdam, Germany. LIGO DCC number G060628-00.
- [136] B. Allen, *A χ^2 time-frequency discriminator for gravitational wave detection*, Phys. Rev. **D71**, 062001 (2005), [gr-qc/0405045](#).
- [137] S. Babak, H. Grote, M. Hewitson, H. Luck and K. A. Strain, *Signal based vetoes for the detection of gravitational waves from inspiralling compact binaries*, Phys. Rev. **D72**, 022002 (2005), [gr-qc/0502002](#).
- [138] C. R. Hanna, *Reducing gravitational wave false alarms using signals at the anti-symmetric port in LIGO detectors*, Class. Quant. Grav. **23**, S17 (2006).

-
- [139] K. Kotter et al., *PQMon: A powerful veto for burst events*, *Class. Quant. Grav.* **20**, S895 (2003).
- [140] M. Hewitson and P. Ajith, *Using the null-stream of GEO 600 to veto transient events in the detector output*, *Class. Quant. Grav.* **22**, 4903 (2005).
- [141] P. Ajith et al., *Physical instrumental vetoes for gravitational-wave burst triggers* (2007), [arXiv:0705.1111\[gr-qc\]](https://arxiv.org/abs/0705.1111).
- [142] A. Di Credico, *Gravitational wave burst vetoes in the LIGO S2 and S3 data analyses*, *Class. Quant. Grav.* **22**, S1051 (2005), [gr-qc/0504106](https://arxiv.org/abs/gr-qc/0504106).
- [143] S. Hild, P. Ajith, M. Hewitson, H. Grote and J. R. Smith, *A statistical veto method employing an amplitude consistency check*, *Class. Quant. Grav.* **24** 15, 3783 (2007). URL <http://stacks.iop.org/0264-9381/24/3783>
- [144] T. Akutsu et al., *Veto analysis for gravitational wave burst signals in TAMA300 data using an ALF filter*, *Class. Quant. Grav.* **23**, S23 (2006).
- [145] *QScan*.
URL <http://www.ligo.caltech.edu/~shourov/q/qscan/>
- [146] Y. Gürsel and M. Tinto, *Near optimal solution to the inverse problem for gravitational-wave bursts*, *Phys. Rev. D* **40** 12, 3884 (1989).
- [147] R. Balasubramanian et al., *Results from the first burst hardware injections performed on GEO 600*, *Class. Quant. Grav.* **22**, 3015 (2005).
- [148] I. S. Heng, R. Balasubramanian, B. S. Sathyaprakash and B. F. Schutz, *First steps towards characterizing the hierarchical algorithm for curves and ridges pipeline*, *Class. Quant. Grav.* **21**, S821 (2004).
- [149] R. Salvador, J. Valeriano, X. Pons and R. Diaz-Delgado, *A semi-automatic methodology to detect fire scars in shrubs and evergreen forests with Landsat MSS time series*, *Int. J. of Remote Sensing* **21**, 655 (2000).
- [150] P. Fischer, A. Helmich, M. Lindner, N. Wermes and L. Blanquart, *A photon counting pixel chip with energy windowing*, *IEEE Trans. on Nuclear Science* **47**, 881 (2000).
- [151] R. Balasubramanian, S. Babak, D. Churches and T. Cokelaer, *GEO600 on-line detector characterization system*, *Class. Quant. Grav.* **22**, 4973 (2005), [gr-qc/0504140](https://arxiv.org/abs/gr-qc/0504140).
- [152] *GEO Summary Reports*.
URL <http://www.geo600.uni-hannover.de/georeports/>
- [153] S. W. Smith, *The Scientist and Engineer's Guide to Digital Signal Processing*, California Technical Publishing (1997), available at www.dspguide.com.
URL <http://www.dspguide.com>

- [154] J. R. Smith et al., *Linear projection of technical noise for interferometric gravitational-wave detectors*, *Class. Quant. Grav.* **23**, 527 (2006).
- [155] G. B. Arfken and H. J. Weber, *Mathematical methods for physicists*, Academic Press (2001).
- [156] P. Johnson and D. Long, *The Probability Density of Spectral Estimates Based on Modified Periodogram Averages*, *IEEE Transactions on Signal Processing* **47**, 1255 (1999).
- [157] R. A. Fisher, *Biometrika* **10**, 507 (1915).
- [158] P. R. Bevington and D. K. Robinson, *Data Reduction and Error Analysis for the Physical Sciences*, McGraw Hill, second edition (1992).
- [159] J. R. Smith, *Formulation of Instrument Noise Analysis Techniques and Their Use in the Commissioning of the Gravitational Wave Observatory, GEO600*, Ph.D. thesis, University of Hannover (2006).
- [160] L. L. Scharf, *Statistical signal processing: detection, estimation, and time series analysis*, Addison-Wesley (1991).
- [161] A. Lazzarini et al., *Optimal combination of signals from co-located gravitational wave interferometers for use in searches for a stochastic background*, *Phys. Rev. D* **70**, 062001 (2004), [gr-qc/0403093](#).
- [162] M. Hewitson et al., *Optimal time-domain combination of the two calibrated output quadratures of GEO 600*, *Class. Quant. Grav.* **22**, 4253 (2005).
- [163] G. Heinzl, A. Freise, H. Grote, K. Strain and K. Danzmann, *Dual recycling for GEO 600*, *Class. Quant. Grav.* **19**, 1547 (2002).
- [164] H. Grote et al., *Dual recycling for GEO 600*, *Class. Quant. Grav.* **21**, S473 (2004).
- [165] M. Hewitson et al., *Calibration of the power-recycled gravitational wave detector, GEO 600*, *Rev. Sci. Instrum.* **74**, 4184 (2003).
- [166] M. Hewitson, G. Heinzl, J. R. Smith, K. A. Strain and H. Ward, *Principles of calibrating the dual-recycled GEO 600*, *Rev. Sci. Instrum.* **75**, 4702 (2004).
- [167] T. Damour, B. R. Iyer and B. S. Sathyaprakash, *Improved filters for gravitational waves from inspiraling compact binaries*, *Phys. Rev. D* **57**, 885 (1998).
- [168] A. Buonanno and T. Damour, *Effective one-body approach to general relativistic two-body dynamics*, *Phys. Rev. D* **59**, 084006 (1999), [gr-qc/9811091](#).
- [169] F. Herrmann, I. Hinder, D. Shoemaker and P. Laguna, *Unequal-Mass Binary Black Hole Plunges*, *Class. Quantum Gravity* **24**, S33 (2007).
- [170] U. Sperhake, *Binary black-hole evolutions of excision and puncture data* (2006), [gr-qc/0606079](#).

-
- [171] B. Brügmann, J. A. González, M. Hannam, S. Husa, U. Sperhake and W. Tichy, *Calibration of Moving Puncture Simulations* (2006), [gr-qc/0610128](#).
- [172] J. Thornburg, P. Diener, D. Pollney, L. Rezzolla, E. Schnetter, E. Seidel and R. Takahashi, *Are moving punctures equivalent to moving black holes?*, *Class. Quantum Grav.* **24**, 3911 (2007), [gr-qc/0701038](#).
- [173] Z. B. Etienne, J. A. Faber, Y. T. Liu, S. L. Shapiro and T. W. Baumgarte, *Filling the holes: Evolving excised binary black hole initial data with puncture techniques* (2007), [arXiv:0707.2083\[gr-qc\]](#).
- [174] J. G. Baker, J. Centrella, D.-I. Choi, M. Koppitz, J. van Meter and M. C. Miller, *Getting a kick out of numerical relativity*, *Astrophys. J* (2007), [astro-ph/0603204](#).
- [175] J. A. González, U. Sperhake, B. Brügmann, M. Hannam and S. Husa, *Total recoil: the maximum kick from nonspinning black-hole binary inspiral*, *Phys. Rev. Lett.* **98**, 091101 (2007), [gr-qc/0610154](#).
- [176] M. Campanelli, C. O. Lousto and Y. Zlochower, *Gravitational radiation from spinning-black-hole binaries: The orbital hang up*, *Phys. Rev. D* **74**, 041501 (2006), [gr-qc/0604012](#).
- [177] M. Campanelli, C. O. Lousto and Y. Zlochower, *Spin-orbit interactions in black-hole binaries*, *Phys. Rev. D* **74**, 084023 (2006), [gr-qc/0608275](#).
- [178] F. Herrmann, I. Hinder, D. Shoemaker, P. Laguna and R. A. Matzner, *Gravitational recoil from spinning binary black hole mergers* (2007), [gr-qc/0701143](#).
- [179] M. Koppitz, D. Pollney, C. Reisswig, L. Rezzolla, J. Thornburg, P. Diener and E. Schnetter, *Getting a kick from equal-mass binary black hole mergers* (2007), [gr-qc/0701163](#), [gr-qc/0701163](#).
- [180] J. A. González, M. D. Hannam, U. Sperhake, B. Brügmann and S. Husa, *Supermassive Recoil Velocities for Binary Black-Hole Mergers with Antialigned Spins*, *Phys. Rev. Lett.* **98** 23, 231101 (2007), [gr-qc/0702052](#).
- [181] M. Campanelli, C. O. Lousto, Y. Zlochower and D. Merritt, *Large Merger Recoils and Spin Flips From Generic Black-Hole Binaries*, *Astrophys. J.* **659**, L5 (2007), [gr-qc/0701164](#).
- [182] M. Campanelli, C. O. Lousto, Y. Zlochower, B. Krishnan and D. Merritt, *Spin Flips and Precession in Black-Hole-Binary Mergers*, *Phys. Rev.* **D75**, 064030 (2007), [gr-qc/0612076](#).
- [183] D. Pollney et al., *Recoil velocities from equal-mass binary black-hole mergers: a systematic investigation of spin-orbit aligned configurations* (2007), [arXiv:0707.2559\[gr-qc\]](#).
- [184] L. Rezzolla, E. N. Dorband, C. Reisswig, P. Diener, D. Pollney, E. Schnetter and B. Szilágyi, *Spin Diagrams for equal-mass black-hole binaries with aligned spins* (2007), [arXiv:0708.3999\[gr-qc\]](#).

- [185] J. G. Baker, J. Centrella, D.-I. Choi, M. Koppitz and J. van Meter, *Binary black hole merger dynamics and waveforms*, Phys. Rev. D **73**, 104002 (2006), [gr-qc/0602026](#).
- [186] J. G. Baker, J. R. van Meter, S. T. McWilliams, J. Centrella and B. J. Kelly, *Consistency of post-Newtonian waveforms with numerical relativity* (2006), [gr-qc/0612024](#).
- [187] A. Buonanno, G. B. Cook and F. Pretorius, *Inspiral, merger and ring-down of equal-mass black-hole binaries*, Phys. Rev. **D75**, 124018 (2007), [gr-qc/0610122](#).
- [188] E. Berti et al., *Inspiral, merger and ringdown of unequal mass black hole binaries: A multipolar analysis* (2007), [gr-qc/0703053](#).
- [189] Y. Pan et al., *A data-analysis driven comparison of analytic and numerical coalescing binary waveforms: Nonspinning case* (2007), arXiv:0704.1964 [gr-qc], [arXiv:0704.1964\[gr-qc\]](#).
- [190] P. Ajith et al., *Phenomenological template family for black-hole coalescence waveforms*, Class. Quant. Grav. **24**, S689 (2007), [arXiv:0704.3764\[gr-qc\]](#).
- [191] M. Hannam, S. Husa, U. Sperhake, B. Brügmann and J. A. González, *Where post-Newtonian and numerical-relativity waveforms meet* (2007), [arXiv:0706.1305\[gr-qc\]](#).
- [192] M. Boyle et al., *High-accuracy comparison of numerical relativity simulations with post-Newtonian expansions* (2007), [arXiv:0710.0158\[gr-qc\]](#).
- [193] B. Brügmann, J. A. Gonzalez, M. Hannam, S. Husa and U. Sperhake, *Exploring black hole superkicks* (2007), [arXiv:0707.0135\[gr-qc\]](#).
- [194] C. O. Lousto and Y. Zlochower, *Further insight into gravitational recoil* (2007), [arXiv:0708.4048\[gr-qc\]](#).
- [195] M. A. Scheel, H. P. Pfeiffer, L. Lindblom, L. E. Kidder, O. Rinne and S. A. Teukolsky, *Solving Einstein's Equations With Dual Coordinate Frames*, Phys. Rev. D **74**, 104006 (2006), [gr-qc/0607056](#).
- [196] H. P. Pfeiffer, D. Brown, L. E. Kidder, L. Lindblom, G. Lovelance and M. A. Scheel, *Reducing orbital eccentricity in binary black hole simulations* (2007), [gr-qc/0702106](#).
- [197] S. Husa, J. A. González, M. Hannam, B. Brügmann and U. Sperhake, *Reducing phase error in long numerical binary black hole evolutions with sixth order finite differencing* (2007), [arXiv:0706.0740\[gr-qc\]](#).
- [198] S. Husa, M. Hannam, J. A. González, U. Sperhake and B. Brügmann, *Reducing eccentricity in black-hole binary evolutions with initial parameters from post-Newtonian inspiral* (2007), [arXiv:0706.0904\[gr-qc\]](#).
- [199] A. Buonanno et al., *Toward faithful templates for non-spinning binary black holes using the effective-one-body approach* (2007), [arXiv:0706.3732\[gr-qc\]](#).

-
- [200] E. Berti, J. Cardoso, V. Cardoso and M. Cavaglia, *Matched-filtering and parameter estimation of ringdown waveforms* (2007), [arXiv:0707.1202\[gr-qc\]](#).
- [201] P. Ajith et al., *Parameter estimation using binary black hole coalescence waveforms* (2007), in preparation.
- [202] K. G. Arun, B. R. Iyer, B. S. Sathyaprakash, S. Sinha and C. V. D. Broeck, *Higher signal harmonics, LISA's angular resolution and dark energy* (2007), [arXiv:0707.3920\[astro-ph\]](#).
- [203] D. R. Brill and R. W. Lindquist, *Interaction energy in geometrostatics*, Phys. Rev. **131**, 471 (1963).
- [204] J. M. Bowen and J. W. York, *Time-Asymmetric Initial Data for Black Holes and Black Hole Collisions*, Phys. Rev. D **21** 8, 2047 (1980).
- [205] S. Brandt and B. Brügmann, *A Simple Construction of Initial Data for Multiple Black Holes*, Phys. Rev. Lett. **78** 19, 3606 (1997), [gr-qc/9703066](#).
- [206] T. Nakamura, K. Oohara and Y. Kojima, *General Relativistic Collapse to Black Holes and Gravitational Waves from Black Holes*, Prog. Theor. Phys. Suppl. **90**, 1 (1987).
- [207] M. Shibata and T. Nakamura, *Evolution of three-dimensional gravitational waves: Harmonic slicing case*, Phys. Rev. D **52**, 5428 (1995).
- [208] T. W. Baumgarte and S. L. Shapiro, *On the numerical integration of Einstein's field equations*, Phys. Rev. D **59**, 024007 (1999), [gr-qc/9810065](#).
- [209] C. Bona, J. Massó, E. Seidel and J. Stela, *New Formalism for Numerical Relativity*, Phys. Rev. Lett. **75**, 600 (1995), [gr-qc/9412071](#).
- [210] M. Alcubierre, B. Brügmann, P. Diener, M. Koppitz, D. Pollney, E. Seidel and R. Takahashi, *Gauge conditions for long-term numerical black hole evolutions without excision*, Phys. Rev. D **67**, 084023 (2003), [gr-qc/0206072](#).
- [211] M. Alcubierre and B. Brügmann, *Simple excision of a black hole in 3+1 numerical relativity*, Phys. Rev. D **63**, 104006 (2001), [gr-qc/0008067](#).
- [212] M. Hannam, S. Husa, D. Pollney, B. Brügmann and N. Ó Murchadha, *Geometry and Regularity of Moving Punctures* (2006), [gr-qc/0606099](#).
- [213] E. Schnetter, B. Krishnan and F. Beyer, *Introduction to dynamical horizons in numerical relativity*, Phys. Rev. D **74**, 024028 (2006), [gr-qc/0604015](#).
- [214] K. A. Dennison, T. W. Baumgarte and H. P. Pfeiffer, *Approximate initial data for binary black holes*, Phys. Rev. **D74**, 064016 (2006), [gr-qc/0606037](#).
- [215] W. Tichy and B. Brügmann, *Quasi-equilibrium binary black hole sequences for puncture data derived from helical Killing vector conditions*, Phys. Rev. D **69**, 024006 (2004), [gr-qc/0307027](#).

- [216] G. B. Cook, *Three-dimensional initial data for the collision of two black holes II: Quasi-circular orbits for equal-mass black holes*, Phys. Rev. D **50** 8, 5025 (1994).
- [217] T. W. Baumgarte, *Innermost stable circular orbit of binary black holes*, Phys. Rev. D **62**, 024018 (2000), [gr-qc/0004050](#).
- [218] E. T. Newman and R. Penrose, *An Approach to Gravitational Radiation by a Method of Spin Coefficients*, J. Math. Phys. **3** 3, 566 (1962), erratum in J. Math. Phys. **4**, 998 (1963).
- [219] J. M. Stewart, *Advanced general relativity* (1990).
- [220] A. Nagar and L. Rezzolla, *Gauge-invariant non-spherical metric perturbations of Schwarzschild black-hole spacetimes*, Class. Quant. Grav. **22**, R167 (2005), [gr-qc/0502064](#).
- [221] L. Blanchet, *Gravitational Radiation from Post-Newtonian Sources and Inspiralling Compact Binaries*, Living Reviews in Relativity **9** 4 (2006), [gr-qc/0202016](#).
URL <http://www.livingreviews.org/lrr-2006-4>
- [222] T. Damour, P. Jaranowski and G. Schäfer, *Dynamical invariants for general relativistic two-body systems at the third post-Newtonian approximation*, Phys. Rev. D **62** 4, 044024 (2000).
- [223] T. Damour, P. Jaranowski and G. Schäfer, *Equivalence between the ADM-Hamiltonian and the harmonic-coordinates approaches to the third post-Newtonian dynamics of compact binaries*, Phys. Rev. D **63**, 044021 (2001), erratum-ibid **66**, 029901(E) (2002).
- [224] L. Blanchet and G. Faye, *Equations of motion of point-particle binaries at the third post-Newtonian order*, Phys. Lett. A **271**, 58 (2000), [gr-qc/0004009](#).
- [225] L. Blanchet and G. Faye, *General relativistic dynamics of compact binaries at the third post-Newtonian order*, Phys. Rev. D **63**, 062005 (2001), [gr-qc/0007051](#).
- [226] V. de Andrade, L. Blanchet and G. Faye, *Third post-Newtonian dynamics of compact binaries: Noetherian conserved quantities and equivalence between the harmonic-coordinate and ADM-Hamiltonian formalisms*, Class. Quantum Grav. **18**, 753 (2001).
- [227] L. Blanchet, T. Damour and G. Esposito-Farèse, *Dimensional regularization of the third post-Newtonian dynamics of point particles in harmonic coordinates*, Phys. Rev. D **69**, 124007 (2004), [gr-qc/0311052](#).
- [228] Y. Itoh and T. Futamase, *New derivation of a third post-Newtonian equation of motion for relativistic compact binaries without ambiguity*, Phys. Rev. D **68**, 121501(R) (2003).
- [229] Y. Itoh, *Equation of motion for relativistic compact binaries with the strong field point particle limit: Third post-Newtonian order*, Phys. Rev. D **69**, 064018 (2004).

-
- [230] L. Blanchet, G. Faye, B. R. Iyer and B. Joguet, *Gravitational-wave inspiral of compact binary systems to $7/2$ post-Newtonian order*, Phys. Rev. D **65**, 061501(R) (2002), Erratum-ibid **71**, 129902(E) (2005), [gr-qc/0105099](#).
- [231] L. Blanchet, *Innermost circular orbit of binary black holes at the third post-Newtonian approximation*, Phys. Rev. D **65** 12, 124009 (2002).
- [232] C. Cutler and E. E. Flanagan, *Gravitational waves from merging compact binaries: How accurately can one extract the binary's parameters from the inspiral wave form?*, Phys. Rev. **D49**, 2658 (1994), [gr-qc/9402014](#).
- [233] S. Babak, R. Balasubramanian, D. Churches, T. Cokelaer and B. S. Sathyaprakash, *A template bank to search for gravitational waves from inspiralling compact binaries. I: Physical models*, Class. Quant. Grav. **23**, 5477 (2006), [gr-qc/0604037](#).
- [234] B. Abbott et al., *Search for gravitational waves from binary black hole inspirals in LIGO data*, Phys. Rev. **D73**, 062001 (2006), [gr-qc/0509129](#).
- [235] T. A. Apostolatos, *Search templates for gravitational waves from precessing, inspiraling binaries*, Phys. Rev. **D52**, 605 (1995).
- [236] P. Ajith et al., *Gravitational-wave data analysis using numerical-relativity waveforms* (2007), in preparation.
- [237] <http://www.lsc-group.phys.uwm.edu/daswg/projects/lal.html>.
- [238] B. Schutz, *Data processing, analysis and storage for interferometric antennas*, in D. Blair, editor, *The Detection of Gravitational Waves*, pp. 406–452, Cambridge University Press, Cambridge, U.K.; New York, U.S.A. (1991).
- [239] J. Nelder and R. Mead, *A simplex method for function minimization*, The Computer Journal **7**, 308 (1964).
- [240] L. M. Goggin, *Search for black hole ringdown signals in LIGO S4 data*, Class. Quant. Grav. **23**, S709 (2006).
- [241] B. Allen and B. Sathyaprakash, private Communication.
- [242] J. G. Baker, M. Campanelli, F. Pretorius and Y. Zlochower, *Comparisons of binary black hole merger waveforms*, Class. Quant. Grav. **24**, S25 (2007), [gr-qc/0701016](#).
- [243] S. J. W. (for the LIGO Science Collaboration), *Status of LIGO at the start of the fifth science run*, Classical and Quantum Gravity **23** 19, S653 (2006).
URL <http://stacks.iop.org/0264-9381/23/S653>
- [244] F. Acernese et al., *The Virgo status*, Classical and Quantum Gravity **23** 19, S635 (2006).
URL <http://stacks.iop.org/0264-9381/23/S635>
- [245] S. H. (for the LIGO Scientific Collaboration), *The status of GEO 600*, Classical and Quantum Gravity **23** 19, S643 (2006).
URL <http://stacks.iop.org/0264-9381/23/S643>

- [246] M. Ando and the TAMA Collaboration, *Current status of the TAMA300 gravitational-wave detector*, Classical and Quantum Gravity **22** 18, S881 (2005). URL <http://stacks.iop.org/0264-9381/22/S881>
- [247] T. Damour, B. R. Iyer and B. S. Sathyaprakash, *A comparison of search templates for gravitational waves from binary inspiral*, Phys. Rev. **D63**, 044023 (2001), [gr-qc/0010009](#).
- [248] E. Poisson, *Gravitational-radiation from a particle in circular orbit around a black-hole. I. Analytical results for the nonrotating case*, Phys. Rev. D **47**, 1497 (1993).
- [249] E. Poisson, *Gravitational radiation from a particle in circular orbit around a black-hole. VI. Accuracy of the post-Newtonian expansion*, Phys. Rev. D **52**, 5719 (1995), erratum Phys. Rev. D **55**, 7980, (1997).
- [250] H. Tagoshi and T. Nakamura, *Gravitational waves from a point particle in circular orbit around a black hole: Logarithmic terms in the post-Newtonian expansion*, Phys. Rev. D **49**, 4016 (1994).
- [251] M. Shibata, *Gravitational waves induced by a particle orbiting around a rotating black hole: Spin-orbit interaction effect*, Phys. Rev. D **48** 2, 663 (1993).
- [252] T. Tanaka, H. Tagoshi and M. Sasaki, *Gravitational Waves by a Particle in Circular Orbit around a Schwarzschild Black Hole*, Prog. Theor. Phys. **96**, 1087 (1996).
- [253] H. T. Misao Sasaki, *Analytic Black Hole Perturbation Approach to Gravitational Radiation*, Living Reviews in Relativity **6** 6 (2003). URL <http://www.livingreviews.org/lrr-2003-6>
- [254] T. Damour, P. Jaranowski and G. Schäfer, *On the determination of the last stable orbit for circular general relativistic binaries at the third post-Newtonian approximation*, Phys. Rev. D **62**, 084011 (2000), [gr-qc/0005034](#).
- [255] T. Damour, P. Jaranowski and G. Schäfer, *Poincaré invariance in the ADM Hamiltonian approach to the general relativistic two-body problem*, Phys. Rev. D **62**, 021501(R) (2000), erratum-ibid **63**, 029903(E) (2000).
- [256] T. Damour, P. Jaranowski and G. Schäfer, *Dimensional regularization of the gravitational interaction of point masses*, Phys. Lett. B **513**, 147 (2001).
- [257] L. Blanchet, T. Damour, B. R. Iyer, C. M. Will and A. G. Wiseman, *Gravitational radiation damping of compact binary systems to second post-Newtonian order*, Phys. Rev. Lett. **74**, 3515 (1995), [gr-qc/9501027](#).
- [258] L. Blanchet, T. Damour and B. R. Iyer, *Gravitational waves from inspiralling compact binaries: Energy loss and wave form to second post-Newtonian order*, Phys. Rev. D **51**, 5360 (1995), [gr-qc/9501029](#).
- [259] L. Blanchet, B. R. Iyer, C. M. Will and A. G. Wiseman, *Gravitational wave forms from inspiralling compact binaries to second-post-Newtonian order*, Class. Quantum Grav. **13**, 575 (1996), [gr-qc/9602024](#).

-
- [260] C. Will and A. Wiseman, *Gravitational radiation from compact binary systems: Gravitational waveforms and energy loss to second post-Newtonian order*, Phys. Rev. D **54**, 4813 (1996).
- [261] L. Blanchet, *Energy losses by gravitational radiation in inspiralling compact binaries to five halves post-Newtonian order*, Phys. Rev. D **54**, 1417 (1996), Erratum-ibid. **71**, 129904(E) (2005), [gr-qc/9603048](#).
- [262] L. Blanchet, B. R. Iyer and B. Joguet, *Gravitational waves from inspiralling compact binaries: Energy flux to third post-Newtonian order*, Phys. Rev. D **65**, 064005 (2002), Erratum-ibid **71**, 129903(E) (2005), [gr-qc/0105098](#).
- [263] L. Blanchet and B. R. Iyer, *Hadamard regularization of the third post-Newtonian gravitational wave generation of two point masses*, Phys. Rev. D **71**, 024004 (2005), [gr-qc/0409094](#).
- [264] L. Blanchet, T. Damour and B. R. Iyer, *Surface-integral expressions for the multipole moments of post-Newtonian sources and the boosted Schwarzschild solution*, Class. Quantum Grav. **22**, 155 (2005), [gr-qc/0410021](#).
- [265] C. Cutler and E. Flanagan, *Gravitational waves from merging compact binaries: How accurately can one extract the binary's parameters from the inspiral waveform?*, Phys. Rev. D **49**, 2658 (1994).
- [266] L. Blanchet, *On the accuracy of the post-Newtonian approximation* (2002), in *A relativistic spacetime odyssey*, edited by I. Ciufolini *et al*, World Scientific, p. 411, [gr-qc/0207037](#).
- [267] E. E. Flanagan and S. A. Hughes, *Measuring gravitational waves from binary black hole coalescences. II: The waves' information and its extraction, with and without templates*, Phys. Rev. **D57**, 4566 (1998), [gr-qc/9710129](#).
- [268] E. E. Flanagan and S. A. Hughes, *Measuring gravitational waves from binary black hole coalescences. I. Signal to noise for inspiral, merger, and ringdown*, Phys. Rev. D **57** 8, 4535 (1998).
- [269] A. Buonanno and T. Damour, *Transition from inspiral to plunge in binary black hole coalescences*, Phys. Rev. D **62**, 064015 (2000), [gr-qc/0001013](#).
- [270] A. Buonanno, Y. Chen and M. Vallisneri, *Detection template families for gravitational waves from the final stages of binary black-holes binaries: Nonspinning case*, Phys. Rev. D **67**, 024016 (2003), erratum-ibid. **D 74**, 029903(E) (2006), [gr-qc/0205122](#).
- [271] T. Damour, B. R. Iyer, P. Jaranowski and B. S. Sathyaprakash, *Gravitational waves from black hole binary inspiral and merger: The span of third post-Newtonian effective-one-body templates*, Phys. Rev. D **67**, 064028 (2003), [gr-qc/0211041](#).
- [272] Y. Tsunesada *et al.*, *On detection of black hole quasi-normal ringdowns: Detection*

- efficiency and waveform parameter determination in matched filtering*, Phys. Rev. **D71**, 103005 (2005), [gr-qc/0410037](#).
- [273] T. Damour, B. R. Iyer and B. S. Sathyaprakash, *Frequency-domain P -approximant filters for time-truncated inspiral gravitational wave signals from compact binaries*, Phys. Rev. D **62**, 084036 (2000), [gr-qc/0001023](#).
- [274] T. Damour, B. R. Iyer and B. S. Sathyaprakash, *Comparison of search templates for gravitational waves from binary inspiral: 3.5PN update*, Phys. Rev. D **66** 2, 027502 (2002).
- [275] K. G. Arun, B. R. Iyer, B. S. Sathyaprakash and P. A. Sundararajan, *Parameter estimation of inspiralling compact binaries using 3.5 post-Newtonian gravitational wave phasing: The non-spinning case*, Phys. Rev. D **71**, 084008 (2005), erratum-ibid. **D 72**, 069903 (2005), [gr-qc/0411146](#).
- [276] Y. Mino, M. Sasaki, M. Shibata, H. Tagoshi and T. Tanaka, *Black Hole Perturbation*, Prog. Theor. Phys. Suppl. **128**, 1 (1997).
- [277] F. Pretorius, *Simulation of binary black hole spacetimes with a harmonic evolution scheme*, Class. Quantum Grav. **23**, S529 (2006), [gr-qc/0602115](#).
- [278] M. Campanelli, C. O. Lousto and Y. Zlochower, *The last orbit of binary black holes*, Phys. Rev. D **73**, 061501(R) (2006), [gr-qc/0601091](#).
- [279] U. Sperhake, *Binary black-hole evolutions of excision and puncture data* (2006), [gr-qc/0606079](#).
- [280] M. Koppitz et al., *Getting a kick from equal-mass binary black hole mergers* (2007), [gr-qc/0701163](#).
- [281] L. E. Kidder, C. M. Will and A. G. Wiseman, *Coalescing binary systems of compact objects to (post) $^{\frac{5}{2}}$ -Newtonian order. III. Transition from inspiral to plunge*, Phys. Rev. D **47** 8, 3281 (1993).
- [282] C. M. W. L E Kidder and A. G. Wiseman, *Innermost stable orbits for coalescing binary systems of compact objects*, Classical and Quantum Gravity **9** 9, L125 (1992).
URL <http://stacks.iop.org/0264-9381/9/L125>
- [283] F. Echeverria, *Gravitational-wave measurements of the mass and angular momentum of a black hole*, Phys. Rev. D **40** 10, 3194 (1989).
- [284] E. E. Flanagan and S. A. Hughes, *Measuring gravitational waves from binary black hole coalescences. I: Signal to noise for inspiral, merger, and ringdown*, Phys. Rev. **D57**, 4535 (1998), [gr-qc/9701039](#).
- [285] L. Goggin, *hpeak calculation* (2005), LSC Internal document.
- [286] S. A. Hughes, *Untangling the merger history of massive black holes with LISA*, Mon. Not. Roy. Astron. Soc. **331**, 805 (2002), [astro-ph/0108483](#).

- [287] C. L. Fryer, D. E. Holz and S. A. Hughes, *Gravitational wave emission from core-collapse of massive stars*, *Astrophys. J.* **565**, 430 (2002), [astro-ph/0106113](#).

□

Acknowledgments

This thesis would not have materialized if not for the invaluable help of a number of individuals and institutions. Firstly, I would like to thank Bernard Schutz for giving me the opportunity to work at one of the finest places in the world for doing Physics, and for his aid and guidance throughout my Ph.D. I am also grateful to Karsten Danzmann and Bruce Allen for their constant encouragement and support.

In the last three years, Martin Hewitson has been my closest adviser and collaborator. I am profoundly grateful to him for his understanding, patience and support. Bala Iyer also has been a close and kind adviser for the last several years.

I had the fortune to collaborate with some of the best people in the field, without whom the work reported in this thesis would not have been possible. Much of the credit goes to Martin Hewitson, Bala Iyer, Yanbei Chen, B. S. Sathyaprakash, Badri Krishnan, Sascha Husa and Mark Hannam. I also thank Stas Babak, Bernd Brügmann, Peter Diener, Nils Dorband, Jose Gonzalez, Hartmut Grote, Siong Heng, Stefan Hild, Michael Koppitz, Harald Lück, Denis Pollney, Luciano Rezzolla, Craig Robinson, Lucia Santamaria, Alicia Sintès, Josh Smith, Ulrich Sperhake, Ken Strain, Jonathan Thornburg, John Whelan and Benno Willke for fruitful collaborations and very useful discussions.

I have also benefited from enlightening discussions with numerous people. I can't help naming Bruce Allen, K. G. Arun, R. Balasubramanian, Sukanta Bose, Chris Van Den Broeck, Duncan Brown, Laura Cadonati, Shourov Chatterji, Jolien Creighton, Steve Fairhurst, Iraj Gholami, Lisa Goggin, Jan Harms, Erik Katsvaunidis, Sergei Klimentko, Archana Pai, Maria Alessandra Papa, Reinhard Prix, Peter Saulson, Peter Shawhan, Patrick Sutton and Linqing Wen. I am also much obliged to the numerical-relativity groups of the Albert Einstein Institute and University of Jena for sharing the results from their simulations of binary black holes. I also have benefited from numerous discussions with many members of the various working groups of the LIGO Scientific Collaboration. Conversations with Albrecht Rüdiger and Roland Schilling were particularly inspiring.

A number of people have helped me to improve the various parts of this thesis by their careful and critical reading, insightful comments and corrections. For this, I would like to thank K. G. Arun, Sukanta Bose, Stas Babak, Yanbei Chen, Mark Hannam, Jan Harms, Martin Hewitson, Sascha Husa, Bala Iyer, Badri Krishnan, Reinhard Prix, Luciano Rezzolla, B. S. Sathyaprakash, Peter Saulson, Peter Shawhan, Alicia Sintès, Josh Smith, Ken Strain and Benno Willke. I am especially grateful to K. G. Arun, Sukanta Bose, Jan Harms, Martin Hewitson, Bala Iyer, Reinhard Prix, Josh Smith and Ken Strain for their careful reading of the final versions. I also extend my gratitude to Luciano Rezzolla and Harry Dimmelmeier for their updates on the status of the numerical simulations

of binary neutron stars and core-collapse supernovae, and Stefan Goßler, Luca Spani Molella and Reinhard Prix for their help in translating the ‘Zusammenfassung’.

I am greatly indebted to the Albert Einstein Institute for the excellent working atmosphere and facilities. I also thank the LIGO Scientific Collaboration for allowing me to use the data of LIGO and GEO 600 detectors. Raman Research Institute, Cardiff University and University of Jena provided me hospitality at various points.

The administrative and supportive staff of the Albert Einstein Institute and the University of Hannover have been extremely helpful throughout these years. I thank Claus Ebert, Walter Graß, Klaus Haupt, Brigitte Hauschild, Heidi Kruppa, Anne Lampe Kirsten Naceur, Sabine Rehmert, Ute Reuter, Karin Salatti-Tara, Ute Schlichting and Susanne Witte for all their help.

Special thanks to Merlin and Morgane for burning their CPU cycles for crunching my numbers, and Steffen Grunewald for administering them! I am also thankful to the computer support and the library staff of the Albert Einstein Institute, in particular, to Konrad Mors and Andreas Donath. Gerrit Kühn has also been so kind to offer help on a number of computer-related problems. I have also benefited from a large amount of software authored by numerous developers. It is almost impossible to count them! But it would be ungrateful to forget Martin Hewitson and the developers of the LSC Algorithms Library. The \LaTeX style file used for this thesis is an ‘uglified’ version of the one written by Andreas Freise.

K. Indulekha, G. V. Vijayagovindan and Sanjeev Dhurandhar were the ones who introduced me to this subject. My friends K. G. Arun and Koshy George updated me over these years on various aspects of gravitational-wave, and traditional astronomy. I am also grateful to Bala Iyer, Sanjeev Dhurandhar, Badri Krishnan, Curt Cutler and Maria Alessandra Papa for helping me to start my graduate studies at the Albert Einstein Institute.

My friends and colleagues made Hannover not only a great place to work, but also a wonderful place to live. I warmly thank all the members of the Albert Einstein Institute. I particularly enjoyed the company of Carsten Aulbert, Felipe Guzmán Cervantes, Jerome Degallaix, James DiGuglielmo, Henning Fehrmann, Stefan Goßler, Hartmut Grote, Jan Harms, Siong Heng, Martin Hewitson, Stefan Hild, Michaela Malec, Chris Messenger, Luca Spani Molella, Rejish Nath, Holger Pletsch, Luciano Ribichini, Josh Smith, Frank Steier, Dipongkar Talukder, Michael Tröbs and many others.

Finally, but immensely, I thank my family back home for their love, understanding and support.

Curriculum Vitae

Ajith Parameswaran
Dieckmannstr. 5, 30171 Hannover, Germany
E-mail: Ajith.Parameswaran@aei.mpg.de
Homepage: <http://www.aei.mpg.de/~ajpram>

Personal profile

Date of Birth : 27 May 1980
Place of Birth : Chemmaniyode, Kerala, India
Sex : Male
Marital Status : Single
Nationality : Indian

Education

Ph. D. Physics: Max Planck Institute for Gravitational Physics (Albert Einstein Institute) and Leibniz University of Hannover, Hannover, Germany. (2004 – 2007)

M. Sc. Physics (Astrophysics): School of Pure and Applied Physics, Mahatma Gandhi University, Kottayam, India. (2000 – 2003).

B. Sc. Physics: University of Calicut, Calicut, India. (1997 – 2000).

Pre Degree (Physics, Mathematics, Chemistry): University of Calicut, Calicut, India. (1995 – 1997).

Secondary School: R. M. High School, Melattur, Kerala, India. (1990 – 1995).

Primary School: Govt. L. P. School, Chemmaniyode, Kerala, India. (1985 – 1990).

Research experience

- ↪ Graduate student at the Max Planck Institute for Gravitational Physics (Albert Einstein Institute), Hannover, Germany (November 2004 – December 2007).
- ↪ Visiting student at the Max Planck Institute for Gravitational Physics (Albert Einstein Institute), Hannover, Germany (July 2004 – October 2004).

- ↪ Visiting student at the Theoretical Physics Group, Raman Research Institute, Bangalore, India (October 2003 – May 2004).
- ↪ Visiting student at the Inter University Center for Astronomy and Astrophysics, Pune, India (Summer 2002).
- ↪ Visiting student at the Theoretical Astrophysics Group, Tata Institute of Fundamental Research, Bombay, India (Summer 2001).

Professional memberships & activities

- ↪ Member, LIGO Scientific Collaboration.
- ↪ Member, GEO Collaboration.
- ↪ Member, Integrated Large Infrastructures for Astroparticle Science-GW Working Group for Data Analysis (WGII).
- ↪ Referee of Classical and Quantum Gravity.

List of Publications

1. P. Ajith, *Gravitational-wave data analysis using binary-black-hole coalescence waveforms*, Invited contribution to the proceedings of Amaldi 7 meeting; To be submitted to *Class. Quantum Grav.* (2007).
2. P. Ajith *et al*, *A template bank for gravitational waveforms from coalescing binary black holes: I. non-spinning binaries*, Submitted to *Phys. Rev. D* (2007), arXiv:0710.2335 [gr-qc].
3. P. Ajith, M. Hewitson, J. R. Smith, H. Grote, S. Hild and K. A. Strain, *Physical instrumental vetoes for gravitational-wave burst triggers*, *Phys. Rev. D* **76** 042004 (2007).
4. P. Ajith *et al*, *Phenomenological template family for black-hole coalescence waveforms*, *Class. Quantum Grav.* **24** S689–S699 (2007).
5. S. Hild, P. Ajith, M. Hewitson, H. Grote and J. R. Smith, *A statistical veto method employing an amplitude consistency test*, *Class. Quantum Grav.* **24** 3783–3798 (2007).
6. P. Ajith, M. Hewitson, J. R. Smith and K. A. Strain, *Robust vetoes for gravitational-wave burst triggers using known instrumental couplings*, *Class. Quantum Grav.* **23** 5825–5837 (2006).
7. P. Ajith, M. Hewitson and I. S. Heng, *Null-stream veto for two co-located detectors: Implementation issues*, *Class. Quantum Grav.* **23** S741–S749 (2006).
8. J R Smith, P Ajith, H Grote, M Hewitson, S Hild, H Lück, K A Strain, B Willke, J Hough and K Danzmann, *Linear projection of technical noise for interferometric gravitational-wave detectors*, *Class. Quantum Grav.* **23** 527–537 (2006).
9. M. Hewitson and P. Ajith, *Using the null-stream of GEO 600 to veto transient events in the detector output*, *Class. Quantum Grav.* **22** 4903–4912 (2005).
10. M. Hewitson, H. Grote, S. Hild, H. Lück, P. Ajith, J. R. Smith, K. A. Strain, B. Wilke and G. Woan, *Optimal time-domain combination of the two calibrated output quadratures of GEO 600*, *Class. Quantum Grav.* **22** 4253–4261 (2005).
11. P. Ajith, B. R. Iyer, C. A. K. Robinson and B. S. Sathyaprakash, *Complete adiabatic waveform templates for a test-mass in the Schwarzschild spacetime: VIRGO and Advanced LIGO studies*, *Class. Quantum Grav.* **22** S1179–S1188 (2005).

12. P. Ajith, B. R. Iyer, C. A. K. Robinson and B. S. Sathyaprakash, *A new class of post-Newtonian approximants to the waveform templates of inspiralling compact binaries: Test-mass in the Schwarzschild spacetime*, Phys. Rev. D **71** 044029 (2005).

Selected publications from the LIGO Scientific Collaboration

1. B. Abbott *et al.* (LIGO Scientific Collaboration and ALLEGRO Collaboration), *First cross-correlation analysis of interferometric and resonant-bar gravitational-wave data for stochastic backgrounds*, Phys. Rev. D **76**, 022001 (2007).
2. B. Abbott *et al.* (LIGO Scientific Collaboration and ALLEGRO Collaboration), *Upper limit map of a background of gravitational waves*, Phys. Rev. D **76**, 082003 (2007).
3. B. Abbott *et al.* (LIGO Scientific Collaboration), *Search for gravitational wave radiation associated with the pulsating tail of the SGR 1806-20 hyperflare of 27 December 2004 using LIGO*, Phys. Rev. D **76**, 062003 (2007).
4. B. Abbott *et al.* (LIGO Scientific Collaboration), *Search for gravitational-wave bursts in LIGO data from the fourth science run*, arXiv:0704.0943 [gr-qc].
5. B. Abbott *et al.* (LIGO Scientific Collaboration), *Upper limits on gravitational wave emission from 78 radio pulsars*, Phys. Rev. D **76**, 042001 (2007).
6. B. Abbott *et al.* (LIGO Scientific Collaboration), *Searching for a stochastic background of gravitational waves with LIGO*, Astrophys. J. **659**, 918 (2007).
7. B. Abbott *et al.* (LIGO Scientific Collaboration), *Coherent searches for periodic gravitational waves from unknown isolated sources and Scorpius X-1: Results from the second LIGO science run*, arXiv:gr-qc/0605028.
8. B. Abbott *et al.* (LIGO Scientific Collaboration and TAMA Collaboration), *Joint LIGO and TAMA300 search for gravitational waves from inspiralling neutron star binaries*, Phys. Rev. D **73**, 102002 (2006).
9. B. Abbott *et al.* (LIGO Scientific Collaboration), *Search for gravitational wave bursts in LIGO's third science run*, Class. Quant. Grav. **23**, S29 (2006).
10. B. Abbott *et al.* (LIGO Scientific Collaboration), *Search for gravitational waves from binary black hole inspirals in LIGO data*, Phys. Rev. D **73**, 062001 (2006).
11. B. Abbott *et al.* (LIGO Scientific Collaboration), *First all-sky upper limits from LIGO on the strength of periodic gravitational waves using the Hough transform*, Phys. Rev. D **72**, 102004 (2005).
12. B. Abbott *et al.* (LIGO Scientific Collaboration and TAMA Collaboration), *Upper limits from the LIGO and TAMA detectors on the rate of gravitational-wave bursts*, Phys. Rev. D **72**, 122004 (2005).

13. B. Abbott *et al.* (LIGO Scientific Collaboration), *Upper limits on a stochastic background of gravitational waves*, Phys. Rev. Lett. **95**, 221101 (2005).

Selected publications from the GEO Collaboration

1. B. Willke *et al.*, *The GEO-HF project*, Class. Quant. Grav. **23**, S207 (2006).
2. H. Luck *et al.*, *Status of the GEO600 detector*, Class. Quant. Grav. **23**, S71 (2006).

Postscript

“I couldn’t afford to learn it.” said the Mock Turtle with a sigh.
“I only took the regular course.”
“What was that?” inquired Alice.
“Reeling and Writhing, of course, to begin with,” the Mock Turtle replied; “and then the different branches of Arithmetic— Ambition, Distraction, Uglification, and Derision.”